Nonlinear Normal Modes and multi-parametric continuation of bifurcations : Application to vibration absorbers and architectured MEMS sensors for mass detection

Clément Grenat

N° d'ordre NNT : 2018LYSEI078

THÈSE de DOCTORAT DE L'UNIVERSITÉ DE LYON
préparée au sein de
l'INSA LYON

École Doctorale ED 162 MEGA
Mécanique, Énergétique, Génie Civil, Acoustique

Spécialité de doctorat :
GÉNIE MÉCANIQUE

Soutenue publiquement le 30/10/2018, par :
Clément GRENAT

Nonlinear Normal Modes and multi-parametric continuation of bifurcations: application to vibration absorbers and architectured MEMS sensors for mass detection

---

Devant le jury composé de

A. TANGUY	Professeur, INSA Lyon	Présidente du jury
S. HENTZ	Habilité à Diriger des Recherches, CEA Leti	Rapporteur
B. COCHELIN	Professeur, École Centrale de Marseille	Rapporteur
E. SARROUY	Maître de Conférences, École Centrale de Marseille	Examinatrice
G. KERSCHEN	Professeur, Université de Liège	Examinateur
R. DUFOUR	Professeur, INSA Lyon	Directeur de thèse
S. BAGUET	Maître de Conférences, INSA Lyon	Co-Directeur
C-H. LAMARQUE	Professeur, ENTPE	Co-Encadrant de thèse

LaMCoS - UMR CNRS 5259 - INSA de Lyon
20, avenue Albert Einstein, 69621 Villeurbanne Cedex (France)

Département FEDORA – INSA Lyon - Ecoles Doctorales – Quinquennal 2016-2020

SIGLE	ECOLE DOCTORALE	NOM ET COORDONNEES DU RESPONSABLE
CHIMIE	**CHIMIE DE LYON** **http://www.edchimie-lyon.fr** Sec. : Renée EL MELHEM Bât. Blaise PASCAL, 3e étage **secretariat@edchimie-lyon.fr** INSA : R. GOURDON	M. Stéphane DANIELE Institut de recherches sur la catalyse et l'environnement de Lyon IRCELYON-UMR 5256 Équipe CDFA 2 Avenue Albert EINSTEIN 69 626 Villeurbanne CEDEX **directeur@edchimie-lyon.fr**
E.E.A.	**ÉLECTRONIQUE, ÉLECTROTECHNIQUE, AUTOMATIQUE** **http://edeea.ec-lyon.fr** Sec. : M.C. HAVGOUDOUKIAN **ecole-doctorale.eea@ec-lyon.fr**	M. Gérard SCORLETTI École Centrale de Lyon 36 Avenue Guy DE COLLONGUE 69 134 Écully Tél : 04.72.18.60.97 Fax 04.78.43.37.17 **gerard.scorletti@ec-lyon.fr**
E2M2	**ÉVOLUTION, ÉCOSYSTÈME, MICROBIOLOGIE, MODÉLISATION** **http://e2m2.universite-lyon.fr** Sec. : Sylvie ROBERJOT Bât. Atrium, UCB Lyon 1 Tél : 04.72.44.83.62 INSA : H. CHARLES **secretariat.e2m2@univ-lyon1.fr**	M. Philippe NORMAND UMR 5557 Lab. d'Ecologie Microbienne Université Claude Bernard Lyon 1 Bâtiment Mendel 43, boulevard du 11 Novembre 1918 69 622 Villeurbanne CEDEX **philippe.normand@univ-lyon1.fr**
EDISS	**INTERDISCIPLINAIRE SCIENCES-SANTÉ** **http://www.ediss-lyon.fr** Sec. : Sylvie ROBERJOT Bât. Atrium, UCB Lyon 1 Tél : 04.72.44.83.62 INSA : M. LAGARDE **secretariat.ediss@univ-lyon1.fr**	Mme Emmanuelle CANET-SOULAS INSERM U1060, CarMeN lab, Univ. Lyon 1 Bâtiment IMBL 11 Avenue Jean CAPELLE INSA de Lyon 69 621 Villeurbanne Tél : 04.72.68.49.09 Fax : 04.72.68.49.16 **emmanuelle.canet@univ-lyon1.fr**
INFOMATHS	**INFORMATIQUE ET MATHÉMATIQUES** **http://edinfomaths.universite-lyon.fr** Sec. : Renée EL MELHEM Bât. Blaise PASCAL, 3e étage Tél : 04.72.43.80.46 Fax : 04.72.43.16.87 **infomaths@univ-lyon1.fr**	M. Luca ZAMBONI Bât. Braconnier 43 Boulevard du 11 novembre 1918 69 622 Villeurbanne CEDEX Tél : 04.26.23.45.52 **zamboni@maths.univ-lyon1.fr**
Matériaux	**MATÉRIAUX DE LYON** **http://ed34.universite-lyon.fr** Sec. : Marion COMBE Tél : 04.72.43.71.70 Fax : 04.72.43.87.12 Bât. Direction **ed.materiaux@insa-lyon.fr**	M. Jean-Yves BUFFIÈRE INSA de Lyon MATEIS - Bât. Saint-Exupéry 7 Avenue Jean CAPELLE 69 621 Villeurbanne CEDEX Tél : 04.72.43.71.70 Fax : 04.72.43.85.28 **jean-yves.buffiere@insa-lyon.fr**
MEGA	**MÉCANIQUE, ÉNERGÉTIQUE, GÉNIE CIVIL, ACOUSTIQUE** **http://edmega.universite-lyon.fr** Sec. : Marion COMBE Tél : 04.72.43.71.70 Fax : 04.72.43.87.12 Bât. Direction **mega@insa-lyon.fr**	M. Jocelyn BONJOUR INSA de Lyon Laboratoire CETHIL Bâtiment Sadi-Carnot 9, rue de la Physique 69 621 Villeurbanne CEDEX **jocelyn.bonjour@insa-lyon.fr**
ScSo	**ScSo*** **http://ed483.univ-lyon2.fr** Sec. : Viviane POLSINELLI Brigitte DUBOIS INSA : J.Y. TOUSSAINT Tél : 04.78.69.72.76 **viviane.polsinelli@univ-lyon2.fr**	M. Christian MONTES Université Lyon 2 86 Rue Pasteur 69 365 Lyon CEDEX 07 **christian.montes@univ-lyon2.fr**

*ScSo : Histoire, Géographie, Aménagement, Urbanisme, Archéologie, Science politique, Sociologie, Anthropologie

Acknowledgments

This thesis has been financed by the ministry of education of France by a ministrial contract. The research works of this thesis have been carried out at LaMCoS, "Laboratoire de Mécanique des Contacts et des Structures", UMR CNRS 5259, INSA Lyon. I would like to thanks its director, Pr. Daniel NELIAS for having hosted me.

I want to address my thanks to my advisers Pr. Régis DUFOUR, Dr. Sébastien BAGUET and Pr. Claude-Henri Lamarque for their guidance and unlimited support. It has been a great pleasure to work with them, their expertise in nonlinear dynamics and M/NEMS have greatly contributed to this thesis. It is thanks to their encouragement and their inspiring ideas that I could lead this thesis to the completion.

I sincerely address my thanks to all the members of the jury: Anne Tanguy for presiding the Ph.D. defense, Sébastien Hentz and Bruno Cochelin for their work as rapporteur and their advice concerning the Thesis manuscript and finally Emmanouelle Sarrouy and Gaëtan Kerschen as exterminators.

During my first year of the thesis, I have been teaching mechanics in INSA de Lyon. I want to thanks particularly Arnaud Sandel and Virgil Tavernier for their support and pedagogic advises. They have greatly contributed to the good running of this year of teaching.

I also want to thanks all of my colleges members of the team "Dynamique et Contrôle des Structures (DCS)" and all the PhD students that gave me great joy during these three years of thesis: Lihan, José, Clément J, Yvon Bryan, Emna, Guillaume, Ilaria, Mélodie, Marc-André, Ilyes, Sébastien, Kévin, Mathias, Xiaowen, Khac Long, Quang Thinh ... A special mention goes for the ones that shared my ups and downs by being in my bureau: Arwa, Etienne and Carlos. Without them, the thesis would never have been the same.

It his with a special thought to my family that i want to end these acknowledgments. Especially to my parents and my grand parents to have supported me and raised me the way they did. Finally, the last thanks but not the least goes to my dear Yuqi, for her every day joy, unlimited support, her patience when i need to explained the state of the ongoing work and all the love she gave me.

Abstract

Nonlinear systems possess complex dynamic with phenomena that can either be detrimental or profitable. To better visualize, understand and optimize nonlinear behaviors, new methods such as continuation for single-parametric analysis or for computation of nonlinear normal modes have been proposed in recent studies. However, nonlinear systems can have correlated multiple parameters yielding their analysis fastidious and difficult to apprehend. Therefore, this thesis proposes new methods for efficient parametric analysis and the computation of nonlinear normal modes to better visualize and understand nonlinear behaviors yielding sets of parameters for the optimization of nonlinear systems.

First, the detection, localization and tracking of bifurcation point for parametric analysis along a single variable is recalled. Then, bifurcation tracking is performed on a Jeffcott rotor and a Nonlinear Linear Tunable Vibration Absorber (NLTVA) to better understand their global dynamic. Afterwards, a new method called "multi-parameter recursive continuation method" is provided for parametric analysis of nonlinear system. With this method, parametric analysis of nonlinear system along multiple system parameters can be made. This method has then been applied to a NLTVA to push to apparition of Isolated Solutions (IS) at high amplitude of forcing increasing the efficiency of such absorbers.

Another method is then proposed for nonlinear modal analysis though Nonlinear Normal Modes (NNM) computation using Harmonic Balance Method (HBM). The presented tool permits computing NNM, their stability and bifurcation points. A generalization to non-conservative NNM to compute the phase and the energy resonances is presented. The concept of energy balance is extended to take in account the generalization to non-conservative NNM. It results from this generalization a new concept called fictive force that permits system to target specific point of the NNM. Then, a 2-DOFs nonlinear system are taken as example with respect to several designs. First, a analysis of nonlinear dynamics is provided based on underlying symmetries of the system. Then, symmetry-breaking event is analyzed with the help of NNM and bifurcation tracking. Afterwards, the experimental feasibility of NNM tracking is assessed and a validation of non-conservative NNM is performed on a system with cubic nonlinear damping.

The previous parametric and nonlinear modal analyses are applied to MEMS array in order to provide a better understanding of its nonlinear dynamics and to propose alternative mass sensing technique. Several complex phenomena are detected and explained. A frequency synchronization of bifurcations points due to electrostatic coupling is found in MEMS array and explained. Isolated branches of both periodic solutions and Nonlinear Normal Modes are detected in MEMS array. The properties of merging and apparition of IS and isolated NNM in MEMS array are then analyzed. Then, the mechanisms of detection using MEMS array based on nonlinear phenomena such as hysteresis cycle and symmetry breaking are proposed.

KEYWORDS: Nonlinear Dynamics, Parametric analysis, Multi-parameter recursive continuation, Nonlinear Normal Modes, Non-conservative, Isolated Nonlinear Normal Modes, Isolated Solutions, MEMS array, Mass sensing, Harmonic Balance Method.

Contents

List of Figures

List of Tables

General introduction

Motivations and objectives

Parametric analysis are useful tools to better apprehend nonlinear dynamics of systems. At first analytic parametric analysis were performed. However, these methods were more adapted for system with few degree of freedoms (DOFs). Then, numerical methods, such as continuation methods, were being developed. At the moment, single parameter continuation methods are referent for numerical parametric analysis.

Another way to analyze the nonlinear dynamics of a system is to perform nonlinear modal analysis. The concept of normal modes has been extended from the linear to the nonlinear domain and currently three definitions are available. The first one is attributed to Rosenberg. This definition considers NNMs as synchronized periodic solutions. Since, the definition has being modified to non-necessarily synchronized periodic solutions in order to take modal interactions into account. A second definition based on normal form theory is due to Jezequel and Lamarque. Both of these definitions have the advantage extending the known concept of linear normal modes to the nonlinear domain, whereas the last definition of NNMs yields a new concept for NNM characterization. Indeed, Shaw and Pierre define NNMs as invariant manifolds in phase space. This definition has the advantage of being compatible with non-conservative NNMs computation. However, to establish the NNM, a 2D invariant manifold must be computed. Considering NNMs as periodic solutions is interesting because a large framework of studies on the computation of periodic solutions is available. Currently, stability and bifurcations of NNMs as periodic solutions are not yet addressed with HBM and a generalized method for the computation of conservative and non-conservative NNMs is yet to be developed.

With the advancements in nonlinear dynamics, several methods have been proposed to deal or to exploit the nonlinearities. For nonlinear absorber, it is possible to tune system parameters in order to achieve equal amplitude on the two peaks of the resonances. With bifurcation tracking applied on the resulting nonlinear tuned vibration absorber (NLTVA), isolated solutions are uncovered and limit the operating range of the device. Moreover, theirs evolution depend on multiple system parameters that are inter-correlated. Consequently, new methods for parametric analysis need to be developed to provide the evolution of those isolated solutions with respect to multiple system parameters and designs that can increase the efficiency of the device.

Concerning MEMS resonators, some works proposed to cancel nonlinearities,

whereas other studies came up with the ideas of exploiting some nonlinearities such as bifurcations and associated hysteresis cycles. A second step was to consider the architecture of devices such as arrays of MEMS. Several domains of study were addressed such as parametric resonance, modal interactions, the types of coupling and tunable devices to correct defects or change system properties. Spletzer came up with the idea to use the mode shapes of a MEMS array to increase its sensitivity for mass sensing. The method considers a symmetrical array of MEMS and is called "mode localization" due to the localization of the mode on the beam where the added mass is dropped. However, the nonlinear phenomena behind MEMS arrays are not yet fully understood. With the increase of system parameters, the creation of recursive methods for parametric analysis with respect to multiple system parameters would permit more complete analysis.

In this thesis, the NLTVA and electrostatically actuated resonant MEMS arrays are addressed. Due to nonlinearities, those systems present some complex behaviors often depending on multiple inter-correlated parameters. To analyze, those systems adequately a new efficient multi-parametric analysis method needs to be proposed and NNMs are gonna be used. The parametric analysis must provide efficiently the evolution of point of interest with respect to multiple system parameters. Concerning NNMs, the compatibility between the computation in HBM of periodic solutions and NNM must be insured. Since the NNMs can becomes unstable, encounter bifurcations points and be submitted to symmetry-breaking events, methods for stability and bifurcation analysis of NNMs must be developed. In order to propose a general characterization of NNMs, an extension to non-conservative NNMs must be provided. At the end, these new methods are applied to: the NLTVA to increase the operating range by pushing isolated solutions at higher amplitudes, and MEMS arrays to better understand its nonlinear dynamics and to provide additional mechanisms for mass sensing. Consequently, the thesis has the following objectives:

- Providing a new method for parametric analysis that is both recursive and multi-parametric.
- Providing a method that permits the numerical computation of NNMs, as well as their stability and bifurcations using Harmonic Balance Method.
- Extending the concept of NNMs to the non-conservative case with respect to the extended Rosenberg definitions. To provide a generalized method for NNM computation, the non-conservative NNMs must be computed with the same method as for conservative NNMs.
- Applying these methods to a MEMS array to better understand its dynamics.
- Proposing methods for mass sensing with different configurations of MEMS arrays.

To this end, the thesis is organized as follows.

Overview

In Chapter #1, a state of the art is presented. A summary of available methods for periodic solution, stability and bifurcations calculations is provided and a method based on HBM is detailed. Then, the topics of parametric analysis and NNM are addressed. Finally, a brief review on MEMS for mass sensing, on the improvement of MEMS through the exploitation of nonlinearities and on MEMS arrays is presented. First, the methods for parametric analysis and NMM computation are presented. They are then applied to a MEMS array for mass sensing applications.

In Chapter #2, the topic of parametric analysis is addressed. First, the detection, localization and tracking of bifurcations for parametric analysis is recalled. A NonLinear Tuned Vibration Absorber (NLTVA) and a Jeffcott rotor are taken as examples for bifurcation tracking. Then, a multi-parametric recursive continuation method for parametric analysis is proposed fulfilling the first objective. The method is then applied to the NLTVA to push the ISs at higher amplitude of forcing.

In Chapter #3, the NNM computation based on HBM is explained. First, a method of resolution for computing conservative NNMs is presented. Then, two extensions to non-conservative NNMs are proposed: the phase resonance and the energy resonance. The presented extensions are characterized by new conservative equations taking into account the damping effect into the conservative terms. In order for forced responses to target specific NNMs, forcing vectors applied to the system and achieving energy balance are identified. Finally, by obtaining a new conservative equation characterizing the non-conservative NNMs, the presented method for NNM computation can compute both conservative and non-conservative NNMs, leading to a generalized method for NNM computation using HBM with respect to the extended Rosenberg definition. Moreover, forcing vectors identification allows forced responses to target specific NNMs linking both nonlinear modal analysis and frequency response analysis. Then, the computation of stability and bifurcations of NNM based on HBM is presented and illustrated on several examples. The topics of symmetries, isolated solutions and isolated NNM are addressed.

In Chapter #4, arrays of resonant MEMS for mass sensing are considered. First, NNMs and related responses curves are computed using averaging methods in order to study the effect of the electrostatic coupling on the nonlinear dynamics. When the coupling terms are considered, bifurcations that appear on the different responses curves of the beams occur at the same frequencies. A validation of the results is then made by means of numerical calculations. Then, parametric analysis and nonlinear modal analysis are performed on symmetric MEMS arrays to observe the change in the dynamics before and after symmetry-breaking induced by the addition of a small mass. Finally, mechanisms for mass sensing using MEMS arrays are presented.

Chapter 1

State of the art

This chapter presents the state of art of different topics linked to the analysis of nonlinear dynamics and resonant MEMS for mass sensing. Firstly, some numerical methods for nonlinear dynamics analysis of periodic solutions are presented. Then, the literature related to stability, bifurcation and parametric analysis is summarized and succinctly explained. Secondly, the definitions of Nonlinear Normal Modes (NNMs) are recalled. A summary of some techniques needed for calculating NNMs, their stability and bifurcations is proposed. Finally, review on MEMS for mass sensing applications, the exploitation of nonlinear phenomena and MEMS array are presented.

Contents

1.1 Harmonic balance method for nonlinear dynamics analysis of periodic solutions

Generally speaking, finding non-approximated analytical solutions of nonlinear equations of motions is impossible. Therefore, methods of approximations are used in order to obtain quasi-analytical solutions. At first, analytical methods such as multi-scale methods [NAY 08b], averaging methods [VER 06, VER 18], normal form theory [HOL 81] were used to compute approximated solutions. However, with the arrival of more efficient computers, numerical and pseudo-numerical methods started to be more and more used to solve nonlinear problems. Nowadays, various numerical methods can be found in the literature for the computation of periodic solutions. They belong either to the time domain or to the frequency domain.

Time domain methods based on step by step time integration were used to obtain periodic solutions. Such methods are useful to analyze transient responses generated by punctual events, but they are not efficient to find steady-state periodic solutions because the transient state can be long especially for system with a light damping. Moreover, nonlinear systems can exhibit multiple basins of attraction leading to multiple permanent solutions. Furthermore, only stable permanent solutions can be obtained by time integration techniques with the initial conditions inside a specific basin of attraction. To obtain the basin of attraction of the system, one could use "Cell to Cell mapping" presented in [HSU 13]. One way to improve those methods is to solve the equation of motion using the shooting method presented in [SUN 97, NAY 08a, SEY 09]. The periodic solution is directly computed by solving a boundary value problem (BVP). When applied to large problem, solving the BVP is time consuming. Moreover, the period of the oscillation must be chosen appropriately for the computation. Therefore, several researches were made to improve the computational time. Stoykov and Margenov used parallelization techniques to speed the resolution [STO 14]. Another way to reduce the computational time is to consider a discretized BVP. This method called orthogonal collocation has since been implemented in softwares such as AUTO [DOE 98, DOE 07], MATCONT [DHO 03], COLSYS [ASC 79], DDE-BIF [ENG 00] and COCO [DAN 11]. As example of applications, shooting method was used by Sundararajan in [SUN 97] to study the responses of rigid unbalanced rotor supported by squeeze-film dampers and smooth bearings. Kerschen *et al.* [PEE 09, KER 14] used a shooting method to compute Nonlinear Normal Modes (NNMs). Compared to a frequency domain resolution method, the method cannot filter specific harmonics, resulting in a too precise method in some cases. For example, with an infinite number of modal interactions, the method can lead to an infinite computational time by trying to compute all modal interactions.

Concerning frequency domain approaches, a very popular method is the harmonic balance method (HBM) which expands the unknown state variables and nonlinear forces in truncated Fourier series. By computing directly the periodic solution in the frequency domain, the periodicity of the solution is already imposed by the modelling. This scheme is praised because of its efficiency and its versatility in handling nonlinearities. Krylov

and Bogoliubov were the first to introduce the term of "harmonic balance" by analyzing nonlinear systems with a single harmonic [KRY 16]. With the HBM, the nonlinear terms are computed in the frequency domain by means of the alternating frequency-time (AFT) scheme [CAM 89]. By going back and forth between time and frequency domains with discrete Fourier transform (DFT), the nonlinear terms can be computed. Over time, many improvements have been introduced and the HBM can now handle systems with many types of nonlinearity such as the non-differential [KRA 13] and the non-smooth ones [NAC 03, SCH 16]. The efficiency of the method has been enhanced by adaptive schemes such as the automatic selection of harmonics of interest [JAU 10, GRO 12]. The method also also has been extended to take quasi-periodic solutions into account [SCH 06, GUS 08, PEL 14, ZHO 15]. Coupled with a continuation technique, the method provides the equilibrium curve of periodic solutions with respect to a varying system parameter. Two main continuation techniques are used, the arc-length continuation based on tangent prediction steps and on orthogonal corrections [CRI 81, VON 01, SEY 09] or the asymptotic numerical method [COC 09].

In this section, the analysis of periodic solutions with HBM is addressed. First, the computation of periodic solution is described. Then, the techniques of continuation are recalled. Finally, the computation of nonlinear terms and their derivatives is explained.

1.1.1 Computation of periodic solution with HBM

In order to explain HBM, let a nonlinear dynamical system have n degrees of freedom (DOFs) and the following nonlinear equation of motion:

$$\boldsymbol{M}\ddot{\boldsymbol{x}}(t)+\boldsymbol{C}\dot{\boldsymbol{x}}(t)+\boldsymbol{K}\boldsymbol{x}(t)+\boldsymbol{f}_{nl}(\boldsymbol{x},\dot{\boldsymbol{x}})=\boldsymbol{f}(t) \tag{1.1}$$

with $\boldsymbol{x}(t)$ the displacement vector composed by the n DOFs, $\boldsymbol{M}$, $\boldsymbol{C}$ and $\boldsymbol{K}$ the mass, damping and stiffness matrices, $\boldsymbol{f}_{nl}$ the vector of nonlinear forces, $\boldsymbol{f}$ the external forcing vector. The harmonic balance method allows periodic solutions to be computed directly on the Fourier base $\mathscr{B}(\omega t)$. In order to compute the solution of the equation of motion, $\boldsymbol{x}(t)$ and $\boldsymbol{f}_{nl}$ vectors are approximated by Fourier Series truncated at order H with a pulsation ω.

$$\begin{array}{lcll}
\mathscr{B}(\omega t) & = & [1 \quad \cos(\omega t) \quad \sin(\omega t) \quad \dots \quad \cos(H\omega t) \quad \sin(H\omega t)] & \\
\boldsymbol{x}(t) & = & \boldsymbol{X}^0+\sum_{k=0}^{H}\left[\boldsymbol{X}_c^k\cos(k\omega t)+\boldsymbol{X}_s^k\sin(k\omega t)\right] & =(\mathscr{B}(\omega t)\otimes\boldsymbol{I}_n)\boldsymbol{X} \\
\boldsymbol{f}_{nl}(\boldsymbol{x},\dot{\boldsymbol{x}}) & = & \boldsymbol{F}_{nl}^0+\sum_{k=0}^{H}\left[\boldsymbol{F}_{nl\,c}^k\cos(k\omega t)+\boldsymbol{F}_{nl\,s}^k\sin(k\omega t)\right] & =(\mathscr{B}(\omega t)\otimes\boldsymbol{I}_n)\boldsymbol{F}_{nl} \\
\boldsymbol{f}(t,\boldsymbol{x},\dot{\boldsymbol{x}}) & = & \boldsymbol{F}^0+\sum_{k=0}^{H}\left[\boldsymbol{F}_c^k\cos(k\omega t)+\boldsymbol{F}_s^k\sin(k\omega t)\right] & =(\mathscr{B}(\omega t)\otimes\boldsymbol{I}_n)\boldsymbol{F}
\end{array}$$

with $\otimes$ corresponding to the Kronecker tensor product. Once projected onto the Fourier base $\mathscr{B}(\omega t)$, the Fourier coefficients are obtained with a Galerkin method.

$$\begin{array}{lcll}
\boldsymbol{X} & = & \langle\boldsymbol{x}(t),\mathscr{B}(\omega t)\rangle & =\left[\boldsymbol{X}^{0T},\boldsymbol{X}_c^{1\,T},\boldsymbol{X}_s^{1\,T},\dots,\boldsymbol{X}_c^{H\,T},\boldsymbol{X}_s^{H\,T}\right]^T \\
\boldsymbol{F}_{nl} & = & \langle\boldsymbol{f}_{nl},\mathscr{B}(\omega t)\rangle & =\left[\boldsymbol{F}_{nl}^{0\,T},\boldsymbol{F}_{nl\,c}^{1\;T},\boldsymbol{F}_{nl\,s}^{1\;T},\dots,\boldsymbol{F}_{nl\,c}^{H\;T},\boldsymbol{F}_{nl\,q}^{H\;T}\right]^T \\
\boldsymbol{F} & = & \langle\boldsymbol{f},\mathscr{B}(\omega t)\rangle & =\left[\boldsymbol{F}^{0T},\boldsymbol{F}_c^{1\,T},\boldsymbol{F}_s^{1\,T},\dots,\boldsymbol{F}_c^{H\,T},\boldsymbol{F}_s^{H\,T}\right]^T
\end{array} \tag{1.2}$$

with $\boldsymbol{X}$, $\boldsymbol{F}_{nl}$, $\boldsymbol{F}$ the Fourier coefficients of the displacement vector, the vector of nonlinear forces and the forcing vector of size $L = n(2H+1)$ and $\langle g,h\rangle$ the scalar product corresponding to the Galerkin method:

$$\langle g,h\rangle = \frac{1}{\omega}\int_0^{\frac{2\pi}{\omega}} g.h\,dt \tag{1.3}$$

The Fourier coefficients of the velocity and acceleration vectors can be written as:

$$\begin{aligned}\dot{\boldsymbol{X}} &= \langle \dot{\boldsymbol{x}}(t), \mathscr{B}(\omega t)\rangle &= \omega[\nabla \otimes \boldsymbol{I}_{2H+1}]\boldsymbol{X}\\ \ddot{\boldsymbol{X}} &= \langle \ddot{\boldsymbol{x}}(t), \mathscr{B}(\omega t)\rangle &= \omega^2[\nabla^2 \otimes \boldsymbol{I}_{2H+1}]\boldsymbol{X}\end{aligned}$$

where ∇ represent the time derivative operator.

$$\nabla = \mathrm{diag}(\boldsymbol{0}, \nabla_1, ..., \nabla_j, ..., \nabla_H) \quad \text{with} \quad \nabla_j = j\begin{bmatrix} 0 & 1 \\ -1 & 0 \end{bmatrix} \tag{1.4}$$

By introducing Eqs. (1.2) and (1.4) into Eq. (1.1), the residual $\boldsymbol{R}(\boldsymbol{X},\omega)$ of the nonlinear dynamic equation in the frequency domain is obtained:

$$\boldsymbol{R}(\boldsymbol{X},\omega) = \boldsymbol{Z}(\omega)\boldsymbol{X} + \boldsymbol{F}_{nl}(\boldsymbol{X},\omega) - \boldsymbol{F} = \boldsymbol{0}_L \tag{1.5}$$

with

$$\begin{aligned}\boldsymbol{Z}(\omega) = \omega^2\nabla^2 \otimes \boldsymbol{M} + \omega\nabla \otimes \boldsymbol{C} + \boldsymbol{I}_{2H+1} \otimes \boldsymbol{K} = \mathrm{diag}(\boldsymbol{K}, \boldsymbol{Z}_1, ..\boldsymbol{Z}_j, .., \boldsymbol{Z}_H)\\ \text{with} \quad \boldsymbol{Z}_j = \begin{bmatrix} \boldsymbol{K} - j^2\omega^2\boldsymbol{M} & -j\omega\boldsymbol{C} \\ j\omega\boldsymbol{C} & \boldsymbol{K} - j^2\omega^2\boldsymbol{M} \end{bmatrix}\end{aligned} \tag{1.6}$$

If a direct relation exists between $\boldsymbol{F}_{nl}$ and $\boldsymbol{X}$, one can use such relation. However, some nonlinear forces cannot be expressed directly as a function of $\boldsymbol{X}$. In this case, the Alternative Frequency-Time (AFT) method can be used to compute the nonlinear terms [CAM 89]. The AFT method using Discrete Fourier transforms (DFT) is used to compute the displacement vector $\boldsymbol{x}(t)$ in the time domain, to calculate the nonlinear forces $\boldsymbol{f}_{nl}$ and then to put them back in the frequency domain, see Eq. (1.7). The calculation of $\boldsymbol{F}_{nl}$ and its derivatives is detailed in Section 1.1.3.

$$\boldsymbol{X} \xrightarrow{DFT^{-1}} \boldsymbol{x}(t), \dot{\boldsymbol{x}}(t) \longrightarrow \boldsymbol{f}_{nl}(\boldsymbol{x}, \dot{\boldsymbol{x}}) \xrightarrow{DFT} \boldsymbol{F}_{nl}(\boldsymbol{X}) \tag{1.7}$$

Then, a Newton-Raphson algorithm is used to compute the periodic solution of Eq. (1.5):

$$\left(\begin{array}{lcl} \boldsymbol{R}^k_{\boldsymbol{X}}\delta\boldsymbol{X}^k &=& -\boldsymbol{R}^k \\ \boldsymbol{X}^{k+1} &=& \boldsymbol{X}^k + \delta\boldsymbol{X}^k \end{array}\right) \tag{1.8}$$

with $\boldsymbol{R}_{\boldsymbol{X}}$ the partial derivative of $\boldsymbol{R}$ with respect to $\boldsymbol{X}$, the exponent k indicating the number of the current iteration:

$$\boldsymbol{R}^k = \boldsymbol{R}(\boldsymbol{X}^k, \omega^k) \qquad \boldsymbol{R}^k_{\boldsymbol{X}} = \left.\frac{\partial \boldsymbol{R}}{\partial \boldsymbol{X}}\right|_{\boldsymbol{X}=\boldsymbol{X}^k, \omega=\omega^k} \tag{1.9}$$

The corrections are made until the following relative error criterion is satisfied:

$$\frac{\max(|\boldsymbol{R}|)}{\max(\| \boldsymbol{Z}\cdot\boldsymbol{X} \|, \| \boldsymbol{F}_{nl} \|)} < \varepsilon \tag{1.10}$$

The HBM has the advantage to transform a time-domain differential equation into an algebraic equation in the frequency domain. This method is well adapted for the simulation of resonant MEMS because of the presence of periodic responses.

1.1.2 Continuation techniques

Since nonlinear systems can exhibit complex dynamic behaviors such as multiple solutions, resolution methods are often combined with continuation techniques. The arc-length continuation is one of them. The frequency is added to the variables and a tangent equation is added to the equation of motion as a supplementary constraint equation. The method can then be combined with an adaptive step scheme to enhance the robustness of the continuation algorithm [DOE 07] [SEY 09]. This technique is interesting for nonlinear dynamics analysis because the continuation method can "turn back" in order to obtain the complete response curve, including the multiple solutions. Continuation techniques have been implemented in several softwares such as MATCONT [DHO 03], AUTO [DOE 07], MANLAB [ARQ 07]. Cochelin *et al.* [COC 94] used continuation techniques combined with asymptotical numerical method.
The continuation is carried out in two successive steps, the prediction and the correction.

Initialization of the predictor step The prediction step consists in finding the local tangent of the solution curve. Then the current periodic solution is perturbed along this tangent to obtain an approximated periodic solution following the curve, see Fig.1.1. First, the periodic solution $(\boldsymbol{X}^0, \omega^0)$ is calculated by solving Eq. (1.5) with the Newton-Raphson algorithm presented in Eq. (1.8). The continuation method is then initialized. For any predictor step, the tangent vector $\boldsymbol{t} = (\Delta\boldsymbol{X}, \Delta\omega)^T$ must solve the first variation of Eq. (1.5)

$$\Delta\boldsymbol{R}(\boldsymbol{X}^0, \omega^0) = \left.\frac{\partial \boldsymbol{R}}{\partial \boldsymbol{X}}\right|_{\boldsymbol{X}^0, \omega^0} \Delta\boldsymbol{X}_1 + \left.\frac{\partial \boldsymbol{R}}{\partial \omega}\right|_{\boldsymbol{X}^0, \omega^0} \Delta\omega_1 = \boldsymbol{0}_L \tag{1.11}$$

The equation is then put under the following compact form:

$$\boldsymbol{R}^0_{\boldsymbol{X}} \cdot \Delta\boldsymbol{X}_1 + \boldsymbol{R}^0_{\omega} \cdot \Delta\omega_1 = \boldsymbol{0}_L \tag{1.12}$$

with $\boldsymbol{R}^0_{\boldsymbol{X}}$ and $\boldsymbol{R}^0_{\omega}$ the two partials derivatives, see Eq.(1.24), calculated at the current periodic solution $(\boldsymbol{X}^0, \omega^0)$. The initialization of the continuation method cannot use arc-length equation because no previous tangent vector has been computed. Therefore, to

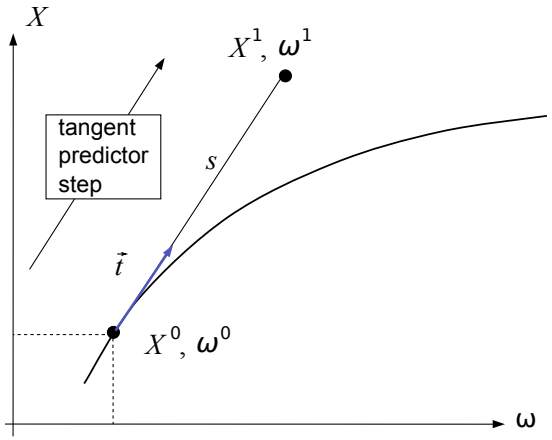

Figure 1.1 – Predictor step

compute the first tangent vector, the value of $\Delta\omega_1$ is chosen as 1 or -1 depending on the targeted direction of continuation:

$$\boldsymbol{R}_{\boldsymbol{X}}^0 \Delta \boldsymbol{X}_1 = \pm \boldsymbol{R}_{\omega}^0 \tag{1.13}$$

Then, the tangent $(\Delta\boldsymbol{X}_1, \Delta\omega_1)$ is multiplied by a step length Δs and added to the point $(\boldsymbol{X}_0, \omega_0)$:

$$\begin{pmatrix} \boldsymbol{X}_1^1 \\ \omega_1^1 \end{pmatrix} = \begin{pmatrix} \boldsymbol{X}_1^0 \\ \omega_1^0 \end{pmatrix} + \Delta s \begin{pmatrix} \Delta\boldsymbol{X}_1 \\ \Delta\omega_1 \end{pmatrix} \tag{1.14}$$

Standard predictor step Once a first step has been performed, a tangent vector can be calculated with Eq. (1.12). Since a previous tangent vector has already been computed, the following arc length equation can be used to normalize the tangent vector$(\Delta\boldsymbol{X}_j, \Delta\omega_j)$:

$$\Delta\boldsymbol{X}_{j-1}{}^T \Delta\boldsymbol{X}_j + \Delta\omega_{j-1}\Delta\omega_j = 1 \tag{1.15}$$

with $(j-1, j)$ the previous and current steps of continuation. To compute the tangent, the Eqs. (1.12) and (1.15) are combined to form the following augmented system:

$$\begin{pmatrix} \boldsymbol{R}_{\boldsymbol{X}}^0 & \boldsymbol{R}_{\omega}^0 \\ \Delta\boldsymbol{X}_{j-1}{}^T & \Delta\omega_{j-1} \end{pmatrix} \begin{pmatrix} \Delta\boldsymbol{X}_j \\ \Delta\omega_j \end{pmatrix} = \begin{pmatrix} \boldsymbol{0}_L \\ 1 \end{pmatrix} \tag{1.16}$$

Then, the tangent is multiplied by a step length Δs and the sign of the scalar product between the current tangent and the previous one. This operation permits an enhanced robustness by preventing any direction leading to previously calculated periodic solutions to be taken. Then the calculated predictor tangent $(\Delta\boldsymbol{X}_j, \Delta\omega_j)$ is added to the system parameters as in Eq. (1.14).

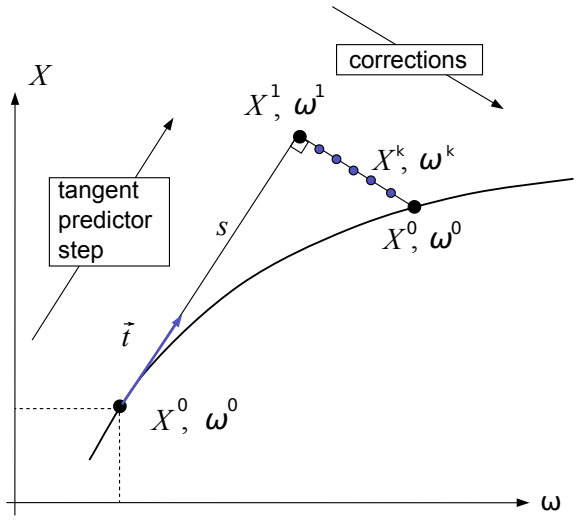

Figure 1.2 – Corrector step

Corrector step However, due to the low order of the approximation and the non-linearity of the analyzed equation, the prediction step does not provide a sufficiently accurate periodic solution. Therefore, a correction step is added to the continuation algorithm to realize corrections $(\delta \boldsymbol{X}_j^k, \delta \omega_j^k)$ in order to minimize the residue, see Fig.1.2.

$$\boldsymbol{R}_X^k \cdot \delta \boldsymbol{X}_j^k + \boldsymbol{R}_\omega^k \cdot \delta \omega_j^k = -\boldsymbol{R}^k \tag{1.17}$$

with k corresponding to the current iteration of Newton-Raphson algorithm. The correction are made orthogonal to the tangent direction $(\Delta \boldsymbol{X}_j, \Delta \omega_j)$ calculated in Eq. (1.16).

$$\Delta \boldsymbol{X}_j{}^T \delta \boldsymbol{X}_j^k + \Delta \omega_j \delta \omega_j^k = 0 \tag{1.18}$$

To calculate the correction, the following augmented system of equations composed of Eqs. (1.17) and (1.18) is solved.

$$\boldsymbol{J}^k \begin{Bmatrix} \delta \boldsymbol{X}^k \\ \delta \omega^k \end{Bmatrix} = \begin{bmatrix} \boldsymbol{R}_X^k & \boldsymbol{R}_\omega^k \\ \Delta \boldsymbol{X}_j{}^T & \Delta \omega_j \end{bmatrix} \begin{Bmatrix} \delta \boldsymbol{X}_j^k \\ \delta \omega_j^k \end{Bmatrix} = \begin{Bmatrix} -\boldsymbol{R}^k \\ 0 \end{Bmatrix} \tag{1.19}$$

with $\boldsymbol{J}$ the jacobian of the augmented system of equations used for continuation. Once the correction $(\delta \boldsymbol{X}_j^k, \delta \omega_j^k)$ are calculated, they are added to $(\boldsymbol{X}^k, \omega^k)$ to obtain the new corrected variables.

$$\begin{cases} \boldsymbol{X}^{k+1} & = \boldsymbol{X}^k + \delta \boldsymbol{X}_j^k \\ \omega^{k+1} & = \omega^k + \delta \omega_j^k \end{cases} \tag{1.20}$$

The corrections are made until the error criterion in Eq. (1.10) is satisfied. The obtained set of parameters $(\boldsymbol{X}, \omega)$ corresponds to a the new periodic solution along the continuated curve. To compute the complete response curve, the continuation algorithm is repeated with $(\boldsymbol{X}, \omega)$ being the new 0^{th} point of reference for the next continuation process.

1.1.3 Computation of nonlinear terms and its derivatives with AFT scheme

To perform the Newton-Raphson algorithm with HBM, the nonlinear forces and their derivatives have to be computed in frequency domain. It is assumed that nonlinear terms $\boldsymbol{F}_{nl}$ only depend on the displacement vector $\boldsymbol{X}$ and the frequency of excitation ω included in the residual, see Eq. (1.5).

To compute the derivatives of the nonlinear forces, several methods are available. The finite differences method is by far the easiest to implement, however it can be time consuming. The second method is based on Fast Fourier Transform (FFT). The advantage of this method is to store only the derivatives of the nonlinear terms. The third method is based on DFT to compute the nonlinear derivatives [NAR 98]. This method is more compact and more adapted to an implementation in software like MATLAB. However, the method based on DFT requires to store full matrix such as Γ and Γ^{-1} which can increase the computational time, see Eq. (1.23). In the remaining of this thesis, all simulations are made with MATLAB. Therefore, the nonlinear terms are calculated with the AFT method based on DFT, see Eq. (1.7).

First, an inverse Discrete Fourier Transform (DFT^{-1}) is applied. To do so, the periodic solution is sampled. Time sample vector $\bar{\boldsymbol{t}}$ of size N is taken evenly every $\Delta_t = \frac{T}{N}$ to cover the entire period of periodic solution. For sampling reason, the number of samples N must be greater than $(2H+1)$. In the rest of the thesis, the number of samples is $N = 2(2H+1)$. Then, the displacement vector $\bar{\boldsymbol{x}}$ and its corresponding velocity $\bar{\dot{\boldsymbol{x}}}$ are sampled at those time samples. The following expression of those vectors is obtained by expressing time sample as in Eq. (1.2).

$$\begin{aligned}
\bar{\boldsymbol{x}} &= [\boldsymbol{x}(t_1), \ldots, \boldsymbol{x}(t_N)]^T \\
&= [\mathbb{T}(\omega t_1) \otimes \boldsymbol{I}_n, \ldots, \mathbb{T}(\omega t_N) \otimes \boldsymbol{I}_n]^T \boldsymbol{Q} \\
&= (\Gamma \otimes \boldsymbol{I}_n)\boldsymbol{X} \\
\bar{\dot{\boldsymbol{x}}} &= [\boldsymbol{x}(t_1), \ldots, \boldsymbol{x}(t_N)]^T \\
&= [\mathbb{T}(\omega t_1) \otimes \boldsymbol{I}_n, \ldots, \mathbb{T}(\omega t_N) \otimes \boldsymbol{I}_n]^T (\nabla \otimes \boldsymbol{I}_n)\boldsymbol{X} \\
&= \omega(\Gamma \otimes \boldsymbol{I}_n)(\nabla \otimes \boldsymbol{I}_n)\boldsymbol{X} = \omega[(\Gamma\nabla) \otimes \boldsymbol{I}_n]\boldsymbol{X}
\end{aligned} \tag{1.21}$$

Finally, the time vector of nonlinear terms $\bar{\boldsymbol{f}}_{nl}$ is computed using the displacement and velocity vectors. The nonlinear terms in the frequency domain is then obtained by applying a Discrete Fourier Transform (DFT) :

$$\boldsymbol{F}_{nl} = (\Gamma^{-1} \otimes \boldsymbol{I}_n)\bar{\boldsymbol{f}}_{nl}(\bar{\boldsymbol{x}}, \bar{\dot{\boldsymbol{x}}}) \tag{1.22}$$

with

$$\Gamma = \begin{bmatrix} 1 & \cos\theta_1 & \sin\theta_1 & \dots & \cos H\theta_1 & \sin H\theta_1 \\ \vdots & \vdots & \vdots & & \vdots & \vdots \\ 1 & \cos\theta_N & \sin\theta_N & \dots & \cos H\theta_N & \sin H\theta_N \end{bmatrix} \qquad \Gamma^{-1} = \frac{1}{N} \begin{bmatrix} 2 & \dots & 2 \\ \cos\theta_1 & \dots & \cos\theta_N \\ \sin\theta_1 & \dots & \sin\theta_N \\ \vdots & & \vdots \\ \cos H\theta_1 & \dots & \cos H\theta_N \\ \sin H\theta_1 & \dots & \sin H\theta_N \end{bmatrix} \tag{1.23}$$

One can note that Γ and its inverse Γ^{-1} do not depend on ω and do not need to be updated during the continuation. During the two continuation steps presented in the two previous subsections, the following derivatives are used:

$$\boldsymbol{R}_X = \boldsymbol{Z}(\omega) + \frac{\partial \boldsymbol{F}_{nl}}{\partial \boldsymbol{X}}, \qquad \boldsymbol{R}_\omega = \boldsymbol{Z}_\omega \boldsymbol{X} + \frac{\partial \boldsymbol{F}_{nl}}{\partial \omega} \tag{1.24}$$

with

$$\boldsymbol{Z}_\omega = \frac{\partial \boldsymbol{Z}}{\partial \omega} = 2\omega\nabla^2 \otimes \boldsymbol{M} + \nabla \otimes \boldsymbol{C} \tag{1.25}$$

The derivatives of nonlinear terms are computed as follows:

$$\begin{aligned} \frac{\partial \boldsymbol{F}_{nl}}{\partial \boldsymbol{X}} &= \frac{\partial \boldsymbol{F}_{nl}}{\partial \bar{\boldsymbol{f}}_{nl}} \frac{\partial \bar{\boldsymbol{f}}_{nl}}{\partial \bar{\boldsymbol{x}}} \frac{\partial \bar{\boldsymbol{x}}}{\partial \boldsymbol{X}} + \frac{\partial \boldsymbol{F}_{nl}}{\partial \bar{\boldsymbol{f}}_{nl}} \frac{\partial \bar{\boldsymbol{f}}_{nl}}{\partial \dot{\bar{\boldsymbol{x}}}} \frac{\partial \dot{\bar{\boldsymbol{x}}}}{\partial \boldsymbol{X}} \\ &= (\Gamma^{-1} \otimes \boldsymbol{I}_n) \frac{\partial \bar{\boldsymbol{f}}_{nl}}{\partial \bar{\boldsymbol{x}}} (\Gamma \otimes \boldsymbol{I}_n) + (\Gamma^{-1} \otimes \boldsymbol{I}_n) \frac{\partial \bar{\boldsymbol{f}}_{nl}}{\partial \dot{\bar{\boldsymbol{x}}}} \omega [(\Gamma\nabla) \otimes \boldsymbol{I}_n] \\ \frac{\partial \boldsymbol{F}_{nl}}{\partial \omega} &= \frac{\partial \boldsymbol{F}_{nl}}{\partial \bar{\boldsymbol{f}}_{nl}} \frac{\partial \bar{\boldsymbol{f}}_{nl}}{\partial \dot{\bar{\boldsymbol{x}}}} \frac{\partial \dot{\bar{\boldsymbol{x}}}}{\partial \omega} = (\Gamma^{-1} \otimes \boldsymbol{I}_n) \frac{\partial \bar{\boldsymbol{f}}_{nl}}{\partial \dot{\bar{\boldsymbol{x}}}} [(\Gamma\nabla) \otimes \boldsymbol{I}_n] \boldsymbol{X} \end{aligned} \tag{1.26}$$

with the diagonal matrices:

$$\begin{aligned} \frac{\partial \bar{\boldsymbol{f}}_{nl}}{\partial \bar{\boldsymbol{x}}} &= \operatorname{diag}\left(\left.\frac{\partial \boldsymbol{f}_{nl}}{\partial \boldsymbol{x}}\right|_{t=t_1}, \dots, \left.\frac{\partial \boldsymbol{f}_{nl}}{\partial \boldsymbol{x}}\right|_{t=t_N} \right) \\ \frac{\partial \bar{\boldsymbol{f}}_{nl}}{\partial \dot{\bar{\boldsymbol{x}}}} &= \operatorname{diag}\left(\left.\frac{\partial \boldsymbol{f}_{nl}}{\partial \dot{\boldsymbol{x}}}\right|_{t=t_1}, \dots, \left.\frac{\partial \boldsymbol{f}_{nl}}{\partial \dot{\boldsymbol{x}}}\right|_{t=t_N} \right) \end{aligned} \tag{1.27}$$

1.2 Stability and bifurcation analysis

For nonlinear systems, continuation techniques permit obtaining all the periodic solutions with respect to a varying frequency of excitation. Due to the nonlinearities, solutions can be multiple and be either stable or unstable. Various types of stability such as the stability of Lyapunov, the orbital stability or the asymptotic stability can be found in the litterature. Ge *et al.* in [GE 01] used the direct Lyapunov method to compute the stability of

periodic solutions of a rotated pendulum excited by the base. Wiggins *et al.* in [WIG 03] used asymptotic stability to analyze the evolution of the fixed point on the Poincaré sections. Further information on stability calculation are included in the following references: Nayfeh and Balachandran [NAY 08a], Govaerts [GOV 00], Kuznetsov [KUZ 13], Seydel [SEY 09], Guckenheimer [GUC 13] and Verhulst [VER 06]. For the computation of periodic solutions, the linearized stability is considered. The Floquet theory is based on the analysis of the eigenvalues of the so-called monodromy matrix in the time domain, whereas it relies on a quadratic eigenvalue problem obtained by Hill's method and HBM in the frequency domain.

At some specific points, the stability of the periodic solution is ill-posed and the implicit function theorem is invalidated. Such points, called bifurcations, are indicative of a number of solutions greater than one, amplitude jumps, loss of stability, change of dynamical regime, quasi-periodicity, chaos, etc ... [SEY 09]. Their precise computation is therefore of high interest. Bifurcation points are computed with two main classes of algorithms. The first one comprises the so-called minimally extended systems which add to the equilibrium equation a single scalar equation defined with a bordering technique. The other class relies on standard extended systems which add a set of equations characterizing the bifurcation by means of the eigenvectors. Bifurcation points can be classified by their co-dimension. Co-dimension 1 bifurcations found on limit cycles are composed by Limit Points (LPs), Branch Points (BPs) and Neimark-Sacker points (NSs). LP bifurcations are associated with dynamical phenomena such as loss of stability, amplitude jumps or generation of ISs that can lead to unexpected behavior. The first calculation of LPs with standard extended systems was proposed by Seydel [SEY 79b, SEY 79a], then by Moore and Spence [MOO 80] and Wriggers and Simo [WRI 90] amongst others. The calculation of LPs with minimaly extended systems was first proposed by Griewank and Reddien [GRI 84], then used in multiple works [GOV 00, BAT 03]. The coupling of standard extended systems with HBM was developed by Petrov [PET 16] in the case of branch points and by Xie *et al.* [XIE 16a] in the case of LPs. However, the characterization of codimention-2 bifurcations in the framework of the HBM is not addresses in the literature. In Section 2.1, descriptions for the detection and localization of Bogdanov-Takens and Zero-Hopf bifurcations are proposed. The detection, the localization and the tracking of codimension-1 bifurcations is also recalled.

In Subsections 1.2.1 and 1.2.2, the two methods used for linearized stability computation are recalled. Then, in the Subsection 1.2.3, bifurcations analysis is detailed, based on the previously recalled linearized stability. Hill's method and the associated bifurcation analysis are taken as references in the rest of the thesis.

1.2.1 Floquet Theory

Floquet theory is used for stability calculation of periodic solutions in the time domain. This theory is based on the analysis of the eigenvalues of the so-called monodromy matrix. First, the equation of motion (1.1) is reduced to a first order differential equation:

$$\tilde{\boldsymbol{x}}(t) = \mathscr{F} \cdot \tilde{\boldsymbol{x}}(t) - \tilde{\boldsymbol{f}}_{nl}(\tilde{\boldsymbol{x}}, \tilde{\dot{\boldsymbol{x}}}) + \tilde{\boldsymbol{f}}(t)$$

$$\text{with} \quad \mathscr{F} = \begin{bmatrix} \boldsymbol{0}_n & \boldsymbol{I}_n \\ -\boldsymbol{M}^{-1}\boldsymbol{K} & -\boldsymbol{M}^{-1}\boldsymbol{C} \end{bmatrix}, \quad \tilde{\boldsymbol{x}} = [\boldsymbol{x}(t),\ \dot{\boldsymbol{x}}(t)]^T,$$

$$\tilde{\boldsymbol{f}}_{nl}(\tilde{\boldsymbol{x}}, \tilde{\dot{\boldsymbol{x}}}) = [\boldsymbol{0}_n,\ \boldsymbol{M}^{-1}\boldsymbol{f}_{nl}(\boldsymbol{x}, \dot{\boldsymbol{x}})]^T, \quad \tilde{\boldsymbol{f}}(t) = [\boldsymbol{0}_n,\ \boldsymbol{M}^{-1}\boldsymbol{f}(t)]^T \tag{1.28}$$

$\boldsymbol{x}(t)$ is composed of a small perturbation $\boldsymbol{y}(t)$ added to the periodic solution $\boldsymbol{x}_0(t)$ of the Eq. (1.28):

$$\boldsymbol{x}(t) = \boldsymbol{x}_0(t) + \boldsymbol{y}(t) \tag{1.29}$$

Then a Taylor series is applied to the combination of Eqs. (1.29) and (1.28). By keeping only the linear terms, the following equation is obtained:

$$\dot{\boldsymbol{y}} = \boldsymbol{J}^f(\tilde{\boldsymbol{x}}_0, t) \cdot \boldsymbol{y}(t) = \left(\mathscr{F} - \left. \frac{\partial \tilde{\boldsymbol{f}}_{nl}}{\partial \tilde{\boldsymbol{x}}} \right|_{\tilde{\boldsymbol{x}} = \tilde{\boldsymbol{x}}_0} \right) \cdot \boldsymbol{y}(t)$$

$$\text{with} \quad \frac{\partial \tilde{\boldsymbol{f}}_{nl}}{\partial \tilde{\boldsymbol{x}}} = \begin{bmatrix} \boldsymbol{0}_n & \boldsymbol{0}_n \\ \boldsymbol{M}^{-1}\frac{\partial \boldsymbol{f}_{nl}}{\partial \boldsymbol{x}} & \boldsymbol{M}^{-1}\frac{\partial \boldsymbol{f}_{nl}}{\partial \dot{\boldsymbol{x}}} \end{bmatrix} \tag{1.30}$$

The differential equation possesses exactly $2n$ independent solutions $\boldsymbol{y}_j$, with $j = 1, 2, ..., 2n$, which form the following solution matrix, see [DIE 68]:

$$\mathscr{Y}(t) = [\boldsymbol{y}_1(t)\ \ \boldsymbol{y}_2(t)\ \cdots\ \boldsymbol{y}_n(t)] \tag{1.31}$$

$\boldsymbol{J}^f$ being periodic of the same periodic as $\boldsymbol{x}(t)$, the solution matrix respects the following equation:

$$\dot{\mathscr{Y}} = \boldsymbol{J}^f(\tilde{\boldsymbol{x}}_0, t)\mathscr{Y} \tag{1.32}$$

t is then replaced by $t' = t + T$ in Eq. (1.32). As $\boldsymbol{J}^f$ is periodic of period T, the following equation is obtained:

$$\frac{d\mathscr{Y}}{dT} = \boldsymbol{J}^f(\tilde{\boldsymbol{x}}_0, t)\mathscr{Y}(t) = \boldsymbol{J}^f(\tilde{\boldsymbol{x}}_0, t)\mathscr{Y}(t') \tag{1.33}$$

The obtained equation is equivalent to Eq. (1.30) but with $\mathscr{Y}(t+T)$ as solution. However, it exists only $2n$ independent solutions, therefore $\mathscr{Y}(t+T)$ can be expressed as the multiplication of $\mathscr{Y}(t)$ with a transformation matrix Φ.

$$\mathscr{Y}(t+T) = \mathscr{Y}(t)\Phi \tag{1.34}$$

Φ performs a change of basis and is called the monodromy matrix. The initial conditions $\mathscr{Y}(t=0)$ are the identity matrix $\mathbf{I}_{2n}$. Therefore, the monodromy matrix Φ is equal to $\mathscr{Y}(T)$. In order to compute the monodromy matrix Φ, the following equation has to be integrated in the time domain:

$$\boldsymbol{M}\ddot{\boldsymbol{\phi}}(t) + (\boldsymbol{C} + \frac{\partial \boldsymbol{f}_{nl}}{\partial \dot{\boldsymbol{x}}})\dot{\boldsymbol{\phi}}(t) + (\boldsymbol{K} + \frac{\partial \boldsymbol{f}_{nl}}{\partial \boldsymbol{x}})\boldsymbol{\phi}(t) = \boldsymbol{0}_n \tag{1.35}$$

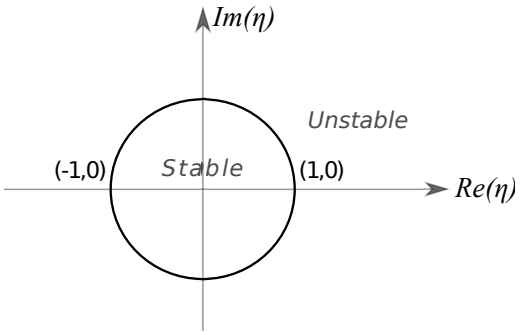

Figure 1.3 – Stability with respect to Floquet multipliers displayed on the complex plan

with the following initial conditions:

$$\phi(t=0) = [\boldsymbol{I}_n \; \mathbf{0}_n] \quad \text{et} \quad \dot{\phi}(t=0) = [\mathbf{0}_n \; \boldsymbol{I}_n] \tag{1.36}$$

Being inconditionnally stable, the implicit Newmark schema is used to integrate this linear system. The monodromy matrix is then obtained after one period of time integration. Then, the eigenvalues of the monodromy matrix, called Floquet multipliers, are used to perform the stability analysis of periodic solutions. The solution is stable when all eigenvalues are within the unity circle $(Re, Im), (|\eta_j| \leq 1 \forall j \in [0, 2n])$. Conversely, when an eigenvalue cross the unity cercle $(\exists j \; tq : |\eta_j| > 1)$, the solution becomes unstable, a bifurcation appears and the theorem of implicit function is invalidated, see Fig. 1.3

1.2.2 Hill's method

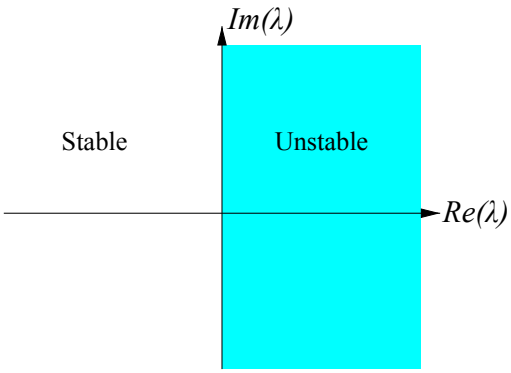

Figure 1.4 – Stability with respect to Floquet exponents displayed on the complex plan

For frequency domain methods, computing the stability directly in the frequency domain is more advantageous. A variant of the Floquet theory, called Hill's method, uses the Floquet exponents to compute the stability of the periodic solutions in the frequency domain [VON 01] [PEL 14]. The following equation represents the relation between the

Floquet multipliers η and the Floquet exponents λ:

$$\eta_j = e^{\frac{\lambda_j 2\pi}{\Omega}} \tag{1.37}$$

Hill's method is also a perturbation method. The periodic solution $\boldsymbol{x}^0(t)$ of the equation of motion (1.1) is perturbed with a small periodic perturbation modulated by an exponential $\boldsymbol{s}(t) = \tilde{\boldsymbol{s}}(t)e^{\Lambda t}$:

$$\boldsymbol{x}(t) = \boldsymbol{x}^0(t) + \boldsymbol{s}(t) \tag{1.38}$$

Since the perturbation is considered small, a linear approximation is retained:

$$\boldsymbol{f}_{nl}(\tilde{\boldsymbol{x}}, \dot{\tilde{\boldsymbol{x}}}) \approx \boldsymbol{f}_{nl}(\tilde{\boldsymbol{x}}^0, \dot{\tilde{\boldsymbol{x}}}^0) + \frac{\partial \boldsymbol{f}_{nl}}{\partial \tilde{\boldsymbol{x}}}(\tilde{\boldsymbol{x}}^0, \dot{\tilde{\boldsymbol{x}}}^0)\boldsymbol{s}(t) + \frac{\partial \boldsymbol{f}_{nl}}{\partial \dot{\tilde{\boldsymbol{x}}}}(\tilde{\boldsymbol{x}}^0, \dot{\tilde{\boldsymbol{x}}}^0)\dot{\boldsymbol{s}}(t) \tag{1.39}$$

Combining Eqs. (1.1), (1.38) and (1.39), yields:

$$\boldsymbol{M}\ddot{\boldsymbol{s}}(t) + \left(\boldsymbol{C} + \frac{\partial \boldsymbol{f}_{nl}}{\partial \dot{\tilde{\boldsymbol{x}}}}(\tilde{\boldsymbol{x}}^0, \dot{\tilde{\boldsymbol{x}}}^0)\right)\dot{\boldsymbol{s}}(t) + \left(\boldsymbol{K} + \frac{\partial \boldsymbol{f}_{nl}}{\partial \tilde{\boldsymbol{x}}}(\tilde{\boldsymbol{x}}^0, \dot{\tilde{\boldsymbol{x}}}^0)\right)\boldsymbol{s}(t) = \boldsymbol{0}_n \tag{1.40}$$

$\tilde{\boldsymbol{s}}(t)$ is approximated by a truncated Fourier series at the order H:

$$\tilde{\boldsymbol{s}}(t) = \boldsymbol{\phi}^0 + \sum_{k=1}^{H}\left(\boldsymbol{\phi}_c^k \cos k\omega t + \boldsymbol{\phi}_s^k \sin k\omega t\right) = (T(\omega t) \otimes \boldsymbol{I})\boldsymbol{\phi} \tag{1.41}$$

By applying the same Galerkin procedure as in Section.1.1.1, the following quadratic eigenvalues problem (QEP) is obtained:

$$\boldsymbol{Q}(\boldsymbol{X}, \lambda, \boldsymbol{\phi}) = (\boldsymbol{R}_X + \Lambda\boldsymbol{\Delta}_1 + \Lambda^2\boldsymbol{\Delta}_2)\boldsymbol{\phi} = \boldsymbol{0}_L \tag{1.42}$$

with Λ the complex eigenvalues, $\boldsymbol{\phi} = \boldsymbol{\phi}_r + i\boldsymbol{\phi}_i$ the complex eigenvectors, $\boldsymbol{R_X}$ the jacobian matrix defined in Eq. (1.24) and:

$$\begin{aligned}\boldsymbol{\Delta}_1 &= \boldsymbol{\Delta}_{1l} + \boldsymbol{\Delta}_{1nl} \\ &= 2\omega\nabla \otimes \boldsymbol{M} + \boldsymbol{I}_{2H+1} \otimes \boldsymbol{C} + \boldsymbol{\Delta}_{1nl} \\ &= diag\left(\boldsymbol{C}, \begin{bmatrix} \boldsymbol{C} & 2\omega\boldsymbol{M} \\ -2\omega\boldsymbol{M} & \boldsymbol{C} \end{bmatrix}, \ldots, \begin{bmatrix} \boldsymbol{C} & 2H\omega\boldsymbol{M} \\ -2H\omega\boldsymbol{M} & \boldsymbol{C} \end{bmatrix}\right) + (\Gamma^{-1} \otimes \boldsymbol{I}_n)\frac{\partial \boldsymbol{f}_{nl}}{\partial \dot{\tilde{\boldsymbol{x}}}}(\Gamma \otimes \boldsymbol{I}_n)\end{aligned} \tag{1.43}$$

$$\boldsymbol{\Delta}_2 = \boldsymbol{I}_{2H+1} \otimes \boldsymbol{M} \tag{1.44}$$

The quadratic eigenvalue problem from Eq. (1.42) can be reduced to a classical linear eigenvalue problem:

$$(\hat{\boldsymbol{J}} - \Lambda \cdot \boldsymbol{I}_{2L})\bar{\boldsymbol{\phi}} = \boldsymbol{0}_{2L} \tag{1.45}$$

with

$$\hat{\boldsymbol{J}} = \begin{bmatrix} \boldsymbol{0}_L & I_L \\ -{\boldsymbol{\Delta}_2}^{-1}\boldsymbol{R}_Q & -{\boldsymbol{\Delta}_2}^{-1}\boldsymbol{\Delta}_1 \end{bmatrix} \quad \text{and} \quad \bar{\boldsymbol{\phi}} = \begin{pmatrix} \boldsymbol{\phi} \\ \Lambda\boldsymbol{\phi} \end{pmatrix} \tag{1.46}$$

Once solved, $2L$ complex eigenvalues Λ of $\hat{\boldsymbol{J}}$ are obtained.

$$\Lambda_k = \lambda_j + il\omega$$
$$\text{with} \quad j \in [0,2n]\,,\, k \in [0,2L]\,,\, l \in [-H,H]\,,\, 2L = 2n \times (2H+1) \text{ and } i^2 = -1 \quad (1.47)$$

For an infinite number of harmonics, only $2n$ of the found eigenvalues are equal to the Floquet exponents [MOO 05] with n being the number of DOFs of the system. However, the difficulty lies in finding the $2n$ eigenvalues among the $2L$ found eigenvalues that are the closest to the $2n$ Floquet exponents. In the rest of the thesis, the $2n$ eigenvalues with the smallest imaginary parts are retained. As an alternative, Lazarus and Thomas [LAZ 10] proposed to use the eigenvalues associated with the most symmetric eigenvectors of the Hill matrix. A solution is stable when the real part of all exponents are below zero. Conversely, when a single eigenvalue crosses the imaginary axis, the solution becomes unstable, see Fig. 1.4.

1.2.3 Bifurcation analysis

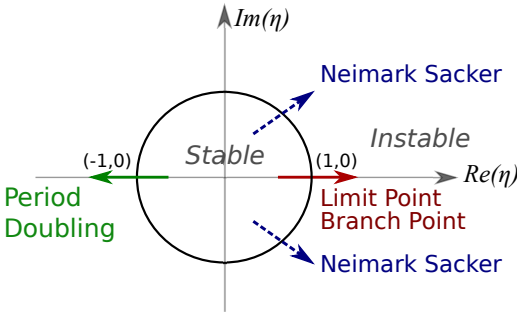

Figure 1.5 – Bifurcations with respect to Floquet multipliers displayed on the complex plan.

The methods for bifurcation localization and calculation depend on the domain in which the bifurcation analysis is performed. For time domain, the bifurcation analysis uses the Floquet multipliers obtained from the monodromy matrix, see Subsection. 1.2.1. A bifurcation point occurs when one of the Floquet multiplier crosses the unit circle, see Fig. 1.3. The following types of bifurcations can appears during the continuation of Nonlinear Normal Modes (NNMs) and periodic solution of discrete time dynamical forced system [KUZ 13]:

- A Limit Point (LP) and a Branch Point (BP) are co-dimension 1 bifurcations that appears for $\eta = 1$.
- A Neimark Sacker (NS) is a co-dimension 1 bifurcation that appears for $\eta = e^{\frac{2\pi\omega_2}{\omega_1}}$ with $\frac{\omega_1}{\omega_2} \notin \mathbb{Q}$.

- A Strong resonance (SR) are co-dimension 2 bifurcations characterized by $\eta = \frac{2\pi\omega_2}{\omega_1}$ with $\frac{\omega_1}{\omega_2} \in \mathbb{Q}$. The period doubling (PD) is a co-dimension 1 bifurcation that is a special case of Strong Resonance (SR) bifurcations with $\eta = -1$.

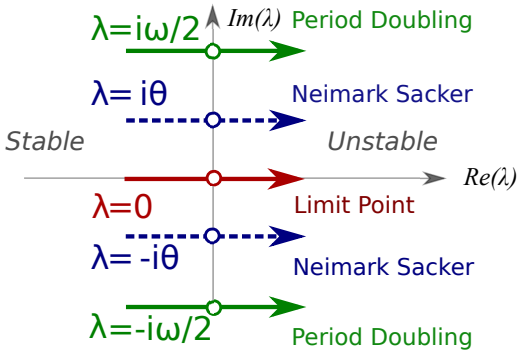

Figure 1.6 – Bifurcations with respect to Floquet exponents displayed on the complex plan. $\theta \notin 2\pi\mathbb{Q}$

In the case of discrete frequency methods such as the HBM, the characterization of these bifurcations is based on Hill's method. With Hill's method, a bifurcation appears when a Floquet exponent λ crosses the imaginary axis, see Fig. 1.6. As stated in Subsection 1.2.2, the Floquet multipliers η and the Floquet exponents λ are linked by Eqs. (1.37) and (1.47). Therefore, performing stability analysis using Hill's method transforms the unity circle from the Floquet theory into the imaginary axis. Contrarily to the characterization of bifurcations obtained in the time domain, Hill's method provides a frequency domain characterization with new considerations. Bifurcation points in the frequency domain are characterized as follows:

- A LP appears for $\lambda = 0$ and $\boldsymbol{R}_{\omega}^{T}\boldsymbol{\phi} \neq 0$
- A BP appears for $\lambda = 0$ and $\boldsymbol{R}_{\omega}^{T}\boldsymbol{\phi} = 0$.
- A NS bifurcation appears for $\lambda = \frac{2\pi\omega_2}{\omega_1}$ with $\frac{\omega_1}{\omega_2} \notin \mathbb{Q}$.
- A SR bifurcation appears for $\lambda = \frac{2\pi\omega_2}{\omega_1}$ with $\frac{\omega_1}{\omega_2} \in \mathbb{Q}$. One can see from Eq. 1.47, that for $\frac{\omega_1}{\omega_2} \in \mathbb{N}$ it exists $l \in [-H, H]$ such that an eigenvalue $\Lambda = 0$. In such case, when the HBM is used to compute the periodic solution, SR bifurcation can be computed as a pitchfork bifurcation which is a particular case of BP. This remark is based on a generalization of the characterization of PD as a pitchfork bifurcation when the HBM is used, see [PIC 94]. The period doubling bifurcation is a special case of Strong Resonance (SR) bifurcations. PD bifurcation appears for $\lambda = -1$.

Limit Point (LP) A co-dimension 1 bifurcation called Limit Point (LP), saddle-node or fold bifurcation, occurs when $\eta = 1$, see Fig. 1.5, and no additional branch of solutions exists. The LP is a point where two fixed points respectively stable and unstable collide together and then disappear, see Fig. 1.7. In order to obtain both solutions, resolution methods combined with continuation technique such as the ones presented respectively in presented in Subsections 1.1.1 and 1.1.2 are needed. Such methods permit following the periodic solutions through the LP bifurcation while being able to compute unstable solutions.

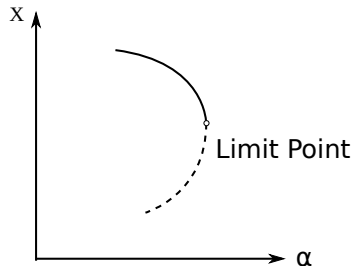

Figure 1.7 – Limit Point bifurcation

Branch point (BP) A co-dimension 1 bifurcation Branch Point (BP) occurs when $\eta = 1$, see Fig. 1.5, and an additional branch of solutions exists. Before the BP, a unique solution exits. After the BP, the previous solution changes its stability and two new stable or unstable solutions appear from the critical point, see Fig.1.8. In order to follow the new branch of solutions, branching methods are used. Two types of Branch Point can be highlighted, the transcritical bifurcation and the pitchfork bifurcation. A transcritical bifurcation is a point where the continuated curve loops back on itself. At such point, the stability of the new branch of solutions changes, see Fig.1.8a. A pitchfork bifurcation represents the breaking of an underlying symmetry of the system, see [SEY 09]. Locally, the new branch is symmetric with respect to the main branch, see Fig. 1.8b. The stability of the new branch does not change at the pitchfork bifurcation. Two types of pitchfork bifurcation can occur, the super- and the sub-critical bifurcations which are characterized by the stability of the appearing branch of periodic solutions. For the supercritical pitchfork bifurcation, the new solution branch is stable, see Fig. 1.8b. Conversely, for the subcritical pitchfork bifurcation, the new solution branch is unstable, see Fig.1.8c.

Neimark Sacker (NS) A co-dimension 1 bifurcation Neimark Sacker (NS), also called secondary Hopf bifurcation [SEY 09], occurs when $\eta = e^{\pm i\theta}$ and $\theta = \frac{2\pi\omega_2}{\omega_1}$ where $\frac{\omega_1}{\omega_2} \notin \mathbb{Q}$. It is not necessary to verify that $\frac{\omega_1}{\omega_2} \notin \mathbb{Q}$ since NS bifurcations are the only co-dimension 1 bifurcations with $Im(\lambda) \neq 0$, see Fig. 1.5. At such bifurcation point, the periodic solution changes its stability and a new branch of quasi-periodic solutions appears from the critical point. The quasi-periodic solutions can be represented as a torus composed by

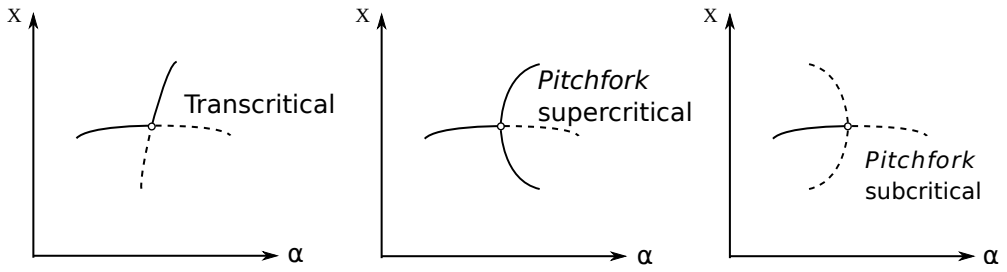

(a) Transcritical bifurcation (b) Supercritical pitchfork bifurcation (c) Subcritical pitchfork bifurcation

Figure 1.8 – Branch Point bifurcation

the pulsation ω_1 of the previous limit cycle and a new pulsation ω_2, see [KUZ 13]. The NS bifurcation can either be supercritical, see Fig. 1.9a, or subcritical, see Fig. 1.9b.

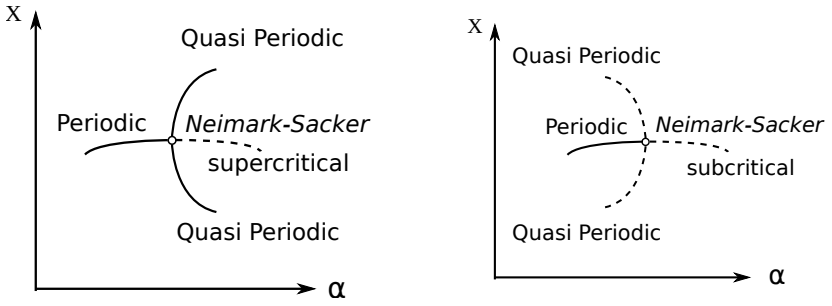

(a) Supercritical NS (b) Subcritical NS

Figure 1.9 – Neimark-Sacker bifurcation

Strong Resonances (SR) The co-dimension 2 bifurcation Strong Resonance (SR), also called internal resonance, occurs when $\eta = e^{\pm i\theta}$ with $\theta = \frac{2\pi\omega_2}{\omega_1}$ and $\frac{\omega_1}{\omega_2} \in \mathbb{Q}$. When encountered on Nonlinear Normal Modes (NNMs) the SRs are also called modal interaction bifurcations. At such a bifurcation point, the solution of period ω_1 changes its stability and a new branch of periodic solutions with a period ω_2 appears from the critical point. At the bifurcation point, the topology of the periodic solutions is the same as the pitchfork bifurcation. Co-dimension 1 bifurcation Flip, also called period doubling, occurs when $\eta = -1$, see Fig. 1.5. Its a special case of strong resonances with $\frac{\omega_1}{\omega_2} = \frac{1}{2}$. The periodic solution changes its stability by going through the Flip bifurcation and a new branch of solutions appears. However, the new branch of solutions is now $2T$ periodic instead of T periodic.

1.3 Parametric analysis by continuation of localized point

A parametric analysis is difficult to perform in the case of nonlinear dynamical systems. Because of all the complex behaviors such as multiple solutions and branching points, specific methods. A first step to more efficient parametric analysis has been achevied by creating bifurcation tracking algorithms. They permit a chosen bifurcation to be tracked with respect to a single varying system parameter. Although bifurcation tracking permits to visualize the evolution of the system dynamics, a mono-parametric analysis method is not sufficient to deal with the complex topology of nonlinear systems. Therefore, multi-parametric continuation methods need to be created. In this thesis, a multi-parametric continuation method for the recursive continuation of specific points is proposed. The idea behind the method proposed in Chapter 2 is to use a constraint equation characterizing extremum points to provide additional equations. With the obtained equations, a recursive algorithm that can perform multi-parametric analysis of nonlinear systems is proposed. In the literature, some researchers use constraint equations coming from the domain of optimization to perform optimization by continuation. Kernevez and Doedel [KER 90] used a descent optimization algorithm coupled with a shooting method and continuation to perform optimization of Isolated Solutions (IS) of nonlinear systems by tracking specific bifurcation points. To our knowledge, the use of constraint equations from the optimization domain to perform multi-parametric recursive continuation is not addressed in the literature.

The proposed multi-parametric recursive continuation method, applied to nonlinear dynamical systems, is conveniently initialized by the continuation of bifurcations. Section 2.3 describes the IS analysis of the forced responses of a NonLinear Tuned Vibration Absorber (NLTVA). In this investigation, the multi-parametric recursive continuation method uses bifurcation tracking as an initialization.

First, a summary of the literature on bifurcation tracking is presented. Then, a proposed method for multi-parametric recursive continuation is contextualized with research combining continuation, optimization and recursion by taking into account critical points.

1.3.1 Bifurcation tracking

The tracking of bifurcations permits efficient parametric analysis to better understand the complexity of the dynamical behavior of nonlinear systems. LP tracking was first done by Jepson and Spence [JEP 85] with standard extended systems. It was also used to analyze the sensitivity of critical buckling loads to imperfections [ERI 99, BAG 02, REZ 14]. Codimension-1 bifurcation tracking for dynamical systems has been incorporated in several softwares. Algorithms based on minimally extended systems can be found in the books of Kuznetsov [KUZ 13] and Govaerts [GOV 00] and have been implemented in the MATCONT software [DHO 03]. On the other hand, bifurcation tracking based on standard extended systems is used in the softwares AUTO [DOE 07], LOCA [SAL 05] and COCO [DAN 11]. The tracking of codimension-1 bifurcations points using minimaly

extended system combined with the HBM with application to large-scale mechanical systems was proposed by Detroux *et al.* [DET 15b]. Xie *et al.* [XIE 16a] implemented the continuation of LPs and Neimark-Sacker bifurcations using standard extended systems and HBM to analyze a nonlinear energy sink (NES), see Fig. 1.10, and a nonlinear Jeffcott rotor.

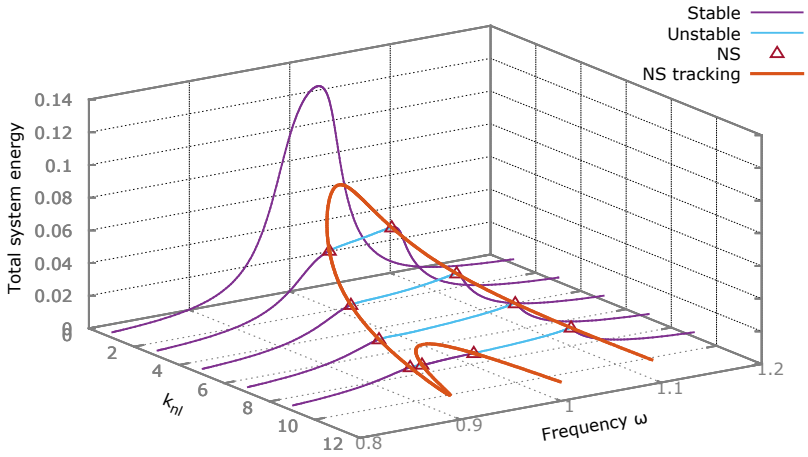

Figure 1.10 – Frequency responses and Neimark-Sacker bifurcation tracking extracted, after [XIE 16a]

1.3.2 Multi-parametric method

When dealing with nonlinear systems, one parameter continuation methods may be too limited because system parameters are often inter-correlated. Therefore, multi-parametric continuation methods are interesting tools for analyzing the behavior of a system when several or all the parameters vary. To develop such a method, additional constraint equations need to be appended to the extended system in order to free additional system parameters. Constraint equations characterizing extremum points are good candidates for this purpose. In this case, multi-parametric continuation methods are close to the methods of the literature dealing with optimization. Several references deal with optimization algorithms coupled with continuation techniques to provide new multi-parametric methods. For instance, it was used in homotopy techniques where a small parameter is introduced to link two problems. This technique was notably used in optimization for smoothing techniques [NG 02, DES 09, MOB 15] and for the fitting of optimal system kinematics [HAN 95, LIU 99]. Continuation methods were also used to explore the topology of extremums for large parametric deformations [RAO 89]. The methods resulting from the coupling of optimization algorithm and continuation techniques have since been extended in several directions such as multi-parametric algorithms, recursive methods and critical

set point analysis [JON 86, GUD 88]. Concerning multi-parametric algorithms, Wolf and Sanders [WOL 96] proposed a multi-parametric homotopy technique for computing operating points of nonlinear circuits. Then, Vanderbeck [VAN 01] used a multi-parametric optimization by recursion to optimize a manufactering cutting process. Recursion-based optimization was addressed by Schuetze *et al.* [SCH 05] who proposed a recursive subdivision technique to perform multi-objective and multi-parametric optimization. Since then, multi-parametric optimization was coupled with continuation, Kernevez and Doedel [KER 90] used a descent optimization algorithm coupled with a continuation method to perform the optimization of ISs of nonlinear systems. Later, Balaram *et al.* [BAL 12] combined the method from Kernevez and Doedel with a genetic algorithm in order to provide a global algorithm of optimization by continuation. They used this method to minimize the acceleration of a Duffing oscillator and to tune nonlinear vibration absorbers.

From the different examples of research, the constraint equations corresponding to extrema have been retained. There are the most likely to occur during continuation and are points of high interest for parametric analysis. Moreover, tracking extrema allows the same structure of augmented system to be used at each level of continuation, thus permitting multi-parametric recursive continuation method to be created.

1.3.3 Applications

Optimization of NLTVA In the litterature, the NLTVA was used for many applications. Wang [WAN 11] tuned a NLTVA to minimize the critical limiting depth induced by chatter during machining process. An optimized hysteretic NLTVA was used by Carpineto *et al.* [CAR 14] for minimizing the vibrations of structures. Detroux *et al.* [HAB 15] optimized a NLTVA by generalizing Den Hartog's equal-peak method to nonlinear systems. The NLTVA was also used in passive control of Airfoil flutter by Mahler *et al.* [MAL 16] who optimized a NLTVA to push the appearance of the post-critical regime at higher flux velocities. Besides its advantageous properties, the NLTVA also presents some unwanted adverse dynamical phenomena such as the generation of ISs. These isolated resonance curves are periodic solutions detached from the main response curves. They are therefore difficult to compute by simply continuating the main response curves.

Isolated solution (IS) In order to properly design nonlinear systems, it is important to be able to detect ISs. ISs were first studied in 1951 by Abramson [ABR 55]. Since then, several scenarios for the creation of ISs have been revealed. DiBerardino and Dankowicz [DIB 14] showed that ISs can be created by introducing asymmetry into a nonlinear system. In [MAN 16], the presence of IS is explained analytically by analyzing the 1:3 internal resonance configuration between two Duffing oscillators for different couplings. In [ARR 16], an experiment was carried out to illustrate the IS phenomenon between a Duffing oscillator and a clamped-clamped beam at a 1:3 internal resonance configuration. In both papers, the frequency gap between the response curve and the IS was calculated and explained by means of phase-locking. Gatti investigated a mechanical system composed of a primary mass linked with nonlinear coupling to a smaller second mass. He used

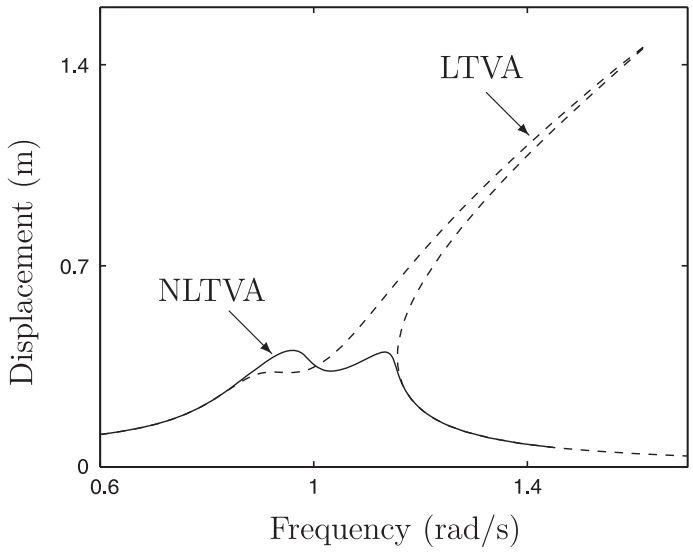

Figure 1.11 – Frequency responses of the primarily mass with a LTVA and a NLTVA under equal peak constraints, after [HAB 15]

analytical methods to compute frequency response curves of coupled oscillators and uncovered IS [GAT 10], then he used LP curves to predict the appearance of IS [GAT 16b]. These researches have since been applied to a nonLinear vibration absorber to predict its dynamics while reducing the vibration of the primiraly mass [GAT 16a, GAT 18]. Detroux *et al.* [DET 15a] presented a method to localize the ISs in a NLTVA using LP continuation. The presence of IS was also explained with NNM continuation and internal resonances. In [HIL 16], Hill *et al.* calculated the NNMs of a NLTVA system composed of a Duffing oscillator coupled to a linear oscillator with a cubic spring. They used an energy balance method to link the energy of the modes to the amplitude of the force to be injected into the damped system in order to obtain a frequency response curve with the same level of energy. By superimposing the obtained NNM with the response curve, IS phenomenon was explained by means of internal resonances. Using singularity theory and HBM, Habib *et al.* [HAB 17] analyzed the mechanism of IS creation in a Duffing oscillator with nonlinear damping and demonstrated the link between the damping force and ISs, see Fig. 1.12b. The same singularity theory was used by Cirillo *et al.* [CIR 17] to study IS topology based on hysteresis, bifurcation and isola center points.

Some references dealing with IS optimization also exist. For a NES system, Starosvetsky and Gendelman [STA 09] showed that it is possible to remove ISs by adding a well tuned piece-wise quadratic damping into the mechanical system. Gourc *et al.* [GOU 14] showed that ISs can be removed while conserving the energy pumping property by working on the values of the system parameters. Concerning the NLTVA, Cirillo *et al.* [CIR 17] showed that a fith order nonlinear spring can be tuned to remove the ISs generated by the cubic spring. However, it turned out that IS can be generated when increasing the order of the nonlinear additional spring. Kernevez and Doedel [KER 90] mixed a continuation method with a steepest descent algorithm to obtain a unique local optimum.

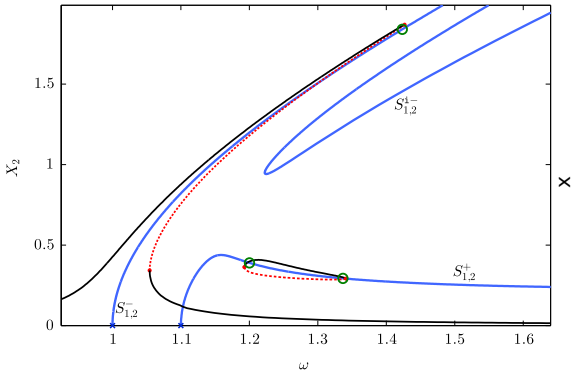

(a) Presence of IS and INNM in an asymmetric system, after [HIL 16]

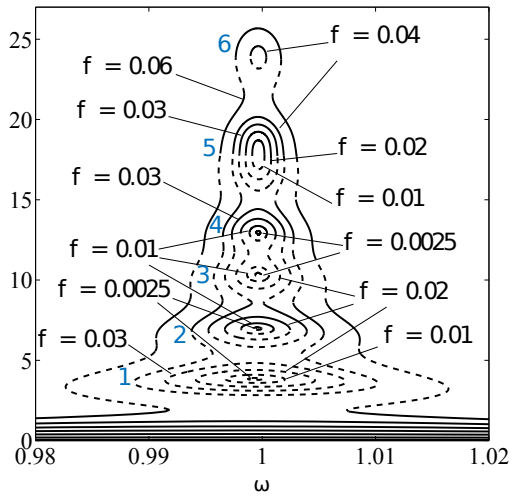

(b) System with sinusoidal damping presenting multiple IS, after [HAB 17]

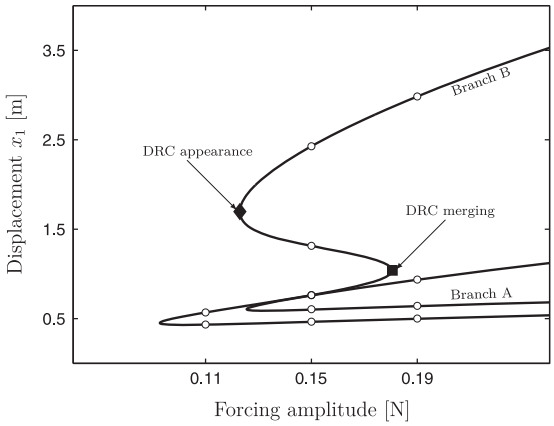

(c) Detection of IS with LP continuation, extracted, after [DET 15a]

Figure 1.12 – Some IS analysis present in the literature

They used a so-called optimization by continuation of isola center with respect to one system parameter to optimize ISs.

1.4 Nonlinear Normal Modes for nonlinear modal analysis

Normal modes analysis is central to the understanding and the simulation of vibrating systems. In classical linear theory, Linear Normal Modes (LNMs) can be used to uncouple equations of motion and are closely associated to the property of linear superposition. Thanks to this, the LNMs are exploited for various purposes such as modal reduction, finite element model, experimental vibration analysis.

Linear modal theory is based on multiple properties of LNMs. The invariant property insure that modes shapes and frequency associated to the LNMs do not change in time. The orthogonality property allows any free or forced vibration to be expressed as a linear superposition of LNMs. Another interesting property of LNMs is their unconditional stability. However, the properties of superposition and unconditional stability are not conserved in nonlinear systems. Thus, the generalization of LNMs to NNMs is needed and several definitions of NNMs have been proposed in order to extend the concept of normal modes to the nonlinear equation of motions.

1.4.1 Definition of Nonlinear Normal modes (NNMs)

The concept of Nonlinear Normal Modes is the result of many attempts to extend the concept of Linear Normal Modes to nonlinear dynamics. The first step towards NNMs was made by Lyapunov by proving the existence of synchronous periodic solutions in a Hamiltonian system next to equilibrium points. By using this theorem, Rosenberg [ROS 62] extended the definition of normal modes to define NNMs as synchronous periodic solutions. Recently the Rosenberg's definition of NNMs was extended by Peeters *et al.* to take into account non necessarily synchronous periodic solutions [PEE 09]. The extension of Rosenberg's definition allows internal resonances to occur. By using the theorem provided by Poincaré [POI 15] and Dulac [DUL 12], a second definition for NNMs based on normal form theory was presented by Jézéquel and Lamarque [JEZ 91]. Considering NNMs as non-necessarily synchronous periodic solutions or normal forms provides a direct extension of linear modes to nonlinear dynamics. Other theorems were used to yield new concepts for NNMs characterization. The center manifold theorem introduced by Carr [CAR 12] was used by Shaw and Pierre [SHA 91] to define a NNM as an invariant manifold in phase space. The definition of NNMs as invariant manifolds can be viewed as a new representation of NNMs. The extended definition of Rosenberg for NNMs is the one retained for the computation of NNMs in this Thesis.

1.4.2 Linear vs Nonlinear modal analysis

Nonlinearities appear frequently in real systems and trying to model such systems with linear modal theory without considering the nonlinearities leads to erroneous solutions. Therefore, a nonlinear modal analysis needs to be performed to take into account the complex behavior arising from the nonlinearities of the system. When generalizing the concept of normal modes to the nonlinear domain, the orthogonality and the superposition properties have been lost. Consequently, NNMs loss the main properties used for model reduction. On the other hand, NNMs are still invariant and present some interesting features:

Forced Resonances As in linear modal analysis, NNMs can be used to understand forced resonances. A forced resonance occurs when a NNM of the system is excited. For a nil amplitude of oscillation, the forced resonances happen as in linear theory. However, with an increase of energy in the system, the frequency and the modal shape of the NNM change. The frequency of the modes can decrease leading to a softening effect, or increase leading to a hardening effect. Sometimes in MEMS applications, some cases of mixed behavior can be observed. Mixed behaviors in MEMS are characterized by an hardening effect for lower amplitude and a softening behavior for high amplitude, see Fig. 1.13. These effects can be seen as a dependency of the equivalent linear stiffness coefficient with the amplitude of oscillation.

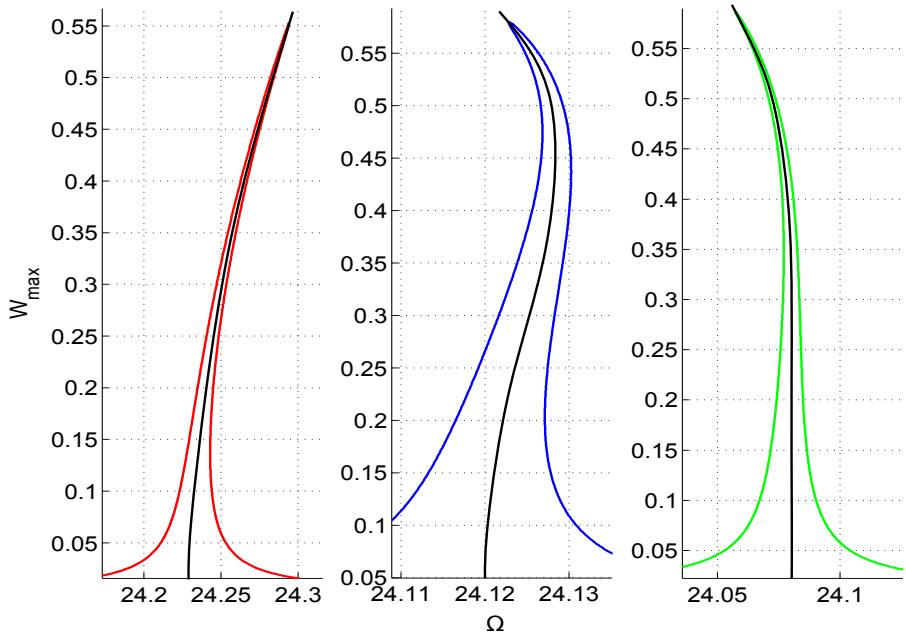

Figure 1.13 – Frequency responses of a single MEMS resonator with hardening, mixte and softening configuration, after [NGU 13], superimposed with their corresponding NNMs

Changes of stability and bifurcations In nonlinear modal analysis, the concepts of stability and bifurcation points are additional features. Stability and bifurcation analysis are important parts of nonlinear modal analysis because they give interesting information about the local changes of the nonlinear dynamics of NNMs. In linear modal analysis, the stability of the modes cannot change, bifurcations cannot appears and the number of normal modes cannot exceed the number of Degree Of Freedom (DOF) of the system. However, in nonlinear modal analysis, NNMs can become unstable with the increase of the amplitude of excitation, leading to the establishment of phenomena such as hysteresis cycles and jumps. As in nonlinear frequency responses, NNMs can contain bifurcations. Bifurcation points are symptomatic of new behaviors such as new branches of periodic, quasi-periodic and static equilibrium, leading to a number of NNMs superior to the number of DOFs. Figure. 1.14 shows a bifurcation on the second NNM leading to two new stable NNMs and an unstable one. Some bifurcations are strongly related to symmetries present in the equation of motion and can exist only in these symmetric configurations. If ever these symmetries are to be broken, so do their associated bifurcations. The breaking of such bifurcations leads to the birth of isolated branches of NNMs (INNM). Therefore, a symmetry analysis of the equation of motion is important, because these symmetries determine the birth of INNMs.

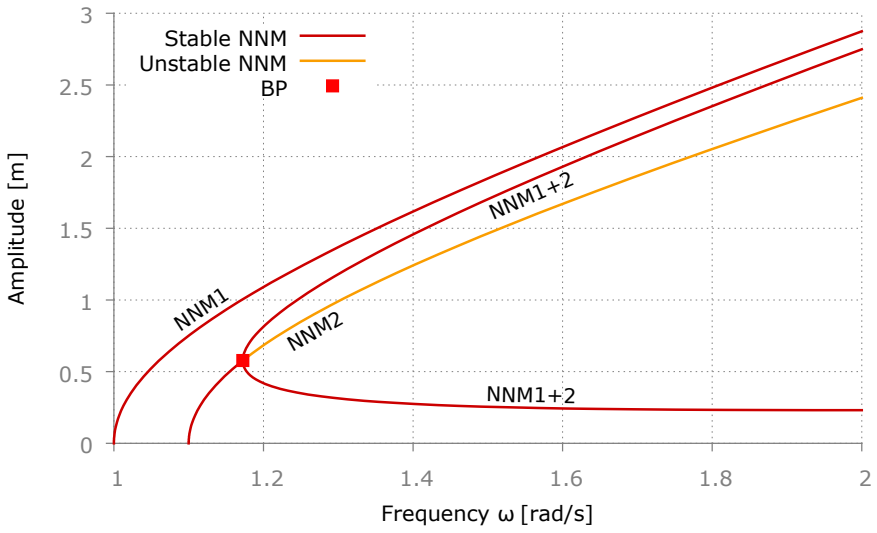

Figure 1.14 – Stable and unstable NNMs with a single bifurcation from Subsection 3.5.2

Modal interactions The notion of modal interaction is not new and is already present in linear modal analysis and in rotor dynamics. In linear modal analysis, a modal interaction occurs when the frequencies of two modes are equal. Therefore, the two LNMs respond at the same frequency but are distinct from each other because of the orthogonality property. In rotor dynamics, the gyroscopic matrix is proportional to the speed of rotation and is superimposed to the damping matrix. However, the resulting equations of motions stay

linear with respect to the displacement. Therefore, in rotor dynamics modal interactions are more often encountered since modes can cross each other. Nevertheless, due to the orthogonality property the modes stay distinct. But in nonlinear modal analysis, due to the changes of frequency, of modal shape of the NNMs and due to the absence of the orthogonality property, NNMs can cross each other and be equal at some points; see for example the 3:1 modal interaction represented in Fig. 1.15.

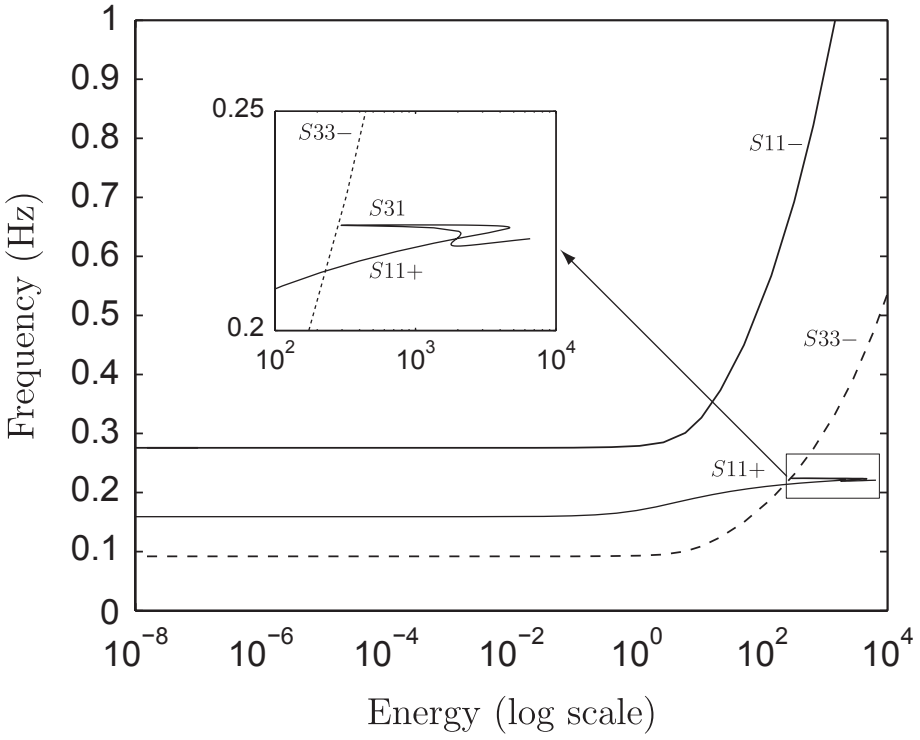

Figure 1.15 – Representation of NNMs with a 3:1 modal interaction, after [KER 09]

One can see the advantage of using nonlinear modal analysis to observe the dynamics of nonlinear systems. Indeed, it brings important information on the dynamics that are not accessible with classical linear modal analysis.

1.4.3 Computation of conservative NNMs

The first investigations defined and computed NNMs as periodic solutions by using analytical methods [MAN 72, JOH 79, RAN 92, NAY 94, VAK 01, GEN 04, MIK 10]. Then, with the appearance of continuation methods, NNMs started to get computed numerically. Pesheck *et al.* [PES 01a] used a numerical method based on invariant manifold theory to compute the NNMs of a rotor blade. Lee *et al.* [LEE 05] proposed to use Pilichuk work, see [PIL 85], to compute NNMs by solving an associated nonlinear boundary value problem with a shooting method. Then Arquier *et al.* [ARQ 06] used a shooting method coupled with the Asymptotic Numerical Method (ANM) to compute NNMs. Peeters *et al.* [PEE 09] proposed a shooting method to compute NNMs. Some others researchers,

such as Lewandowski [LEW 94, LEW 97a, LEW 97b], used HBM to compute NNMs with respect to the synchronous definition of NNMs. Since then, the same methodwas used to compute NNMs by Ribeiro [RIB 99a, RIB 99b], by Stoykov [STO 11] and by Arquier [ARQ 06]. Then, NNMs as non-necessarily synchronous periodic solutions were introduced. Sarrouy [SAR 11] used HBM to compute NNMs of a structure with cyclic symmetry. Krack [KRA 13] proposed a method to compute NNMs with distincts states using HBM. Moussi *et al.* [MOU 13] used HBM coupled with ANM to compute non-smooth NNMs of a system under impact forces. Renson *et al.* [REN 16] presented a review of methods for NNM computation in both time and frequency domain.

Phase condition and continuation method To compute NNMs as non-necessarily synchronous periodic solutions, a phase condition has to be introduced. Indeed, unlike periodic solutions of forced systems, NNMs are computed from an autonomous differential equation. Consequently, the phase of the NNM is unknown and needs to be imposed. To do so, an augmented system is considered. One simple way to eliminate the arbitrariness of the phase is to impose a component of the solution to zero at the beginning of a period. Rinzel [RIN 80] used this phase condition to compute periodic solutions of the Hodgkin-Huxely equation. Renson *et al.* [REN 16] used the velocity displacement vector obtained in the frequency domain set to zero as phase condition. However, not all NNM can be computed by using such a phase condition. Chua and Lin [CHU 75] presented an algorithm that automatically selects an adapted phase condition consisting in fixing a specific component of the periodic solution. This method fixes the problem but is still not optimal.

Other phases conditions can be found in the literature. Some phase conditions presented by Doedel [DOE 81] are based on the orthogonality between the vectors describing the periodic solution and its velocity. Accordingly to the author, the phase condition representing the orthogonality law at a specific time is better used for theoretical purpose, whereas the phase condition based on the integral of the orthogonality law over one period is best suited for numerical methods. These two phase conditions are notably analyzed and used in the literature by Seydel *et al.* [SEY 09] and Beyn *et al.* [BEY 07] for the computation of periodic solutions computation. However, the resulting augmented system composed of the equation of motion and the phase condition is overconstrained. To perform continuation methods based on matrix inversions, various methods can be found in the literature. Renson *et al.* in [REN 16] used the Moore-Penrose pseudo inverse to perform the continuation of the overconstrained augmented system. An alternative method to the Moore Penrose inversion is proposed by Munoz-Almaraz in [MUN 03]. By introducing an parameter of relaxation into the equation of motion, this method permits a square jacobian to be generated in order to perform the continuation with standard inversion and the computation of linearized stability.

Stability and bifurcation analysis Linearized stability analysis of periodic solutions can be performed by means of Floquet theory. Nevertheless, during the computation of NNMs as non-necessarily synchronized solutions, the non-uniqueness coming from the

undetermined phase generates a trivial singularity. One method to perform the stability analysis consists in considering the eigenvalues without the trivial singularity. After implementing this stability analysis method in AUTO, Doedel *et al.* [DOE 03] provided minimally extended systems characterizing both the trivial singularity and co-dimension 1 bifurcation points. However this method can lead to false detection of bifurcations points due to numerical errors. By using deflation techniques the trivial singularity can be removed. In [NET 15], Net and Sanchez used the shooting method combined with deflation techniques to obtain a modified jacobian characterizing bifurcations points.

1.4.4 Extension to non-conservative NNMs

Shaw and Pierre [SHA 93] used the invariant manifold definition of NNMs presented in [SHA 91] to compute non-conservative NNMs. Pesheck was the first to use the definition proposed by Shaw and Pierre. In [PES 01b], he used a Fourier-Galerkin method to compute the invariant manifold of a rotating beam. Then, the proposed method was used by Legrand *et al.* [LEG 04] to compute NNMs of a rotating shaft and by Laxalde and Thouverez [LAX 09] to asses the non-conservative NNMs of turbomachinery bladings with dry friction. In [REN 14], the invariant manifold definition for NNMs wasused to provide a finite-element based method to compute non-conservative NNMs. However, all these descriptions consider non-conservative NNMs as oscillations that gradually loss energy.

In Section 3.2, an extension to non-conservative NNMs using the extended definitions of Rosenberg is proposed. The idea behind this extension is to compensate the energy decrease due to damping by introducing additional terms in the equation of motion while not modifying the original non-conservative NNM. To our knowledge, the definition proposed by Rosenberg has only been used by Krack [KRA 14] for the computation of non-conservative NNMs, see Fig. 1.16. He introduced artificial negative damping matrix to insure the energy balance of the problem. However, it was not proven that the introduction of the artificial damping matrix did not modify the non-conservative NNMs.

1.5 Nonlinear dynamics of resonant MEMS

Micro-Electro-Mechanical-Systems, conviniently called MEMS, are used for many everyday life applications such as aeronautic, automobile, telecommunication, biomedical and so on. Due to their very small size MEMS sensors present many advantages such as being lightweight, cheap to produce, energy efficient and offering the possibility to work in parallel. Compared to other types of MEMS, resonant MEMS sensors present the advantage to work close to the resonant frequency giving several advantages. The high amplitude of vibrations permits to work outside the ambient noise, to increase the dynamical range and the system sensitivity up to $\approx 10^{18} g$ [EKI 04]. Moreover, the characteristics specific to the resonance such as the resonance frequency or the maximum of amplitude can be used to detect very small perturbations. For instance, a change in the axial force or an added mass dropped onto the sensor can be detected by monitoring the

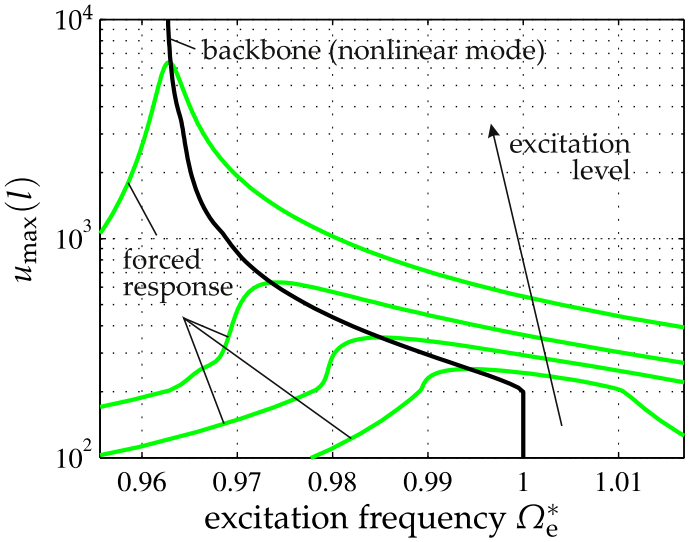

Figure 1.16 – Frequency responses and non-conservative NNM of a forced friction-damped rod, after [KRA 14]

resonance of the MEMS sensor. This process was used for many applications such as measurements of acceleration in [ALB 91], of forces in [HAG 02] or of added mass in [NGU 15].

The MEMS part of the sensor is usually made of a micro-beam which can be driven by thermal, electromagnetic, piezoelectric, electrostatic actuators. The electrostatic actuation is easy to implement even if the control of the actuation force is less efficient than other techniques such as piezoelectric or thermal actuation. To implement an electrostatic actuation of the MEMS, the side of the micro-beam must be made conductive. Then, the micro-beam is actuated by electrostatic forces generated between the beam and the electrodes. The electrostatic force is influenced by the bias voltage V_{dc} and by the alternative voltage V_{ac}. V_{dc} controls the static deflection of the beam, whereas V_{ac} controls the amplitude of oscillations around its static deflection. When both V_{ac} and V_{dc} are used for actuation, their respective effects on the nano-beam response influence each other.

1.5.1 Electrostatic actuated MEMS for mass sensing

At present time, using M/NEMS resonators makes the detection of very tiny mass possible. The MEMS sensor is forced on its fundamental mode by an electrostatic actuator. Then an added mass is dropped onto the resonant MEMS, see Fig. 1.17. By analyzing the difference in the dynamic of the MEMS, the added mass is quantified. For example, a mass sensor operating at ultra-high frequency (1.3 GHz) is capable to detect $10^{-18}g$ [PEN 06] and recently a NEMS-based mass spectrometer accessed masses above 500kDa ($1Da = 1.66 \times 10^{-27}kg$) [HAN 12]. The approach used by Hannay permits the molecules to be detected in real time. It consists in tracking simultaneously multiples frequencies of the resonant sensor. By tracking multiple modes, the localization and the mass of the

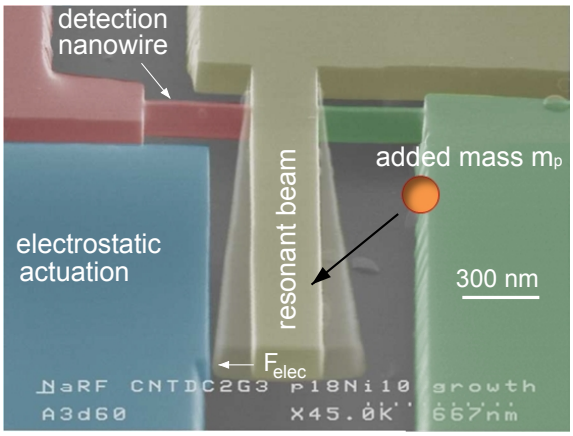

Figure 1.17 – Single MEMS resonator employed for mass sensing (CEA Leti)

molecule can be obtained. However, it is difficult to detect simultaneously many particles and separate one of them in order to drop it onto a micro/nano beam. Detecting several masses at the same time legitimates the research on resonator arrays.

Alternative techniques for mass sensing are being developed. In [YOU 08], [YOU 09], a MEMS device is excited at a frequency close to two times the principal resonance. This excitation gives a clear transition between the state without and with an added mass onto the MEMS. Moreover, it seems that the quality factor has little influence onto the phenomena. Others researchers compared the sensitivity of the torsion and bending modes of the micro-bream [LOB 08]. Xie *et al.* used the first torsion mode based on Rayleigh-Ritz theory [XIE 08]. Experimental results show that the sensitivity of the first bending mode compared to the second one is superior by one order of magnitude. Moreover, the sensitivity increases when the added mass is closer to the edge of the micro-beam. In [JAB 16], the dynamics of higher modes of a clamped-clamped microbeam resonator was analyzed. Then, a proof a concept was realized. The higher modes of the beam were excited experimentally by using partial electrodes.

Zhang *et al.* [ZHA 05] and Thomas *et al.* [THO 13] studied the parametric resonance and showed that the sensitivity is highly increased due to the sharpness of amplitude transition in this regime. In [TUR 01] and [ZHA 04], the mass variation is computed by means of the frequency shift of the first order stable limit of the parametric resonances. This method has for advantage to not depend on the quality factor and is therefore more adapted to applications in open air such as chemistry or biology. Moreover, the sensitivity is higher by one to two more orders of magnitude than the detection using primary resonance with the same resonant sensor.

Davis *et al.* [DAV 07] proposed a new architecture of free-free MEMS resonator for mass sensing application. The idea was to integrate the readout and the actuation into the device to improve the quality factor of the sensor into the device. At first characterization, a quality factor up to 38000 in high vacuum and 13000 at medium vacuum was reached.

1.5.2 Improving MEMS by exploiting nonlinearities

One of the application of resonant MEMS sensors using electrostatic actuation is mass sensing. In the last decade, the dimensions of MEMS have been reduced down to sub-micro-metric regime, thus improving the detection sensitivity up to the zepto-gram (10^{-24}kg) [YAN 06]. However, with the reduction of the dimensions comes the appearance of adverse nonlinear behaviors.

First, the main consideration was to control these adverse nonlinear behaviors in order to insure the integrity of the devices. Ruzziconi *et al.* [RUZ 13] studied a microbeam under axial load and electric excitation. The robustness of stable motions, the disappearance of main attractors and potential jumps to pull-in were studied under disturbances with dynamical integrity concepts. In [KAC 10b], the nonlinear dynamic of a clamped-clamped nanobeam was studied and two critical amplitudes were proposed: one representing the limit of voltage above which the dynamics presents multiple solutions, and the other one defining the limit of voltage above which pull-in occurs. In [NAY 07] and [KAC 12] the authors show pull-in effects can happen and potentially damage the sensor. Other research focused on canceling the nonlinearities. In [KAC 15], Kacem *et al.* showed that the combination of simultaneous resonance and compensation of nonlinear terms can lead to dynamic stabilization of the nanoresonator and make the amplitude of vibration possible close to the gap without pull-in, see Fig. 1.18. Pallay *et al.* [PAL 17] proposed to use repulsive electrostatic actuation to avoid pull-in instability and to achieve large out-of-plane oscillations. An analysis of MEMS dynamics under repulsive actuation was made leading to the following conclusions. The use of repulsive actuation prevents some behaviors, such as pull-in phenomena, to appear. The softening and hardening behaviors are inverted compared to attractive actuation. The softening part appears for low amplitudes of oscillations, whereas the hardening behavior appears for high amplitudes of oscillations.

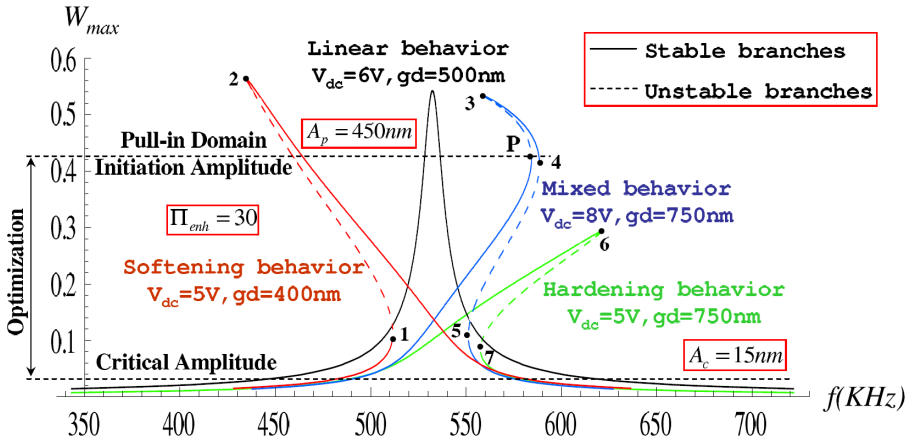

Figure 1.18 – Canceling nonlinearities in single resonant MEMS sensor, extracted from [KAC 10a]

Then, exploring and exploiting nonlinear phenomena to improve performance has

recently received significant attention. A review of past, present researches on the use of nonlinear phenomena in MEMS was proposed by Rhoads [RHO 10]. Indeed, with the excitation of MEMS in the nonlinear regime comes an increase in sensitivity [YUR 06]. For example, in [YUR 95], the nonlinear resonance is used to suppress amplification noise from an circuit of oscillators. In [ALD 05], the noise induced by the switch between two stable states in the nonlinear resonance permits an accurate measurement of the frequency. In the nonlinear regime, the mass sensitivity limit imposed by the thermo-mechanical noise during utilization in the linear regime can be overtaken [BUK 06].

Kumar *et al.* proposed a new technique based on amplitude jumps induced by instability of the frequency resonance in nonlinear regime [KUM 12]. The operating point of the device is chosen close to a Limit Point bifurcation. As a result, when a small added mass drops onto the MEMS, a large amplitude jump occurs. With this technique, the previous limitations induced by the mass detection based on frequency shift are overcome. Indeed, even a very small mass could generate large jumps in amplitude, resulting in a considerable increase of mass sensitivity. The method has since been improved by Nguyen *et al.* [NGU 15] with an automatic re-initialization exploiting hysteresis cycles and paving the way for real-time detection. Figure 1.19 shows for $m = 0$ the responses of the MEMS going from $\Omega_{min} \rightarrow A_1 \rightarrow \Omega_{min}$. But with the additional small mass, the response of the MEMS goes from $\Omega_{min} \rightarrow B_1 \rightarrow B_2 \rightarrow A_2 \rightarrow D_2 \rightarrow D_1 \rightarrow \Omega_{min}$. Contrarily to the first cycle, the second cycle shows an amplitude $W_{max} > 0.2$ which is therefore considered as the threshold for the detection. Then, the quantification of the added mass m is made by comparing $\Delta\Omega$ to a chart.

Pull-in can also be used to increase the sensitivity of the device. Younis *et al.* [YOU 09] used the pull-in instability phenomenon of a micro-resonator to design a new method for mass detection in which the jump to pull-in acts as a switch with a mass threshold. Khater *et al.* [KHA 09, KHA 11] studied two actuation modes, one static mode with V_{dc} and one dynamical mode with additional V_{ac}. They concluded that the sensitivity increases when the forcing levels lead to amplitudes of oscillation close to the pull-in.

To either give more flexibility to the use of the device or to correct possible defects, tunable MEMS are needed. The recent work by Li *et al.* [LI 17] showed that the nonlinear behavior of MEMS can be tailored to a specific dynamics by using structural optimization. Two examples of beams were presented. One was designed to minimize the cubic nonlinearity whereas the second was designed to maximize it. Hajhashemi *et al.* [HAJ 12] proposed a method to adjust the bandwidth and the resonance frequency of two micro-resonators that are electrostatically coupled using a middle electrode. Walter *et al.* [WAL 16] used a method based on tunable electrostatic actuation and mode localization to compensate manufacturing defects in a single MEMS.

1.5.3 MEMS array

Current technology permits fabricating large arrays composed of a few as well as of thousands of MEMS or NEMS, the dynamics of which results from electrical, magnetical and mechanical couplings. The dynamical behavior of such arrays is studied experimentally

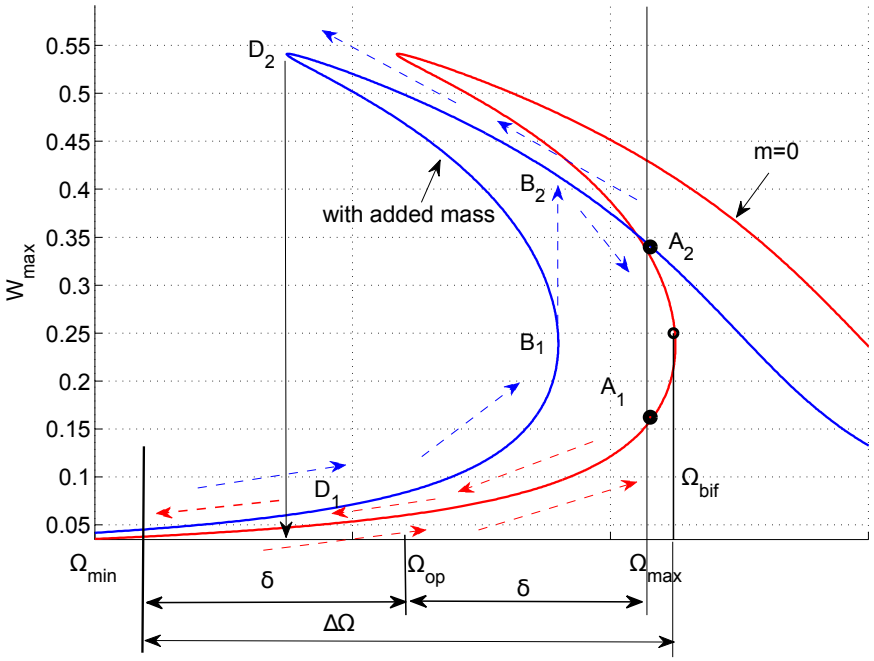

Figure 1.19 – Canceling nonlinearities in single resonant MEMS sensor, extracted from [KAC 10a]

or theoretically in [BUK 02, LIF 03, CRO 04, LIF 11].

Theoretical models are still not fully established and exploited because of the complex nonlinear dynamics induced by nonlinear couplings and higher number of DOFs. Some recent works adressed these complex behaviors. For example, Karabalin *et al.* [KAR 09] considered an array of two nanoresonators coupled by an elastic force and independently excited around their resonant frequencies. They showed that the linear and low nonlinear responses of a nano-resonator can be modified by the excitation of the other nano-resonators. The vibration of one oscillator can be used to change the nonlinear dynamics of another oscillator and thus increase its dynamical range. When two resonators are strongly excited in their nonlinear domain, the response curves become more complex. Lifshitz *et al.* [LIF 03] used perturbation methods to study the response of a MEMS array under parametric excitation in the weak nonlinear regime. Their results showed that increasing the number of oscillators makes the branches of solutions more and more numerous. Multistability and bifurcations of parametric resonances have also been studied by Bitar *et al.* [BIT 15, BIT 17]. In addition to the numerous branches of solutions, modal couplings also occur in the dynamics of a beam array. For example Gutschmidt *et al.* [GUT 08, GUT 10a, GUT 10b, GUT 12] studied a beam array in a 1:1 resonance configuration as well as 3:1 internal resonances near pull-in. Kambali *et al.* [KAM 15] focused on understanding the coupling of different modal frequencies and their tuning mechanisms. In the study, modal frequencies were tuned by adjusting V_{dc} in order to

rescale the beam array into a specific configuration. Studies on modal couplings and internal resonances not only permit a better understanding of the dynamics of beam arrays, but also give some insights on specific configurations such as the symmetric one.

Because a real MEMS array is not composed of trully identical beams, researchs are currently working on correcting the manufacturing defects by tuning specific features of the MEMS array. Porfiri [POR 08] showed that the vibrational properties of an array of identical microplates can be tuned by properly adjusting V_{dc} applied across adjacent microplates. In the same way, Akgul [AKG 11] proposed to tune voltages in order to correct the phase and frequency mismatches of the MEMS array. Ashok *et al.* [ASH 18] proposed to use non-uniform beams to increase the bandwidth of MEMS array device. Tao and Choubey [TAO 18] analyzed the consequences of variability on MEMS arrays. The results showed that due to variability, the quality factor of the device diminishes. These works offer several possibilities to compensate defects and to bring the sensor back into the desired configuration.

Spletzer *et al.* [SPL 08] compared mass sensing methods based on the change of the MEMs array eigenmodes with the frequency shift method obtained with a single resonant MEMS sensors. The addition of an added mass onto one of the beams of the array affects the shape of the modes. The change is as much as three orders of magnitude greater and improve the sensitivity of mass sensing. A localization of the mode occurs where the mass was added. This study opens the door to new methods for mass sensing based on the localization effect of modes rather than the shift in frequency. In [THI 09], the authors used the method of mode localization for mass sensing purposes. A study of the influence of asymmetry in the MEMS array was performed. Wang *et al.* [WAN 12] used 5 mechanically coupled beams to perform a mode localization analysis. For a symmetrical configuration, the added mass generates a higher amplitude of oscillation on the beams at both ends of the array. A review of studies using mode localization is provided by Zhao *et al.* [ZHA 16].

Chapter 2

Parametric analysis by tracking of bifurcations and extremum points

This chapter focuses first on the numerical aspects related to the detection, the calculation and the tracking of bifurcations. A Nonlinear Tuned Vibration Absorber (NLTVA) and a Jeffcott rotor are treated as examples for bifurcation tracking. Then a multi-parametric recursive continuation method of specific points such as bifurcation points is provided. The method, based on successive continuation of extremum, is then applied to a NLTVA to push the birth of IS at higher amplitude of forcing.

Contents

This chapter builds on the theoretical aspects introduced in the previous chapter to address advanced topics such as detection and the multi-parametric tracking of bifurcation points.

First, indicators for bifurcation detection along a followed curve are presented. Then, augmented systems for the accurate calculation of bifurcations are described. By using both continuation techniques and augmented systems characterizing bifurcation points, an approach for direct parametric analysis by tracking bifurcation points of nonlinear dynamical systems is recalled. Instead of computing multiple responses curves with various values of system parameters, bifurcation tracking permits performing an efficient parametric analysis with respect to one varying system parameter. The method is based on the HBM for the calculation of periodic solutions. Then, bifurcation tracking is applied to a Jeffcott rotor and a NLTVA to perform parametric analysis and observe the evolution of LP and NS bifurcations.

Secondly, an algorithm based on multi-parametric recursive continuation of extremum points is presented. The notion of extremum point is used to propose an original method of multi-parametric recursive continuation. Then, the characterization of the extremum point with an equality constraint function from continuated curve method is described. Then, this characterization is used to establish a recursive extremum point in successive increasing codimension. To finish, the multi-parametric recursive continuation algorithm is presented.

Finally, the multi-parametric recursive continuation method is applied in Section #2.3 to the NLTVA to optimize Isolated Solutions (IS). By applying the multi-parametric recursive continuation method to the NLTVA, the topological skeleton and extremum points of the IS are obtained. The limit of existence of IS and extremum points optimizing the zone without IS are found and used to improve the NLTVA.

Conclusions are drawn in the last section.

2.1 Bifurcation analysis

For nonlinear dynamical systems, an important role on the dynamics is played by nonlinear phenomena such as bifurcations. Bifurcations are periodic solutions where the implicit function theorem is ill-posed and where most of the dynamical changes of the systems occur. Therefore, a parametric analysis based on bifurcation tracking seems a good way to apprehend the nonlinear dynamic of the system. In this subsection, the detection, localization and tracking of bifurcation points using indicators and standard extended system are presented. First, codimension-1 bifurcations are recalled based on the works from [XIE 16a]. Then two codimension-2 bifurcations, Resonance 1:1 (R1) and Limit Point Neimark Sacker (LPNS) bifurcations, are presented. The characterization of bifurcation points with respect to Hill's method combined with the equation of motion in HBM is used to compute the bifurcation points.

2.1.1 Detection of bifurcations

A bifurcation point appears when a Floquet exponent λ crosses the imaginary axis, see 1.6. As stated in the state of the art Subsection 1.2.3, codimension-1 bifurcations can be distinguished from each other by the way the Floquet exponents cross the imaginary axis. In Subsection 2.1.2, the localization and the tracking of these bifurcations is recalled. During the continuation, the augmented system used for bifurcation tracking can again be ill-posed at some points. These points are called codimension-2 bifurcations. The codimension-2 bifurcations R1 and LPNS are treated in this Section.

Codimention-1 bifurcations To detect codimention-1 bifurcation points along the continuated curve of periodic solutions, the following properties are used:

- Regular Points are well define, therefore $\boldsymbol{R_X}$ is not singular.

- Limit Points (LP) are characterized by a singularity in the jacobian $\boldsymbol{R_X}$. Its determinant $det(\boldsymbol{R_X})$ can be used as an indicator in order to detect such bifurcations. The bifurcation is detected when the corresponding indicator $det(\boldsymbol{R_X})$ changes its sign along the continuated curve. To be sure that no additional branch appears from the bifurcation, the jacobian $\boldsymbol{J}$ of the extended system defined in Eq. (1.19), must be invertible, i.e., $det(\boldsymbol{J}) \neq 0$.

- Branch Points (BP) are associated with the birth of a new branch of solutions. When a new branch of solutions appears, the jacobian $\boldsymbol{J}$ becomes singular. Consequently, the determinant $det(\boldsymbol{J})$ can be used as an indicator of BP along the continuated curve.

- Neimarck-Sacker bifurcations (NS) are associated with the birth of quasi-periodic regime. At a NS bifurcation, a quasi-periodic branch of solutions appears and the stability of the periodic solution on the main branch changes. A NS bifurcation appears when a pair of Floquet exponent crosses the imaginary axis with $\lambda = \pm i\kappa = \frac{2\pi\omega_2}{\omega_1}$ with $\frac{\omega_1}{\omega_2} \notin \mathbb{Q}$. Indicators used for NS detection have been proposed in the following documents [SEY 09][KUZ 13][GOV 00]. These indicators also detect SR with $\frac{\omega_1}{\omega_2} \notin \mathbb{N}$.

$$\begin{aligned} \varphi_{NS1} &= \prod_{1 \leq j < i \leq n} \lambda_i + \lambda_j \\ \varphi_{NS2} &= \det(2\boldsymbol{J}_B \odot \boldsymbol{I}_{2n}) \end{aligned} \tag{2.1}$$

  where $\boldsymbol{J}_B$ is a diagonal matrix composed by the $2n$ Floquet exponents and $\odot$ stands for the bialternate product. However, these indicators can also detected Neutral Saddle points where (λ_i, λ_j) form a pair of opposite reals.

Codimension-2 bifurcations Codimension-2 bifurcations are detected on the curve obtained by bifurcation tracking. To detect codimention-2 bifurcation points onto the continuated curve of bifurcations, the following properties are used:

- A 1 : 1 Resonance (R1) appears during the continuation of LPs when a second eigenvalues becomes zero. Therefore, there exist two singular eigenvalues $\lambda_1 = \lambda_2 = 0$. When the jacobian $\boldsymbol{R_X}$ contains two singularities, the quadratic eigenvalue problem has a singular eigenvalue with algebraic multiplicity equal to two and geometric multiplicity equal to one. In order to detect a R1 using the LP indicator, a small modification needs to be done to the jacobian. Since the jacobian $\boldsymbol{R_X}$ already presents a singularity associated with an eigenvector $\boldsymbol{v}$, the regularized jacobian $\boldsymbol{R_X} + \boldsymbol{v}\boldsymbol{v}^T$ can be used to detect a R1 along the LP tracking curve. Therefore, a R1 occurs when the determinant $det(\boldsymbol{R_X} + \boldsymbol{v}\boldsymbol{v}^T)$ changes sign. Additional information on possible new branch of solutions can be obtained with respect to the current bifurcation tracking curve. For LP continuation, the birth of a new branch of solution is indicated by a change of sign of the determinant of the jacobian $\boldsymbol{J}$ defined in Eq. (1.19). For BP continuation, the indicator must be regularized with respect to the eigenvector $\boldsymbol{v_J}$ associated to the singularity of $\boldsymbol{J}$. Then, the apparition of a new branch can be detected by a change of sign of the determinant of the regularized jacobian $\boldsymbol{J} + \boldsymbol{v_J}\boldsymbol{v_J}^T$.
- A Limit Point Neimarck Sacker (LPNS) bifurcation can appear either on branches of NS or LP bifurcations. This bifurcation is characterized by the combination of NS and LP bifurcations with $\lambda_1 = 0$ and $\lambda_2 = \frac{2\pi\omega_2}{\omega_1}$ with $\frac{\omega_1}{\omega_2} \notin \mathbb{Q}$. Therefore, the detection of the LPNS bifurcation differs depending on which bifurcation is continuated. For LP continuation, the LPNS is detected when a pair of eigenvalues crosses the imaginary axis with $\lambda = \pm\frac{2\pi\omega_2}{\omega_1}$ with $\frac{\omega_1}{\omega_2} \notin \mathbb{Q}$. Therefore the same indicator as for NS can be used. On the other hand, for NS continuation, the LPNS is detected when a single eigenvalue crosses the imaginary axis. Therefore, the LP indicator can be used.

2.1.2 Localization and tracking of bifurcations

In this subsection, the localization of the presented bifurcations is considered. Then, the topic of bifurcation tracking is addressed. The added value of this subsection lies in the localization of the codimension-2 bifurcations in the HBM framework.

Limit Point (LP) At LPs, the stability of the periodic solution changes. In forced system, the LPs also represent extremums with respect to the frequency of the periodic solution. They are detected by monitoring the eigenvalues Λ of $\boldsymbol{Q}$ which is equivalent to $\det(\boldsymbol{R_X}) = 0$, see Eq. (1.42). The LP bifurcations are characterized as follows [XIE 16a]:

$$\left[\begin{array}{l} \boldsymbol{R_X}\boldsymbol{\phi} = 0_L \\ \boldsymbol{\phi}^T\boldsymbol{\phi} - 1 = 0 \end{array}\right. \tag{2.2}$$

Once detected, the augmented system obtained by adding Eq. (2.2) to (1.5) can be used to localize a LP bifurcation:

$$LP(\boldsymbol{Y}) = \begin{pmatrix} \boldsymbol{R} \\ \boldsymbol{R_X}\phi \\ \phi^T\phi - 1 \end{pmatrix} = \boldsymbol{0}_{2L+2} \tag{2.3}$$

with $\boldsymbol{Y} = (\boldsymbol{X}, \omega, \phi)$. Then a Newton-Raphson algorithm is used to solve the nonlinear system (2.3):

$$\begin{array}{rcl} LP_{\boldsymbol{Y}}(\boldsymbol{Y}^k)\delta\boldsymbol{Y}^k & = & -LP(\boldsymbol{Y}^k) \\ \boldsymbol{Y}^{k+1} & = & \boldsymbol{Y}^k + \delta\boldsymbol{Y}^k \end{array} \tag{2.4}$$

where $(k, k+1)$ indicate respectively the current and the next iteration and the jacobian $LP_{\boldsymbol{Y}}$ is given by:

$$LP_{\boldsymbol{Y}} = \begin{bmatrix} \boldsymbol{R_X} & \boldsymbol{0}_{L\times L} & \boldsymbol{R}_\omega \\ (\boldsymbol{R_X}\phi)_X & \boldsymbol{R_X} & (\boldsymbol{R_X}\phi)_\omega \\ \boldsymbol{0}_L^T & 2\phi^{k^T} & 0 \end{bmatrix} \tag{2.5}$$

Branch Point (BP) and branching BPs are bifurcation points from which new branches of solutions emerge. One branch changes its stability by crossing the BP, while the other one can be either stable or unstable. The most common types of BP that can occur are the transcritical and the pitchfork bifurcations. The transcritical bifurcation is a point where the curve crosses itself and generates a loop in the response curve. It plays an important role in the creation of ISs, see imperfect transcritical bifurcations in [SEY 09]. On the other hand, the Pitchfork bifurcation is usually associated with the breaking of an underlying $\mathbb{Z}_2$ symmetry, see [SEY 09] p. 238. At such a point, the new branch of solutions arising from the BP does not respect the symmetry. The BP is thus detected when both the stability changes and the new branch appears. The BP bifurcation can be characterized by the following equations, see [XIE 16a]:

$$\begin{bmatrix} \boldsymbol{R_X}\phi = 0_L \\ \boldsymbol{R}_\omega^T\phi = 0 \\ \phi^T\phi - 1 = 0 \end{bmatrix} \tag{2.6}$$

Once detected, the augmented system of size $2L+2$ obtained by adding Eq. (2.6) to (1.5) can be used to compute a BP bifurcation:

$$BP(\boldsymbol{Y}) = \begin{pmatrix} \boldsymbol{R} \\ \boldsymbol{R_X}\phi \\ \boldsymbol{R}_\omega^T\phi \\ \phi^T\phi - 1 \end{pmatrix} = \boldsymbol{0}_{2L+3} \tag{2.7}$$

with $\boldsymbol{Y} = (\boldsymbol{X}, \omega, \phi)$. Then a Newton-Raphson algorithm is used to solve this nonlinear system (2.7):

$$\begin{array}{rcl} BP_{\boldsymbol{Y}}(\boldsymbol{Y}^k)\delta\boldsymbol{Y}^k & = & -BP(\boldsymbol{Y}^k) \\ \boldsymbol{Y}^{k+1} & = & \boldsymbol{Y}^k + \delta\boldsymbol{Y}^k \end{array} \tag{2.8}$$

where $(k, k+1)$ indicate respectively the current and the next iteration and the jacobian $BP_{\boldsymbol{Y}}$ is given by:

$$BP_{\boldsymbol{Y}} = \begin{bmatrix} \boldsymbol{R}_X & \mathbf{0}_{L\times L} & \mathbf{R}_\omega & \mathbf{e}_j \\ g_{\boldsymbol{X}}{}^T & \mathbf{0}_L^T & 0 & 0 \\ (\boldsymbol{R}_{\boldsymbol{X}}\phi)_X & \boldsymbol{R}_X & (\boldsymbol{R}_{\boldsymbol{X}}\phi)_\omega & \mathbf{0}_L \\ \mathbf{0}_L^T & 2\phi^{k\,T} & 0 & 0 \\ \mathbf{0}_L^T & \boldsymbol{R}_\omega^T & 0 & 0 \end{bmatrix} \tag{2.9}$$

The difference between Transcritical and Pitchfork bifurcations lies in the degeneracies of their normal form. Once localized, the distinction between them can be made by calculating the term $\phi^T(\boldsymbol{R}_{\boldsymbol{X}}\phi)_{\boldsymbol{X}}\phi$.

$$\begin{array}{lrcl} \text{Transcritical} & \Rightarrow \quad \phi^T(\boldsymbol{R}_{\boldsymbol{X}}\phi)_{\boldsymbol{X}}\phi & \neq & 0 \quad \text{(0 Degeneracy)} \\ \text{Pitchfork} & \Rightarrow \quad \phi^T(\boldsymbol{R}_{\boldsymbol{X}}\phi)_{\boldsymbol{X}}\phi & = & 0 \quad \text{(1 Degeneracy)} \end{array} \tag{2.10}$$

Once the BP bifurcation has computed, the branching onto the new branch of solution can be operated. For a regular point on the frequency response curve, the regularized continuation (3.14) gives a unique tangent of the solution, but at a BP two tangents exist. Therefore there are two independent vectors $\phi = (\phi_1, \phi_2) \in \mathbb{R}^{L+1}$ solution of $\boldsymbol{R}_{\boldsymbol{P}}\phi = 0$ with $\boldsymbol{P} = (\boldsymbol{X}, \omega)$ and a unique left eigenvector $\phi_g \in \mathbb{R}^L$ of $\boldsymbol{R}_{\boldsymbol{P}}$ such that $\boldsymbol{R}_{\boldsymbol{P}}^T\phi_g = 0$. Consequently, Eq. (2.7) has to be calculated at the second order to obtain the two tangents.

$$\begin{array}{rcl} \boldsymbol{P} & = & \boldsymbol{P}_0 + \varepsilon\boldsymbol{Y}_1 + \varepsilon^2\boldsymbol{Y}_2 \\ \boldsymbol{R}(\boldsymbol{P}) & = & \boldsymbol{R}(\boldsymbol{P}_0) + \varepsilon\boldsymbol{R}_{\boldsymbol{P}}\boldsymbol{P}_1 + \varepsilon^2(\boldsymbol{R}_{\boldsymbol{P}}\boldsymbol{P}_2 + \boldsymbol{R}_{\boldsymbol{P}\boldsymbol{P}}\boldsymbol{P}_1\boldsymbol{P}_1) \end{array} \tag{2.11}$$

with ε being the pseudo-arclength path parameter. So the differential at order two is equal to:

$$\boldsymbol{R}_{\boldsymbol{P}}\boldsymbol{P}_2 + (\boldsymbol{R}_{\boldsymbol{P}}\boldsymbol{P}_1\boldsymbol{P}_1) = 0 \tag{2.12}$$

By multiplying equation (2.12) by ϕ_g^T, the following equation is obtained:

$$\phi_g^T(\boldsymbol{R}_{\boldsymbol{X}\boldsymbol{X}}\boldsymbol{X}_1\boldsymbol{X}_1 + \boldsymbol{R}_{\boldsymbol{X}\omega}\boldsymbol{X}_1\omega_1 + \boldsymbol{R}_{\omega\omega}\omega_1\omega_1) = 0 \tag{2.13}$$

Since there are two independent vectors $\phi = (\phi_1, \phi_2) \in \mathbb{R}^{L+1}$ solution of $\boldsymbol{R}_{\boldsymbol{P}}\phi = 0$, the new tangent can be written as $(\boldsymbol{X}_1, \omega_1) = (\phi_1 + \alpha\phi_2, \alpha)$ with ϕ_1 the eigenvector in Eq. (2.7) and ϕ_2 the displacement part $\Delta\boldsymbol{X}$ of the tangent predictor step calculated in Eq. (3.15). By introducing the tangent into Eq. (2.13), the following equation is obtained:

$$a\alpha^2 + b\alpha + c = 0 \tag{2.14}$$

with

$$\begin{aligned} a &= \phi_g^T \left((\boldsymbol{R}_{\boldsymbol{X}} \phi_2)_{\boldsymbol{X}} \phi_2 + 2(\boldsymbol{R}_{\boldsymbol{X}} \phi_2)_\omega + \boldsymbol{R}_{\omega\omega} \right) \\ b &= \phi_g^T \left((\boldsymbol{R}_{\boldsymbol{X}} \phi_1)_{\boldsymbol{X}} \phi_2 + (\boldsymbol{R}_{\boldsymbol{X}} \phi_1)_\omega \right) \\ c &= \phi_g^T \left(\boldsymbol{R}_{\boldsymbol{X}} \phi_1 \right)_{\boldsymbol{X}} \phi_1 \end{aligned} \tag{2.15}$$

The resulting tangent solution depends on the type of the BP bifurcation:

- Transcritical: $c \neq 0$

  There are two solutions:

$$\begin{aligned} \alpha_1 &= \frac{-b + \sqrt{b^2 - ac}}{a} \\ \alpha_2 &= \frac{-b - \sqrt{b^2 - ac}}{a} \end{aligned} \tag{2.16}$$

- Pitchfork: $c = 0$

  There are two solutions:

$$\begin{aligned} \alpha_1 &= 0 \\ \alpha_2 &= \frac{-2b}{a} \end{aligned} \tag{2.17}$$

Finally the branching can be made by perturbing $(\boldsymbol{X}, \omega)$ in the direction of the new determined tangent.

Neimark-Sacker NS bifurcations are points representing the birth of quasi-periodic solutions. They occur when a pair of Floquet exponents crosses the imaginary axis with $\lambda = \pm i\kappa$ and $\kappa = \frac{2\pi\omega_2}{\omega_1}$ with $\frac{\omega_1}{\omega_2} \notin \mathbb{Q}$. These exponents are then introduced into Eq. (1.42). The obtained equation, characterizing NS bifurcation, is separated in two equations representing respectively the real and the imaginary part.

$$\begin{aligned} EQ^1_{NS} = \\ EQ^2_{NS} = \end{aligned} \begin{cases} \boldsymbol{R}_{\boldsymbol{X}} \phi_1 - \kappa \boldsymbol{\Delta}_1 \phi_2 - \kappa^2 \boldsymbol{\Delta}_2 \phi_1 = \mathbf{0}_L \\ \boldsymbol{R}_{\boldsymbol{X}} \phi_2 + \kappa \boldsymbol{\Delta}_1 \phi_1 - \kappa^2 \boldsymbol{\Delta}_2 \phi_2 = \mathbf{0}_L \\ \boldsymbol{q}^T \phi_1 \\ \phi_1^T \phi_1 - 1 \end{cases} \tag{2.18}$$

with $\boldsymbol{q}$ an arbitrary vector such that $\langle \boldsymbol{q}, \phi_1 \rangle \neq 0$. The results of NS localization can vary depending on the chosen normalization vectors. For the following normalization conditions $\phi_1^T \phi_2 = 0$ and $\phi_1^T \phi_1 = 1$, $\kappa = 0$ and $\phi_2 = 0$ are solution of Eq. (2.18). The resulting equations correspond to Eq. (2.2) that characterizes LP bifurcations [GRI 83] [ROO 85]. Because R1 bifurcations are located at the beginning or the end of a curve of NS bifurcations, this formulation could be useful in that case to go through the bifurcation, thus

allowing the detection. Once detected, the augmented system of size $3L+2$ characterizing NS bifurcation is obtained by adding Eq. (2.18) to Eq. (1.5). The initial value of κ is taken equal to the evaluation of the eigenvalue λ after the detection.

$$NS(\boldsymbol{Y}) = \begin{pmatrix} \boldsymbol{R}(\boldsymbol{X},\omega) \\ \boldsymbol{R}_{\boldsymbol{X}}\phi_1 - \kappa\boldsymbol{\Delta}_1\phi_2 - \kappa^2\boldsymbol{\Delta}_2\phi_1 \\ \boldsymbol{R}_{\boldsymbol{X}}\phi_2 + \kappa\boldsymbol{\Delta}_1\phi_1 - \kappa^2\boldsymbol{\Delta}_2\phi_2 \\ \boldsymbol{q}^T\phi_1 \\ \phi_1^T\phi_1 - 1 \end{pmatrix} = \boldsymbol{0}_{3L+2} \tag{2.19}$$

with $\boldsymbol{Y} = (\boldsymbol{X}, \phi_1, \phi_2, \kappa, \omega)$. Then a Newton-Raphson algorithm is used to solve this nonlinear system (2.19):

$$\begin{aligned} NS_{\boldsymbol{Y}}(\boldsymbol{Y}^k)\delta\boldsymbol{Y}^k &= -NS(\boldsymbol{Y}^k) \\ \boldsymbol{Y}^{k+1} &= \boldsymbol{Y}^k + \delta\boldsymbol{Y}^k \end{aligned} \tag{2.20}$$

where $(k, k+1)$ indicate respectively the current and the next iteration and the jacobian $NS_{\boldsymbol{Y}}$ is given by:

$$NS_{\boldsymbol{Y}} = \begin{bmatrix} \boldsymbol{R}_{\boldsymbol{X}} & \boldsymbol{0}_{L\times L} & \boldsymbol{0}_{L\times L} & \boldsymbol{0}_L & \boldsymbol{R}_\omega \\ EQ^1_{\boldsymbol{X}} & \boldsymbol{R}_{\boldsymbol{X}} - (\kappa)^2\boldsymbol{\Delta}_2 & -\kappa\boldsymbol{\Delta}_1 & -\boldsymbol{\Delta}_1\phi_2 - 2\kappa\boldsymbol{\Delta}_2\phi_1 & EQ^1_\omega \\ EQ^2_{\boldsymbol{X}} & \kappa\boldsymbol{\Delta}_1 & \boldsymbol{R}_{\boldsymbol{X}} - (\kappa)^2\boldsymbol{\Delta}_2 & +\boldsymbol{\Delta}_1\phi_1 - 2\kappa\boldsymbol{\Delta}_2\phi_2 & EQ^2_\omega \\ \boldsymbol{0}_L^T & \boldsymbol{q}^T & \boldsymbol{0}_L^T & 0 & 0 \\ \boldsymbol{0}_L^T & 2{\phi_1}^T & \boldsymbol{0}_L^T & 0 & 0 \end{bmatrix} \tag{2.21}$$

with

$$\begin{aligned} EQ^1_{\boldsymbol{X}} &= (\boldsymbol{R}_{\boldsymbol{X}}\phi_1)_{\boldsymbol{X}} - \kappa(\boldsymbol{\Delta}_1\phi_2)_{\boldsymbol{X}} \\ EQ^2_{\boldsymbol{X}} &= (\boldsymbol{R}_{\boldsymbol{X}}\phi_2)_{\boldsymbol{X}} + \kappa(\boldsymbol{\Delta}_1\phi_1)_{\boldsymbol{X}} \\ EQ^1_\omega &= (\boldsymbol{R}_{\boldsymbol{X}}\phi_1)_\omega - \kappa(\boldsymbol{\Delta}_1\phi_2)_\omega \\ EQ^2_\omega &= (\boldsymbol{R}_{\boldsymbol{X}}\phi_2)_\omega + \kappa(\boldsymbol{\Delta}_1\phi_1)_\omega \end{aligned} \tag{2.22}$$

The branching onto a branch of quasi-periodic solutions is out of the scope of this thesis.

Resonance 1:1 (R1) A R1 bifurcation can be encountered on a NS curve or on a LP curve. On the NS curve, the R1 bifurcation either starts or ends the continuated curve, whereas the R1 bifurcation can be encountered everywhere on a LP curve. These bifurcations are interesting for quasi-periodic analysis because they represent the limits of existence of NS bifurcations. A R1 bifurcation is characterized by two singular eigenvalues $\lambda_1 = \lambda_2 = 0$ of the jacobian $\boldsymbol{R}_{\boldsymbol{X}}$ and solutions of the quadratic eigenvalues problem of

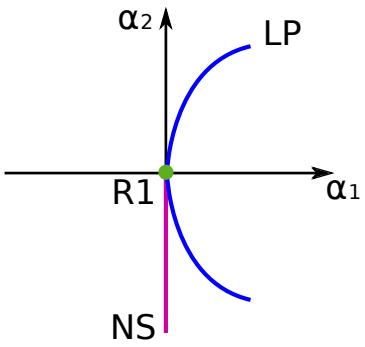

Figure 2.1 – R1 bifurcation

Eq. (1.42). Since it is the quadratic eigenvalue problem that rules the stability of the system, the characterization must be done on the quadratic eigenvalue problem and not on the jacobian $\boldsymbol{R_X}$. If the characterization was made on the jacobian $\boldsymbol{R_X}$, the R1 bifurcation would be characterized with the two following equations:

$$\left[\begin{array}{l} \boldsymbol{R_X}\phi = 0_L \\ \boldsymbol{R_X}\xi = \phi \end{array}\right. \tag{2.23}$$

On the other hand, when the characterization is made with the quadratic eigenvalue problem, the two equations characterizing the R1 bifurcation are:

$$\left[\begin{array}{l} \boldsymbol{R_X}\phi_1 = 0_L \\ \boldsymbol{R_X}\phi_2 = -\boldsymbol{\Delta}_1\phi_1 \end{array}\right. \tag{2.24}$$

One can see that those two augmented systems are not the same. Only the second augmented system Eq. (2.24) can localize R1 bifurcation appropriately. Once the R1 bifurcation is detected on either a LP or a NS curve, the augmented system obtained by adding Eq. (2.24) to Eq. (1.5) can be used to compute R1 bifurcation.

$$R1(\boldsymbol{Y}) = \begin{pmatrix} \boldsymbol{R} \\ \boldsymbol{R_X}\phi_1 \\ \boldsymbol{R_X}\phi_2 + \boldsymbol{\Delta}_1\phi_1 \\ \phi_1^T\phi_1 - 1 \\ \phi_2^T\phi_1 \end{pmatrix} = \mathbf{0}_{3L+2} \tag{2.25}$$

where $\boldsymbol{Y} = (\boldsymbol{X}, \phi_1, \phi_2, \omega, \alpha)$ with α the varying parameter used during NS or LP continuation. ϕ is initialized with the eigenvector obtained during LP or NS continuation when the detection occurs. Then a Newton-Raphson algorithm is used toto solve the nonlinear system (2.25):

$$\begin{array}{lcl} R1_{\boldsymbol{Y}}(\boldsymbol{Y}^k)\delta\boldsymbol{Y}^k & = & -R1(\boldsymbol{Y}^k) \\ \boldsymbol{Y}^{k+1} & = & \boldsymbol{Y}^k + \delta\boldsymbol{Y}^k \end{array} \tag{2.26}$$

where $(k,k+1)$ indicate respectively the current and the next iteration and the jacobian $R1_{\boldsymbol{Y}}$ is given by:

$$R1_{\boldsymbol{Y}} = \begin{bmatrix} \boldsymbol{R_X} & \mathbf{0}_{L\times L} & \mathbf{0}_{L\times L} & \boldsymbol{R_\omega} & \boldsymbol{R_\alpha} \\ (\boldsymbol{R_X}\phi_1)_{\boldsymbol{X}} & \boldsymbol{R_X} & \mathbf{0}_{L\times L} & (\boldsymbol{R_X}\phi_1)_\omega & (\boldsymbol{R_X})_\alpha\phi_1 \\ (\boldsymbol{R_X}\phi_2)_{\boldsymbol{X}} + (\boldsymbol{\Delta}_1\phi_1)_{\boldsymbol{X}} & \boldsymbol{\Delta}_1 & \boldsymbol{R_X} & (\boldsymbol{R_X}\phi_2 + \boldsymbol{\Delta}_1\phi_1)_\omega & (\boldsymbol{R_X})_\alpha\phi_2 + (\boldsymbol{\Delta}_1)_\alpha\phi_1 \\ \mathbf{0}_L^T & 2{\phi_1}^T & \mathbf{0}_L^T & 0 & 0 \\ \mathbf{0}_L^T & \phi_2^T & \phi_1^T & 0 & 0 \end{bmatrix} \tag{2.27}$$

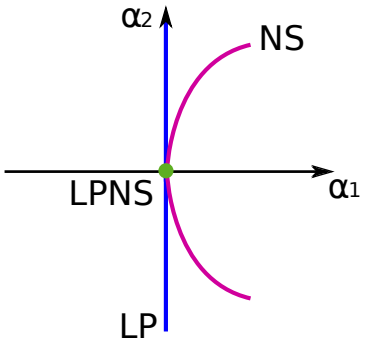

Figure 2.2 – LPNS bifurcation

Limit Point Neimark Sacker (LPNS) A LPNS bifurcation can be encountered anywhere on a NS or on a LP curve. These bifurcations represent a point of coalescence of LP and NS curves. Therefore, a LPNS bifurcation is characterized by the combination of the LP characterization $\lambda_1 = 0$ and the characterization of NS bifurcation $(\lambda_2,\lambda_3) = \pm i\kappa$ with $\kappa = \frac{2\pi\omega_2}{\omega_1}$ and $\frac{\omega_1}{\omega_2} \notin \mathbb{Q}$. The equation of characterization of LPNS is the following:

$$\begin{aligned} EQ^1_{NS} = & \\ EQ^2_{NS} = & \end{aligned} \begin{bmatrix} \boldsymbol{R_X}\phi_2 - \kappa\boldsymbol{\Delta}_1\phi_3 - \kappa^2\boldsymbol{\Delta}_2\phi_2 = \mathbf{0}_L \\ \boldsymbol{R_X}\phi_3 + \kappa\boldsymbol{\Delta}_1\phi_2 - \kappa^2\boldsymbol{\Delta}_2\phi_3 = \mathbf{0}_L \\ \phi_1^T\phi_1 - 1 = 0 \\ \boldsymbol{q}^T\phi_2 = 0 \\ \phi_2^T\phi_2 - 1 = 0 \end{bmatrix} \tag{2.28}$$

Concerning the normalization vector, an analogy with ZH normalization vectors can be made [KUZ 13] p330. It is said that the Fredholm Alternative Theorem insure the following orthogonality properties $\langle \phi_1^T(\phi_2 + i\phi_3)\rangle = 0$. Once the LPNS bifurcation is detected on either a LP or a NS curve, the augmented system obtained by adding Eq. (2.28) to

Eq. (1.5) can be used to localize it. When the detection occurs, the eigenvector obtained during LP or NS continuation is used for the initialization of the associated ϕ.

$$LPNS(\boldsymbol{Y}) = \begin{pmatrix} \boldsymbol{R} \\ \boldsymbol{R_X}\phi_1 \\ \boldsymbol{R_X}\phi_2 - \kappa\boldsymbol{\Delta}_1\phi_3 - \kappa^2\boldsymbol{\Delta}_2\phi_2 \\ \boldsymbol{R_X}\phi_3 + \kappa\boldsymbol{\Delta}_1\phi_2 - \kappa^2\boldsymbol{\Delta}_2\phi_3 \\ \phi_1^T\phi_1 - 1 \\ \boldsymbol{q}^T\phi_2 \\ \phi_2^T\phi_2 - 1 \end{pmatrix} = \mathbf{0}_{4L+3} \tag{2.29}$$

where $\boldsymbol{Y} = (\boldsymbol{X}, \phi_1, \phi_2, \phi_3, \omega, \alpha)$ with α the varying parameter used during NS or LP continuation. Then a Newton-Raphson algorithm is used to localize solve the nonlinear system (2.29):

$$\begin{array}{lcl} LPNS_{\boldsymbol{Y}}(\boldsymbol{Y}^k)\delta\boldsymbol{Y}^k & = & -LPNS(\boldsymbol{Y}^k) \\ \boldsymbol{Y}^{k+1} & = & \boldsymbol{Y}^k + \delta\boldsymbol{Y}^k \end{array} \tag{2.30}$$

where $(k, k+1)$ indicate respectively the current and the next iteration and the jacobian $LPNS_{\boldsymbol{Y}}$ is given by:

$$LPNS_{\boldsymbol{Y}} = \begin{bmatrix} \boldsymbol{R_X} & \mathbf{0}_{L\times L} & \mathbf{0}_{L\times L} & \mathbf{0}_{L\times L} & \mathbf{0}_L & \boldsymbol{R}_\omega & \boldsymbol{R}_\alpha \\ (\boldsymbol{R_X}\phi_1)_{\boldsymbol{X}} & \boldsymbol{R_X} & \mathbf{0}_{L\times L} & \mathbf{0}_{L\times L} & \mathbf{0}_L & (\boldsymbol{R_X}\phi_1)_\omega & (\boldsymbol{R_X}\phi_1)_\alpha \\ EQ^1_{NS\boldsymbol{X}} & \mathbf{0}_{L\times L} & \boldsymbol{R_X} - (\kappa)^2\boldsymbol{\Delta}_2 & -\kappa\boldsymbol{\Delta}_1 & EQ^1_{NS\kappa} & EQ^1_{NS\omega} & EQ^1_{NS\alpha} \\ EQ^2_{NS\boldsymbol{X}} & \mathbf{0}_{L\times L} & \kappa\boldsymbol{\Delta}_1 & \boldsymbol{R_X} - (\kappa)^2\boldsymbol{\Delta}_2 & EQ^2_{NS\kappa} & EQ^2_{NS\omega} & EQ^2_{NS\alpha} \\ \mathbf{0}_L^T & 2{\phi_1}^T & \mathbf{0}_L^T & \mathbf{0}_L^T & 0 & 0 & \\ \mathbf{0}_L^T & \mathbf{0}_L^T & \boldsymbol{q}^T & \mathbf{0}_L^T & 0 & 0 & 0 \\ \mathbf{0}_L^T & \mathbf{0}_L^T & 2{\phi_1}^T & \mathbf{0}_L^T & 0 & 0 & 0 \end{bmatrix} \tag{2.31}$$

with

$$
\begin{aligned}
EQ^1_{NS\boldsymbol{X}} &= (\boldsymbol{R}_{\boldsymbol{X}}\phi_2)_{\boldsymbol{X}} - \kappa(\boldsymbol{\Delta}_1\phi_3)_{\boldsymbol{X}} \\
EQ^2_{NS\boldsymbol{X}} &= (\boldsymbol{R}_{\boldsymbol{X}}\phi_3)_{\boldsymbol{X}} + \kappa(\boldsymbol{\Delta}_1\phi_2)_{\boldsymbol{X}} \\
EQ^1_{NS\kappa} &= -(\boldsymbol{\Delta}_1\phi_2)_\omega - 2\kappa\boldsymbol{\Delta}_2\phi_1 \\
EQ^2_{NS\kappa} &= (\boldsymbol{\Delta}_1\phi_1)_\omega - 2\kappa\boldsymbol{\Delta}_2\phi_2 \\
EQ^1_{NS\omega} &= (\boldsymbol{R}_{\boldsymbol{X}}\phi_2)_\omega - \kappa(\boldsymbol{\Delta}_1\phi_3)_\omega \\
EQ^2_{NS\omega} &= (\boldsymbol{R}_{\boldsymbol{X}}\phi_3)_\omega + \kappa(\boldsymbol{\Delta}_1\phi_2)_\omega \\
EQ^1_{NS\alpha} &= (\boldsymbol{R}_{\boldsymbol{X}})_\alpha\phi_1 - \kappa(\boldsymbol{\Delta}_1)_\alpha\phi_2 - \kappa^2(\boldsymbol{\Delta}_2)_\alpha\phi_2 \\
EQ^2_{NS\alpha} &= (\boldsymbol{R}_{\boldsymbol{X}})_\alpha\phi_2 + \kappa(\boldsymbol{\Delta}_1)_\alpha\phi_1 - \kappa^2(\boldsymbol{\Delta}_2)_\alpha\phi_3
\end{aligned}
\tag{2.32}
$$

Bifurcation tracking When a system parameter α is modified, dynamical phenomena such as bifurcation points can vary continuously. Therefore, a direct continuation of bifurcations can be used for parametric analysis. First, the bifurcation has to be localized with the default value of the chosen system parameter α_0 chosen at the beginning of the simulation. Once the bifurcation has been localized, the chosen system parameter α is added as a new unknown to the set of system parameters $\boldsymbol{Y}$ used to compute the bifurcation. Then, as for the continuation method presented in Subsection 1.1.2, the continuated augmented system is formed by an arc-length equation and by the augmented system B characterizing the bifurcation. The continuation of bifurcations is performed in two steps, a predictor step and a corrector step.

Before applying the predictor step, the initialization of the continuation method has to be performed. To initialize the continuation method, the tangent vector $\boldsymbol{t} = (\Delta\boldsymbol{Y}_1, \Delta\alpha_1)^T$ is computed with $\Delta\alpha_1 = \pm 1$ depending on the desired direction of continuation:

$$
\boldsymbol{B}_{\boldsymbol{Y}^0}\Delta\boldsymbol{Y}_1 = -\Delta\alpha_1\boldsymbol{B}_\alpha \tag{2.33}
$$

Then, the obtained tangent $t_1 = (\Delta\boldsymbol{Y}_1, \Delta\alpha_1)^T$ is normalized, multiplied by a step length Δs and added to the starting point $(\boldsymbol{Y}_1^0, \alpha_1^0)$:

$$
(\boldsymbol{Y}_1^1, \alpha_1^1)^T = (\boldsymbol{Y}_1^0, \alpha_1^0)^T + \Delta s t 1 \tag{2.34}
$$

Then, a Newton-Raphson algorithm is used for the corrections. The correction vector $(\delta\boldsymbol{Y}_1^k, \delta\alpha_1^k)$ is searched in the direction orthogonal to the tangent vector $\boldsymbol{t}_1$ of the prediction step:

$$
\begin{bmatrix} \boldsymbol{B}_{\boldsymbol{Y}}^k & \boldsymbol{B}_\alpha^k \\ (\Delta\boldsymbol{Y}_1)^T & \Delta\alpha_1 \end{bmatrix} \begin{Bmatrix} \delta\boldsymbol{Y}_1^k \\ \delta\alpha_1^k \end{Bmatrix} = - \begin{Bmatrix} \boldsymbol{B}^k \\ 0 \end{Bmatrix} \tag{2.35}
$$

Then, the correction vector is added to the previous computed point:

$$
\begin{pmatrix} \boldsymbol{Y}_1^{k+1} \\ \alpha_1^{k+1} \end{pmatrix} = \begin{pmatrix} \boldsymbol{Y}_1^k \\ \alpha_1^k \end{pmatrix} + \begin{pmatrix} \delta\boldsymbol{Y}_1^k \\ \delta\alpha_1^k \end{pmatrix} \tag{2.36}
$$

The corrections are made until convergence with respect to the error criterion presented in Eq. (1.10). The obtained point is taken as the new starting point $(\boldsymbol{Y}_2^0, \alpha_2^0)$ for the next predictor step. Once the continuation method has been initialized with a first step, the predictor step can be performed. A constraint equation is appended to ensure that the tangent vector $\boldsymbol{t}_1 = (\Delta \boldsymbol{Y}_j, \Delta\alpha_j)^T$ at the step j of continuation is parallel to the previous tangent vector:

$$\begin{bmatrix} \boldsymbol{B}_{\boldsymbol{Y}}^0 & \boldsymbol{B}_\alpha^0 \\ (\Delta \boldsymbol{Y}_{j-1})^T & \Delta\alpha_{j-1} \end{bmatrix} \begin{Bmatrix} \Delta \boldsymbol{Y}_j \\ \Delta\alpha_j \end{Bmatrix} = - \begin{Bmatrix} \boldsymbol{B}^0 \\ 1 \end{Bmatrix} \tag{2.37}$$

The tangent vector is then normalized and multiplied by a step length Δs and by the sign of the scalar product between the current tangent and the previous one. This step prevents the continuation method to go backwards on a previously calculated point. Once the tangent vector has been computed, a succession of prediction and correction steps are performed until the chosen range for the system parameter α has been swept.

2.1.3 Computation of derivatives during localization and tracking of bifurcation

During the bifurcation analysis, the derivatives of $\boldsymbol{R}$, $\boldsymbol{R}_{\boldsymbol{X}}\phi$ and $\boldsymbol{\Delta}_1\phi$ with respect to the free parameters $(\boldsymbol{X}, \omega, \alpha)$ have to be computed. The derivatives of the jacobian $\boldsymbol{R}_{\boldsymbol{X}}$ and $\boldsymbol{R}_\omega$ are described in Eq. (1.24) in Subsection 1.1.3. The derivatives $\boldsymbol{R}_\alpha$, $(\boldsymbol{R}_{\boldsymbol{X}}\phi)_{\boldsymbol{X}}$, $(\boldsymbol{R}_{\boldsymbol{X}}\phi)_\omega$, $(\boldsymbol{R}_{\boldsymbol{X}}\phi)_\alpha$, $(\boldsymbol{\Delta}_{1nl}\phi)_{\boldsymbol{X}}$, $(\boldsymbol{\Delta}_{1nl}\phi)_\omega$ and $(\boldsymbol{\Delta}_{1nl}\phi)_\alpha$ are constructed as follows:

$$\begin{aligned}
\boldsymbol{R}_\alpha &= \boldsymbol{Z}_\alpha \boldsymbol{X} + \boldsymbol{F}_{nl\,\alpha}(\boldsymbol{X}, \omega, \alpha) - \boldsymbol{F}_\alpha(\boldsymbol{X}, \omega, \alpha) \\
(\boldsymbol{R}_{\boldsymbol{X}}\phi)_{\boldsymbol{X}} &= (\boldsymbol{F}_{nl\,\boldsymbol{X}}\phi)_{\boldsymbol{X}} \\
(\boldsymbol{R}_{\boldsymbol{X}}\phi)_\omega &= \boldsymbol{Z}_\omega\phi + (\boldsymbol{F}_{nl\,\boldsymbol{X}}\phi)_\omega \\
(\boldsymbol{R}_{\boldsymbol{X}}\phi)_\alpha &= \boldsymbol{Z}_\alpha\phi + (\boldsymbol{F}_{nl\,\boldsymbol{X}}\phi)_\alpha \\
\boldsymbol{R}_{\omega\omega} &= 2(\nabla^2 \otimes \boldsymbol{M})\boldsymbol{X} + \boldsymbol{F}_{nl\,\omega\omega}(\boldsymbol{X}, \omega, \alpha) \\
(\boldsymbol{\Delta}_1\phi)_{\boldsymbol{X}} &= (\boldsymbol{\Delta}_{1nl}\phi)_{\boldsymbol{X}} \\
(\boldsymbol{\Delta}_1\phi)_\omega &= 2(\nabla \otimes \boldsymbol{M})\phi + (\boldsymbol{\Delta}_{1nl}\phi)_\omega \\
(\boldsymbol{\Delta}_1\phi)_\alpha &= (\boldsymbol{\Delta}_{1l}\phi)_\alpha + (\boldsymbol{\Delta}_{1nl}\phi)_\alpha
\end{aligned} \tag{2.38}$$

with $\boldsymbol{Z}_\omega$ computed with Eq. (1.25), the nonlinear terms $\boldsymbol{F}_{nl\,\alpha}$ and the derivative $\boldsymbol{F}_\alpha$ of the forcing vector obtained with the AFT method described in Section 1.1.1. $\boldsymbol{Z}_\alpha$ and $(\boldsymbol{\Delta}_{1l})_\alpha$ are build depending on which system parameter has been chosen as α. Before computing $(\boldsymbol{F}_{nl\,\boldsymbol{X}}\phi)_{\boldsymbol{X}}$, $(\boldsymbol{F}_{nl\,\boldsymbol{X}}\phi)_\omega$, $(\boldsymbol{F}_{nl\,\boldsymbol{X}}\phi)_\alpha$, $(\boldsymbol{\Delta}_{1nl}\phi)_{\boldsymbol{X}}$, $(\boldsymbol{\Delta}_{1nl}\phi)_\omega$ and $(\boldsymbol{\Delta}_{1nl}\phi)_\alpha$ with the AFT approach, the vector ϕ is sampled as in 1.1.3.

$$\begin{aligned}
\bar{\boldsymbol{\varphi}}_1 &= [\boldsymbol{\varphi}_1(t_1), \ldots, \boldsymbol{\varphi}_1(t_N)]^T = (\Gamma \otimes \boldsymbol{I}_n)\phi \\
\bar{\boldsymbol{\varphi}}_2 &= [\boldsymbol{\varphi}_2(t_1), \ldots, \boldsymbol{\varphi}_2(t_N)]^T = (\Gamma \otimes \boldsymbol{I}_n)(\nabla \otimes \boldsymbol{I}_n)\phi \\
\bar{\boldsymbol{\varphi}}_3 &= [\boldsymbol{\varphi}_3(t_1), \ldots, \boldsymbol{\varphi}_3(t_N)]^T = (\Gamma \otimes \boldsymbol{I}_n)(\nabla \otimes \boldsymbol{I}_n)\boldsymbol{X}
\end{aligned} \tag{2.39}$$

Once the sampled vectors $(\bar{\boldsymbol{\varphi}}_1, \bar{\boldsymbol{\varphi}}_2, \bar{\boldsymbol{\varphi}}_3)$ are obtained, $(\boldsymbol{F}_{nl\boldsymbol{X}}\boldsymbol{\phi})_{\boldsymbol{X}}$, $(\boldsymbol{F}_{nl\boldsymbol{X}}\boldsymbol{\phi})_{\omega}$, $(\boldsymbol{F}_{nl\boldsymbol{X}}\boldsymbol{\phi})_{\alpha}$, $(\boldsymbol{\Delta}_{1nl}\boldsymbol{\phi})_{\boldsymbol{X}}$, $(\boldsymbol{\Delta}_{1nl}\boldsymbol{\phi})_{\omega}$ and $(\boldsymbol{\Delta}_{1nl}\boldsymbol{\phi})_{\alpha}$ can be computed.

$$\begin{array}{lcll}
(\boldsymbol{F}_{nl\boldsymbol{X}}\boldsymbol{\phi})_{\boldsymbol{X}} & = & (\Gamma^{-1}\otimes\boldsymbol{I}_n) & \left(\frac{\partial}{\partial\bar{\boldsymbol{x}}}\left(\frac{\partial\bar{\boldsymbol{f}}_{nl}}{\partial\bar{\boldsymbol{x}}}\bar{\boldsymbol{\varphi}}_1+\frac{\partial\bar{\boldsymbol{r}}}{\partial\dot{\bar{\boldsymbol{x}}}}\bar{\boldsymbol{\varphi}}_2\right)(\Gamma\otimes\boldsymbol{I}_n)\right. \\
 & & & \left.+\frac{\partial}{\partial\dot{\bar{\boldsymbol{x}}}}\left(\frac{\partial\bar{\boldsymbol{f}}_{nl}}{\partial\bar{\boldsymbol{x}}}\bar{\boldsymbol{\varphi}}_1+\frac{\partial\bar{\boldsymbol{f}}_{nl}}{\partial\dot{\bar{\boldsymbol{x}}}}\bar{\boldsymbol{\varphi}}_2\right)\boldsymbol{\omega}\big((\Gamma\nabla)\otimes\boldsymbol{I}_n\big)\right) \\
(\boldsymbol{F}_{nl\boldsymbol{X}}\boldsymbol{\phi})_{\omega} & = & (\Gamma^{-1}\otimes\boldsymbol{I}_n) & \left(\frac{\partial}{\partial\dot{\bar{\boldsymbol{x}}}}\left(\frac{\partial\bar{\boldsymbol{f}}_{nl}}{\partial\bar{\boldsymbol{x}}}\bar{\boldsymbol{\varphi}}_1+\frac{\partial\bar{\boldsymbol{f}}_{nl}}{\partial\dot{\bar{\boldsymbol{x}}}}\bar{\boldsymbol{\varphi}}_2\right)+\frac{\partial\bar{\boldsymbol{f}}_{nl}}{\partial\dot{\bar{\boldsymbol{x}}}}\right)\big((\Gamma\nabla)\otimes\boldsymbol{I}_n\big)\boldsymbol{X} \\
(\boldsymbol{F}_{nl\boldsymbol{X}}\boldsymbol{\phi})_{\alpha} & = & (\Gamma^{-1}\otimes\boldsymbol{I}_n) & \frac{\partial}{\partial\bar{\alpha}}\left(\frac{\partial\bar{\boldsymbol{f}}_{nl}}{\partial\bar{\boldsymbol{x}}}\bar{\boldsymbol{\varphi}}_1+\frac{\partial\bar{\boldsymbol{f}}_{nl}}{\partial\dot{\bar{\boldsymbol{x}}}}\bar{\boldsymbol{\varphi}}_2\right) \\
\boldsymbol{F}_{nl\,\omega\omega} & = & (\Gamma^{-1}\otimes\boldsymbol{I}_n) & \left(\frac{\partial}{\partial\dot{\bar{\boldsymbol{x}}}}\left(\frac{\partial\bar{\boldsymbol{f}}_{nl}}{\partial\dot{\bar{\boldsymbol{x}}}}\bar{\boldsymbol{\varphi}}_3\right)\right)\big((\Gamma\nabla)\otimes\boldsymbol{I}_n\big)\boldsymbol{X} \\
(\boldsymbol{\Delta}_{1nl}\boldsymbol{\phi})_{\boldsymbol{X}} & = & (\Gamma^{-1}\otimes\boldsymbol{I}_n) & \left(\frac{\partial}{\partial\dot{\bar{\boldsymbol{x}}}}\left(\frac{\partial\bar{\boldsymbol{f}}_{nl}}{\partial\dot{\bar{\boldsymbol{x}}}}\bar{\boldsymbol{\varphi}}_1\right)(\Gamma\otimes\boldsymbol{I}_n)+\frac{\partial}{\partial\dot{\bar{\boldsymbol{x}}}}\left(\frac{\partial\bar{\boldsymbol{f}}_{nl}}{\partial\dot{\bar{\boldsymbol{x}}}}\bar{\boldsymbol{\varphi}}_1\right)\boldsymbol{\omega}\big((\Gamma\nabla)\otimes\boldsymbol{I}_n\big)\right) \\
(\boldsymbol{\Delta}_{1nl}\boldsymbol{\phi})_{\omega} & = & (\Gamma^{-1}\otimes\boldsymbol{I}_n) & \frac{\partial}{\partial\dot{\bar{\boldsymbol{x}}}}\left(\frac{\partial\bar{\boldsymbol{f}}_{nl}}{\partial\dot{\bar{\boldsymbol{x}}}}\bar{\boldsymbol{\varphi}}_1\right)\boldsymbol{\omega}\big((\Gamma\nabla)\otimes\boldsymbol{I}_n\big)\boldsymbol{X} \\
(\boldsymbol{\Delta}_{1nl}\boldsymbol{\phi})_{\alpha} & = & (\Gamma^{-1}\otimes\boldsymbol{I}_n) & \frac{\partial}{\partial\bar{\alpha}}\left(\frac{\partial\bar{\boldsymbol{f}}_{nl}}{\partial\dot{\bar{\boldsymbol{x}}}}\bar{\boldsymbol{\varphi}}_1\right)
\end{array} \tag{2.40}$$

where $\frac{\partial\overline{\boldsymbol{f}_{nl}}}{\partial\dot{\bar{\boldsymbol{x}}}}$ is computed in Section 1.1.3 and $\left(\frac{\partial\overline{\boldsymbol{f}_{nl\boldsymbol{x}}\boldsymbol{\varphi}}}{\partial\bar{\boldsymbol{x}}}, \frac{\partial\overline{\boldsymbol{f}_{nl\dot{\boldsymbol{x}}}\boldsymbol{\varphi}}}{\partial\dot{\bar{\boldsymbol{x}}}}, \frac{\partial\overline{\boldsymbol{f}_{nl\dot{\boldsymbol{x}}}\boldsymbol{\varphi}}}{\partial\bar{\boldsymbol{x}}}, \frac{\partial\overline{\boldsymbol{f}_{nl\dot{\boldsymbol{x}}}\boldsymbol{\varphi}}}{\partial\dot{\bar{\boldsymbol{x}}}}\right)$ are $(nN\times nN)$ size blocs diagonal matrix build as follows in the time domain:

$$\begin{array}{lcl}
\frac{\partial\overline{\boldsymbol{f}_{nl\boldsymbol{x}}\boldsymbol{\varphi}}}{\partial\bar{\boldsymbol{x}}} & = & \mathrm{diag}\left(\left.\frac{\partial\boldsymbol{f}_{nl\boldsymbol{x}}\boldsymbol{\varphi}}{\partial\boldsymbol{x}}\right|_{t=t_1},\ldots,\left.\frac{\partial\boldsymbol{f}_{nl\boldsymbol{x}}\boldsymbol{\varphi}}{\partial\boldsymbol{x}}\right|_{t=t_N}\right) \\
\frac{\partial\overline{\boldsymbol{f}_{nl\boldsymbol{x}}\boldsymbol{\varphi}}}{\partial\dot{\bar{\boldsymbol{x}}}}=\frac{\partial\overline{\boldsymbol{f}_{nl\dot{\boldsymbol{x}}}\boldsymbol{\varphi}}}{\partial\bar{\boldsymbol{x}}} & = & \mathrm{diag}\left(\left.\frac{\partial\boldsymbol{f}_{nl\boldsymbol{x}}\boldsymbol{\varphi}}{\partial\dot{\boldsymbol{x}}}\right|_{t=t_1},\ldots,\left.\frac{\partial\boldsymbol{f}_{nl\boldsymbol{x}}\boldsymbol{\varphi}}{\partial\dot{\boldsymbol{x}}}\right|_{t=t_N}\right) \\
\frac{\partial\overline{\boldsymbol{f}_{nl\dot{\boldsymbol{x}}}\boldsymbol{\varphi}}}{\partial\dot{\bar{\boldsymbol{x}}}} & = & \mathrm{diag}\left(\left.\frac{\partial\boldsymbol{f}_{nl\dot{\boldsymbol{x}}}\boldsymbol{\varphi}}{\partial\dot{\boldsymbol{x}}}\right|_{t=t_1},\ldots,\left.\frac{\partial\boldsymbol{f}_{nl\dot{\boldsymbol{x}}}\boldsymbol{\varphi}}{\partial\dot{\boldsymbol{x}}}\right|_{t=t_N}\right)
\end{array} \tag{2.41}$$

The jacobians can be computed analytically or by finite differences. The finite differences can be performed either in the time domain:

$$\begin{array}{lcll}
(\boldsymbol{r}_{\boldsymbol{x}}\boldsymbol{\varphi})_{\boldsymbol{x}} & = & \frac{\partial\boldsymbol{r}_{\boldsymbol{x}}\boldsymbol{\varphi}}{\partial\boldsymbol{x}} & \simeq \frac{1}{\varepsilon_{\boldsymbol{x}}}[\boldsymbol{r}_{\boldsymbol{x}}(\boldsymbol{x}+\boldsymbol{\varepsilon}_{\boldsymbol{x}}\boldsymbol{\varphi})-\boldsymbol{r}_{\boldsymbol{x}}(\boldsymbol{x})] \\
(\boldsymbol{r}_{\boldsymbol{x}}\boldsymbol{\varphi})_{\dot{\boldsymbol{x}}} & = & \frac{\partial\boldsymbol{r}_{\boldsymbol{x}}\boldsymbol{\varphi}}{\partial\dot{\boldsymbol{x}}} & \simeq \frac{1}{\varepsilon_{\dot{\boldsymbol{x}}}}[\boldsymbol{r}_{\boldsymbol{x}}(\dot{\boldsymbol{x}}+\boldsymbol{\varepsilon}_{\dot{\boldsymbol{x}}}\boldsymbol{\varphi})-\boldsymbol{r}_{\boldsymbol{x}}(\dot{\boldsymbol{x}})] \\
(\boldsymbol{r}_{\boldsymbol{x}}\boldsymbol{\varphi})_{\alpha} & = & \frac{\partial\boldsymbol{r}_{\boldsymbol{x}}\boldsymbol{\varphi}}{\partial\alpha} & \simeq \frac{1}{\varepsilon_{\alpha}}[\boldsymbol{r}_{\boldsymbol{x}}(\alpha(1+\boldsymbol{\varepsilon}_{\alpha}))-\boldsymbol{r}_{\boldsymbol{x}}(\alpha)]
\end{array} \tag{2.42}$$

or in the frequency domain:

$$\begin{array}{lcll}
(\boldsymbol{R}_{\boldsymbol{X}}\boldsymbol{\phi})_{\boldsymbol{X}} & \simeq & \frac{1}{\varepsilon_{\boldsymbol{X}}} & [\boldsymbol{R}_{\boldsymbol{X}}(\boldsymbol{X}+\boldsymbol{\varepsilon}_{\boldsymbol{X}}\boldsymbol{\phi})-\boldsymbol{R}_{\boldsymbol{X}}(\boldsymbol{X})] \\
(\boldsymbol{R}_{\boldsymbol{X}}\boldsymbol{\phi})_{\omega} & \simeq & \frac{1}{\varepsilon_{\omega}} & [\boldsymbol{R}_{\boldsymbol{X}}(\omega(1+\boldsymbol{\varepsilon}_{\omega}))-\boldsymbol{R}_{\boldsymbol{X}}(\omega)] \\
(\boldsymbol{R}_{\boldsymbol{X}}\boldsymbol{\phi})_{\alpha} & \simeq & \frac{1}{\varepsilon_{\alpha}} & [\boldsymbol{R}_{\boldsymbol{X}}(\alpha(1+\boldsymbol{\varepsilon}_{\alpha}))-\boldsymbol{R}_{\boldsymbol{X}}(\alpha)] \\
(\boldsymbol{\Delta}_1\boldsymbol{\phi})_{\boldsymbol{X}} & \simeq & \frac{1}{\varepsilon_{\boldsymbol{X}}} & [\boldsymbol{\Delta}_1(\boldsymbol{X}+\boldsymbol{\varepsilon}_{\boldsymbol{X}}\boldsymbol{\phi})-\boldsymbol{\Delta}_1(\boldsymbol{X})] \\
(\boldsymbol{\Delta}_1\boldsymbol{\phi})_{\omega} & \simeq & \frac{1}{\varepsilon_{\omega}} & [\boldsymbol{\Delta}_1(\omega(1+\boldsymbol{\varepsilon}_{\omega}))-\boldsymbol{\Delta}_1(\omega)] \\
(\boldsymbol{\Delta}_1\boldsymbol{\phi})_{\alpha} & \simeq & \frac{1}{\varepsilon_{\alpha}} & [\boldsymbol{\Delta}_1(\alpha(1+\boldsymbol{\varepsilon}_{\alpha}))-\boldsymbol{\Delta}_1(\alpha)]
\end{array} \tag{2.43}$$

$\varepsilon = 10^{-6}$ is used to compute the perturbations $\varepsilon_{\boldsymbol{x}}$, $\varepsilon_{\dot{\boldsymbol{x}}}$ and $\varepsilon_{\boldsymbol{X}}$:

$$\varepsilon_{\boldsymbol{x}} = \varepsilon\left(\frac{\|\boldsymbol{x}\|}{\|\boldsymbol{\varphi}\|}+\varepsilon\right) \qquad \varepsilon_{\dot{\boldsymbol{x}}} = \varepsilon\left(\frac{\|\dot{\boldsymbol{x}}\|}{\|\boldsymbol{\varphi}\|}+\varepsilon\right) \qquad \varepsilon_{\boldsymbol{X}} = \varepsilon\left(\frac{\|\boldsymbol{X}\|}{\|\boldsymbol{\phi}\|}+\varepsilon\right) \tag{2.44}$$

By normalizing the $\varepsilon_{\boldsymbol{x}}$, $\varepsilon_{\dot{\boldsymbol{x}}}$ and $\varepsilon_{\boldsymbol{X}}$, the local stiffness of the problem is taken into account leading to a higher precision of the finite differences.

2.1.4 Examples of bifurcation tracking

In this subsection, detection, localization and bifurcation tracking are performed on a NLTVA and a Jeffcott rotor to better visualize and apprehend the global dynamic of those systems.

Bifurcation analysis on the NLTVA A Duffing oscillator coupled with an attached NLTVA, as depicted in Fig. 2.3, is studied. The NLTVA system is a Duffing oscillator tuned in such a way as to absorb the energy vibration from the forced primary mass. The nonlinear dynamical behavior of the system is governed by Eqs. (2.45).

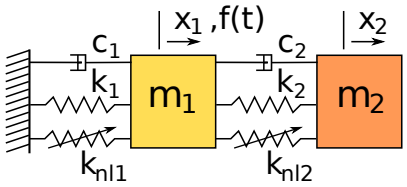

Figure 2.3 – NLTVA mechanical model

$$\begin{aligned} m_1\ddot{x}_1 + c_1\dot{x}_1 + k_1x_1 + k_{nl1}x_1^3 + c_2(\dot{x}_1-\dot{x}_2) + k_2(x_1-x_2) + k_{nl2}(x_1-x_2)^3 &= f_0\cos\omega t \\ m_1\varepsilon\ddot{x}_2 + c_2(\dot{x}_2-\dot{x}_1) + k_2(x_2-x_1) + k_{nl2}(x_2-x_1)^3 &= 0 \end{aligned} \tag{2.45}$$

with k_1 and k_2 the stiffness coefficients of the linear springs, k_{nl_1} and k_{nl2} the coefficients of the nonlinear elastic forces, c_1 and c_2 the damping coefficients, $\varepsilon = m_2/m_1$ the mass ratio. The primary mass is periodically forced at frequency ω and amplitude f_0. The NLTVA parameters k_2, c_2, knl_2 are set according to the nonlinear generalization of the Equal-Peak method presented in [HAB 15]:

$$\begin{aligned} k_2^{opt} &= \frac{8\varepsilon k_1\left[16+23\varepsilon+9\varepsilon^2+2(2+\varepsilon)\sqrt{4+3\varepsilon}\right]}{3(1+\varepsilon)^2\left(64+80\varepsilon+27\varepsilon^2\right)} && [N/(m.kg)] \\ k_{nl2}^{opt} &= \frac{2\varepsilon^2 k_{nl1}}{1+4\varepsilon} && [N/(m^3.kg)] \\ c_2^{opt} &= \sqrt{\frac{k_2 m_2\left(8+9\varepsilon-4\sqrt{4+3\varepsilon}\right)}{4(1+\varepsilon)}} && [Ns/(m.kg)] \end{aligned} \tag{2.46}$$

The remaining parameters of the system are set as follows: $\varepsilon = 0.05$, $m_1 = 1kg$, $c_1 = 0.002Ns/m$, $k_1 = 1N/m$, $knl_1 = 1N/m^3$ in accordance with the literature [HAB 15]. The nonlinear equations of the NLTVA are then put into the following matrix form:

$$\boldsymbol{r}(\boldsymbol{x},\omega,t) = \boldsymbol{M}\ddot{\boldsymbol{x}}(t) + \boldsymbol{C}\dot{\boldsymbol{x}}(t) + \boldsymbol{K}\boldsymbol{x}(t) + \boldsymbol{f}_{nl}(\boldsymbol{x}) - \boldsymbol{f}(\omega,t) = \boldsymbol{0} \tag{2.47}$$

The vector $\boldsymbol{x}(t)$ gathers the displacements of the $n = 2$ DOFs, $\boldsymbol{\alpha}$ is the vector of the system parameters. The matrices $\boldsymbol{M}$, $\boldsymbol{C}$, $\boldsymbol{K}$ correspond to the mass, damping and stiffness matrix, $\boldsymbol{f}_{nl}$ represents the non linear forces and $\boldsymbol{p}$ the periodic excitation at frequency ω. By applying the HBM to the differential Eq. (2.47) as detailled in [XIE 16b], the following nonlinear algebraic system of size $L = n(2H+1)$ in the frequency domain is obtained:

$$\boldsymbol{R}(\boldsymbol{X},\omega) = \boldsymbol{Z}(\omega)\boldsymbol{X} + \boldsymbol{F}_{nl}(\boldsymbol{X}) - \boldsymbol{F} = \boldsymbol{0} \tag{2.48}$$

with

$$\boldsymbol{Z}(\omega) = \omega^2\nabla^2 \otimes \boldsymbol{M} + \omega\nabla \otimes \boldsymbol{C} + \boldsymbol{I}_{2H+1} \otimes \boldsymbol{K} = \mathrm{diag}(\mathbf{K}, \mathbf{Z}_1, ..\mathbf{Z}_j, ..\mathbf{Z}_H) \tag{2.49}$$

$$\mathbf{Z}_j = \begin{bmatrix} \boldsymbol{K} - j^2\omega^2\boldsymbol{M} & \omega\boldsymbol{C} \\ -\omega\boldsymbol{C} & \boldsymbol{K} - j^2\omega^2\boldsymbol{M} \end{bmatrix}$$

where $\otimes$ stands for the Kronecker tensor product. The nonlinear frequency response curves of the system for a fixed initial set of parameters $(\omega, \boldsymbol{\alpha})$ and various amplitudes of forcing are then obtained by coupling Eq. (2.48) with a continuation procedure such as a pseudo arc-length technique [CRI 81, XIE 16a] as presented in Section 1.1.1. For a forcing amplitude $f_0 = 0.005N$, the curve is entirely stable, see Fig 2.4. For a higher

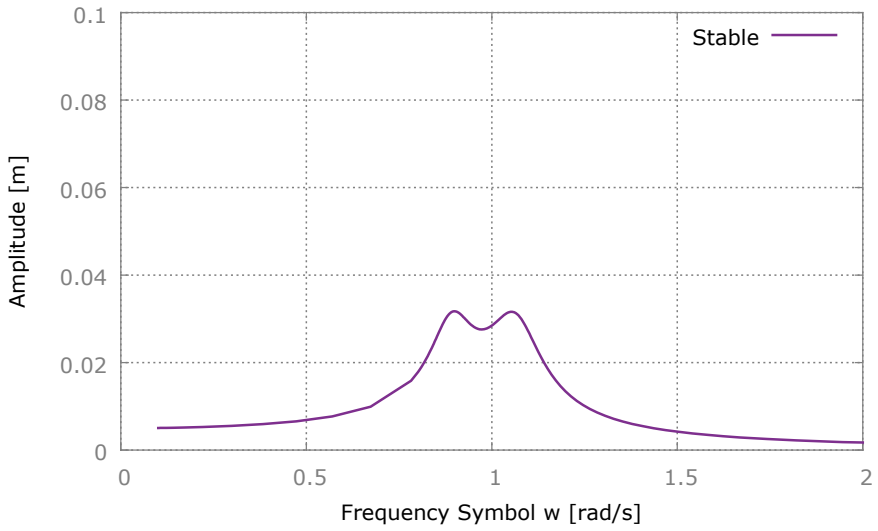

Figure 2.4 – NLTVA frequency response - $f_0 = 0.005N$

amplitude, such as $f_0 = 0.095N$, LPs appear on the second peak of the response curve, see

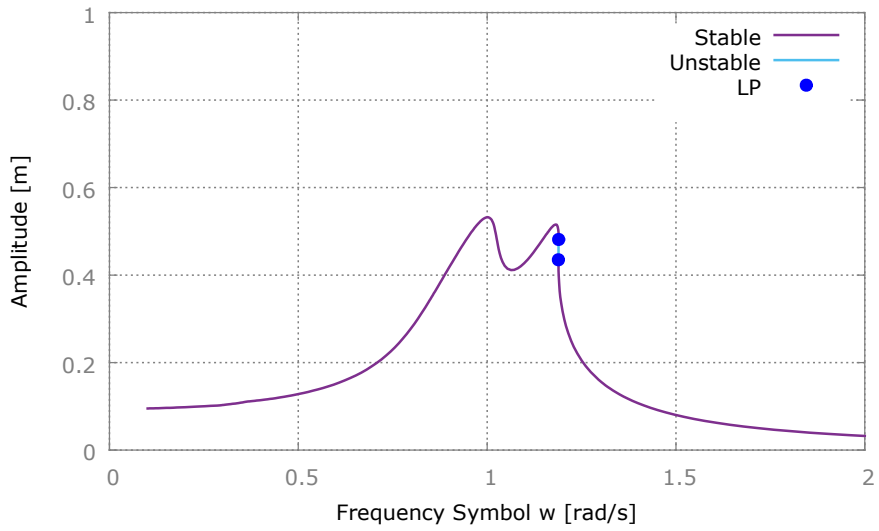

Figure 2.5 – NLTVA frequency response - $f_0 = 0.0095N$

Fig. 2.5. LPs are localized with the augmented system presented in Eq. (2.3). For $f_0 = 0.11N$, a zone of quasi-periodic solutions is delimited by two NS bifurcations, see Fig. 2.6. NS bifurcations are computed with the augmented system presented in Eq. (2.19). For $f_0 = 0.15N$, the frequency response curve in Fig. 2.7 contains new LP bifurcations

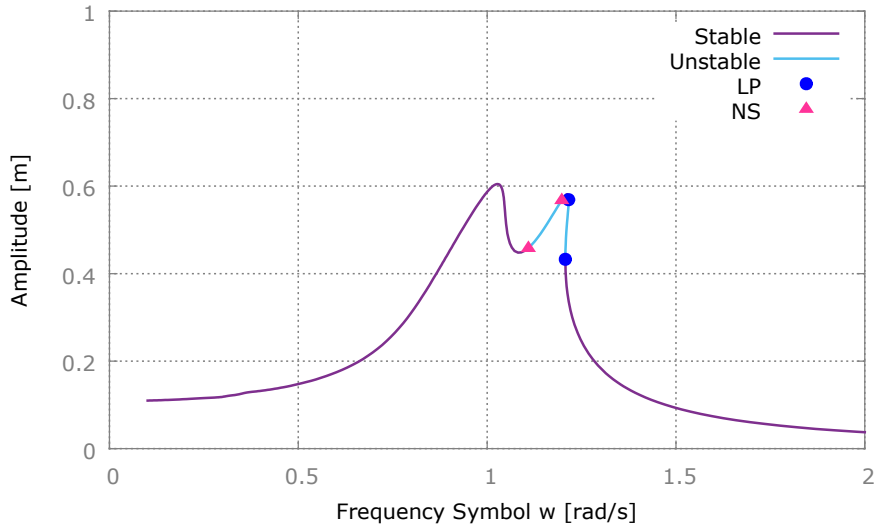

Figure 2.6 – NLTVA frequency response - $f_0 = 0.011N$

on the second peak of resonance and an isolated solution (IS). Then for $f_0 = 0.19N$, the amplitude of the response curve is suddenly multiplied by a factor three, see Fig. 2.8, due to the sudden merge of an IS and the response curve. To better visualize the evolution of bifurcations with respect to the forcing amplitude, bifurcation tracking of

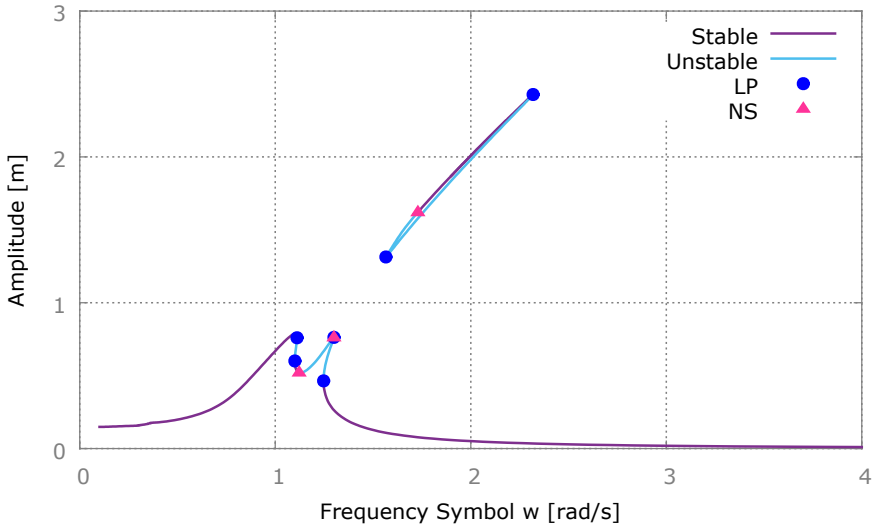

Figure 2.7 – NLTVA frequency response - $f_0 = 0.015N$

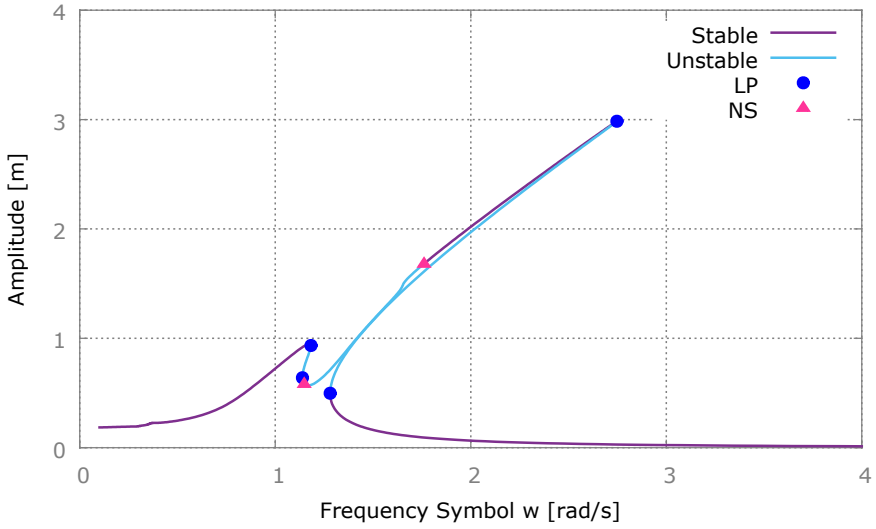

Figure 2.8 – NLTVA frequency response - $f_0 = 0.019N$

LP and NS bifurcations present in Fig. 2.8 are realized. The parametric analysis with respect to the forcing amplitude f_0 is performed with the method presented in Section 2.1.2. First, the LP of the second peak are continuated, see Fig. 2.9. The LP curve

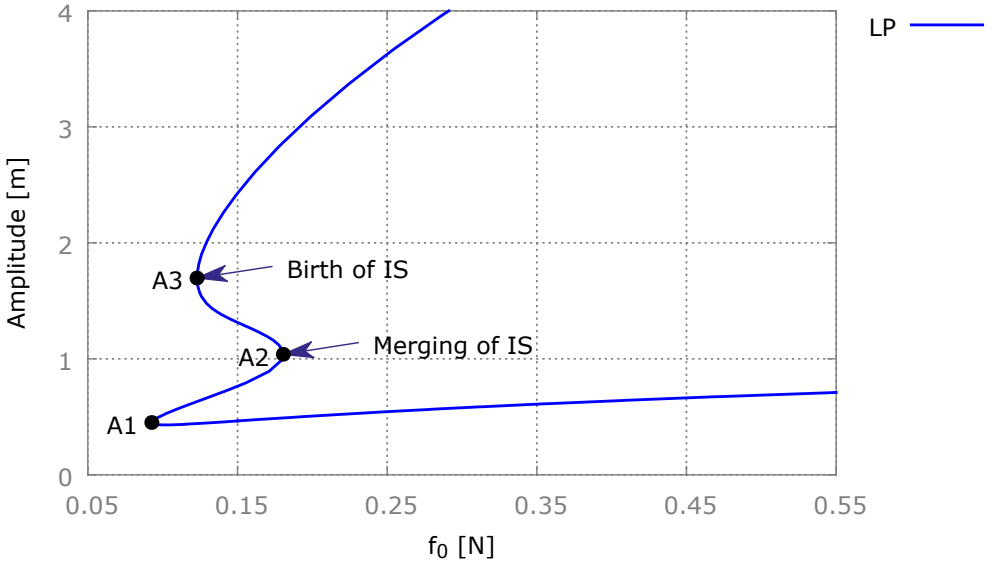

Figure 2.9 – NLTVA - LP curve from the second peak of resonance

presents three extremums with respect to the forcing amplitude. The first A_1 extremum appears around $f_0 = 0.93N$ and represents the birth of the LP bifurcations on the second peak of the response curve. The second extremum $A2$ appears around $f_0 = 0.123N$. This extremum, called an isola center, represents the birth of additional LP bifurcations at a point detached from the response curve. For higher forcing amplitudes, a branch of solutions detached from the main response curve is emanating from the isola center. These detached response curves are called isolated solutions (ISs) and are analyzed with more details in Section 2.3. The third extremum $A3$ represents the merging point of the isolated solutions with the main response curve. This is the reason why the amplitude of oscillation increases so much with forcing amplitude higher than this extremum point, see Fig. 2.8. Then, bifurcation tracking of the LPs present on the first peak on the response curve is performed, see Fig. 2.10. The LP curve presents a single extremum point $B1$ with respect to the forcing amplitude. Therefore, those LPs are not associated with any IS. Finally, the continuation of the NS bifurcations is performed, see Fig. 2.11. One can see that both ends of each NS curve are stopped by a R1 bifurcation. The R1 bifurcations are detected using the augmented system presented in Eq. (2.25). A R1 bifurcation represents the birth of a NS curve from a LP curve [KUZ 13]. Therefore, the continuated LP curve must pass by all the detected R1 bifurcations. As seen in Fig. 2.11, the LP curve passes by all the R1 bifurcations except one. Consequently, there must be an undetected LP curve passing by this R1. For a forcing amplitude $f_0 = 0.3N$, LP bifurcations appear between the already merged isolated solution and the response curve, see Fig. 2.12. Once

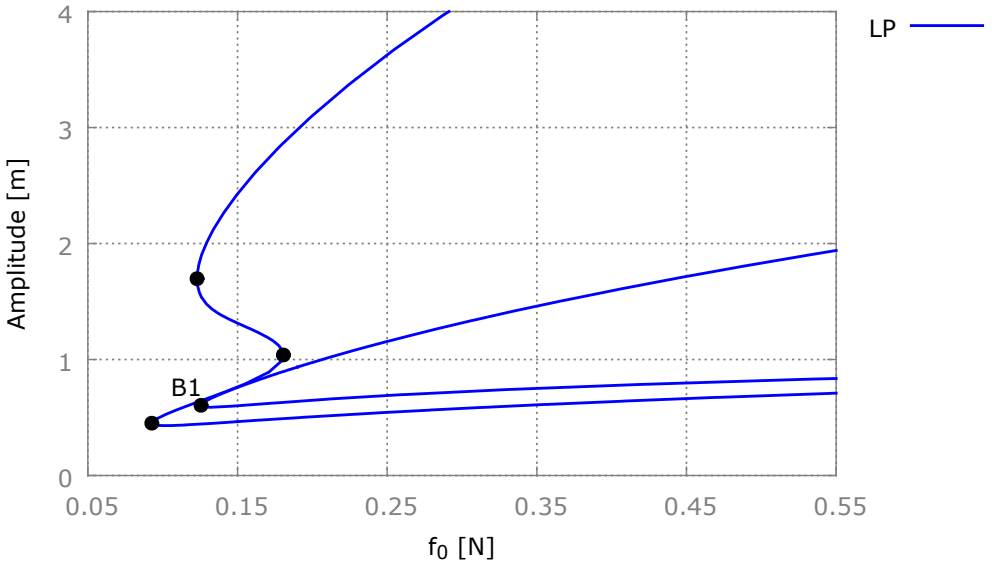

Figure 2.10 – NLTVA - LP curves from both peaks of resonance

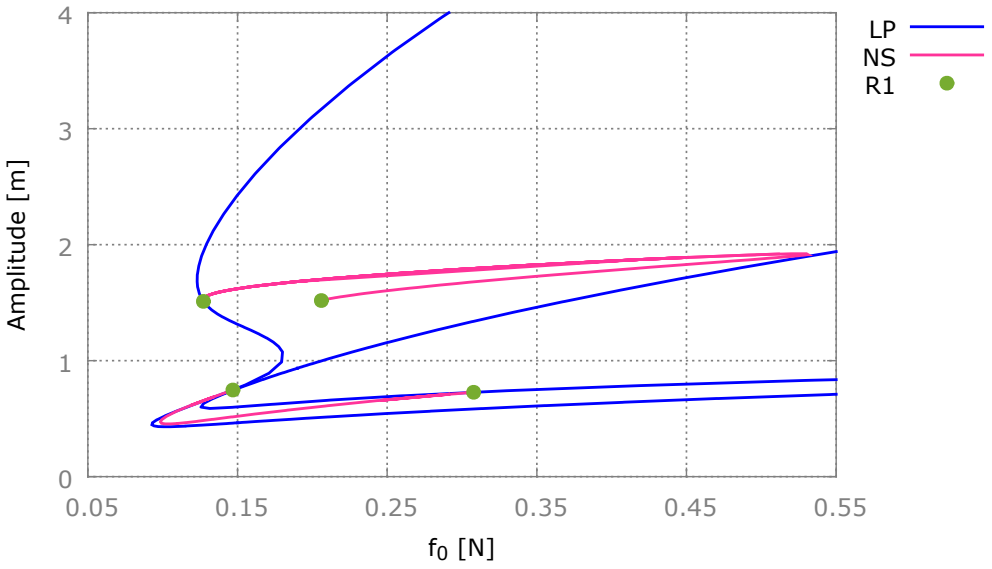

Figure 2.11 – NLTVA - LP and NS curve from the resonance

continuated and plotted with all the bifurcations curves, these LPs form a new branch to which the previous R1 bifurcation belongs, see Fig. 2.13

The bifurcation tracking of LPs and NSs have lead to a better understanding of the nonlinear dynamics of the NLTVA. Moreover, complex dynamical behaviors such as isolated solutions have been uncovered. In Section 2.3, the analysis of isolated solutions is conducted with the use of the multi-parametric recursive continuation presented in Section 2.2. In the next paragraph the bifurcation tracking is applied to LPs and NSs present in a Jeffcott rotor.

Bifurcation analysis on the Jeffcott rotor In a Jeffcott rotor, the amplitude of the lateral displacement is limited by the rotor/stator gap. When the contact is established, Coulomb friction and contact stiffness are considered as in [JIA 09] [PEL 14] [XIE 16b]. A disk of mass m is disposed at the middle of the shaft. The shaft is considered to have a negligible mass compared to the disk. The contact stiffness is modeled by an isotropic stiffness k_c. According to these assumptions the rotor can be modeled by the following equations normalized by the mass of the disk:

$$\begin{cases} \ddot{x} + c\dot{x} + kx + k_c \left\{1 - \frac{h}{r}\right\}^+ (x - \mu y \operatorname{sign}(v_{rel})) = p_b \omega^2 \cos \omega t \\ \ddot{y} + c\dot{y} + ky + k_c \left\{1 - \frac{h}{r}\right\}^+ (\mu x \operatorname{sign}(v_{rel}) + y) = p_b \omega^2 \sin \omega t \end{cases} \tag{2.50}$$

with the following parameters $c = 5Ns/(kg.m)$, $k = 100N/(kg.m)$, $k_c = 2500N/(kg.m)$, $h = 0.105m$, $p_b = 0.1$, $R_{disc} = 20h$, $\omega_0 = \sqrt{k_c/m}$ being respectively the damping of the shaft, the stiffness of the shaft, the isotropic stiffness during contact, the rotor/stator gap, the amplitude of the disk, the radius of the the disk and the resonance frequency. The unknown parameters $r = \sqrt{x^2 + y^2}$ and $v_{rel} = (\frac{x}{r}\dot{y} - \frac{y}{r}\dot{x}) + R_{disc}\omega$ correspond to the eccentricity of the disk and the relative speed at the contact. $\{.\}^+$ represent the positive part operator. Problems with friction must be treated specially in order to be well-posed. In this work, the Coulomb friction is automatically regularized in the frequency domain by the AFT method which guaranty a well-posed problem.

First, the response curve is plotted with $\mu = 0.05$, see Fig. 2.14. No quasi-periodic solution is present on the response curve. However, two LPs are encountered near $\frac{\omega}{\omega_0} = (0.85, 1)$. The first LP is a degenerated one. It appears when the contact is established. The change of state between contact and non contact generate the degeneracy. The second LP is non-degenerated. During the frequency sweep excitation, an hysteresis cycle appears and the LP bifurcations delimit the cycle. For a high friction coefficient such as $\mu = 0.11$, see Fig. 2.15, the zone of quasi-periodic solutions delimited by NS bifurcations appears. Such quasi-periodic solutions can lead to inverse precession which can destroy the rotor. To sum up, it is important to obtain the evolution of LP and NS bifurcations to properly design a Jeffcott rotor. Such parametric analysis are made with the bifurcation tracking method presented in Section 2.1.2 with respect to the friction coefficient μ. The LP and NS curves are obtained and presented in Fig. 2.16. The bifurcation curves obtained by bifurcation tracking pass by each computed bifurcation. The bifurcation tracking allows to obtain the all evolution of these bifurcations with respect to

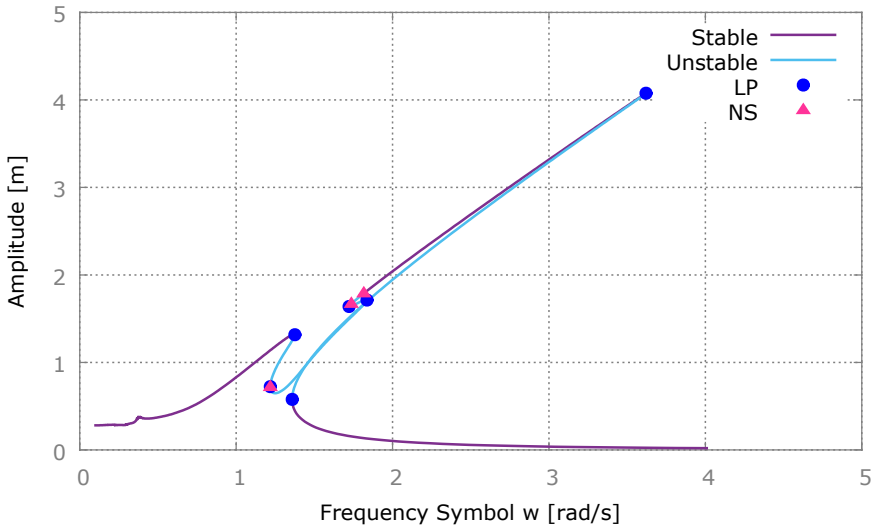

Figure 2.12 – NLTVA frequency response - $f_0 = 0.030N$

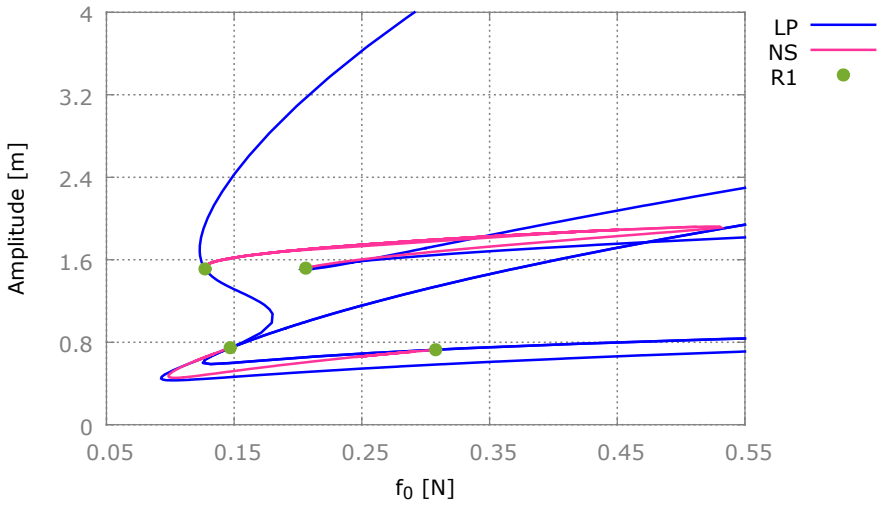

Figure 2.13 – NLTVA - LP and NS curves from the resonance, LP curve appearing at the location of the merge of the isolated solution with the main response curve

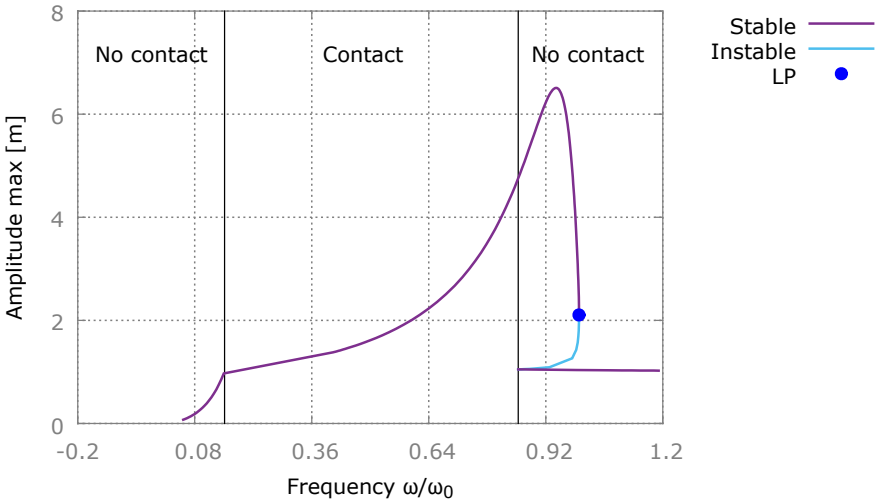

Figure 2.14 – Jeffcott frequency response - $\mu = 0.005$

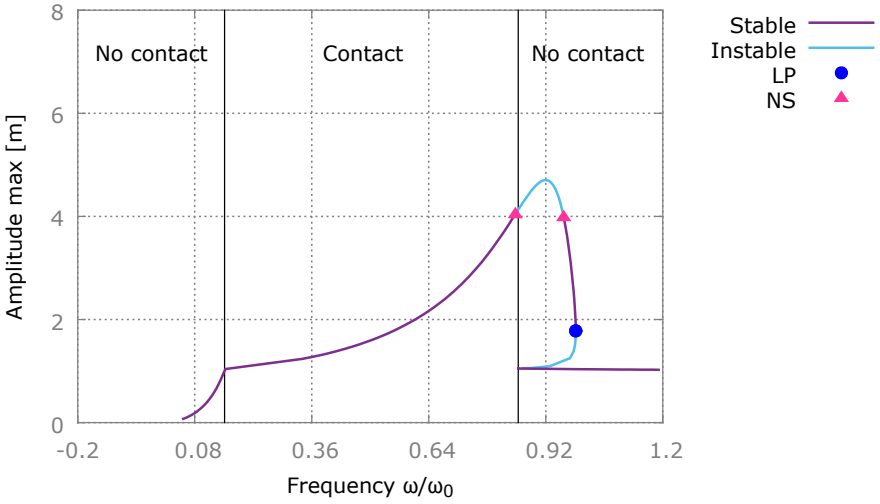

Figure 2.15 – Jeffcott frequency response - $\mu = 0.011$

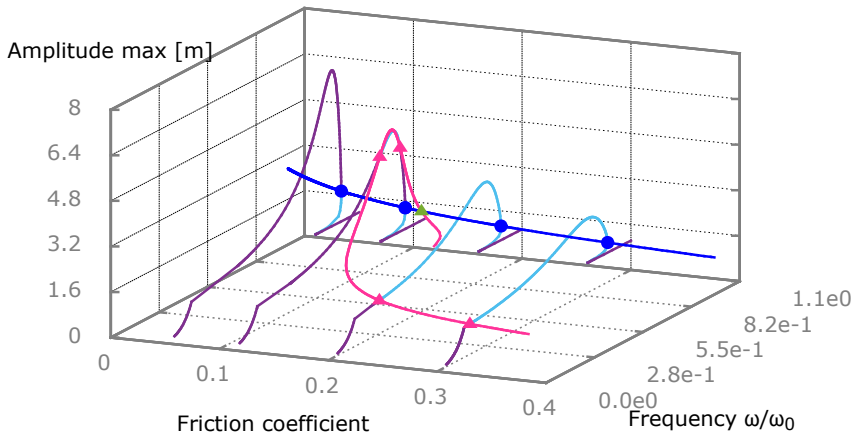

Figure 2.16 – Jeffcott - 3D LP and NS curves

a single system parameter with a single computation. To better see the evolution of the bifurcations with respect to the friction coefficient, Fig. 2.16 is projected onto the plane $(\omega/\omega_0, \mu)$ in Fig. 2.17. One can see that the LP and NS curves are coincident at a specific

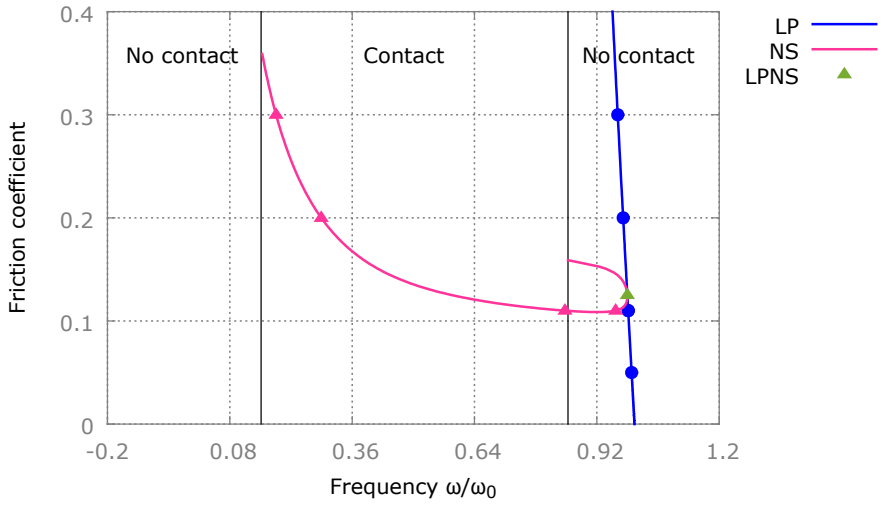

Figure 2.17 – Jeffcott - 2D LP and NS curves

point. This point represents a LPNS bifurcation. During the continuation of the LP and NS curves, this bifurcation point is detected and localized with Eq. (2.29). Contrarily to the NLTVA example, the end of the NS curve is not delimited by R1 resonances but by bifurcations points degenerated by the change of state between contact and non-contact of the rotor and stator.

In this subsection, the usefulness of bifurcation analysis and bifurcation analysis has been presented with two examples, a NLTVA and a Jeffcott rotor. The parametric analysis has allowed the dynamic of those systems to be better visualized. Moreover, some complex phenomena such as isolated solutions in the NLTVA were uncovered during bifurcation tracking. In the next Section 2.2, a multi-parametric recursive continuation method is proposed.

2.2 Multi-parametric recursive continuation

Continuation methods are efficient tools for parametric analysis and more specifically for tracking specific points such as bifurcations which govern the dynamical behavior of nonlinear systems. However, a mono-parametric analysis is sometimes not enough and multi-parametric continuation methods, i.e., when several or all parameters vary at the same time, are essential to properly analyze and design nonlinear systems. Nevertheless, a conventional multi-parametric continuation of solution points is almost unfeasible in practice because of the disproportionate computational time required to obtain the whole multi-dimensional solution surface. A more efficient approach consists in restricting this surface to a set of points or curves by means of additional constraint equations. The presented multi-parametric recursive continuation uses recursive augmented systems based on constraint equations characterizing extremum points. The key objective of the method is to explore the topology of specific points found onto the frequency response curves by tracking extremum points in the successive co-dimensions of the problem. The results can then be used to optimize the safe operating zone of the nonlinear system and to make it more robust with respect to adverse dynamical phenomena such as ISs.

In this section, the characterization of extremum points by a constraint equation and its associated extended system are presented. Then, a recursive algorithm is generated by successively appending new constraint equations to the extended system at each new level of continuation, i.e., when a new parameter is freed.

2.2.1 Extremum point

The originality of the work lies in the fact that extremum point under equality constraint can be rewritten depending on the constraint function alone. During continuation methods with HBM, the continuated curve can be seen as the constraint in the following problem. Therefore such characterization permits calculating extremums by using only the analytic equation of the system obtained by HBM. Let the following problem be composed of the function $\alpha(\boldsymbol{Y})$ and the constraint $\boldsymbol{G}(\boldsymbol{Y},\alpha)=0$ with $\boldsymbol{G}$ being an arbitrary extended system:

$$\begin{cases} \alpha(\boldsymbol{Y}) & \\ \boldsymbol{G}(\boldsymbol{Y},\alpha) & =0 \end{cases} \tag{2.51}$$

Let assume that within a local neighborhood there is a local extremum. The extremum of the function $\alpha(\boldsymbol{Y})$ with respect to $\boldsymbol{Y}$ is characterized by:

$$\frac{\partial \alpha}{\partial \boldsymbol{Y}} = 0 \tag{2.52}$$

By writing the first variation of the problem (2.51) and combining it with Eq. (2.52), the following relationships are obtained:

$$\frac{\partial \alpha}{\partial \boldsymbol{Y}} = 0 \iff \left\{ \begin{array}{cc} \Delta\alpha = \frac{\partial \alpha}{\partial \boldsymbol{Y}} \Delta \boldsymbol{Y} & = 0 \\ \Delta \boldsymbol{Y}^T & \neq 0 \end{array} \right. \iff \left\{ \begin{array}{cc} \boldsymbol{G_Y} \Delta_{\boldsymbol{Y}} & = 0 \\ \Delta \boldsymbol{Y}^T \boldsymbol{G}_\alpha & \neq 0 \end{array} \right. \tag{2.53}$$

So, when $\Delta\alpha = 0$, an extremum of the constrained problem (2.51) is solution of the following augmented system:

$$\left\{ \begin{array}{cc} \frac{\partial \alpha}{\partial \boldsymbol{Y}} & = 0 \\ \boldsymbol{G}(\boldsymbol{Y}, \alpha) & = 0 \end{array} \right. \iff \left\{ \begin{array}{cc} \boldsymbol{G}(\boldsymbol{Y}, \alpha) & = 0 \\ \boldsymbol{G_Y} \phi & = 0 \\ \phi^T \boldsymbol{G}_\alpha & \neq 0 \end{array} \right. \tag{2.54}$$

The condition $\phi^T \boldsymbol{G}_\alpha \neq 0$ that insures $\Delta\alpha = 0$ can be seen as a non-degeneracy condition. Such a condition is important if one wants to avoid degenerated points resulting in an ill-conditioned jacobian during continuation. However, some of these degenerated points will be calculated as the result of the recursive continuation in increasing codimension. Therefore it is important to extend the augmented system (2.54) characterizing the extremum points when $\phi^T \boldsymbol{G}_\alpha \to 0$ in order to also support such degenerated points.

When $\phi^T \boldsymbol{G}_\alpha \to 0$, a normalization equation has to be added to the augmented system (2.54) in order to avoid an ill-posed problem, leading to the following extended augmented system:

$$\left\{ \begin{array}{cc} \boldsymbol{G}(\boldsymbol{Y}, \alpha) & = 0 \\ \boldsymbol{G_Y} \phi & = 0 \\ \phi^T \boldsymbol{G}_\alpha & = 0 \\ \phi^T \phi - 1 & = 0 \end{array} \right. \tag{2.55}$$

In order to obtain an augmented system that provides both degenerated and non generated extremum points, the equation associated with the degeneracy characterization has to be withdrawn.

$$\left\{ \begin{array}{cc} \boldsymbol{G}(\boldsymbol{Y}, \alpha) & = 0 \\ \boldsymbol{G_Y} \phi & = 0 \\ \phi^T \phi - 1 & = 0 \end{array} \right. \tag{2.56}$$

With an augmented system supporting the degeneracy, the robustness of the continuation of extremum point is improved. One can note that this augmented system has the same structure as the standard extended system used to characterize LP bifurcations. The augmented system (2.56) has the advantage of characterizing the extremum points of a single parameter α with respect to a vector of parameters $\boldsymbol{Y}$ just by using the constraint function. It also allows a recursive characterization of extremum points in increasing dimension.

2.2.2 Recursive continuation of extremum points in increasing codimension.

The multi-parametric recursive continuation method is based on the recursivity of the extended system (2.56).

Initialization of the recursive continuation The recursive continuation can be started from any solution point $\boldsymbol{Y}_0$ that can be characterized by an extended system $\boldsymbol{G}_0(\boldsymbol{Y}_0) = \boldsymbol{0}$, e.g., a bifurcation point or an extremum point (see [XIE 16a] for the definition of such an extended system). For instance, if a LP of an equilibrium branch is chosen as starting point, the extended system can be written as:

$$\boldsymbol{G}_0(\boldsymbol{Y}_0) = \begin{pmatrix} \boldsymbol{R}(\boldsymbol{X},\omega) \\ \boldsymbol{R}_{\boldsymbol{X}}\phi_0 \\ \phi_0^T\phi_0 - 1 \end{pmatrix} = \boldsymbol{0}_{2L+1} \tag{2.57}$$

where the subsystem $\boldsymbol{R}(\boldsymbol{X},\omega) = \boldsymbol{0}_L$ is the equilibrium equation, and $\boldsymbol{Y}_0 = (\boldsymbol{X},\phi_0,\omega)$ with $\boldsymbol{X}$ the vector of L unknown variables, ϕ_0 the null right eigenvector of the jacobian $\boldsymbol{R}_{\boldsymbol{X}}$ and ω a system parameter.

Recursive continuation A system parameter $\alpha_1 \in \boldsymbol{\alpha}$ is then considered as a new unknown and the branch of solutions of the system $\boldsymbol{G}_0(\boldsymbol{Y}_0,\alpha_1) = \boldsymbol{0}_{2L+1}$ is followed with a continuation method. During the continuation, an extremum point is detected when $\Delta\alpha_1 = 0$. The extremum point at the first level of continuation is called 1-extremum point. To locate this point more precisely, an extended system similar to Eq. (2.56) is used:

$$\boldsymbol{G}_1(\boldsymbol{Y}_1) = \begin{pmatrix} \boldsymbol{G}_0(\boldsymbol{Y}_0,\alpha_1) \\ \boldsymbol{G}_{0\boldsymbol{Y}_0}\phi_1 \\ \phi_1^T\phi_1 - 1 \end{pmatrix} = \boldsymbol{0}_{4L+3} \quad \text{with} \quad \boldsymbol{Y}_1 = \big(\boldsymbol{Y}_0,\phi_1,\alpha_1\big) \tag{2.58}$$

Then, another parameter $\alpha \in \boldsymbol{\alpha}\ \alpha_1$ is considered as a new unknown and the branch of solutions of $\boldsymbol{G}_1(\boldsymbol{Y}_1,\alpha) = \boldsymbol{0}_{4L+3}$ is followed in order to find its extremum points with respect to both parameters $\boldsymbol{Y}$ and α. This procedure is repeated in a recursive manner until all the parameters in the set $\boldsymbol{\alpha}$ have been used. In the following, the extremum points found at the k^{th} level of continuation are called N-extremum points. During the continuation of $\boldsymbol{G}_{k-1}(\boldsymbol{Y}_{k-1},\alpha_n)$, the k-extremum points with respect to α_j, $j = 1..k$ are detected with $\Delta\alpha_j = 0$ and then precisely located by solving:

$$\boldsymbol{G}_k(\boldsymbol{Y}_k) = \begin{pmatrix} \boldsymbol{G}_{k-1}(\boldsymbol{Y}_{k-1},\alpha_k) \\ \boldsymbol{G}_{k-1\boldsymbol{Y}_{k-1}^j}\phi_k \\ \phi_k^T\phi_k - 1 \end{pmatrix} = \boldsymbol{0}_{2^{k+1}(L+1)-1} \quad \text{with} \quad \begin{matrix} \boldsymbol{Y}_k & = & (\boldsymbol{Y}_{k-1},\phi_k,\alpha_k) \\ \boldsymbol{Y}_{k-1}^j & = & \big((\boldsymbol{Y}_{k-1},\alpha_k)\backslash\alpha_j,\alpha_k\big) \end{matrix} \tag{2.59}$$

In summary, the extended system (2.56) characterizing extremum points is used to create a recursive extended system characterizing extremum points in increasing dimension. By

using such a recursive characterization of extremum points, a multi-parametric recursive continuation method can be implemented and applied to any specific point characterized by the initial augmented system $\boldsymbol{G}_0(\boldsymbol{Y}_0)$.

2.2.3 Algorithm of multi-parametric recursive continuation

In order to recursively obtain all the branches of extremum points by continuation with respect to a predefined set of parameters, the algorithm presented in Tab. 2.1 is used.

2.2.4 Results interpretation

The branches of extremum points obtained with the recursive continuation form a tree with ramifications indicating increasing co-dimensions. The tree of extremum points can be used to find local optimal sets of system parameters $\boldsymbol{\alpha}$, while the surrounding branches form a topological skeleton defining the global dynamics of the system. In more concrete terms, this skeleton can be used for instance to find the values of the parameters $\boldsymbol{\alpha}$ for which specific bifurcation points appear or collapse, i.e. by extension, the range of values for which such points exist. This knowledge can then be exploited to appropriately choose the value of the system parameters and insure a safe design.

2.3 Multi-parametric analysis of IS in a NLTVA

In this section, the multi-parametric recursive continuation is used to analyze the ISs present in the NLTVA responses curves. The HBM is applied to the mechanical model and standard extended systems are used to characterize LP bifurcations. Then, the recursive continuation method presented in Section.2.2 is applied to these LPs. The recursive continuation is composed of three levels of continuation with respect to a subset of three system parameters: the amplitude f_0 of the applied force, the nonlinear stiffness coefficient knl_2 and the damping coefficient c_2 of the NLTVA. On the first level, the LPs are continuated with respect to the amplitude of the force f_0. This level is used to explain the birth and merging of ISs. On the second level, the birth and merging points of the IS are tracked with respect to the previous subset of parameters plus the nonlinear stiffness coefficient knl_2 of the vibration absorber as additional parameter. Finally, on the third level, the extremum points, where birth and merging of the ISs occur simultaneously, are followed with respect to the previous subset of parameters plus the damping coefficient c_2 of the absorber. Finally, it is shown how the results of the multi-parametric tracking can be used to optimize the dynamical behavior of the NLTVA and for robust design by identifying sets of parameters insuring safe operating conditions.

Step 0:	Initialization - Choose the set of system p parameters $\boldsymbol{\alpha} = (\alpha_1, .., \alpha_p)$ to use for the multi-parametric recursive continuation. - Define the bounded domain $\boldsymbol{D}_{\boldsymbol{\alpha}} = \boldsymbol{D}_{\alpha_1} \times ... \times \boldsymbol{D}_{\alpha_p}$ in which the set of parameters $\boldsymbol{\alpha}$ is allowed to vary. - Solve the extended system $\boldsymbol{G}_0(\boldsymbol{Y}_0) = \boldsymbol{0}_{2L+1}$ to locate the selected initial point $\boldsymbol{Y}_0$ to be continuated recursively.
Step 1:	Level 1 of continuation and detection of 1-extremum (a) Level 1 of continuation * Consider α_1 as a new unknown. * Continue the branch $\boldsymbol{G}_0(\boldsymbol{Y}_0, \alpha_1) = \boldsymbol{0}$ with α_1 spanning $\boldsymbol{D}_{\alpha_1}$ * Detect all the 1-extremum points with the indicator $\Delta_{\alpha_1} = 0$ (b) Solve the extended system $\boldsymbol{G}_1(\boldsymbol{Y}_1) = \boldsymbol{0}$ to precisely locate all the 1-extremums $\boldsymbol{Y}_1$. (c) End the algorithm if no 1-extremum is detected. Otherwise, go to step 2.
Step k: $k = [2, ..., p]$	Level k of continuation and detection of k-extremums For each $(k-1)$-extremum $\boldsymbol{Y}_{k-1}$ located during step $k-1$: (a) Level k of continuation * Consider α_k as a new unknown. * Continue the branch $\boldsymbol{G}_{k-1}(\boldsymbol{Y}_{k-1}, \alpha_k) = \boldsymbol{0}$ with α_k spanning $\boldsymbol{D}_{\alpha_k}$ * Detect all the k-extremum with respect to each parameters $\alpha_j \in [\alpha_1, .., \alpha_k]$ with the indicators $\Delta\alpha_j = 0$ (b) Solve the extended system $\boldsymbol{G}_k(\boldsymbol{Y}_k) = \boldsymbol{0}$ to precisely locate all the k-extremum points $\boldsymbol{Y}_k$ detected in (a) (c) End the algorithm if no k-extremum is detected or if $k = p$. Otherwise, go to Step $(k+1)$.

Table 2.1 – Algorithm of the multi-parametric recursive continuation method

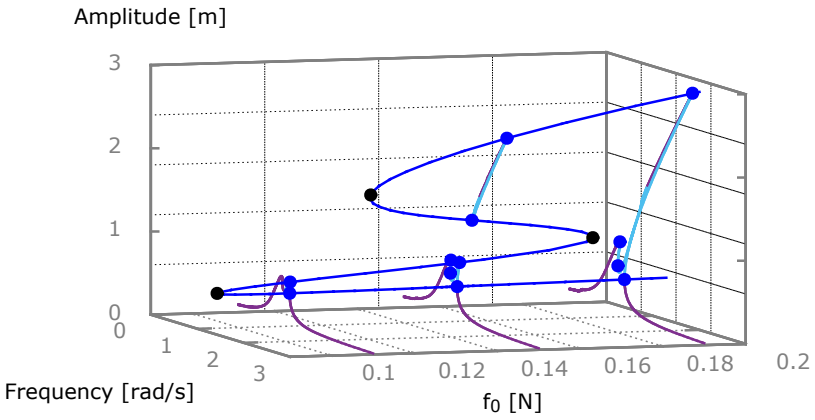

Figure 2.18 – Level 1: Continuation of LP. Stable (Purple), Unstable (Light Blue), LP (Dark Blue), 1-extremum (Black)

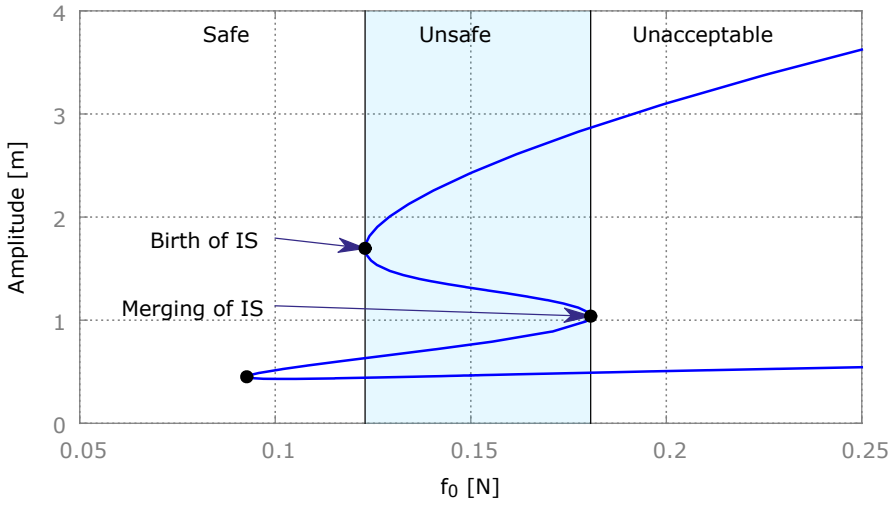

Figure 2.19 – Continuation of LP in the amplitude-f_0 plane.
LP (Dark Blue), 1-extremum (Black)

2.3.1 Level-1 of LP continuation: ISs of the NLTVA

The parametric analysis is performed on the same system presented in the Subsection2.1.4. The system under consideration possesses ISs for some range of parameters. The objective here is to characterize and track ISs in order to identify three zones: without IS, with unmerged IS and with merged IS

In order to show the ISs and their various behaviors, the frequency response curves

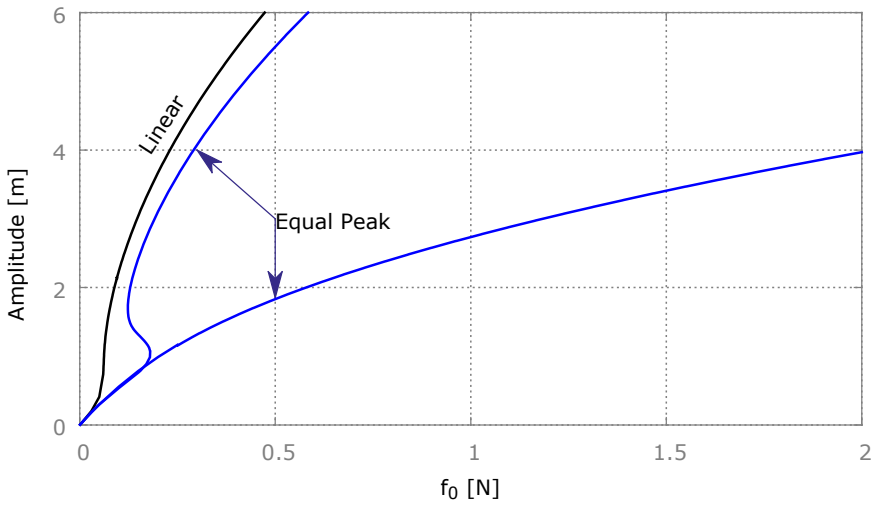

Figure 2.20 – Continuation of the maximums of amplitude. Linear $knl_2 = 0$ (Black), Equal peak $knl_2 = 0.0042N/m^3$

of the NLTVA are plotted in Fig. 2.18 for $f_0 = [0.1, 0.15, 0.21]N$. For a low f_0, there is no IS. Then, an IS appears for a slighty higher f_0 and finally merges for higher values f_0. Detroux *et al.* [DET 15a] have shown that it is possible to characterize the birth and merging of ISs by tracking LP bifurcations with respect to f_0 using the extended system $\boldsymbol{G}_0(\boldsymbol{Y}_0) = \boldsymbol{0}$ described in Subsection 2.2.2.

To perform the parametric analysis of the ISs, the multi-parametric recursive continuation method is applied to the NLTVA model with a LP as initial point for the method. The continuation is performed with respect to the following set of system parameters: the forcing amplitude f_0, the coefficients of nonlinear stiffness k_{nl2} and of damping c_2. This results in three levels of recursive continuation:

- Level 1: (f_0) Continuation of LP
- Level 2: (f_0, k_{nl2}) Continuation of the birth and merging point of ISs
- Level 3: (f_0, k_{nl2}, c_2) Continuation of the point where ISs appear and merge simultaneously

The branch of LPs obtained at level 1 is plotted in Fig. 2.18. Fig. 2.19 shows the projection of this branch onto the amplitude-f_0 plane. One can see that the two extremum points obtained when $\Delta f_0 = 0$ characterize the birth $(f_0 = 0.12N)$ and the merging $(f_0 = 0.18N)$ of ISs. By varying the systems parameters, three regions can be identified: without IS, with IS and with merged IS. Following the classification introduced by Detroux *et al.* [DET 15a], these regions are characterized as "Safe" when the response curve has no IS, "Unsafe" when the response curve exhibits an IS and "Unacceptable" when the IS has merged with the response curve. These three regions present different dynamical behaviors. Concerning the "Safe" region, there is no IS for any value of the applied force f_0, i.e.,

there is no possibility of jumping onto a higher amplitude stable solution. Conversely, inside the "Unsafe" region, ISs with higher amplitude exist. Therefore, this region presents a risk of jumping onto a stable solution at high amplitude. Finally the last region is called "Unacceptable" because the IS has already merged with the response curve and exhibits high amplitude solutions. These three regions have been defined by using the maximum of amplitude as design criterion. One can see that there is no IS in the "Safe" and "Unacceptable" zone since ISs regions either do not exist or have already merged. One can see in Fig. 2.20 that the amplitude of the primarily mass is much more attenuated with the equal peak design compared to a design of the vibration absorber without any nonlinearity ($knl_2 = 0$). Moreover, the vibration absorber under equal peak design remains more efficient even after the merging of the IS.

2.3.2 Level-2 of LP continuation: continuation of the coincident birth and merging of IS

Once the 1-extremum points characterizing the birth and merging of ISs have been precisely located with the extended system (2.58), they can be followed by considering the nonlinear stiffness coefficient knl_2 as a new variable and computing the branch of solutions of $\boldsymbol{G}_1(\boldsymbol{Y}_1, knl_2) = \boldsymbol{0}$. The subset of varying parameters at level 2 is then (f_0, knl_2). The resulting branch of 1-extremum points is plotted in Figs. 2.21 and 2.22. Figs 2.21a and 2.21b show the branch for the same range of parameters as before whereas Figs 2.22a and 2.22b show an extended view of the whole branch of 1-extremum points. Two 2-extremum points can be observed on these extended views. The point at high amplitude of forcing represents the upper limit of existence of IS, whereas the point at low amplitude of forcing represent the lower limit of existence of IS. At these points, the birth and merging of ISs are coincident, i.e., the unsafe region has disappeared. For values of f_0 between these two points, ISs exist and for values of f_0 below and above, there is no IS. The level-2 extended system (2.59) $\boldsymbol{G}_2(\boldsymbol{Y}_2) = \boldsymbol{0}$ is used to locate precisely these two points leading to sets of parameters (f_0, knl_2) approximately equal to $(0.0076N, 0.0017N/m^3)$ and $(16N, 0.0076N/m^3)$. To better visualize the absence of the unsafe region at these two 2-extremums, the branches of LP for these sets of parameters are plotted in Figs. 2.23a and 2.23b.

It is clear from these figures that the "safe" region is schrinked in the first case (Fig. 2.23a) whereas it is considerably enlarged in the second case (Fig. 2.23b). In addition, after projecting the 1-extremum branch of Fig. 2.22b onto the knl_2-f_0 plane, see Fig. 2.24, there is no IS for $k_{nl2} > 0.0076N/m^3$ or $k_{nl2} < 0.0017N/m^3$ in the frequency response curves whatever the value of the other level-2 varying system parameter f_0. Moreover, this projected 1-extremum can be used to identify the value of knl_2 required to set the birth of ISs at specific amplitude of forcing f_0 between the upper and lower limit of existence of ISs. For instance, the IS birth can be set at $f_0 = 0.5N$ by choosing $knl_2 \approx 0.0068N/m^3$, as shown in Fig. 2.23c. This confirms the possibility of tuning the birth or merging point of ISs at a specific amplitude of forcing f_0.

The efficiency of the vibration absorber of Fig. 2.25 can be verified by comparing

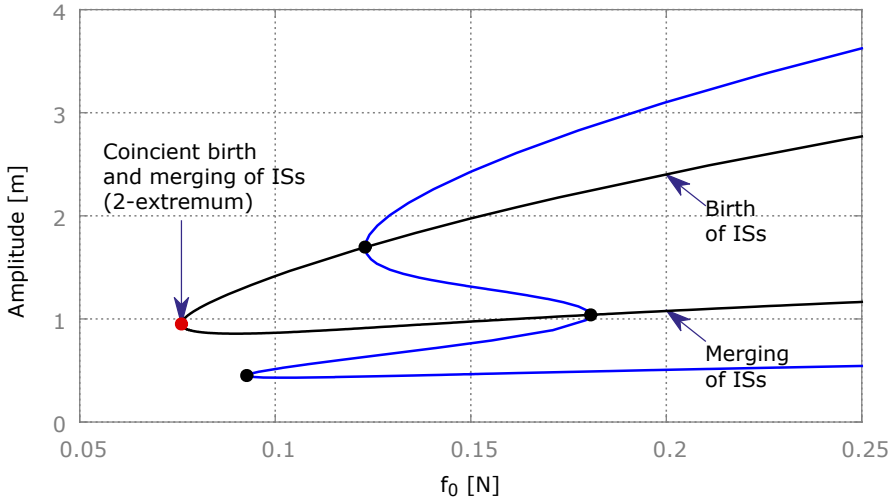

(a) Continuation of the birth and merging of IS in the amplitude-f_0 plane

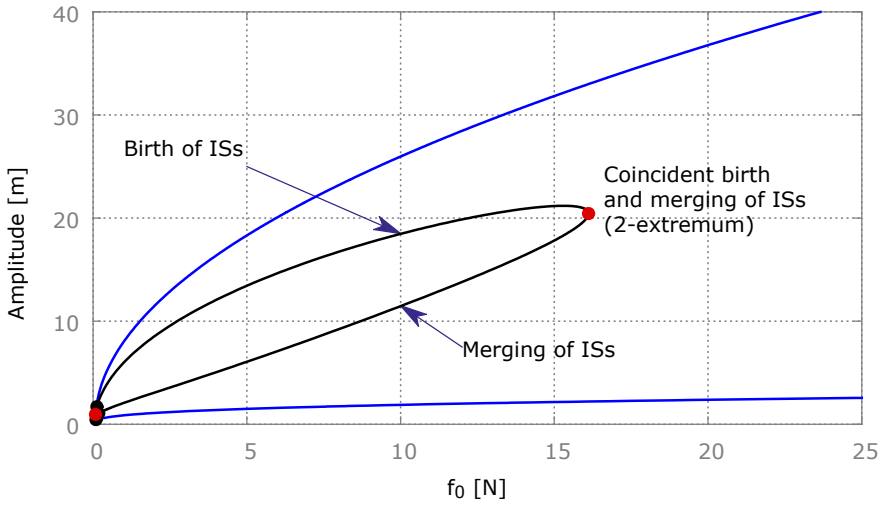

(b) Continuation of the birth and merging of ISs in the amplitude-f_0 plane (extended view)

Figure 2.21 – Continuation of birth and merging points (1-extremum). LP (Blue), 1-extremum (Black), 2-extremum (Red)

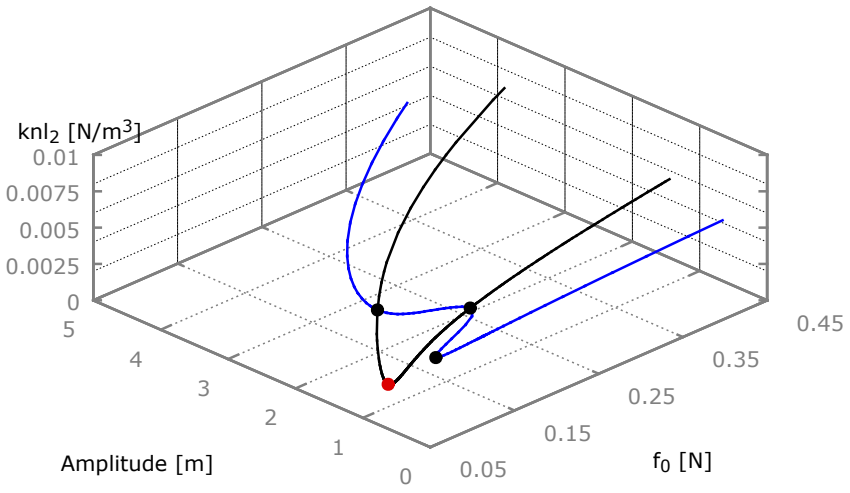

(a) 3D-Continuation of the birth and merging of IS

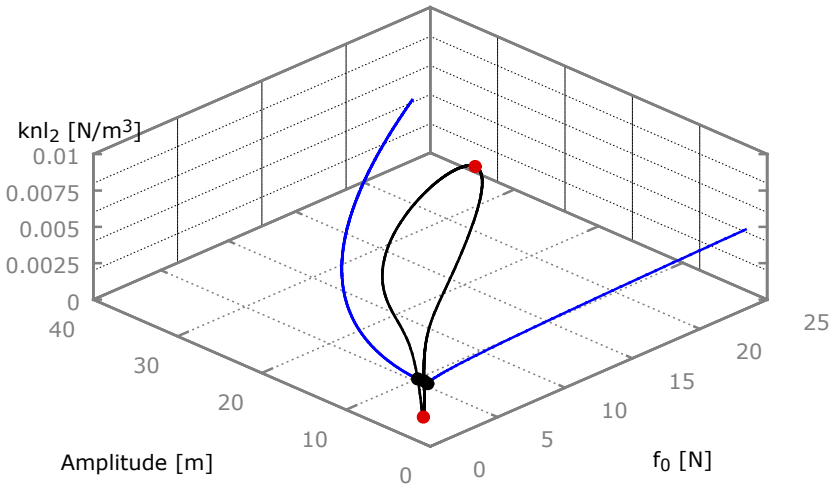

(b) 3D-Continuation of the birth and merging of IS (Extended view)

Figure 2.22 – 3D-Continuation of birth and merging points (1-extremum). LP (Blue), 1-extremum (Black), 2-extremum (Red)

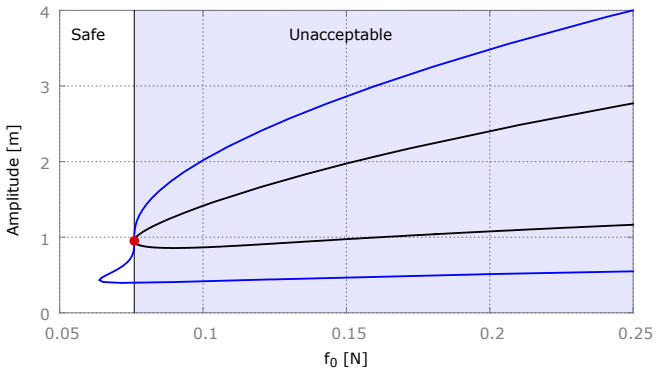

(a) LP curve for $knl_2 \approx 0.0017N/m^3$

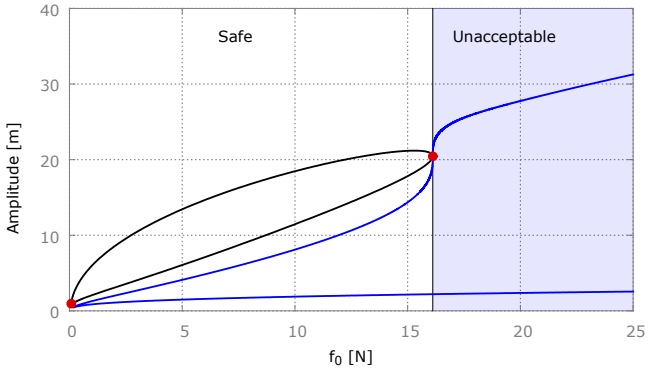

(b) LP curve for $knl_2 \approx 0.0076N/m^3$

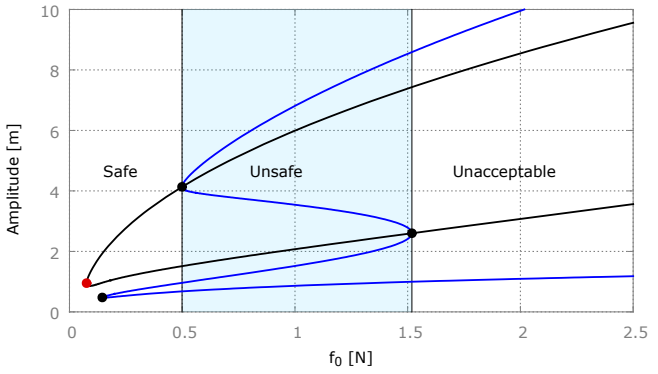

(c) LP curves for $knl_2 \approx 0.0068N/m^3$

Figure 2.23 – LP curves using parameters associated with the two 2-extremum points and the birth point at $f_0 = 0.5N$. LP (Blue), 1-extremum (Black), 2-extremum (Red)

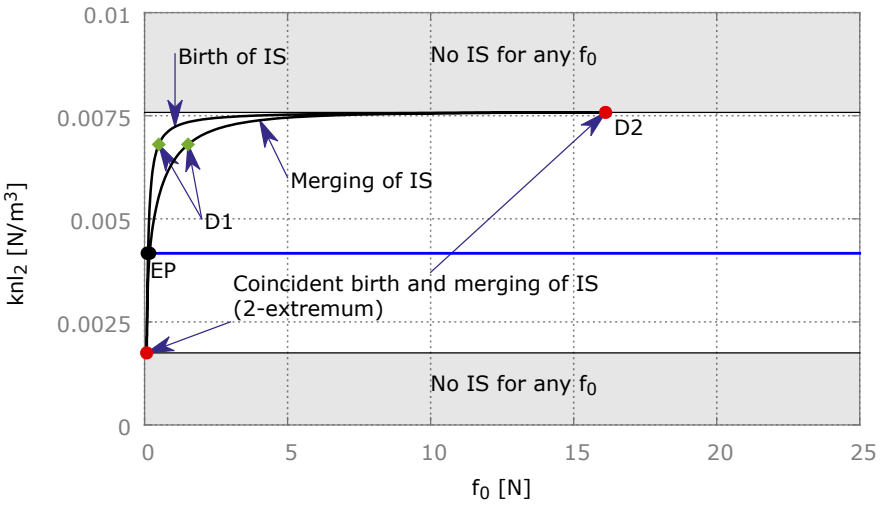

Figure 2.24 – Projection of the branch of birth and merging points (1-extremum). On the knl_2-f_0 LP (Blue) for $knl_2 \approx 0.0042N/m^3$, 1-extremum (Black), 2-extremum (Red)

the maximum of amplitude of the different designs. It can be observed in Fig. 2.25 that the equal peak design is the more efficient design before reaching its IS merging point. However, once the merging point of the equal peak design is crossed, the design with the set of parameters obtained for a birth point at $f_0 = 0.5N$ (Design #1) becomes more efficient. In the same way, once the merging point of the the design with the set of parameters obtained for a birth point at $f_0 = 0.5N$ is crossed, the design obtained at the 2-extremum at high amplitude of forcing (Design #2) becomes more efficient. As a results, the deisgn of the NLTVA can be optimized by appropriately choosing the value of knl_2 accordingly to the operating range of the forcing f_0.

2.3.3 Level-3 of continuation: continuation of the coincident birth and merging points of IS

At level 3 of the recursive continuation, the two 2-extremum points are tracked by considering the NLTVA damping coefficient c_2 as a new unknown in the extended system $\boldsymbol{G}_2(\boldsymbol{Y}_2, \alpha_2) = 0$. The subset of varying parameters at level 3 is then (f_0, knl_2, c_2). The resulting branch of 2-extremum points is plotted in Fig. 2.26. All the points of this branch provide a set of parameters (f_0, knl_2, c_2) for which the birth and merging of ISs are coincident (no "unsafe" region). The projections of this branch on the c_2-f_0 and c_2-knl_2 planes are displayed in Figs. 2.27a and 2.27b. Using the extended system (2.59) at level 3 $\boldsymbol{G}_3(\boldsymbol{Y}_3) = \boldsymbol{0}$, several 3-extremum points are detected on this branch. Two 3-extremum points with respect to c_2 and knl_2 are obtained for $(c_2 = 0.029Ns/m, knl_2 = 0.072N/m^3, f_0 = 1.03N)$ and $(c_2 = 0.0056Ns/m, knl_2 = -0.0022N/m^3, f_0 = 0.036N)$ respectively. The 3-extremum point with respect to c_2 (Design #3) represents the upper limit

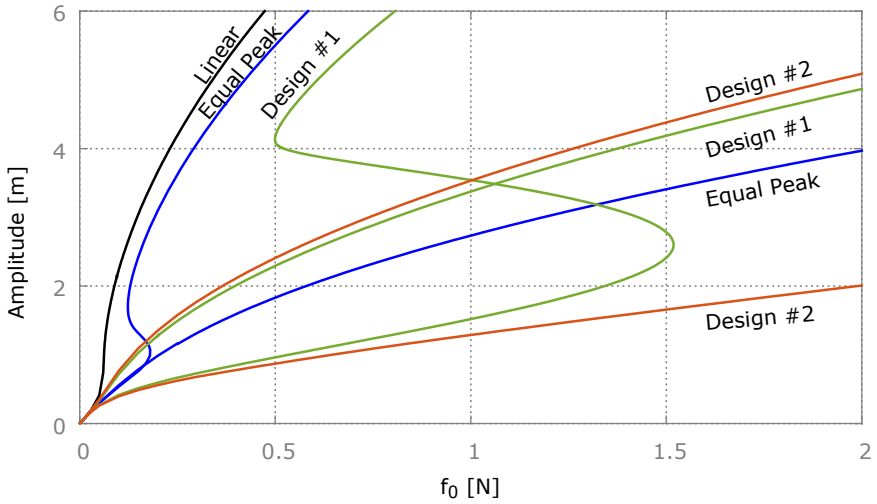

(a) Comparison of the maximum of amplitude.

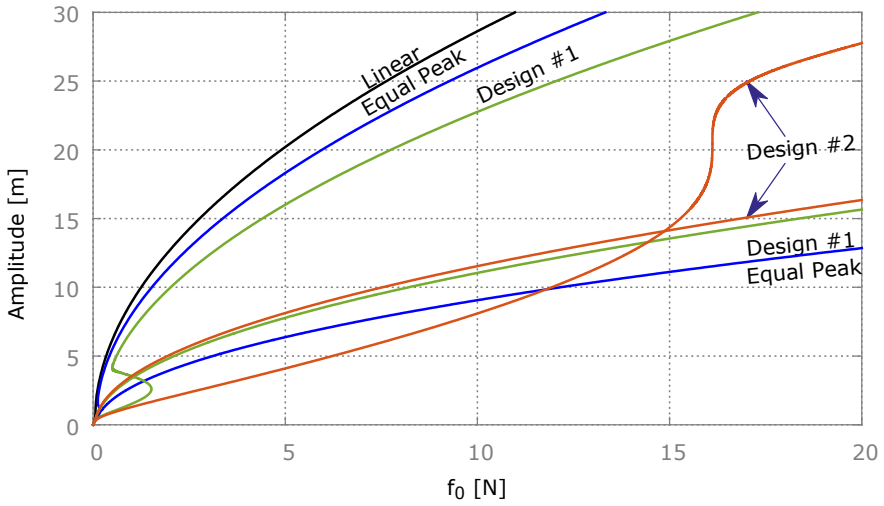

(b) Comparison of the maximum of amplitude (extended view).

Figure 2.25 – Continuation of the maximum of amplitude. Linear for $knl_2 = 0N/m^3$ (Black), Equal Peak for $knl_2 = 0.0042N/m^3$ (Blue), Design #1 for $knl_2 \approx 0.0068N/m^3$ (Green), Design #2 for $knl_2 \approx 0.0076N/m^3$ (Orange)

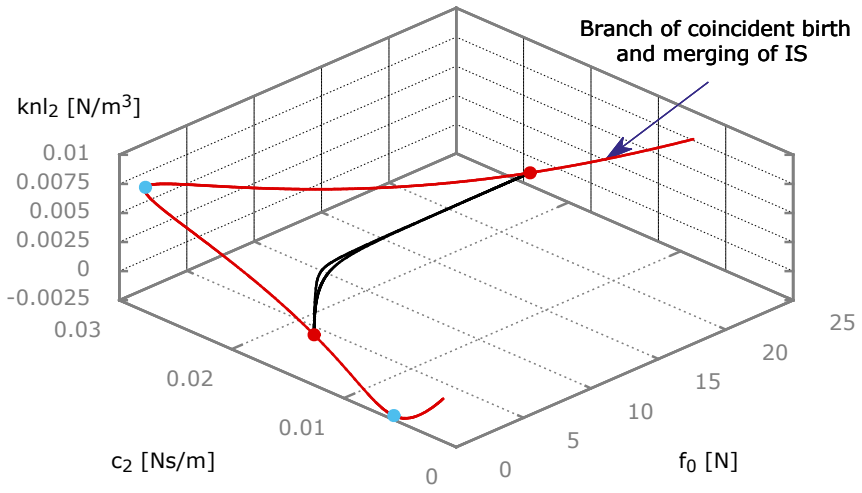

Figure 2.26 – Continuation of 2-extremum points. 1-extremum (Black), 2-extremum (Red), 3-extremum (Blue)

of existence of ISs with respect to c_2. Therefore, for $c_2 > 0.029e-2Ns/m$, there is no IS whatever the value of the other level 3 varying parameters (f_0, knl_2). In the same way, the 3-extremum point with respect to knl_2 (Design #4) represents the lower limit of existence of IS with respect to knl_2. Consequently, for $k_{nl2} < -0.0022N/m^3$, there is no IS whatever the value of the other level 3 varying parameters (f_0, c_2). However, the safe zone is very small on this case ($f_0 = 0N$ to $0.026N$) and the practical realization of such a negative stiffness is not a trivial task. Therefore, this design is not very attractive. For high values of f_0, the damping c_2 and nonlinear stiffness knl_2 coefficients tend to $c_2 = 0Ns/m$ and $knl_2 \approx 0.0076N/m^3$. The corresponding set of parameters is not usable since a system with zero damping is not efficient anymore and may not lead to a periodic solution over time. Above this asymptotic value of knl_2, there is no IS whatever the value of (f_0, c_2). It is noteworthy that the highest 2-extremum point of Fig. 2.27 is close to this asymptote value of knl_2. Therefore, the presence of ISs at this point is almost not influenced by the variation of c_2.

2.3.4 Suitability of the designs of interest

From the previous results, it appears that designs #1, #2 and #3 are potential good candidates for the optimization of the safe operating region of the NLTVA. The corresponding sets of parameters (f_0, knl_2, c_2) are indicated with labels 1, 2 and 3 in Fig. 2.27 and gathered in Tab. 2.2 in order to make their comparison easier. Here, the value of f_0 corresponds to the end of the safe region, i.e., either the birth of ISs (Design #1) or the coincident birth and merging of ISs (Designs #2 and #3). It can also be read as a measure of the width of the safe zone. The values of (knl_2, c_2) obtained with equal peak or with others designs have the same order of magnitude, while the operating range can be greatly

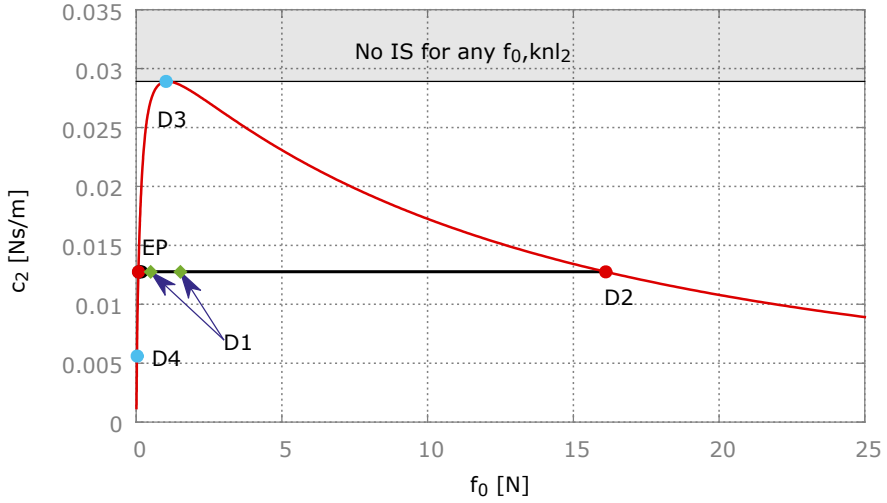

(a) Projection of the c_2-f_0 plane

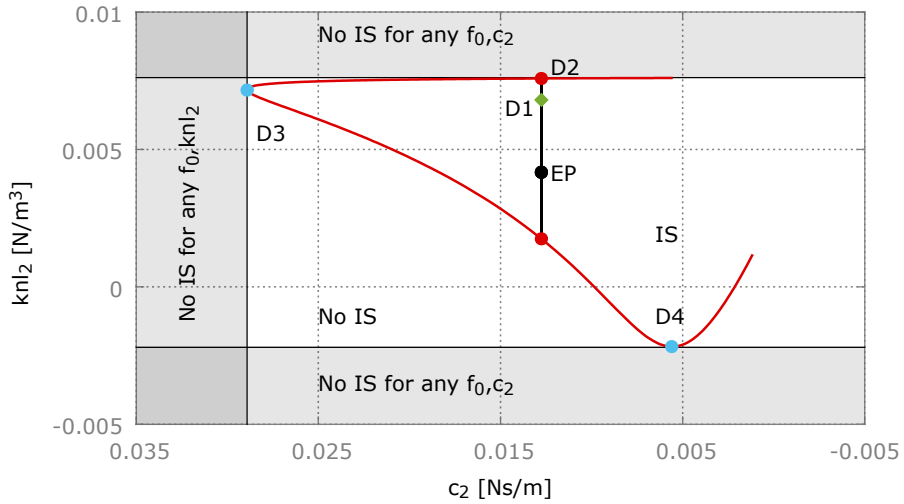

(b) Projection of the knl_2-c_2 plane

Figure 2.27 – Projections of the branch of 2-extremum points. 1-extremum (Black), 2-extremum (Red), 3-extremum (Blue)

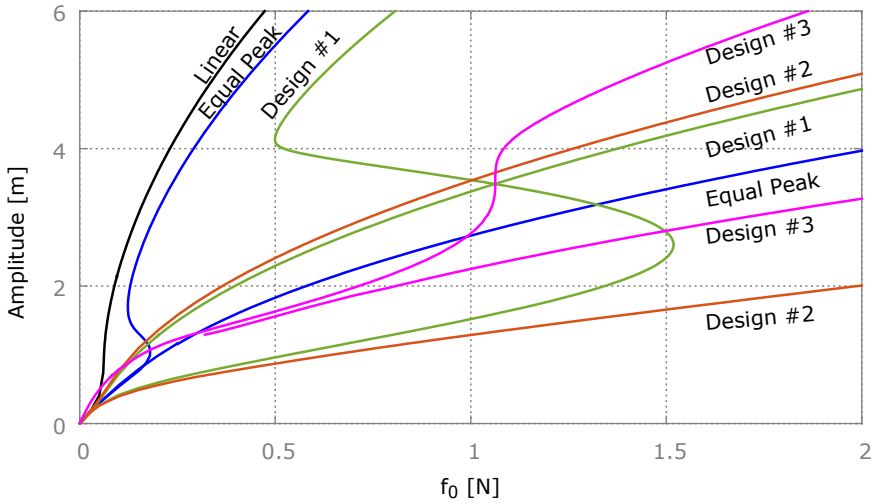

(a) Efficiency comparison of the retained designs

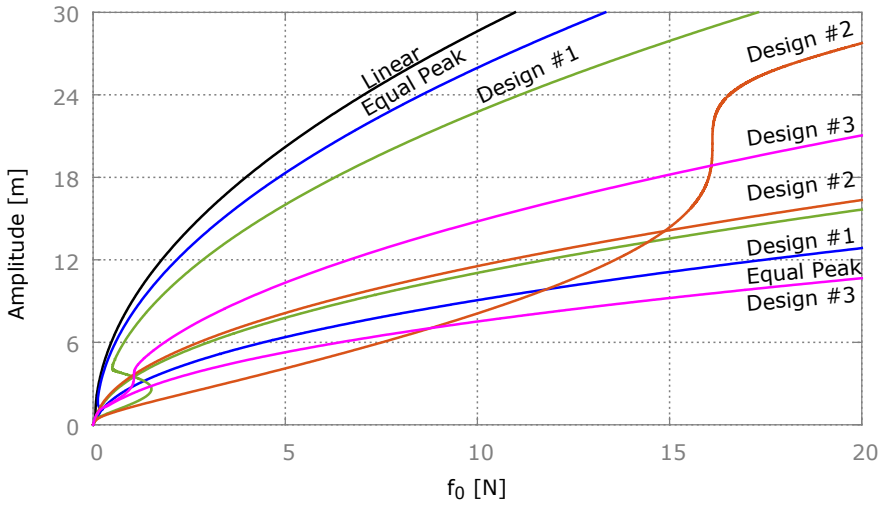

(b) Efficiency comparison of the retained designs (extended view)

Figure 2.28 – Linear for $knl_2 = 0N/m^3$ (Black), Equal Peak for $knl_2 = 0.0042N/m^3$ (Blue), Design #1 for $knl_2 \approx 0.0068N/m^3$ (Green), Design #2 for $knl_2 \approx 0.0076N/m^3$ (Orange), Design #3 for $(knl_2, c_2) \approx (0.0072N/m^3, 0.029Ns/m)$ (Purple)

	Equal Peak (Ref)	Design #1	Design #2	Design #3
$c_2[Ns/m]$	0.0128	0.0128 (idem)	0.0128(idem)	0.029 (+127%)
$k_{nl2}[N/m^3]$	0.042	0.0068 (+62%)	0.0076 (+81%)	0.0072 (+71%)
$f_0[N]$ at IS birth	0.12	0.5 ($\times$4)	16 ($\times$130)	0.12 ($\times$9)

Table 2.2 – Parameters comparison

increased.

The maximum of amplitude of the primary mass for these three designs is plotted in Fig. 2.28 together with the results of the linear vibration absorber ($knl_2 = 0$) and the NLTVA with equal peak design. It is used to assess the efficiency of the absorber with the tested designs.

Form this figure, it can be concluded that the equal peak design is the most efficient one in the range of $f_0 = [0N - 0.12N]$, i.e., in its safe region as defined in Fig. 2.19. Above $f_0 = 0.12N$, the other designs are much more efficient. Design #2 seems superior to design #1 because its gives almost the same amplitude but has a much wider safe region (up to $f_0 = 16N$ instead of $0.5N$) while decorrelating the birth of IS from the damping coefficient c_2. Finally, design #3 might be considered as the best compromise since it provides the lowest amplitude in its safe region up to $f_0 = 1.03N$ while decorrelating the birth of IS from the nonlinear stiffness coefficient knl_2. In comparison with the equal peak design, its safe region is 9 times wider. However, this design has worse performance in the range $f_0 = [0N - 0.1N]$. A way to improvement may consist in using hybrid active/passive control to switch from one design to another one depending on the value of forcing amplitude.

To sum up, the multi-parametric recursive continuation method provides useful information by exploring the topology of the NLTVA ISs such as extremum points and zones of existence. The tested designs have a larger safe region leading to a larger operating range. Moreover, their vibration absorption efficiency is better than the equal peak design for high values of forcing. Designs #2 and #3 provide robustness by limiting the influence of c_2 and knl_2 respectively on the presence of IS. Design #3 is particularly interesting because the appearance of ISs is decorrelated from the nonlinear stiffness coefficient knl_2 while keeping a better efficiency than other designs for high amplitudes of forcing. A perspective for improving the NLTVA would be to track LP curve with respect to the mass ratio ε under equal peak constraints.

2.4 Conclusion

In this Chapter, parametric analysis methods for nonlinear system have been presented. First, the detection, localization and tracking of codimention-1, R1 and LPNS bifurcations have presented. Then, the bifurcation tracking method has been applied to a NLTVA and a Jeffcott rotor. The dynamics of both systems have been analyzed with respect to a single

system parameter. For the NLTVA, the evolution of LP and NS have been computed with respect to the amplitude of forcing as varying parameter. In the Jeffcott rotor, the LP and NS bifurcations have been tracked with respect to the dry friction coefficient. The detection of codimension-2 bifurcations along the curve of codimension-1 bifurcations, such as LP and NS, has given additional information about the dynamic of the system.

Secondly, an original and efficient multi-parametric recursive continuation algorithm is proposed. The method is based on a characterization of extremum point with a constraint equation adapted for continuation process and for recursive characterization of extremum point in increasing codimension. By applying the algorithm to a specific point of a system, its topology and all its extremum are obtained with respect to the chosen parameters. The information obtained with topological exploration can then be used to optimize the system.

The algorithm then is applied to a NLTVA to explore the topology of IS, delimit the zone of existence of IS and improve the efficiency of the vibration absorber. The obtained results allows to visualize the topology of the NLTVA's IS with respect to the amplitude of the force, the nonlinear stiffness and the damping coefficients. Many information are provided such as the topology of ISs, its extremum points and the limits of existence of IS. By using sets of parameters obtained at certain points of interest, the unsafe region can be minimized, the IS can be pushed at high amplitude of forcing and the birth of IS can be decorrelated from certain system parameters leading to a more robust vibration absorber with larger operating range and better absorption efficiency at high amplitude of forcing. As a conclusion, the proposed method improves the efficiency of the NLTVA while making the system more robust to the IS.

As a conclusion, an original and efficient method for parametric analysis is provided. The method can perform parameter analysis with respect to multiple system parameter. Moreover, the method can be applied to any point of any nonlinear system that can be properly characterized. By applying the method to the NLTVA, the evolution of IS with respect to several parameters has been uncovered leading to a robustification and optimization of the system.

Chapter 3

Nonlinear Normal Modes and a generalization to non-conservative systems

This chapter presents a new method to compute Nonlinear Normal Modes (NNMs) and analyze their stability and bifurcations points using HBM. In order to compute the NNMs, a frequency phase condition and a quasi-null damping coefficient are introduced. The formulation is extended to non-conservative NNMs by considering conservative equations characterizing the phase and energy resonances. Then, the topic of energy balance is addressed and the concept of fictive force is introduced with respect to the considered non-conservative NNM. Secondly, the computation of NNM stability and bifurcations is performed with a shifted quadratic eigenvalue problem (QEP). Thirdly, the NNM computation is applied to a 2-ddl system under various designs. NNMs and bifurcations points are analyzed in light of underlying symmetries. LP continuation is performed to compute and analyze the evolution of isolated NNMs that appear due to symmetry breaking. Then, specific points onto at a given level of energy of resonance are targeted with the help of the fictive force. The accuracy of the method is discussed with respect to truncation of the fictive force. Finally, the theory behind the energy resonance NNM is validated on a system with cubic nonlinear damping.

Contents

This chapter builds on the previous chapters to address method of computation for conservative and non-conservative NNMs, their stability and bifurcations based on HBM.

In section 3.1, the continuation method is explained. A phase condition in the frequency domain, based on the integral of the scalar product of the velocity and displacement vectors, is introduced. Then a parameter of relaxation is added to the autonomous differential equation. In Section 3.2, the topic of non-conservative NNMs is addressed. Non-conservative NNMs are characterized using a conservative equation obtained with direct extension of linear modal analysis to the nonlinear domain. Two characterizations of non-conservative NNMs are proposed: the phase resonance and the energy resonance. The energy balance associated to non-conservative NNMs is introduced via the concept of the so-called fictive force. In Section 3.3, a method to perform linearized stability analysis based on a shifted quadratic eigenvalue problem (QEP) is proposed. The two singular eigenvalues originating from the undetermined phase are translated in order to compute the stability of non-autonomous ODEs. In Section 3.4, the bifurcation analysis is performed with respect to this modified QEP. By using augmented systems, bifurcations can be localized and continuated. Finally, in Section 3.5, the method is applied to a 2-ddls system with respect to several designs. The NNMs computed with the first design exhibit various complex dynamical phenomena such as change of stability, bifurcation points, tongues of modal interactions. The topology of the obtained NNMs is analyzed under the light of an underlying symmetry. With the second design, the system presents a geometrical symmetry. The NNMs are then computed and analyzed before and after a simulated symmetry breaking event. It is shown that it is possible to branch onto isolated NNMs (INNMs) by using a LP tracking method along a free varying parameter that breaks the geometrical symmetry of the system. Afterwards, non-conservative designs are considered. First, a design with viscous damping is used to assess the required accuracy for the fictive force to target specific points of NNMs such as points or orbits of modal interaction. Then, a system with cubic nonlinear damping is used to analyze the performance of the energy resonance method.

The originality of this work lies in the theory used to compute the NNMs, their stability and bifurcations using HBM. Moreover, it opens several perspectives of use such as experimental tracking of NNM with the help of the fictive force and the detection of INNMs and ISs.

3.1 NNM computation method using HBM

Let's consider the nonlinear dynamical system with n degrees of freedom (DOFs) of Eq. (1.5). To compute the NNMs, the forcing vector is taken equal to zero, i.e., $\boldsymbol{F} = 0_L$ in order to obtain the following autonomous equation.

$$\boldsymbol{R}(\boldsymbol{X}, \omega) = \boldsymbol{Z}(\omega)\boldsymbol{X} + \boldsymbol{F}_{nl}(\boldsymbol{X}, \omega) = \boldsymbol{0}_L \tag{3.1}$$

To obtain a periodic solution differs from the trivial one $X = \boldsymbol{0}_L$, two more steps are necessary. The first step consists in imposing a phase condition to insure the uniqueness

of the periodic solution. Then, to relax the equation of motion, a fictive energy has to be injected into the system.

3.1.1 Phase Condition

NNMs are solutions of an autonomous nonlinear equation of motion (3.1) which is invariant under the temporal translation transformation:

$$\begin{array}{rccc} \widehat{\boldsymbol{x}} & : & \mathbb{R}^2 & \rightarrow & \mathbb{R} \\ & & (\boldsymbol{x}(t),\Delta t) & \mapsto & \boldsymbol{x}(t+\Delta t) \end{array} \tag{3.2}$$

Therefore, if $\boldsymbol{x}(t)$ is solution, then $\boldsymbol{x}(t+\Delta t)$ is also solution for any Δt. In the time domain, the symmetry of temporal translation of the equation causes the non-uniqueness of the solution. However, with the HBM, time is replaced by frequency. Therefore, the expression of temporal translation symmetry is modified. Let's explicit the invariant transformation $\widehat{\boldsymbol{X}}$ in the frequency domain, $\widehat{\boldsymbol{X}}(\boldsymbol{X},\Delta t)$ being the vector of Fourier coefficients of the translated displacement $\boldsymbol{x}(t+\Delta t)$.

$$\begin{array}{rcl} \boldsymbol{x}(t+\Delta t) & = & \widehat{\boldsymbol{X}}^0(\boldsymbol{X},\Delta t)+\sum_{k=0}^{H}\widehat{\boldsymbol{X}}_c^k(\boldsymbol{X},\Delta t)\cos(k\omega t)+\widehat{\boldsymbol{X}}_s^k(\boldsymbol{X},\Delta t)\sin(k\omega t) \\ & = & (\mathscr{B}(\omega t)\otimes \boldsymbol{I}_n)\widehat{\boldsymbol{X}}(\boldsymbol{X},\Delta t) \\ \boldsymbol{x}(t+\Delta t) & = & \boldsymbol{X}^0+\sum_{k=0}^{H}\boldsymbol{X}_c^k\cos(k\omega(t+\Delta t))+\boldsymbol{X}_s^k\sin(k\omega(t+\Delta t)) \\ & = & \boldsymbol{X}^0+\sum_{k=0}^{H}\boldsymbol{X}_c^k(\cos(k\omega t)\cos(k\omega\Delta t)-\sin(k\omega t)\sin(k\omega\Delta t)) \\ & & +\boldsymbol{X}_s^k(\cos(k\omega t)\cos(k\omega\Delta t)+\sin(k\omega t)\sin(k\omega\Delta t)) \\ & = & (\mathscr{B}(\omega t)\otimes \boldsymbol{I}_n)(Rot(\Delta t)\otimes \boldsymbol{I}_n)\boldsymbol{X} \end{array} \tag{3.3}$$

So for periodical solutions, the invariant transformation becomes the following:

$$\begin{array}{rccc} \widehat{\boldsymbol{X}} & : & \mathbb{R}^2 & \rightarrow & \mathbb{R} \\ & & (X,\Delta t) & \mapsto & (Rot(\Delta t)\otimes \boldsymbol{I}_n)\boldsymbol{X} \end{array} \tag{3.4}$$

with

$$\begin{array}{rcl} Rot(\Delta t) & = & \mathrm{diag}(\mathbf{1},Rot_1(\Delta t),...,Rot_j(\Delta t),...,Rot_H(\Delta t)) \\ Rot_j(\Delta t) & = & \begin{bmatrix} cos(j\omega\Delta t) & -sin(j\omega\Delta t) \\ sin(j\omega\Delta t) & cos(j\omega\Delta t) \end{bmatrix} \end{array} \tag{3.5}$$

So in the frequency domain, the equation of motion (3.1) is invariant under the transformation $\widehat{\boldsymbol{X}}$ (3.4). The resulting non-uniqueness of the solution can be interpreted as an undetermined phase of the periodical solution that generates a singularity in the jacobian

$\boldsymbol{R_X}$. In order to determine the eigenvector associated with the singularity, the first variation of the equation of motion (3.1) under the invariant transformation $\widehat{\boldsymbol{X}}$ (3.4) is written at fixed ω and at $\Delta t = 0$:

$$\begin{aligned}
&\boldsymbol{R}_{\widehat{\boldsymbol{X}}}\big|_{\Delta t=0} \left.\frac{\partial \widehat{\boldsymbol{X}}(X,\Delta t)}{\partial \Delta t}\right|_{\Delta t=0} + \boldsymbol{R}_{\Delta t} &&= 0 \\
&\boldsymbol{R}_{\widehat{\boldsymbol{X}}}\big|_{\Delta t=0} \left.\frac{\partial \widehat{\boldsymbol{X}}(X,\Delta t)}{\partial \Delta t}\right|_{\Delta t=0} &&= 0 \\
&\boldsymbol{R}_{\widehat{\boldsymbol{X}}}\big|_{\Delta t=0} \left(\left.\frac{\partial \mathrm{Rot}(\Delta t)}{\partial \Delta t}\right|_{\Delta t=0} \otimes \boldsymbol{I}_n\right) \boldsymbol{X} &&= 0 \\
&\boldsymbol{R}_{\boldsymbol{X}} \left(-\omega \nabla \otimes \boldsymbol{I}_n\right) \boldsymbol{X} &&= 0
\end{aligned} \tag{3.6}$$

So due to the invariance under the transformation $\widehat{\boldsymbol{X}}$, $\boldsymbol{R_X}$ is singular with $\bar{\varphi_1} = (\nabla \otimes \boldsymbol{I}_n)\boldsymbol{X}$ as eigenvector. Thus, one phase condition $g(\boldsymbol{X})$ must be introduced in order to impose the phase and therefore the uniqueness of the solution. A simple phase condition can be obtained by imposing a Fourier coefficient equal to zero (3.7) as follows:

$$g(\boldsymbol{X}) = \boldsymbol{X}(i) = 0 \tag{3.7}$$

However, this phase condition does not minimize the profile of the solution $\boldsymbol{X}$ between two steps of continuation. Therefore, using a phase condition based on fixed Fourier coefficient leads to a drift of the phase along the curve. This phase drift can make the analysis of solutions more complex, can generate numerical problems at some specific points such as modal interactions and can increase the computational time.

For example, in the case of a cubic nonlinearity, imposing the amplitude of $\cos(3\omega t)$ equal to zero will be problematic if the initialisation of the NNM is made using the first harmonic $cos(\omega t)$. Indeed $cos(\omega t)^3 = \frac{3}{4}cos(\omega t) + \frac{1}{4}\cos(3\omega t)$, therefore setting the amplitude of $\cos(3\omega t)$ equal to zero will make the continuation diverge. Thus, a more general phase condition is needed in order to work independently from the nonlinearities and to provide a solution easy to interpret. To fulfill these requirements, Seydel [SEY 09] proposed the following phase condition in time domain based on the one implemented in AUTO [DOE 81]:

$$g(\dot{\boldsymbol{x}}(t), x(t)) = \int_0^T \boldsymbol{x}_{j-1}(t)^T \dot{\boldsymbol{x}}(t) dt = 0 \tag{3.8}$$

where x_{j-1} is the displacement vector at the end of the previous continuation step. This phase condition $g(\dot{x}(t), x(t))$ can be transposed from the temporal domain to the frequency one. The obtained phase condition $g(\boldsymbol{X})$ in the frequency domain will be the one used in this work:

$$g(\dot{x}(t), x(t)) = \int_0^T x_{j-1}(t)^T \dot{x}(t) dt = 0 \quad \Longrightarrow \quad g(\boldsymbol{X}) = \boldsymbol{X}_{j-1}^T (\boldsymbol{\nabla} \otimes \boldsymbol{I}_n) \boldsymbol{X} = 0 \tag{3.9}$$

This phase condition minimise the change of phase between two consecutive steps of continuation. By keeping the profile of the solution the closest to the former one, the numerical continuation is robustified and the analysis of the curves is made easier. Thanks to

the integral formulation of the phase condition, numerical problems that could be encountered at modal interaction have been removed. Moreover, one can note that the derivative $g_{\boldsymbol{X}}$ is equal to the eigenvector $\bar{\boldsymbol{\varphi}}_1$ (3.6). So, another way to understand the phase condition would be to impose the evolution of the component of $\boldsymbol{X}$ along $\bar{\boldsymbol{\varphi}}_1$ to zero and thus restoring the uniqueness of the solution for whatever the values of the parameters $(\boldsymbol{X}, \omega)$.

3.1.2 Equation of motion regularized by injecting fictive energy

By constraining the nonlinear equation of motion with the proposed phase condition, the uniqueness of the solution has been restored. However, such a system is overconstrainted and posses a non square Jacobian. To perform to the continuation of such a augmented system, the method proposed by Munoz-Almaraz [MUN 03, ARQ 06] is used. This method introduces a non-conservative fictive energy $\boldsymbol{e}_{fic}$ proportional to an relaxation parameter μ into the equation of motion (1.5) in order to obtain a well posed problem.

$$\boldsymbol{M}\ddot{\boldsymbol{x}}(t) + \mu \boldsymbol{e}_{fic}(\dot{\boldsymbol{x}}) + \boldsymbol{K}\boldsymbol{x}(t) + \boldsymbol{f}_{nl}(\boldsymbol{x}, \dot{\boldsymbol{x}}) = \boldsymbol{0}_n \tag{3.10}$$

One can see that the equation of motion is no longer conservative if $\mu \neq 0$. To obtain a periodic solution the input and output of energy have to balance each other. Therefore the relaxation parameter μ in the nonconservative term must converge to zero at a periodic solution [MUN 03]. Thus, the conservative property and the invariant manifold of the equation (1.5) are unchanged while permitting the system to be well posed. Then, by applying the HBM as in Subsection 3.1, the modified equation of motion in frequency domain is obtained:

$$\boldsymbol{R}(\boldsymbol{X}, \omega, \mu) = \boldsymbol{Z}(\omega)\boldsymbol{X} + \boldsymbol{F}_{nl}(\boldsymbol{X}, \omega) + \mu \boldsymbol{E}_{fic}(\boldsymbol{X}) = \boldsymbol{0}_L \tag{3.11}$$

For continuation purpose, the form of the fictive energy is not important as long as it is non-conservative. However during bifurcation analysis the jacobian of the augmented system is used. Therefore, the form of the fictive energy $\boldsymbol{E}_{fic}$ has to be taken equal to the eigenvector $\bar{\boldsymbol{\varphi}}_1$ to leave the eigenvectors and their associated eigenvalues unchanged.

$$\boldsymbol{E}_{fic} = (\boldsymbol{\nabla} \otimes \boldsymbol{I}_n)\, \boldsymbol{X} \tag{3.12}$$

With this form of fictive energy, the derivative $\boldsymbol{R}_\mu$ with respect to the parameter of relaxation μ will be equal to $g_{\boldsymbol{X}}$ at the beginning of each continuation step. Therefore, the Jacobian of the augmented system composed of the phase condition and the fictive energy has only its trivial singularity regularized.

3.1.3 Initialization and continuation

The NMMs are initialized from the LNMs. A linear modal analysis is performed using the Jacobian $\boldsymbol{R}_{\boldsymbol{X}}$ of equation (3.11) at $\boldsymbol{X} = 0_L$. ω represents the frequency of the linear normal mode and ϕ corresponds to the shape of the linear normal mode. Due to the

undetermined phase, two eigenvectors respectively composed of cos terms and of sin terms are found. Then, the NNM calculation is initialized by branching along the chosen linear normal mode. In the rest of the thesis, all initializations will be made along the eigenvector composed of cos terms.

$$(\omega^2 \nabla^2 \otimes \boldsymbol{M} + \boldsymbol{I}_{2H+1} \otimes \boldsymbol{K})\phi = 0 \tag{3.13}$$

Once the solution have been initialized, the continuation of the NNM can be performed. For the purpose, the following augmented system containing both the phase condition (3.9) and the regularized nonlinear equation of motion (3.11) is used.

$$\begin{bmatrix} \boldsymbol{R}(\boldsymbol{X}, \omega, \mu) \\ g(\boldsymbol{X}) \end{bmatrix} = \begin{bmatrix} \boldsymbol{Z}(\omega)\boldsymbol{X} + \boldsymbol{F}_{nl}(\boldsymbol{X}, \omega) + \mu E_{fic} \\ \boldsymbol{X}_j^* (\boldsymbol{\nabla} \otimes \boldsymbol{I}_n) \boldsymbol{X}_{j-1} \end{bmatrix} = \begin{bmatrix} \boldsymbol{0}_{2H+1} \\ 0 \end{bmatrix} \tag{3.14}$$

The pseudo-arc length continuation method uses a predictor-corrector scheme. The prediction consists in adding a predictive tangent step to the solution in order to approximate the next solution along the curve. Then iterative orthogonal corrections are made using a Newton-Raphson algorithm to get back onto the curve. To perform the prediction, a system is solved to obtain the tangent vector $(\Delta \boldsymbol{X}_j, \Delta\omega_j, \Delta\mu_j)$. The Jacobian called $\boldsymbol{J}_{NNM}$ is composed of the Jacobian of the augmented system (3.14) plus the tangent predictor of the previous step $j-1$ on the last row. The resolution is made as follows:

$$\boldsymbol{J}_{NNM} \begin{bmatrix} \Delta \boldsymbol{X}_j \\ \Delta\omega_j \\ \Delta\mu_j \end{bmatrix} = \begin{bmatrix} \boldsymbol{R}_{\boldsymbol{X}} & \boldsymbol{R}_\omega & \boldsymbol{R}_\mu \\ g_{\boldsymbol{X}} & 0 & 0 \\ \Delta \boldsymbol{X}_{j-1} & \Delta\omega_{j-1} & \Delta\mu_{j-1} \end{bmatrix} \begin{bmatrix} \Delta \boldsymbol{X}_j \\ \Delta\omega_j \\ \Delta\mu_j \end{bmatrix} = \begin{bmatrix} \boldsymbol{0}_L \\ 0 \\ 1 \end{bmatrix} \tag{3.15}$$

Then the tangent vector is multiplied by a step length s and added to the starting point:

$$\begin{pmatrix} \boldsymbol{X}_j^1 \\ \omega_j^1 \\ \mu_j^1 \end{pmatrix} = \begin{pmatrix} \boldsymbol{X}_j^0 \\ \omega_j^0 \\ \mu_j^0 \end{pmatrix} + \Delta s \begin{pmatrix} \Delta \boldsymbol{X}_j \\ \Delta\omega_j \\ \Delta\mu_j \end{pmatrix} \tag{3.16}$$

During the second phase, the corrections are computed orthogonaly to the tangent as follows:

$$\begin{bmatrix} \boldsymbol{R}_X & \boldsymbol{R}_\omega & \boldsymbol{R}_\mu \\ g_{\boldsymbol{X}} & 0 & 0 \\ \Delta \boldsymbol{X}_j & \Delta\omega_j & \Delta\mu_j \end{bmatrix} \begin{bmatrix} \delta \boldsymbol{X} \\ \delta\omega \\ \delta\mu \end{bmatrix} = - \begin{bmatrix} \boldsymbol{R} \\ g \\ 0 \end{bmatrix} \tag{3.17}$$

At each iteration k the unknowns are incremented until the residue is smaller than a user-specific accuracy ε.

$$\begin{pmatrix} \boldsymbol{X}_j^{k+1} \\ \omega_j^{k+1} \\ \mu_j^{k+1} \end{pmatrix} = \begin{pmatrix} \boldsymbol{X}_j^k \\ \omega_j^k \\ \mu_j^k \end{pmatrix} + \Delta s \begin{pmatrix} \delta \boldsymbol{X}_j^k \\ \delta\omega_j^k \\ \delta\mu_j^k \end{pmatrix} \tag{3.18}$$

3.2 Generalization of Nonlinear Normal Modes to non-conservative systems

For a usual damping of a few percents, conservative and non-conservative NNMs give almost the same results. However, for higher values of equivalent damping, the obtained NNMs are different and the calculation method has to be chosen appropriately. Moreover, when the damping is nonlinear, a high damping can be obtained at high amplitudes of oscillations. Therefore, efficient methods to compute non-conservative NNMs are needed.

In the literature, some researches concern the influence of damping on the NNM. In [KUE 15], an energy balance is applied to conservative NNMs to explore the connection between NNMs and damped frequency responses. Others researchers take non-conservative NNMs as periodical solutions at iso-energy level. To obtain periodical solutions without losses of energy, an input of energy must be added to the equation. Krack proposed to insure energy balance by introducing a fictive negative damping [KRA 15]. The corresponding energy added to the NNM equation must not modify the non-conservative energy.

In order to obtain the exact energy to be injected in the system, the following approach is used. The conservative part of the nonlinear forces is first discriminated from the non-conservative one. Secondly, Phase and Energy resonances are computed directly from equations properties. The resulting equations characterizing the non-conservative NNMs are conservative. Therefore, standard methods for NNM computation can be used. To link the non-conservative resonances with frequency-responses, a fictive force $\boldsymbol{F}_{fic}$ is introduced. This fictive force can be seen as the input of energy needed to insure the energy balance of the non-conservative equations of motion. Moreover, this fictive force can be used to target a chosen NNM with a forced response.

3.2.1 Characterization of conservative and non-conservative forces

An energy balance is used to characterize the conservative and non-conservative parts of the nonlinear forces. To obtain non-conservative NNMs, the nonlinear force $\boldsymbol{f}_{nl}$ has to be separated into conservative $\boldsymbol{f}_{nlc}$ and non-conservative $\boldsymbol{f}_{nlnc}$ nonlinear forces. To discriminate such forces, an energy balance is made on the equation of motion. We use the fat that viscous damping is a pure dissipating force and the terms associated with the mass and the stiffness are pure conservative forces. A conservative force is characterized by the following property:

$$\begin{aligned} & \int_0^T \dot{\boldsymbol{x}}^* \boldsymbol{f}_{nl}(\boldsymbol{x},\dot{\boldsymbol{x}})dt = 0 \\ \Leftrightarrow \quad & \int_0^{T(1-a)} \dot{\boldsymbol{x}}^* \boldsymbol{f}_{nl}(\boldsymbol{x},\dot{\boldsymbol{x}})dt = \int_0^{Ta} \dot{\boldsymbol{x}}^* \boldsymbol{f}_{nl}(\boldsymbol{x},-\dot{\boldsymbol{x}})dt = 0 \end{aligned} \tag{3.19}$$

with $a \in [0,1]$. For periodic solutions, only $a = \frac{1}{2}$ and forces symmetric with respect to the speed vector $\dot{\boldsymbol{x}}$ are solutions to Eq. (3.19). Therefore, the nonlinear force $\boldsymbol{f}_{nl}$ can be separated into non-conservative $\boldsymbol{f}_{nlnc}$ and conservative $\boldsymbol{f}_{nlc}$ nonlinear forces represented

respectively by the following symmetric and anti-symmetric functions:

$$\boldsymbol{f}_{nl} = \boldsymbol{f}_{nlc} + \boldsymbol{f}_{nlnc} \quad \text{with} \quad \left[\begin{array}{l} \boldsymbol{f}_{nlc} = \frac{1}{2}\left(\boldsymbol{f}_{nl}(\boldsymbol{x},\dot{\boldsymbol{x}}) + \boldsymbol{f}_{nl}(\boldsymbol{x},-\dot{\boldsymbol{x}})\right) \\ \boldsymbol{f}_{nlnc} = \frac{1}{2}\left(\boldsymbol{f}_{nl}(\boldsymbol{x},\dot{\boldsymbol{x}}) - \boldsymbol{f}_{nl}(\boldsymbol{x},-\dot{\boldsymbol{x}})\right) \end{array} \right. \tag{3.20}$$

The conservative and non-conservative parts of the equation of motion are then introduced as:

Now that conservative and non-conservative terms have been separated, the non-conservative NNMs can be characterized.

3.2.2 Phase resonance

In this subsection, the non-conservative NNM corresponding to the phase resonance is presented. The phase ϕ between the damped NNM $\boldsymbol{X}$ and the forcing vector $\boldsymbol{F}$ of Eq. (1.5) is calculated:

$$\phi = \arctan\left(\frac{((\nabla_{bis}\otimes \boldsymbol{I}_n)\boldsymbol{X})^T(\boldsymbol{R}_{nc})}{\boldsymbol{X}^T(\boldsymbol{R}_c)}\right) \quad \text{with} \quad \nabla_{bis} = \begin{bmatrix} 0 & \boldsymbol{0}_{1\times 2L} \\ \boldsymbol{0}_{2L\times 1} & \boldsymbol{I}_H \otimes \begin{bmatrix} 0 & -1 \\ -1 & 0 \end{bmatrix} \end{bmatrix} \tag{3.21}$$

with $(\boldsymbol{R}_c, \boldsymbol{R}_{nc})$ representing the conservative and non-conservative part of Eq. (1.5) calculated in Eq. (3.20). In order to have a phase resonance, $\boldsymbol{X}^T(\boldsymbol{R}_c)$ has to be equal to zero with $\boldsymbol{X}^T(\boldsymbol{R}_{nc}) \neq 0$. Since $\boldsymbol{X} \neq 0$, the equation corresponding to the Phase resonance is obtained (3.22).

$$\boldsymbol{R}_\phi = \left(\omega^2\nabla^2 \otimes \boldsymbol{M} + \boldsymbol{I}\otimes\boldsymbol{K}\right)\boldsymbol{X} + \boldsymbol{F}_{nlc} = \boldsymbol{0}_L \tag{3.22}$$

One can note that Eq. (3.22) corresponds to the classical equation used to calculate undamped unforced NNMs of an equation with viscous damping. Since Eq. (3.22) is autonomous, methods for conservative NNMs computation, presented in Section 3.1, can be used to compute the non-conservative NNMs.

3.2.3 Energy resonance

In this subsection, the non-conservative NNM corresponding to the energy resonance is presented.

Characterization of the energy resonance Let's make the hypothesis that at the energy resonance, all the energy related to the displacement $\boldsymbol{X}$ is provided by the wanted non-conservative NNM $\boldsymbol{X}_E$, resulting in $\boldsymbol{X} = \boldsymbol{X}_E$. The energy resonance occurs when:

$$\frac{\partial \boldsymbol{X}^T\boldsymbol{X}}{\partial \omega} = 0 \tag{3.23}$$

First, the Eq. (1.5) is conventionally rewritten as:

$$\boldsymbol{Z}\boldsymbol{X} + \boldsymbol{F}_{nl} = (\boldsymbol{Z} + \mathbf{MatF_{nl}})\boldsymbol{X} = \boldsymbol{A}\boldsymbol{X} = \boldsymbol{F} \tag{3.24}$$

with $\boldsymbol{A}$ a matrix such that $\boldsymbol{AX} - \boldsymbol{F} = \boldsymbol{R}$ and $\mathbf{MatF_{nl}} = \mathbf{MatF_{nl}}_c + \mathbf{MatF_{nl}}_{nc}$. The matrices $(\mathbf{MatF_{nl}}_c, \mathbf{MatF_{nl}}_{nc})$ do not need to be calculated since they will not be used in the characterizing equation obtained at the end of the development. After some calculation explain in Annexes 4.5, the equation characterizing the energy resonance is obtained:

$$\boldsymbol{R}_E = \left(\left(\omega^2 \nabla^2 \otimes \boldsymbol{M} + \boldsymbol{I} \otimes \boldsymbol{K}\right) \boldsymbol{X} + \left(\boldsymbol{F}_{nlc}\right)\right) - \frac{1}{2}\left(\nabla_1^2 \otimes \boldsymbol{M} + \frac{1}{2\omega}\frac{\partial (\mathbf{MatF_{nl}}_c^T)_1}{\partial \omega}\right)^{-1} \left(\nabla \otimes \boldsymbol{C} + \frac{\partial \mathbf{MatF_{nl}}_{nc}^T}{\partial \omega}\right)\left((\nabla \otimes \boldsymbol{C})\boldsymbol{X} + \frac{\boldsymbol{F}_{nlnc}}{\omega}\right) = \boldsymbol{0}_L \quad (3.25)$$

with ∇_1 and $(\mathbf{MatF_{nl}}_c^T)_1$ defined in Appendix 4.5. The calculation of the partial derivatives in Eq. (3.25) are presented in Appendix 4.5. Since Eq. (3.25) is autonomous, methods for conservative NNMs computation, presented in Section 3.1, can be used to compute the non-conservative NNMs.

Example 1: case of a viscous damping and a pure conservative forcing. In this case, the non-conservative part of the nonlinear forces is null and Eq. (3.25) is reduced to:

$$\boldsymbol{ZX} + \boldsymbol{F}_{nl} - \frac{1}{2}\left(\boldsymbol{I}_{2H+1} \otimes \boldsymbol{M}^{-1}\boldsymbol{C}^2\right)\boldsymbol{X} = \boldsymbol{0}_L \quad (3.26)$$

3.2.4 Fictive Force

In this work, non-conservative NNMs are defined as non-necessary synchronized periodical solutions at iso-energy level. To obtain periodical solutions without loss of energy, an input of energy must be added to the equation of motion. However, the corresponding energy added to the NNM equation must not modify the invariant manifold. To do so, the equations corresponding to the phase and energy resonances are compared with the forced equation of motion. Then, the input of energy, called fictive forces $\boldsymbol{F}_{fic}$, is identified:

$$\begin{pmatrix} \boldsymbol{R} = \boldsymbol{ZX} + \boldsymbol{F}_{nl} - \boldsymbol{F}_{fic} = \boldsymbol{0}_L \\ \boldsymbol{R}_\phi = 0 \text{ ou } \boldsymbol{R}_E = \boldsymbol{0}_L \end{pmatrix} \Rightarrow \boldsymbol{F}_{fic} = \boldsymbol{ZX} + \boldsymbol{F}_{nl} - (\boldsymbol{R}_\phi \text{ ou } \boldsymbol{R}_E) \quad (3.27)$$

with $(\boldsymbol{R}, \boldsymbol{R}_\phi, \boldsymbol{R}_E)$ corresponding respectively to the equations used to compute the forced responses, the phase and the energy resonances. The input of energy, represented by the identified forcing vector $\boldsymbol{F}_{fic}$, corresponds to the required forcing vector that has to be applied to the system in order to pass by the corresponding resonance point. The fictive forces do not modify the non-conservative NNMs since they are identified from equations Eqs. (3.22) and (3.25) characterizing them.

The fictive forces corresponding to the non-conservative NNMs are presented:

- Phase resonance

  By performing the calculation with Eqs. (1.5) and (3.22), the force vector that has to be applied to the system in order to pass through the phase resonance point is given by:

$$\boldsymbol{F}_{fic}^{\phi} = \omega\left(\nabla \otimes \boldsymbol{C}\right)\boldsymbol{X} + \boldsymbol{F}_{nlnc} \quad (3.28)$$

- Energy resonance

  By performing the calculation with the Eqs. (1.5) and (3.25), the force vector that has to be applied to the system in order to pass through the energy resonance point is given by:

$$\boldsymbol{F}_{fic}^{E} = \omega\left(\nabla\otimes\boldsymbol{C}\right)\boldsymbol{X} + \boldsymbol{F}_{nlnc} + \frac{1}{2}\left(\nabla^2\otimes\boldsymbol{M} + \frac{1}{2\omega}\frac{\partial(\mathbf{MatF_{nl}}_{c})}{\partial\omega}\right)^{-1} \left(\nabla\otimes\boldsymbol{C} + \frac{\partial\mathbf{MatF_{nl}}_{nc}}{\partial\omega}\right)\left(\left(\nabla\otimes\boldsymbol{C}\right)\boldsymbol{X} + \frac{1}{\omega}\boldsymbol{F}_{nlnc}\right) \quad (3.29)$$

In previous work, only the phase resonances were computed. To observe the influence of a specific NNM onto the responses associated with a particular forcing vector, an energy balance was made, see [KUE 15]. The energy balance permits to calculated the value of a multiplier d that need to be applied to whatever forcing vector $\boldsymbol{F}$ in order for the forced responses to pass by a specific point of NNM $\boldsymbol{X}$. The energy balance is interesting for experimental purpose since it can provide forcing vector $d\boldsymbol{F}$ simpler that the fictive force $\boldsymbol{F}_{fic}$ which can be complex to realize experimentally. Since the non-conservative NNMs have been extended to take in account energy resonance, the method is adapted as follow:

$$\begin{aligned} & \textstyle\int_0^T \dot{\boldsymbol{x}}^* \boldsymbol{f}_{fic} dt = \int_0^T \dot{\boldsymbol{x}}^* d\boldsymbol{f} dt \\ \Leftrightarrow\quad & \boldsymbol{X}^T\left(\nabla\otimes\boldsymbol{I}\right)\boldsymbol{F}_{fic} = \boldsymbol{X}^T\left(\nabla\otimes\boldsymbol{I}\right)d\boldsymbol{F} \\ \Leftrightarrow\quad & d = \frac{\boldsymbol{X}^T(\nabla\otimes\boldsymbol{I})\boldsymbol{F}_{fic}}{\boldsymbol{X}^T(\nabla\otimes\boldsymbol{I})\boldsymbol{F}} \end{aligned} \quad (3.30)$$

If applied at each step of continuation during the computation of NNM, the energy balance provide the evolution of the multiplier d. These results can then be used to visualize the evolution of the frequency responses with respect to the multiplier d and reveal in some case interesting phenomena such as the presence of ISs.

3.3 Shifted quadratic eigenvalue problem for stability analysis

Contrary to Linear Normal Modes (LNMs), NNMs present complex dynamical behaviors such as instability and bifurcations points. Therefore, stability and bifurcation analysis is essential to apprehend the dynamical behavior of the nonlinear system. The same approach as in the case of forced periodic solutions is applied to the newly obtained equations (3.22) and (3.25), see Subsection 1.2.2. However, the QEP of Eq. (1.42) cannot be directly used and has to be adapted.

Since the equation of motion is autonomous, $\boldsymbol{R}_{\boldsymbol{X}}$ has a trivial singularity that generates two null eigenvalues in the QEP. Theses null eigenvalues prevent a precise computation of either the stability of the system or its bifurcations points. Therefore, to solve this

problem, the two zeros eigenvalues generated by the trivial singularity have to be shifted to a negative value. For this purpose, the method described in [MEI 13] is applied. In order to be regularized, the QEP $\boldsymbol{Q}$ has to be successively shifted twice. $\tilde{\boldsymbol{Q}}$ represent the problem shifted once and $\tilde{\tilde{\boldsymbol{Q}}}$ the problem shifted twice. By shifting the two eigenvalues to -1, the following QEP is obtained:

$$\begin{aligned}\tilde{\tilde{\boldsymbol{Q}}}_(\boldsymbol{X},\tilde{\tilde{\Lambda}},\tilde{\tilde{\phi}},\varphi_1,\boldsymbol{\xi}) &= (\tilde{\tilde{\boldsymbol{R}}}_{\boldsymbol{X}}+\tilde{\tilde{\Lambda}}\tilde{\tilde{\boldsymbol{\Delta}}}_1+\tilde{\tilde{\Lambda}}^2\tilde{\tilde{\boldsymbol{\Delta}}}_2)\tilde{\tilde{\phi}} &&= \mathbf{0}_L \\ &= [\boldsymbol{R}_{\boldsymbol{X}}+\boldsymbol{\Delta}_1(\varphi_1\varphi_1^*+\boldsymbol{\xi}\boldsymbol{\xi}^*)+\boldsymbol{\Delta}_2(\varphi_1\varphi_1^*\boldsymbol{\xi}\boldsymbol{\xi}^*) &&= \mathbf{0}_L \\ &\quad +\tilde{\tilde{\Lambda}}(\boldsymbol{\Delta}_1+\boldsymbol{\Delta}_2(\varphi_1\varphi_1^*+\boldsymbol{\xi}\boldsymbol{\xi}^*))+\tilde{\tilde{\Lambda}}^2\boldsymbol{\Delta}_2]\tilde{\tilde{\phi}}\end{aligned} \tag{3.31}$$

with

$$\begin{aligned}&\bar{\varphi_1}=(\nabla\otimes\boldsymbol{I}_n)\boldsymbol{X}, \quad \boldsymbol{R}_X\bar{\varphi_2}=-\boldsymbol{\Delta}_1\bar{\varphi_1} \\ &\bar{\boldsymbol{\xi}}=\bar{\varphi_1}+\bar{\varphi_2}, \qquad \varphi_1=\tfrac{\bar{\varphi_1}}{||\bar{\varphi_1}||}, \qquad \boldsymbol{\xi}=\tfrac{\bar{\boldsymbol{\xi}}}{||\bar{\boldsymbol{\xi}}||}\end{aligned} \tag{3.32}$$

where ($\boldsymbol{\Delta}_1$, $\boldsymbol{\Delta}_2$) are defined as in Eqs. (1.43) and (1.44) with respect to the new equations (3.22) and (3.25). $\bar{\varphi_1}$ and $\bar{\varphi_2}$ are respectively the eigenvector and generalized eigenvector associated with the double null eigenvalues. One can see that $\frac{\bar{\varphi_2}}{||\bar{\varphi_2}||}$ is the same vector as $\Delta\boldsymbol{X}$ in the tangent predictor step in Eq. (3.15). For the sake of simplicity, the notations (Λ,ϕ) will be used instead of $(\tilde{\tilde{\Lambda}},\tilde{\tilde{\phi}})$ in the rest of this manuscript. The obtained modified QEP permits the stability of the nonlinear system to be computed without the problems generated by the undetermined phase. Therefore, by using the modified QEP, the bifurcation analysis can also be performed.

3.4 Bifurcation analysis

This new QEP is used to obtain equations characterizing the different types of bifurcations. Since the quasi-periodic solutions are out of the scope of this work, only the LP and BP bifurcations are treated.

3.4.1 Limit Point

At LP bifurcations, the stability of the periodic solution changes. Contrary to the forced system, the LP encountered on NNMs does not represent an extremum with respect to the frequency of the periodic solution. Only the stability criteria remains. Instead of using $\det(\boldsymbol{R}_{\boldsymbol{X}})=0$ as for forced responses, LP are detected by monitoring the eigenvalues Λ of $\tilde{\tilde{\boldsymbol{Q}}}$. By introducing $\Lambda=0$ into the quadratic eigenvalue problem, the equation characterizing the LP is obtained:

$$\left[\begin{array}{l}\tilde{\tilde{\boldsymbol{R}}}_{\boldsymbol{X}}\phi=0_L \\ \phi^T\phi-1=0\end{array}\right. \tag{3.33}$$

Therefore, to detect Ls the indicator $\det(\tilde{\tilde{\boldsymbol{R}}}_{\boldsymbol{X}}) = 0$ is used. At LPs, $\boldsymbol{\phi}$ is a liner combination of $\bar{\boldsymbol{\varphi}}_1$ and $\bar{\boldsymbol{\varphi}}_2$. Thus, Eq. (3.33) characterizing the LP bifurcation cannot be reduced to a more standard equation such as $\boldsymbol{R}_{\boldsymbol{X}}\boldsymbol{\phi} = 0_L$.

It's noteworthy that, contrary to the case of forced responses for which having a null eigenvalue in the QEP is equivalent to having a null eigenvalue in the jacobian $\boldsymbol{R}_{\boldsymbol{X}}$, the equivalence does not stand anymore for NNMs. Since bifurcations are characterized by the QEP, it is important to consider the regularized QEP instead of a regularized jacobian for bifurcation characterization. One can see the importance of the regularized QEP presented in Section 3.3. Indeed, if the equation of characterization was based not on the regularized QEP but on a regularized Jacobian such as $\left(\boldsymbol{R}_{\boldsymbol{X}} + \boldsymbol{\varphi}_1\boldsymbol{\varphi}_1^T\right)\boldsymbol{\phi} = 0_L$, the LP would be incorrectly calculated and placed at a wrong location.

The augmented system used to compute LPs is obtained by adding Eq. (3.33) to (3.14).

$$LP(\boldsymbol{Y}) = \begin{pmatrix} \boldsymbol{R}(\boldsymbol{X},\omega,\mu) \\ g(\boldsymbol{X}) \\ \tilde{\tilde{\boldsymbol{R}}}_{\boldsymbol{X}}(\boldsymbol{X},\omega,\boldsymbol{\varphi}_1,\boldsymbol{\varphi}_2)\boldsymbol{\phi} \\ \boldsymbol{\phi}^T\boldsymbol{\phi} - 1 \end{pmatrix} = \boldsymbol{0}_{2L+2} \tag{3.34}$$

with $\boldsymbol{Y} = (\boldsymbol{X},\omega,\mu,\boldsymbol{\varphi}_1,\boldsymbol{\varphi}_2,\boldsymbol{\phi})$. Then a Newton-Raphson algorithm is used to localize the LP bifurcation. The resulting linearized system at iteration k reads:

$$\begin{aligned} LP_{\boldsymbol{Y}}(\boldsymbol{Y}^k)\delta\boldsymbol{Y}^k &= -LP(\boldsymbol{Y}^k) \\ \boldsymbol{Y}^{k+1} &= \boldsymbol{Y}^k + \delta\boldsymbol{Y}^k \end{aligned} \tag{3.35}$$

with $\delta\boldsymbol{Y} = (\delta\boldsymbol{X},\delta\omega,\delta\mu,\delta\boldsymbol{\varphi}_1,\delta\boldsymbol{\varphi}_2,\delta\boldsymbol{\phi})$, $(k,k+1)$ the current and the next iteration respectively and the Jacobian $LP_{\boldsymbol{Y}}$ equals to:

$$LP_{\boldsymbol{Y}} = \begin{bmatrix} \boldsymbol{R}_X & \boldsymbol{0}_{L\times L} & \boldsymbol{R}_\omega & \boldsymbol{R}_\mu \\ {g_{\boldsymbol{X}}}^T & \boldsymbol{0}_L^T & 0 & 0 \\ (\tilde{\tilde{\boldsymbol{R}}}_{\boldsymbol{X}}\boldsymbol{\phi})_X & \boldsymbol{R}_X & (\tilde{\tilde{\boldsymbol{R}}}_{\boldsymbol{X}}\boldsymbol{\phi})_\omega & (\tilde{\tilde{\boldsymbol{R}}}_{\boldsymbol{X}}\boldsymbol{\phi})_\mu \\ \boldsymbol{0}_L^T & 2{\boldsymbol{\phi}^k}^T & 0 & 0 \end{bmatrix} \tag{3.36}$$

3.4.2 Branch Point and branching

On NNMs, BPs possess the same properties as in forced systems. The stability of the main branch changes and a new branch of solution appears at the point of bifurcation. Since the NNM are obtained by resolving autonomous equations, all the symmetries of the system are conserved and thus BPs are often encountered. At those BPs, a new branch of solution arise from the BP due to a symmetry breaking of the system. By introducing $\Lambda = 0$ into the quadratic eigenvalue problem, the equation characterizing the singularity is obtained. Since the geometric property concerning the appearance of a new branch of

solution does not change, the equation characterizing the appearance of a new branch of solution is still valid. Therefore, the augmented system for the characterization of BPs can be written as:

$$\begin{cases} \tilde{\bar{\boldsymbol{R}}}_{\boldsymbol{X}}\boldsymbol{\phi} = 0_L \\ \boldsymbol{R}_{\omega}^T\boldsymbol{\phi} = 0 \\ \boldsymbol{\phi}^T\boldsymbol{\phi} - 1 = 0 \end{cases} \tag{3.37}$$

It is possible to simplify this augmented system by using some properties of the BP bifurcation. $\bar{\boldsymbol{\varphi}}_2$ correspond to a the predictor tangent calculated in Eq. (3.17) with $\delta_\omega = 1$. For BPs, $\boldsymbol{\phi}$ belongs to a subspace which is not spanned by $\bar{\boldsymbol{\varphi}}_1$ and $\bar{\boldsymbol{\varphi}}_2$, i.e., ${\bar{\boldsymbol{\varphi}}_1}^T\boldsymbol{\phi} = 0$ and ${\bar{\boldsymbol{\varphi}}_2}^T\boldsymbol{\phi} = 0$. Using those properties, QEP (3.31) is reduced to:

$$\boldsymbol{R}_{\boldsymbol{X}}\boldsymbol{\phi} = 0_L \tag{3.38}$$

Since $\boldsymbol{R}_{\boldsymbol{X}}$ remains singular, a classical regularization of $\boldsymbol{R}_{\boldsymbol{X}}$ with respect to $\boldsymbol{\varphi}_1$ is going to be used instead of the augmented system (3.37).

$$\begin{cases} \bar{\boldsymbol{R}}_{\boldsymbol{X}}\boldsymbol{\phi} = (\boldsymbol{R}_{\boldsymbol{X}} + \boldsymbol{\varphi}_1\boldsymbol{\varphi}_1^*)\boldsymbol{\phi} = 0_L \\ \boldsymbol{R}_{\omega}^T\boldsymbol{\phi} = 0 \\ \boldsymbol{\phi}^T\boldsymbol{\phi} - 1 = 0 \end{cases} \tag{3.39}$$

Then by adding Eq. (3.39) to (3.14) the following augmented system of size $2L+3$ is obtained:

$$BP(\boldsymbol{Y}) = \begin{pmatrix} \boldsymbol{R}(\boldsymbol{X},\omega,\mu) \\ g(\boldsymbol{X}) \\ \bar{\boldsymbol{R}}_{\boldsymbol{X}}(\boldsymbol{X},\omega,\boldsymbol{\varphi}_1,\boldsymbol{\varphi}_2)\boldsymbol{\phi} \\ \boldsymbol{R}_{\omega}^T\boldsymbol{\phi} \\ \boldsymbol{\phi}^T\boldsymbol{\phi} - 1 \end{pmatrix} = \mathbf{0}_{2L+3} \tag{3.40}$$

with $\boldsymbol{Y} = (\boldsymbol{X},\omega,\mu,\boldsymbol{\varphi}_1,\boldsymbol{\varphi}_2,\boldsymbol{\phi})$. Then a Newton-Raphson algorithm is used to localize the BP bifurcation:

$$\begin{aligned} BP_{\boldsymbol{Y}}(\boldsymbol{Y}^k)\delta\boldsymbol{Y}^k &= -BP(\boldsymbol{Y}^k) \\ \boldsymbol{Y}^{k+1} &= \boldsymbol{Y}^k + \delta\boldsymbol{Y}^k \end{aligned} \tag{3.41}$$

with $\delta\boldsymbol{Y} = (\delta\boldsymbol{X},\delta\omega,\delta\mu,\delta\boldsymbol{\varphi}_1,\delta\boldsymbol{\varphi}_2,\delta\boldsymbol{\phi})$, $(k,k+1)$ respectively the current and the next iteration and the Jacobian $BP_{\boldsymbol{Y}}$ equals to:

$$BP_{\boldsymbol{Y}} = \begin{bmatrix} \boldsymbol{R}_X & \mathbf{0}_{L\times L} & \mathbf{R}_\omega & \boldsymbol{R}_\mu & \mathbf{e}_j \\ {g_{\boldsymbol{X}}}^T & \mathbf{0}_L^T & 0 & 0 & 0 \\ (\bar{\boldsymbol{R}}_{\boldsymbol{X}}\boldsymbol{\phi})_X & \boldsymbol{R}_X & (\bar{\boldsymbol{R}}_{\boldsymbol{X}}\boldsymbol{\phi})_\omega & (\bar{\boldsymbol{R}}_{\boldsymbol{X}}\boldsymbol{\phi})_\mu & \mathbf{0}_L \\ \mathbf{0}_L^T & 2{\boldsymbol{\phi}^k}^T & 0 & 0 & 0 \\ \mathbf{0}_L^T & \boldsymbol{R}_\omega^T & 0 & 0 & 0 \end{bmatrix} \tag{3.42}$$

In order to use the same method as in the Subsection 2.1.2 to discriminate a Transcritical from a Pitchfork bifurcation, the matrix $\bar{\boldsymbol{R}}_{\boldsymbol{X}}$ has to be used instead of $\boldsymbol{R}_{\boldsymbol{X}}$. Once the BP has been detected, the branching can be made. To use the branching techniques presented in the Subsection 2.1.2, the matrix $\bar{\boldsymbol{R}}_{\boldsymbol{P}}$ has to be taken instead of $\boldsymbol{R}_{\boldsymbol{P}}$ resulting in the following method.

At a non-degenerated BP, two tangents vectors exist. Therefore there are two independent vectors $\boldsymbol{\phi} = (\boldsymbol{\phi}_1, \boldsymbol{\phi}_2) \in \mathbb{R}^{L+1}$ solutions of $\boldsymbol{R}_{\boldsymbol{P}}\boldsymbol{\phi} = 0$ with $\boldsymbol{P} = (\boldsymbol{X}, \omega)$ and a unique left eigenvector $\boldsymbol{\phi}_g \in \mathbb{R}^L$ to $\boldsymbol{R}_{\boldsymbol{P}}$ such that $\boldsymbol{R}_{\boldsymbol{P}}^T\boldsymbol{\phi}_g = 0$. Consequently, Eq. (3.39) has to be calculated at the second order to compute the two tangents.

$$\begin{aligned} \boldsymbol{P} &= \boldsymbol{P}_0 + \varepsilon\boldsymbol{P}_1 + \varepsilon^2\boldsymbol{P}_2 \\ \boldsymbol{R}(\boldsymbol{P}) &= \boldsymbol{R}(\boldsymbol{P}_0) + \varepsilon\bar{\boldsymbol{R}}_{\boldsymbol{P}}\boldsymbol{P}_1 + \varepsilon^2\left(\bar{\boldsymbol{R}}_{\boldsymbol{P}}\boldsymbol{P}_2 + \bar{\boldsymbol{R}}_{\boldsymbol{P}\boldsymbol{P}}\boldsymbol{P}_1\boldsymbol{P}_1\right) \end{aligned} \tag{3.43}$$

with ε being the pseudo-arclength path parameter. So the differential of order two is equal to:

$$\bar{\boldsymbol{R}}_{\boldsymbol{P}}\boldsymbol{P}_2 + \left(\bar{\boldsymbol{R}}_{\boldsymbol{P}\boldsymbol{P}}\boldsymbol{P}_1\boldsymbol{P}_1\right) = 0 \tag{3.44}$$

By multiplying equation (3.44) by $\boldsymbol{\phi}_g^T$, the following equation is obtained.

$$\boldsymbol{\phi}_g^T\left(\bar{\boldsymbol{R}}_{\boldsymbol{X}\boldsymbol{X}}\boldsymbol{X}_1\boldsymbol{X}_1 + \bar{\boldsymbol{R}}_{\boldsymbol{X}\omega}\boldsymbol{X}_1\omega_1 + \bar{\boldsymbol{R}}_{\omega\omega}\omega_1\omega_1\right) = 0 \tag{3.45}$$

Since there are two independent vectors $\boldsymbol{\phi} = (\boldsymbol{\phi}_1, \boldsymbol{\phi}_2) \in \mathbb{R}^{L+1}$ solution of $\boldsymbol{R}_{\boldsymbol{P}}\boldsymbol{\phi}_1 = 0$ the new tangent can be written as $(\boldsymbol{X}_1, \omega_1) = (\boldsymbol{\phi}_1 + \alpha\boldsymbol{\phi}_2, \alpha)$ with $\boldsymbol{\phi}_1$ the eigenvector in Eq. (3.39) and $\boldsymbol{\phi}_2$ the displacement part of $\Delta\boldsymbol{X}$ the tangent predictor step calculated in Eq. (3.15). By introducing the tangent into the equation (3.45), the following equations are obtained:

$$a\alpha^2 + b\alpha + c = 0 \tag{3.46}$$

with

$$\begin{aligned} a &= \boldsymbol{\phi}_g^T\left(\left(\bar{\boldsymbol{R}}_{\boldsymbol{X}}\boldsymbol{\phi}_2\right)_{\boldsymbol{X}}\boldsymbol{\phi}_2 + 2(\bar{\boldsymbol{R}}_{\boldsymbol{X}}\boldsymbol{\phi}_2)_\omega + \bar{\boldsymbol{R}}_{\omega\omega}\right) \\ b &= \boldsymbol{\phi}_g^T\left(\left(\bar{\boldsymbol{R}}_{\boldsymbol{X}}\boldsymbol{\phi}_1\right)_{\boldsymbol{X}}\boldsymbol{\phi}_2 + (\bar{\boldsymbol{R}}_{\boldsymbol{X}}\boldsymbol{\phi}_1)_\omega\right) \\ c &= \boldsymbol{\phi}_g^T\left(\bar{\boldsymbol{R}}_{\boldsymbol{X}}\boldsymbol{\phi}_1\right)_{\boldsymbol{X}}\boldsymbol{\phi}_1 \end{aligned} \tag{3.47}$$

The tangent solution depends on the type of the BP bifurcation:

- Transcritical: $c \neq 0$

  There are two solutions:

$$\begin{aligned} \alpha_1 &= \frac{-b + \sqrt{b^2 - ac}}{a} \\ \alpha_2 &= \frac{-b - \sqrt{b^2 - ac}}{a} \end{aligned} \tag{3.48}$$

- Pitchfork: $c = 0$

  There are two solutions:

$$\begin{aligned} \alpha_1 &= 0 \\ \alpha_2 &= \frac{-2b}{a} \end{aligned} \tag{3.49}$$

Finally the branching can be made by perturbing $(\boldsymbol{X}, \omega)$ in the direction of the new determined tangent.

3.5 Examples of nonlinear modal analysis using NNMs

A system with two DOFs with cubic stiffness and non-conservative forces is considered. The mechanical model is represented in Fig. 3.1. and the equations of motion are given

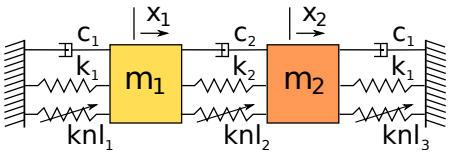

Figure 3.1 – System used as example for NNM computation

by:

$$\begin{gathered} \boldsymbol{M}\ddot{\boldsymbol{x}}(t) + \boldsymbol{C}\dot{\boldsymbol{x}}(t) + \boldsymbol{K}\boldsymbol{x}(t) + \boldsymbol{f}_{nl}(\boldsymbol{x}, \dot{\boldsymbol{x}}) = \boldsymbol{0} \\ \text{with } \boldsymbol{M} = \begin{bmatrix} 1 & 0 \\ 0 & 1 \end{bmatrix}, \quad \boldsymbol{C} = \gamma \boldsymbol{K} = \gamma \begin{bmatrix} 1+k_2 & -k_2 \\ -k_2 & 1+k_2 \end{bmatrix} \end{gathered} \tag{3.50}$$

and the vector of nonlinear forces:

$$\boldsymbol{f}_{nl} = \boldsymbol{f}_{nlc} + \boldsymbol{f}_{nlnc} = \begin{bmatrix} knl_1 x_1^3(t) + knl_2(x_1 - x_2)^3 \\ knl_3 x_2^3(t) + knl_2(x_2 - x_1)^3 \end{bmatrix} + \gamma_3 \begin{bmatrix} \dot{x}_1^3(t) + k_2(\dot{x}_1 - \dot{x}_2)^3 \\ \dot{x}_2^3(t) + k_2(\dot{x}_2 - \dot{x}_1)^3 \end{bmatrix} \tag{3.51}$$

Several designs are considered, see Tab. 3.1. For Design #1, the phase resonance of the system is analyzed in the light of underlying symmetries. The modal analysis shows a lot of nonlinear phenomena such as changes of stability, bifurcations, symmetry breaking and modal interactions. These phenomena are explained with the symmetries of the system. Secondly, a symmetry breaking event is analyzed with the NNMs in the case of Design #2. With the symmetry broken, INNMs are uncovered and tracked with LP continuation.

Afterwards, Design #3 with viscous damping is considered. During the NNM computation, fictive forces are sampled at different points. Their Fourier coefficients, whose relative contribution are less than a given threshold, are truncated. The obtained forcing vectors are then used to compute the corresponding frequency responses curves in order to study the sensitivity of the energy resonance with respect to the value of the truncation threshold. Finally, nonlinear damping is introduced in Design #4 to validate the energy

Design	$k_1[N/m]$	$k_2[N/m]$	$knl_1[N/m^3]$	$knl_2[N/m^3]$	$knl_3[N/m^3]$	$\gamma[s]$	$\gamma_3[s^3]$
1	1	1	0.5	0	0	0	0
2	1	0.105	0.5	0.02	0.5	0	0
3	1	0.105	0.5	0	0	0.05	0
4	1	1	0	0	0	0	10^{-5}

Table 3.1 – Design used for NNM computation

resonance with nonlinear damping and to study the birth of isolated solutions using energy balance.

3.5.1 Phase resonance in the light of underlying symmetries

In this subsection, the Design #1 is considered. This design has already been studied in some other works, e.g., [KER 09] and is known to present complex nonlinear dynamics. It is used here to compare the results with a reference solution and to test the robustness of the method. Moreover, an explanation of the complex topology of the NNMs based on an underlying symmetry of the system is proposed.

The first NNM of the system is plotted in Fig. 3.2. It exhibits various dynamical

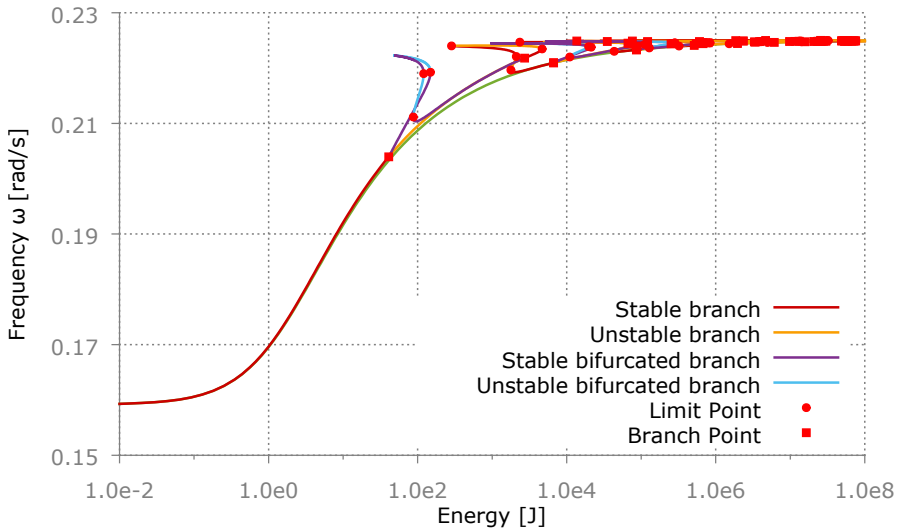

Figure 3.2 – Curve of the first NNM

phenomena such as modal interactions, internal resonance tongues, BP and LP bifurcations and bifurcation degeneracy. Moreover, internal resonance tongues seems to present a specific pattern. Modal interactions with an even sub-harmonic of the second NNM

appear from BP bifurcations, whereas modal interactions with an odd sub-harmonic of the second NNM are present on the main NNM curve. These patterns originate from the anti-symmetric relation present in Eqs. (3.50) and (3.51) of the analyzed system.

Comments on the NNM curve topology As stated in [PEE 09], NNMs of a system with odd nonlinearities which are initialized using linear normal modes are necessarily symmetric with respect to the following symmetry, see Eq. (3.52).

$$\boldsymbol{x}(\tfrac{T_i}{2}) + \boldsymbol{x}(0) = 0 \quad with \quad T_i = \tfrac{2\pi}{i\omega} \tag{3.52}$$

with i corresponding to the i^{th} harmonic used to initialize the NNM. In the frequency domain, the symmetry can be written as follows:

$$\begin{aligned} &\boldsymbol{S}_i \boldsymbol{X} + \boldsymbol{X} = 0 \\ &\text{with} \quad \boldsymbol{S}_i = \text{diag}(\mathbf{1}, \text{Rot}_1(\frac{\pi}{i\omega}), ..., \text{Rot}_p(\frac{\pi}{i\omega}), ..., \text{Rot}_H(\frac{\pi}{i\omega})) \otimes \boldsymbol{I}_{nbddl} \\ &\text{and} \quad \text{Rot}_p(\frac{\pi}{i\omega}) = \begin{bmatrix} cos(\frac{p\pi}{i}) & -sin(\frac{p\pi}{i}) \\ sin(\frac{p\pi}{i}) & cos(\frac{p\pi}{i}) \end{bmatrix} \end{aligned} \tag{3.53}$$

Eq. (3.53) is statisfied when $\cos\left(\frac{p\pi}{i}\right)$ is equal to -1, hence the following definition of the group satisfying the symmetry EH_i is obtained:

$$EH_i = \{\boldsymbol{H}_p / p \in i(2\mathbb{N}+1)\} \tag{3.54}$$

Therefore any NNM initialized using the i^{th} harmonic will be composed only by the harmonics $\boldsymbol{H}_p \in EH_i$. These NNMs are called "Pure NNMs" with respect to the definition introduced into [GOL 12a, GOL 12b]. The NNMs that are obtained exclusively from BP bifurcation will be called "Mixed modes" or "Modal interaction orbit". A mixed NNM has a modal shape that mixes the modal shape of pure NNMs.

When a BP bifurcation is encountered on a NNM calculated on EH_i, a bifurcated branch of solution can be tracked by perturbing in the direction of the eigenvector $\phi \in EH_j$ associated with a singular eigenvalue of the jacobian $\boldsymbol{J}_{NNM}$ of Eq. (3.15). Depending of the result of the intersection between the subsets EH_i and EH_j, the new branch of solution has different properties. Indeed, the bifurcated branch can lead to the j^{th} subharmonic of a NNM where the symmetry is conserved, or to an orbit of modal interaction $j:i$ where the symmetry is broken. To determine in advance which BP leads to which type of branch

of solution, the intersection of the two subsets is calculated as follows:

$$
\begin{aligned}
&\forall (i,j) \in \mathbb{N}^2, \exists ! (k,l,m) \in \mathbb{N}^3 / \\
&\qquad \frac{i}{j} = \frac{mk}{ml} = \frac{k}{l} \text{ is irreductible.} \\
&\text{If } ((k=1, l \in 2\mathbb{N}+1) \text{ or } (k \in 2\mathbb{N}+1, l=1)) \\
&\qquad (EH_j \subset EH_i) \text{ or } (EH_i \subset EH_j) \\
&\text{If } (k,l) \in (2\mathbb{N}+1)^2 \\
&\qquad EH_i \cap EH_j = EH_{mkl} \neq \varnothing \\
&\text{If } \Big((k,l) \in (2\mathbb{N})^2 \text{ or } (k \in 2\mathbb{N}+1 \text{ and } l \in 2\mathbb{N}) \text{ or } (k \in 2\mathbb{N} \text{ and } l \in 2\mathbb{N}+1) \Big) \\
&\qquad EH_i \cap EH_j = \varnothing
\end{aligned}
\tag{3.55}
$$

the subscript ${}_mkl$ holds for the multiplication $m \times k \times l$. From the computed interactions between the two subsets EH_i and EH_j, three relations can be highlighted: Inclusion, Nonempty intersection, Empty intersection.

Inclusion of two EH happens when $(k=1, l \in 2\mathbb{N}+1)$ or $(k \in 2\mathbb{N}+1, l=1)$. So modal interactions can appear on the fundamental NNMs without any other constraint on the two subsets. It is a particular case of the equation (3.55). The second NNM that is initialized with H_1 represents a good example. To do so, the fundamental first NNM is represented without the mixed NNMs, see Fig. 3.3. The notation $NNMa_b$ stand for the

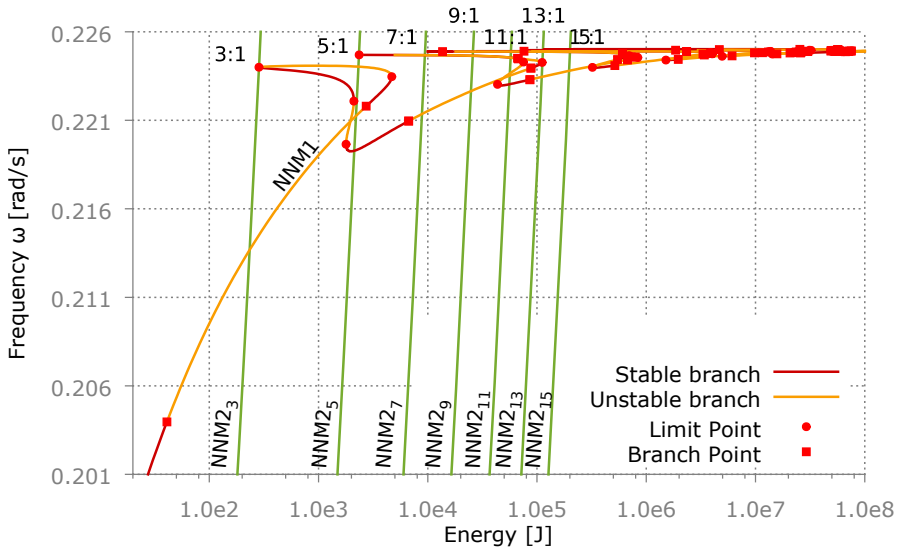

Figure 3.3 – First NNM and its modal interactions without bifurcated branches

b^{th} sub-harmonic of the a^{th} NNM. The pattern imposed by the symmetry S_1 (3.53) can

be observed. All the modal interactions $1:j$ (with j an odd number) are encountered. At each modal interaction point, the Fourier coefficients of the second NNM are indeed included in the subspace EH_j. Of course, since the HBM is used, the modal interactions $1:j$ with either harmonic 1 or j superior to the number H of harmonics used for the HBM can not be represented.

A nonempty intersection of two EH happens when $(k,l) \in (2\mathbb{N}+1)^2$. There is no possible inclusion between the two subspaces, so the point of modal interaction $j:i$ does not exist. A modal interaction $j:i$ cannot happen without breaking the symmetries $\boldsymbol{S}_i$ and $\boldsymbol{S}_j$. Nevertheless, it is interesting to see that the intersection of the two subspaces EH_i and EH_j for $(k,l) \in (2\mathbb{N}+1)^2$ generates another subspace EH_{mkl} on which a NNM of Harmonic mkl^{th} can be calculated. So two modal interactions $mkl:i$ and $mkl:j$ can appear onto the fundamental NNMs of i^{th}, j^{th} and mkl^{th} harmonics. If the modal interactions $mkl:i$ and $mkl:j$ exist, they are linked by the NNM of the mkl^{th} harmonic. As an example, the two first NNMs initialized using the 3^{rd} and the 5^{th} sub-harmonic are linked together by the 15^{th} sub-harmonic of the second NNM, see Fig. 3.4.

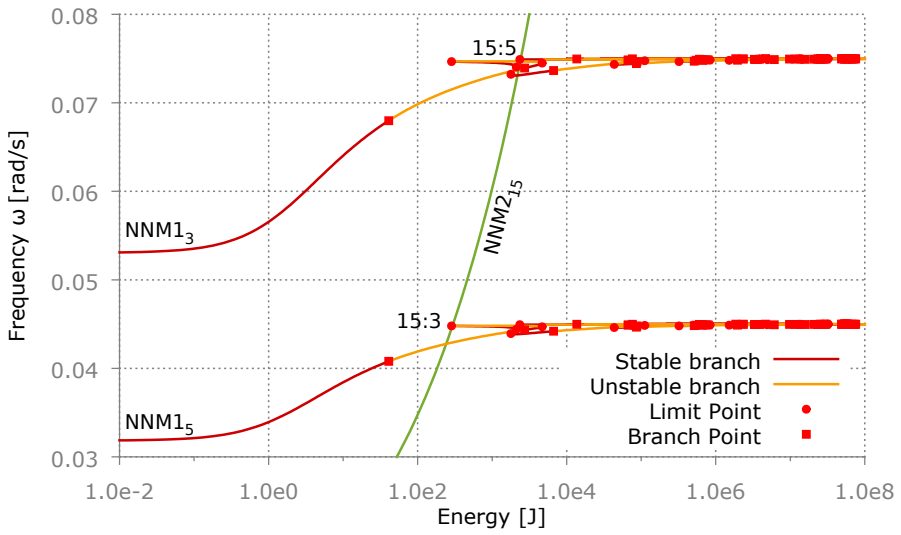

Figure 3.4 – Modal interaction between the 3^{rd}, the 5^{th} sub-harmonic of the first NNM and the 15^{th} sub-harmonic of the second NNM

The intersection of two EH is empty when $(k,l) \in (2\mathbb{N})^2$ or when $(k \in 2\mathbb{N}+1$ and $l \in 2\mathbb{N})$ or $(k \in 2\mathbb{N}$ and $l \in 2\mathbb{N}+1)$. The intersection being empty, there is no relation of inclusion between the two subspaces and no modal interaction point can appear on the two NNM curves simultaneously. Therefore, a modal interaction between the two pure modes calculated in EH_i and EH_j can only manifest itself as an orbit of modal interaction appearing from BP bifurcations. The orbit of modal interaction does not respect the symmetry of Eq. (3.52). Therefore, the subset in which the periodic solution is calculated is a subset in which EH_i and EH_j are included. The only points included in EH_i or EH_j are the BPs and modal interaction bifurcations found on the

orbits of modal interaction $j:i$. To visualize the energy transfer between the two subsets, an alternative representation of the orbit of modal interaction is used. The energy corresponding to the symmetrical and asymmetrical part of the periodic solution $\boldsymbol{X}$ are obtained using one of the symmetric operators $(\boldsymbol{S}_i, \boldsymbol{S}_j)$ introduced in Eq. (3.56). In this work, the symmetric operator $\boldsymbol{S}_i$ corresponding to the tracked NNM is used.

$$\begin{aligned} AE_i &= \tfrac{1}{2}(\boldsymbol{X} + \boldsymbol{S}_i\boldsymbol{X}) \\ SE_i &= \tfrac{1}{2}(\boldsymbol{X} - \boldsymbol{S}_i\boldsymbol{X}) \end{aligned} \tag{3.56}$$

To unfold the orbit of modal interaction $j:i$, the symmetrical and asymmetrical energy are displayed with respect to the frequency.

One can see in Fig. 3.5a that the first NNM always bifurcates from BP bifurcations to reach the modal interaction bifurcation points. Consider for example the tongue of modal interaction $2:1$ that links the first NNM with the second sub-harmonic of the second NNM. The two subsets EH_1 and EH_2 on which the two NNMs are calculated have an empty intersection. Since EH_1 and EH_2 are distinct, the two NNMs calculated on those subsets can only by linked by a orbit of modal interaction $2:1$ emanating from a symmetry breaking bifurcation. In Fig. 3.5b, one can see two Pitchfork points generating a modal interaction tongue $2:1$. This tongue of modal interaction is composed of two distinct orbits of modal interaction emanating from two BP bifurcations on the first NNM and from a degenerated BP on the second sub-harmonic of the second NNM .

On Fig. 3.6, the orbit of modal interaction $2:1$ appearing from the first BP is displayed with respect to the symmetric and asymmetric energies (SE_1, AE_1) defined in Eq. (3.56) and the frequency ω. Contrary to the usual Energy-Frequency representation of 3.5a which displays only a quarter of the total orbit, the new visualization of Fig. 3.6 displays the orbit of modal interaction $2:1$ in its totality. The transfer of energy from the symmetrical energy, corresponding to the energy of the periodical solution included in EH_1, to the asymmetrical energy, corresponding to the periodic solution included in EH_2, is made more visible in Fig. 3.7. Since only a quarter of the orbit was displayed, four different BPs and modal interaction points $2:1$ exist. The BP bifurcations present on the fundamental branch of the first NNM are encountered at maximums of symmetrical energy and null asymmetrical energy. On the other hand, modal interactions $2:1$ are encountered at null symmetrical energy and maximum asymmetrical energy. This representation also helps to understand why the continuation method keeps coming back and forth either on branch 1 or on branch 2 between the modal interaction points and the BPs instead of turning on the other interaction branch when reaching the modal interaction point $2:1$.

Comments on the BPs topology The same way symmetry has shaped the topology of modal interactions, the influence of the symmetry on the topology of the branching point is now explored. At a BP on a NNM initialized with a solution in EH_i, three groups are involved: EH_j the subset on which the BP bifurcation perturbs, EHi and IH_i the symmetric and invariant subsets by the operator of symmetry $\boldsymbol{S}_i$ from Eq. (3.53).

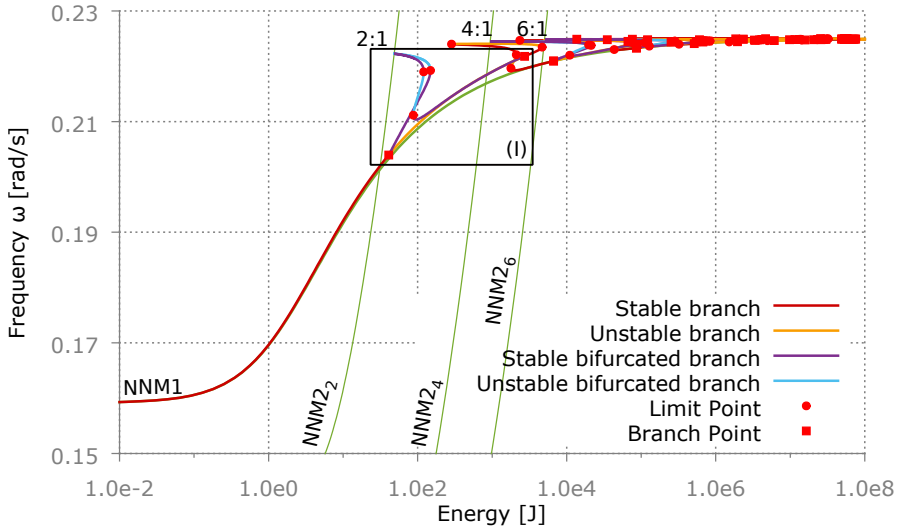

(a)

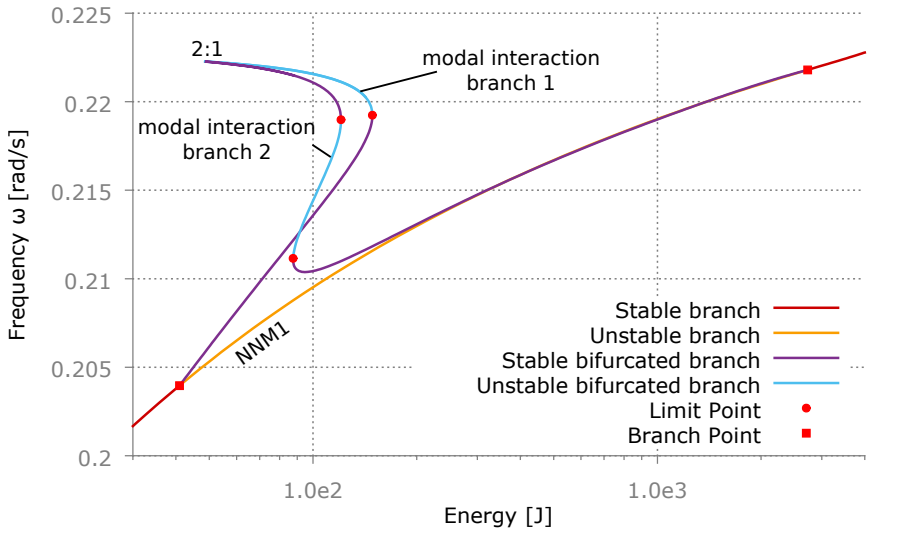

(b) Zoom (I)

Figure 3.5 – First NNM and its modal interactions with bifurcated branches

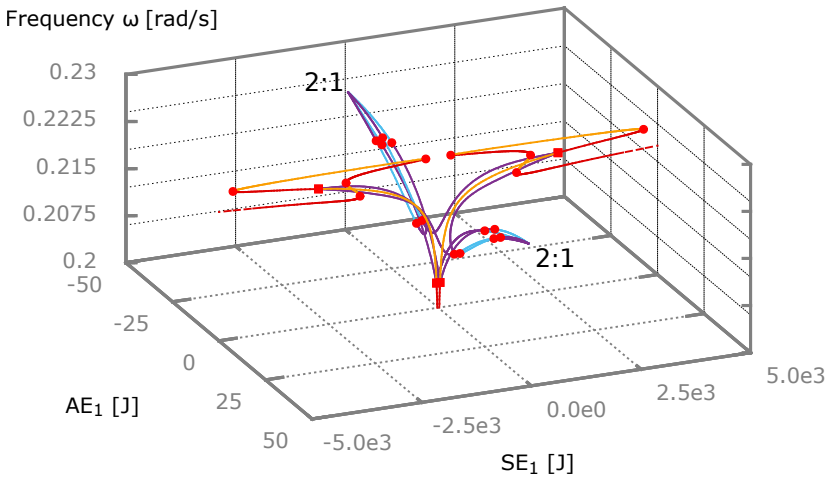

Figure 3.6 – Representation of the orbit of modal interaction $2:1$ with symmetric and asymmetric energy of the NNM resulting from the $\boldsymbol{S}_1$ symmetry. Stable branch (Red), Unstable branch (Orange), Stable bifurcated branch (Purple), Unstable bifurcated branch (Light Blue), LP (Red •), BP (Red ■)

To be invariant by the operator of symmetry $\boldsymbol{S}_i$, $\cos\left(\frac{p\pi}{i}\right)$ must be equal to 1. So the group IH_i invariant by the symmetry $\boldsymbol{S}_i$ can be defined as follows:

$$IH_i = \{H_p / p \in i(2\mathbb{N})\} \tag{3.57}$$

Depending on intersections between EH_j, EH_i and IH_i, the topology of the BP varies. The case $EH_j \cap EH_i$ being already treated in Eq. (3.55), only the intersection $EH_j \cap IH_i$ is dealt with. So, in order to distinguish the different cases that can occur, the intersections between $EH_j \cap IH_i$ are listed below:

$$\begin{array}{ll} \forall (i,j) \in \mathbb{N}^2, \exists ! (k,l,m) \in \mathbb{N}^3 / & \frac{i}{j} = \frac{mk}{ml} = \frac{k}{l} \text{ is irreductible.} \\ \text{If } (l \in 2\mathbb{N}, k = 1) & EH_j \subset IH_i \\ \text{If } (l \in 2\mathbb{N}) & EH_j \cap IH_i = EH_{mkl} \\ \text{If } (l \in 2\mathbb{N}+1) & EH_j \cap IH_i = \varnothing \end{array} \tag{3.58}$$

with mkl standing for $m \times k \times l$. Now let's see how the symmetry can lead to possibly additional singularities in the jacobian.

$$\begin{array}{rll} & \bar{\boldsymbol{R}}_{\boldsymbol{X}} \boldsymbol{\phi} & = 0 \\ \Leftrightarrow & \boldsymbol{S}_i \bar{\boldsymbol{R}}_{\boldsymbol{X}} \boldsymbol{S}_i^{-1} \boldsymbol{S}_1 \boldsymbol{\phi} & = 0 \\ \Leftrightarrow & \bar{\boldsymbol{R}}_{\boldsymbol{X}} \boldsymbol{S}_i \boldsymbol{\phi} & = 0 \end{array} \tag{3.59}$$

One can see from Eq. (3.59) that the symmetry can increase the degeneracy of the jacobian $\bar{\boldsymbol{R}}_{\boldsymbol{X}}$ if $\boldsymbol{\phi}_{sym} = \boldsymbol{S}_i \boldsymbol{\phi} \neq \pm \boldsymbol{\phi}$. Indeed, in that case $\boldsymbol{\phi}_{sym}$ represent a new eigenvector of

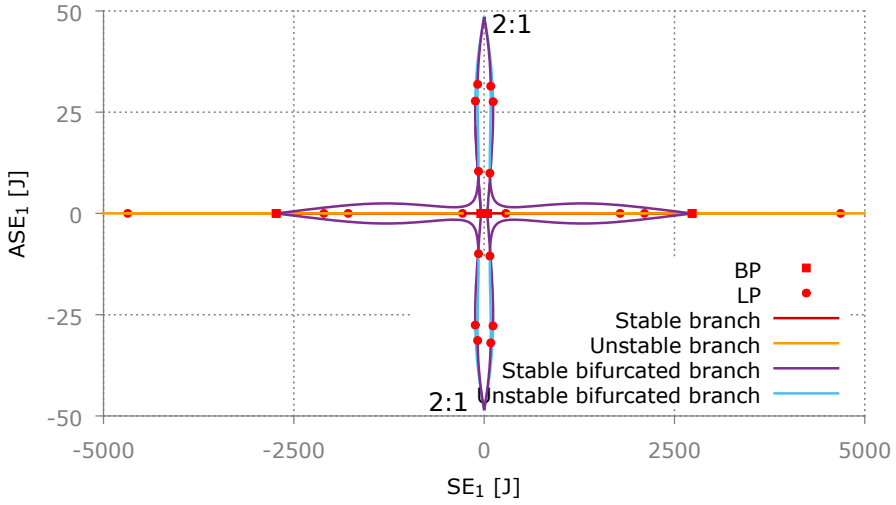

(a) Projection in the SE_1-AE_1 plane

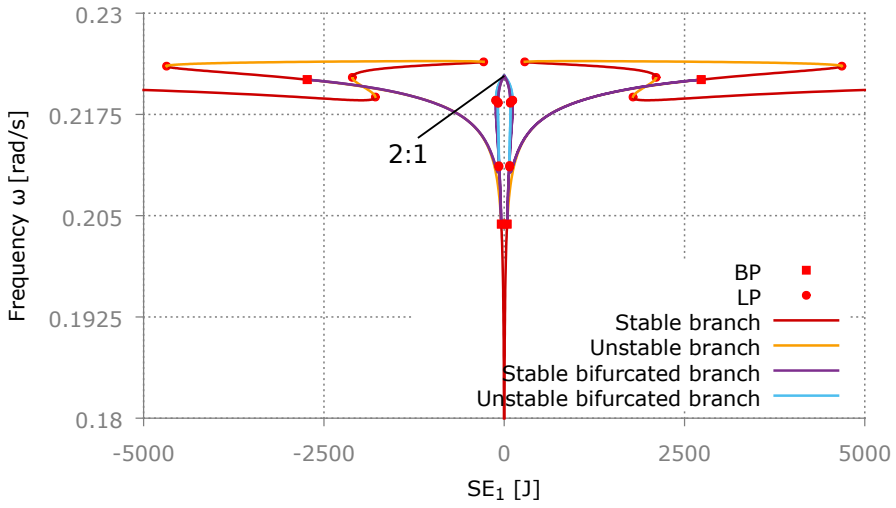

(b) Projection in the SE_1-ω plane

Figure 3.7 – Projections of the orbit of modal interaction 2 : 1

the jacobian $\bar{\boldsymbol{R}}_{\boldsymbol{X}}$. So $\boldsymbol{R}_{\boldsymbol{X}}$ would have two zero eigenvalues associated with two distinct eigenvectors $(\phi, \phi_{sym}) \in EH_j^2$. Therefore, this bifurcation corresponds to a degenerated BP rather than to a R1 bifurcation. So to predict the degeneracy of the BP, we have to analyze in which case the eigenvector $\phi_{sym} = \pm\phi$, i.e., the BP is non-degenerated when:

$$\boldsymbol{S}(\frac{\pi}{i})\phi = \pm\phi \tag{3.60}$$

For this equation to be exact, $\phi \in EH_j$ has to be either in EH_i or IH_i.

- $EH_j \subset EH_i$ has been treated in Eq. (3.55) and requires $\{l \in 2\mathbb{N}+1, k = 1\}$
- $EH_j \subset IH_i$ has been treated in Eq. (3.58) and requires $\{l \in 2\mathbb{N}, k = 1\}$

So when $j \notin i\mathbb{N}$, $\bar{\boldsymbol{R}}_{\boldsymbol{X}}$ would have two zero eigenvalues associated with two distinct eigenvectors $(\phi, \phi_{sym}) \in EH_j^2$. Let's see the example of the two BP bifurcations on the first NNM that lead to the orbits of modal interaction $2:1$. The eigenvectors are included in EH_2 and EH_1 is the group where the first NNM is calculated. So with $i = 1$ and $j = 2$, the symmetry does not generate an additional singularity at the two BP bifurcations, see Fig. 3.8a. On the other hand, when the eigenvector is included in EH_1 and EH_2 is the group where the second sub-harmonic of the second NNM is calculated, the symmetry generates a degenerated BP: the modal interaction bifurcation point $2:1$, see Fig. 3.8b. With $i = 2$ and $j = 1$, j is not a multiple of i. Therefore, the symmetry generates an additional singularity at the branching point.

With the presented NNM computation method, the NNMs of the system have been calculated for Design #1 presenting an odd nonlinearity. A symmetry of the system has been used to better understand the dynamics of the system. The topology of bifurcation points, symmetric and asymmetrical branches has been explained. An alternative way of representing internal resonance tongues have been presented.

3.5.2 Symmetry breaking of phase resonance

In this subsection, Design #2 is considered to analyze the effect of symmetry breaking on NNMs. Then, a LP continuation is performed to visualize the evolution of the NNMs with respect to the system parameter used to break the symmetry. In particular, INNMs are detected and computed.

The NNMs of the symmetric design are plotted in Fig. 3.9. One can see that the first NNM looks like a classical NNM of a Duffing oscillator. On the other hand, the second NNM presents a BP which is a typical characteristic of symmetries in the system. Beyond the BP, the pure NNM changes its stability and becomes unstable. Two mixed NNMs emerge from each side of the BP bifurcation. The BP present on the second NNM comes from the symmetry of the considered design.

The symmetry of the system (3.50) is then broken by taking $knl_3 = 0.37 \neq knl_1$. The asymmetry of the system is represented by the parameter $\Delta knl = knl_3 - knl_1$. The NNMs of the asymmetric system are then plotted in Fig. 3.10. One can see that the previous BP

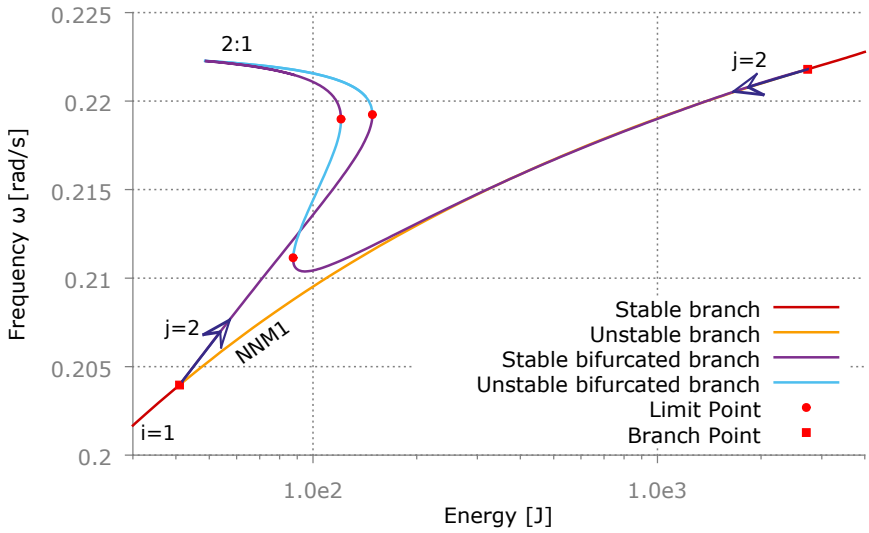

(a) Perturbation from EH_1 ($i = 1$) into EH_2 ($j = 2$) - BPs

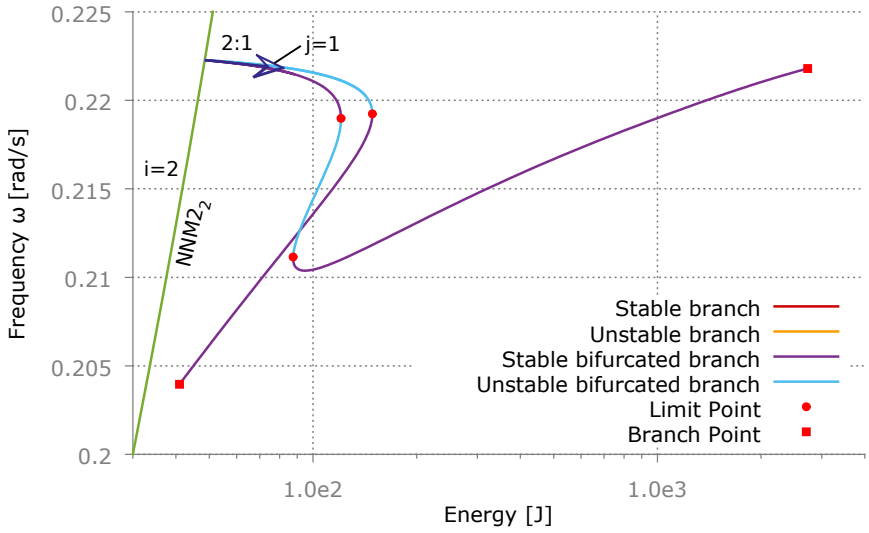

(b) Perturbation from EH_2 ($i = 2$) into EH_1 ($j = 1$) - Degenerated BP

Figure 3.8 – Normal and degenerated BPs on orbit of modal interaction 2 : 1

has been broken by the perturbation of the nonlinear stiffness coefficient knl_3, leading to an imperfect bifurcation point. The mixed NNMs and the second pure NNM are turned into a pure NNM and an INNM. Compared to the unbroken NNM, the resulting pure NNM is moved at lower frequencies for the first mass and at lower amplitude for the second mass. On the other hand, the INNM is on the opposite side of the BP each time. Compared to the unbroken NNM, the INNM is shifted at higher frequencies for the first mass and higher amplitude for the second mass. For an opposite value of Δknl, i.e. , $\Delta knl > 0$ instead of $\Delta knl < 0$, the two masses simply exchange their dynamical behaviour, i.e., the plots of Figs. 3.10a and 3.10b are switched. These numerical results coincide

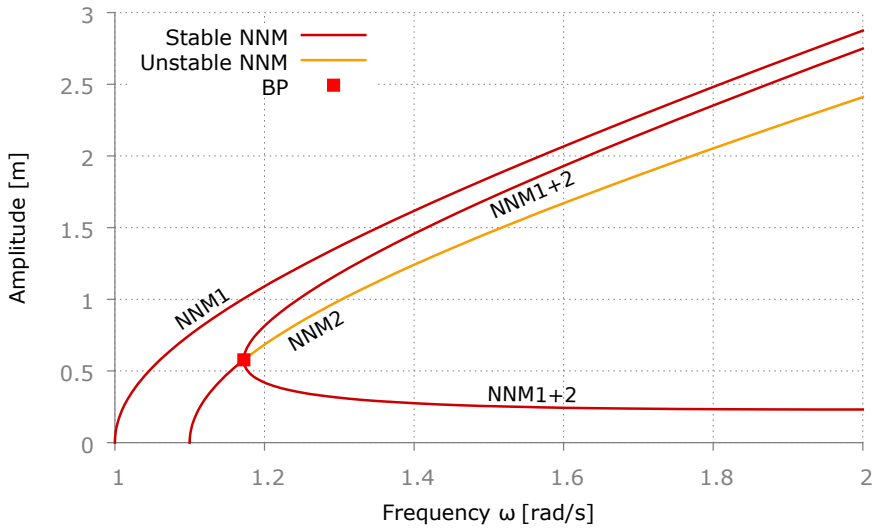

Figure 3.9 – NNMs of the second design representing the amplitude of the two masses

with the analytic ones presented by Hill *et al.* [HIL 16]. To observe the evolution of the INNMs, one could compute each INNM for different values of Δknl. However, this so-called sequential method is time consuming and reveals information only for some chosen values of the varying system parameters. Since the INNMs under consideration contain LPs, a LP tracking method with respect to the parameter Δknl is used with the BP as starting point. With the LP tracking method, the evolution of the INNMs is obtained much faster than with the sequential method. Moreover, the LP continuation method provides a starting point for the computation of the INNM branches. In Fig. 3.11, the INNMs have been obtained using the LP continuation method and branching method. The second NNM in the symmetric case is represented together with the evolution of the INNM with respect to the parameter Δknl that breaks the symmetry of the system. The same pattern as in Fig. 3.10 holds for every Δknl. For the first mass, the lowest branch of LPs corresponds to $\Delta knl < 0$ and the highest are to $\Delta knl > 0$ whereas it is the opposite for the second mass. Also, the more the symmetry is broken, the more the LP bifurcation is moved away from the initial BP bifurcation.

In this subsection, symmetry breaking of the NNMs is analyzed for Design #2. When the symmetry of the system is broken, the BP bifurcation becomes an imperfect bifurcation with a resulting INNM. By using the LP continuation and branching method, INNMs are computed and their evolution is analyzed with respect to a free parameter that breaks the symmetry.

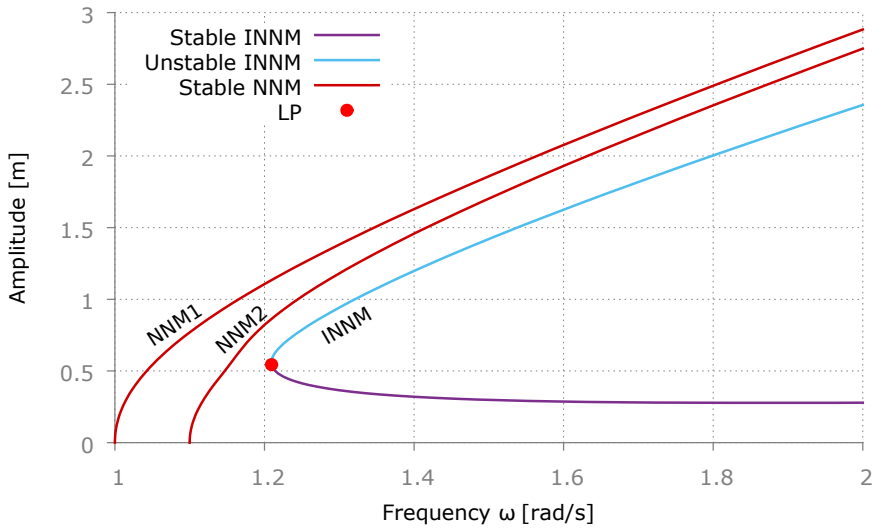

(a) First mass

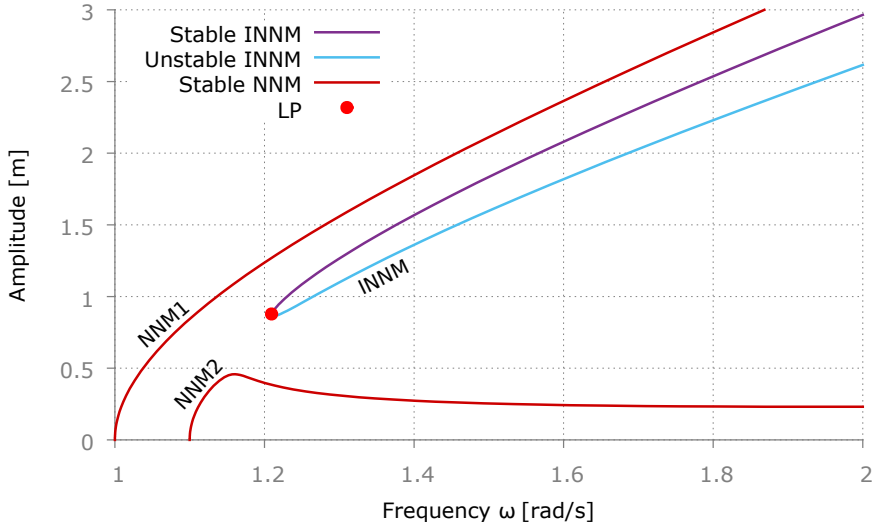

(b) Second mass

Figure 3.10 – NNMs of the system with $\Delta knl = -0.13$

3.5.3 Sensitivity analysis of obtained frequency responses with truncated fictive forces

In this subsection, Design #3 of Tab. 3.1 is used to highlight the usefulness of the fictive force. A viscous damping proportional to the linear stiffness matrix is taken. The coefficient of proportionality γ of Eq. (3.50) is chosen equal to 5% to represent structural damping. Several fictive forces are computed with respect to different points on the NNMs. Theses fictive forces are then used as external forcing to compute the frequency response curves intersecting the NNM at their energy resonance, i.e., at their maximum

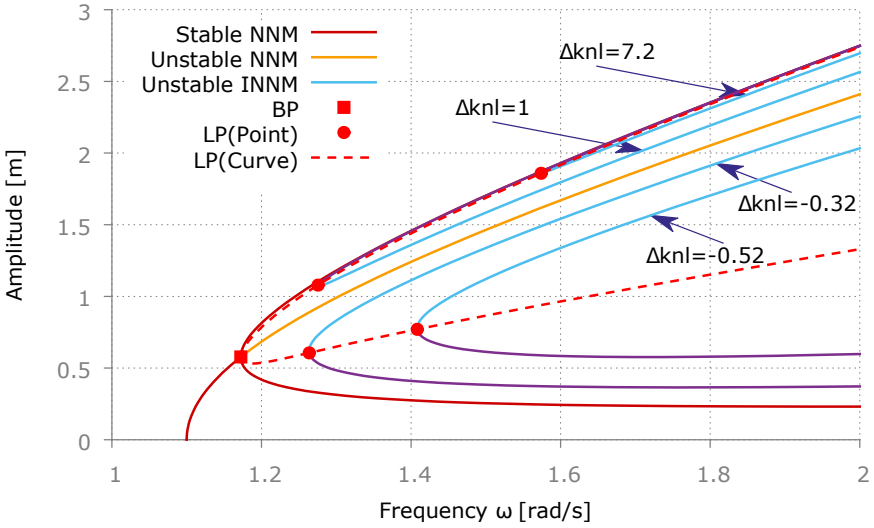

(a) First mass

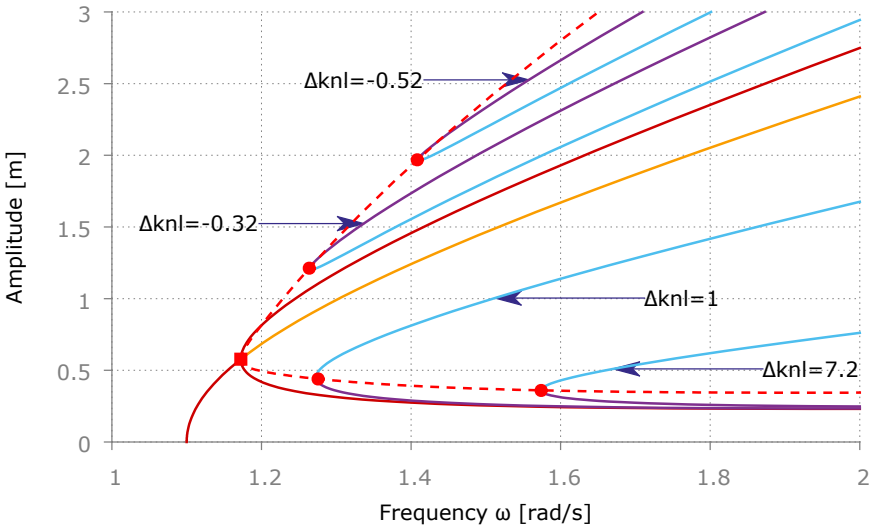

(b) Second mass

Figure 3.11 – Evolution of the INNMs with respect to Δknl. INNM for $\Delta knl = [7.2, 1, -0.32, -0.52] N/m^3$

of energy. Secondly, a sensitivity analysis with respect to the fictive force is performed. Three fictive forces corresponding to three points on the first NNM are used. The first fictive force targets a point on the main branch of the first NNM, whereas the other fictive forces target a point near the modal interaction 3 : 1 and a point on the orbit of modal interaction 2 : 1. The idea is to determine if a simplified fictive force can be used to obtain the frequency response curves intersecting the NNM at the targeted points. Then, for each fictive force, the harmonics with an energy contribution lower than a given threshold are withdrawn in order to study the influence of the accuracy of the fictive force on the global dynamics of the system.

The first NNM for Design #1 is represented in a Frequency-Energy plot instead of in an Energy-Frequency plot. In fig. 3.12, this representation is chosen because it is easier to visualize the forced responses of the system.

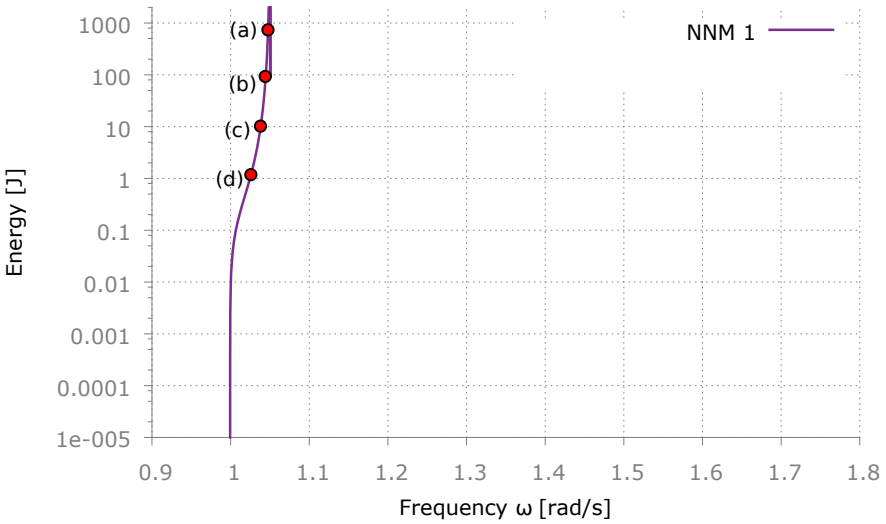

Figure 3.12 – First NNMs of Design #3 in Frequency-Energy

One can see that the frequency shift induced by the viscous damping is negligible. Therefore, standard conservative NNMs can be used to analyze such a system with small viscous damping. However, when nonlinear damping is present, as in Subsection. 3.5.4, the energy resonance differs greatly from conservative NNMs in the case of high high amplitudes of vibration. Several points (a)-(b)-(c)-(d) on this first NNM are chosen to compute the fictive force. The fictive forces in the case of with respect to viscous damping are obtained with Eq. (3.28) in which $\boldsymbol{F}_{nlnc}$ is null:

$$\boldsymbol{F}_{fic}^{\phi} = \omega \nabla \otimes \boldsymbol{C}\boldsymbol{X} \tag{3.61}$$

Once the fictive forces are computed, they are used as forcing vectors $\boldsymbol{F}$ to compute the corresponding frequency responses curves. The obtained frequency responses curves and the NNMs are plotted together in Fig. 3.13. One can see that the forced responses have their maximum of energy exactly on the non-conservative NNM corresponding to

the energy resonance of the system. As expected, the fictive force leads to a localization of energy on the targeted point of the NNM. In Fig. 3.14, the second NNM is also plotted.

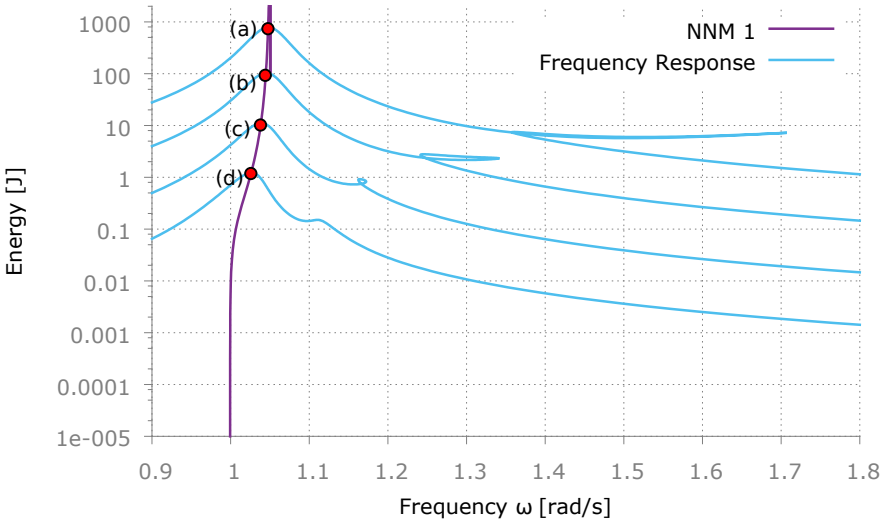

Figure 3.13 – First NNMs of Design #3 with frequency responses

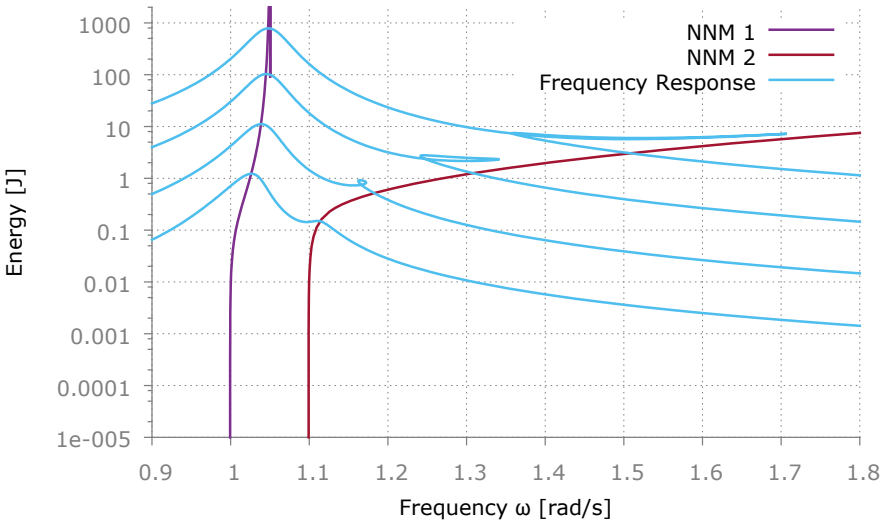

Figure 3.14 – NNMs of Design #3 with frequency responses

Since the orthogonality property is not conserved with NNMs, the second NNM is also responding to the applied forcing. However, since the forcing is designed to target and be orthogonal at the energy resonance of the first mode, the second NNM does not pass by the maximum of energy of the interaction loops. One can also note that the energies of these loops are far lower than the energy associated to the targeted point of the NNM.

The fictive forces are interesting for experimental purposes. By controlling the forcing vector, one could track the NNMs corresponding to the energy resonances of the system. However, it is complicated to reproduce exactly the shape of the forcing vectors. To decide if the exact fictive force $\boldsymbol{F}_{fic}^{\phi}$ from Eq. (3.28) can be replaced with an approximated force $\boldsymbol{F}_{approx}$, a sensitivity analysis is performed. The level of approximation is defined as follows: the harmonics of the fictive force with a relative energetic contribution lower than a threshold T_{thres} (in %) are truncated. The resulting approximated force is given by:

$$\boldsymbol{F}_{approx} = \boldsymbol{F}_{fic}^{\phi}((\boldsymbol{F}_{fic}^{\phi})^2 > T_{thres} \times ||\boldsymbol{F}_{fic}^{\phi}||_2) \tag{3.62}$$

Several locations on the NNM are analyzed, see Fig. 3.15. First, the point a on the main branch previously presented is considered. Then, points onto the 2 : 1 branch of modal interaction and a point near modal interaction 3 : 1 are treated.

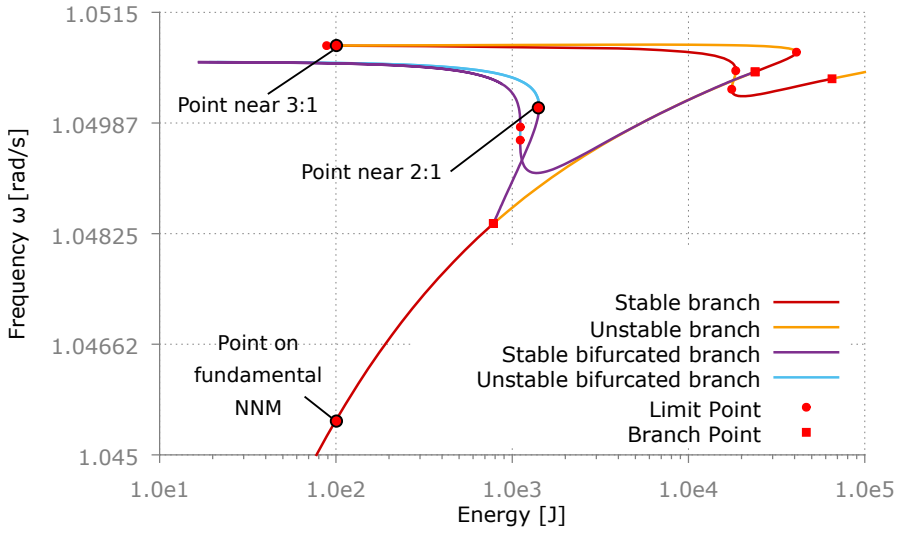

Figure 3.15 – NNM points targeted - Point on fundamental (b), point on 2 : 1 orbit and point near 3 : 1

Point (b) on main branch At the point (b) on the fundamental of the NNM, the fictive force is calculated. In Fig. 3.16, the relative contributions in energy of the harmonics are represented. The fictive force is simple and constituted essentially of harmonic 1. Harmonics 3 and 5 do not contribute much to the fictive force ($\approx 10^{-4}$, $\approx 10^{-6}$). The threshold equals to $T_{thres} = 50\%$ is used to truncate the fictive force resulting in a single harmonic forcing. In Fig. 3.17, the two forced responses are compared.

The truncated fictive force contains only the major harmonic contribution of the fictive force. One can see that the two forced responses are equal. Therefore, it is possible to target experimentally specific NNM using a mono-harmonic forcing vector when the targeted point is far from any modal interaction.

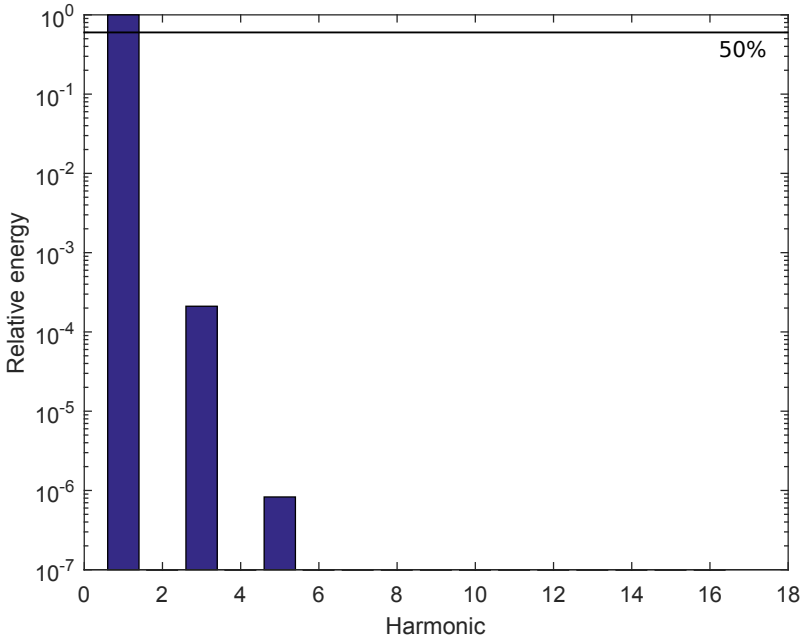

Figure 3.16 – Point (b) on main branch - Harmonic description and threshold

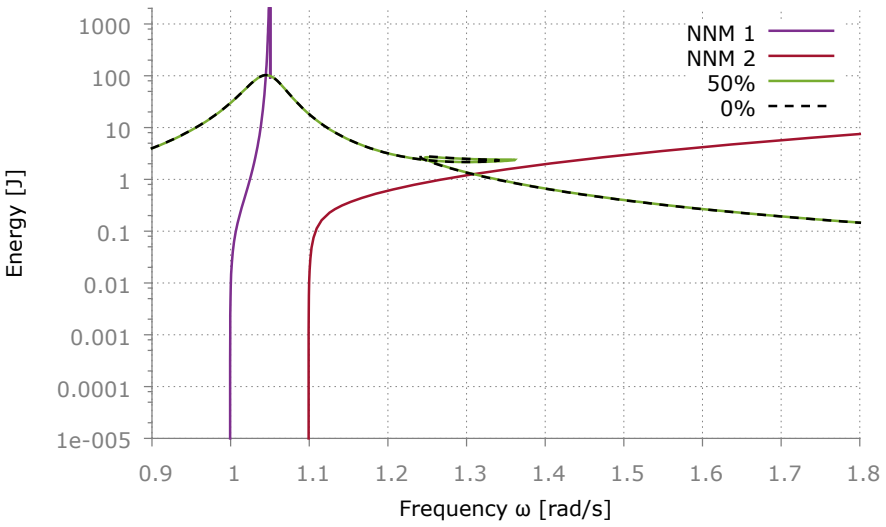

Figure 3.17 – Point (b) on main branch - Comparison between forced-responses obtained with exact and truncated fictive forces

Point near modal interaction $3:1$ At the point near modal interaction $3:1$, the fictive force is calculated. In Fig. 3.20, the relative contributions in energy of the harmonics are represented. The fictive force is more complex than for the one calculated at point (b). It is composed by two main harmonics 1 and 3. The harmonic 9 represents the third highest contribution at the order of 10^{-2} of the total energy. The others odd harmonics that compose the fictive force contribute less. The fictive force is now truncated respectively with $T_{thres} = (0\%, 25\%, 30\%, 50\%)$. With a threshold at 50%, the approximated force is only composed of harmonic 1. With a threshold at 30%, the harmonic 3 of the fictive force is added to the approximated force. With a threshold at 0.4%, the harmonic 9 of the fictive force is added to the approximated force. The corresponding response curves are plotted in Fig. 3.19. One can see that the response curves differ from each other until the

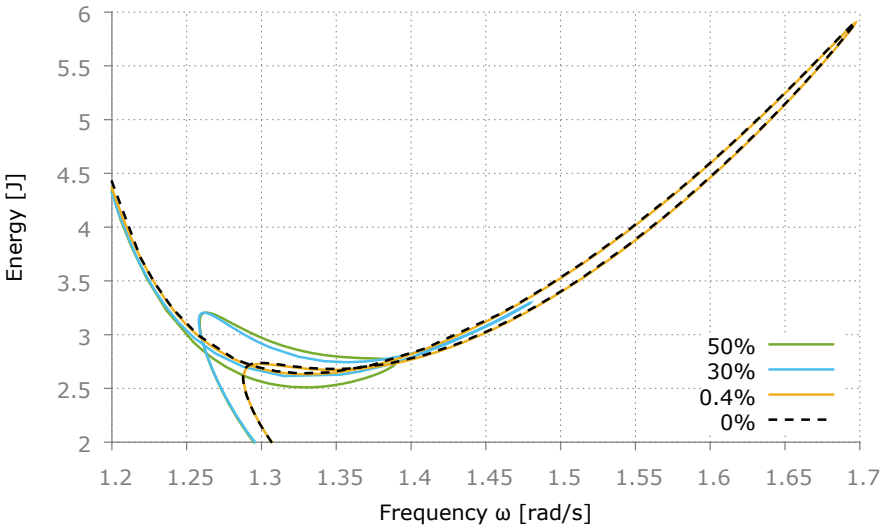

Figure 3.18 – Point near modal interaction $3:1$ - Comparison between forced responses obtained with exact and truncated fictive forces (Zoom I)

threshold reaches $T_{thres} = 0.4\%$. For threshold below $T_{thres} = 0.4\%$, the response curves obtained with a truncated and a non-truncated applied force are similar. At the interaction point $3:1$, the modal shapes of the two NNMs are almost equal. Therefore, the forcing vector excites both NNMs near the modal interaction point, resulting in the appearance of a loop, also called tongue of modal interaction, close to the second NNM. When the fictive forces are truncated, one can see that the energy resonance on the first NNM is not affected. On the other hand, the resonance on the interaction loop is influenced by the truncation, see Fig. 3.18. The more the fictive force is truncated, the more the modal shape of the first NNM is different from the modal shape of the second NNM, resulting in weaker interaction between the two NNMs.

Therefore, an accurate forcing vector is essential to visualize specific phenomena such as modal interactions. Here, a fictive force truncated with a threshold $T_{thres} \leq 25\%$ is enough to represent well the interaction in this case.

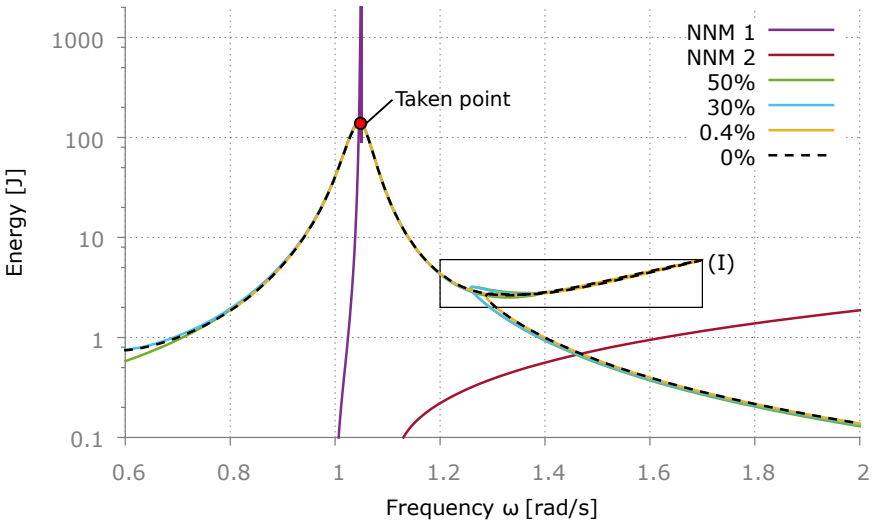

Figure 3.19 – Point near modal interaction 3 : 1 - Comparison between forced responses obtained with exact and truncated fictive forces

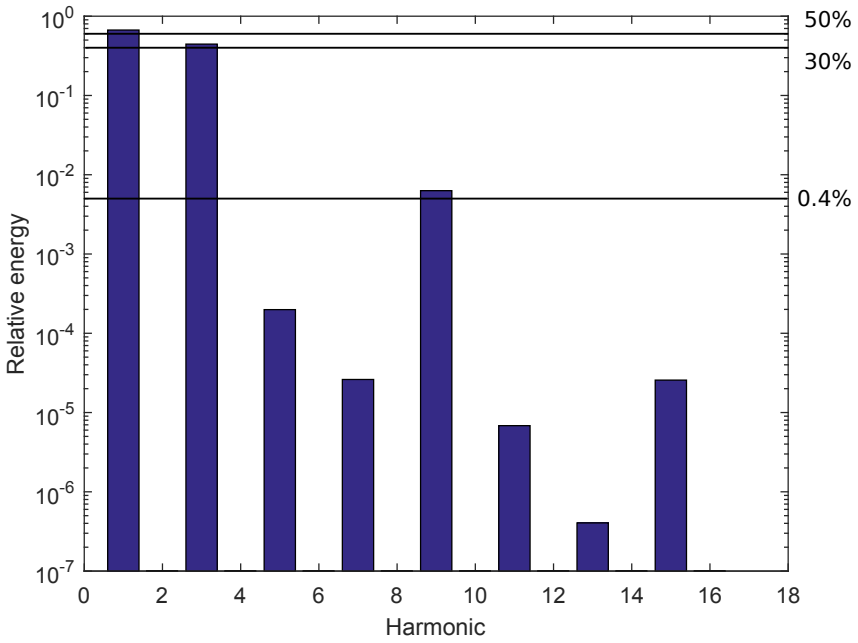

Figure 3.20 – Point near 3 : 1 - Harmonic description and threshold

Point on the branch of modal interaction $2:1$ Finally, an analysis with a fictive force targeting the branch of modal interaction $2:1$ is performed. In Fig. 3.21, the relative contributions in energy of the harmonics of the fictive force are represented. The fictive force is composed by odd and even harmonics. This is because, the symmetry of the system is broken on orbit of modal interaction, see Section 3.5.1. It is composed by mainly by harmonic 1. The harmonic 2 represents the second highest contribution at the order of 10^{-2} of the total energy. The others harmonics that compose the fictive force contribute less. The fictive force is now truncated respectively with $T_{thres} = (0\%, 0.01\%, 0.1\%, 1\%)$. With a threshold at 1%, the approximated force is only composed of harmonic 1. With a threshold at 0.1%, the harmonic 2 of the fictive force is added to the approximated force. With a threshold at 0.4%, the harmonic 3 and 5 of the fictive force are added to the approximated force. The forced responses are computed with respect to the following thresholds $T_{thres} = (0\%, 0.01\%, \%0.1, \%1)$, see Fig 3.22. The same phenomena of exci-

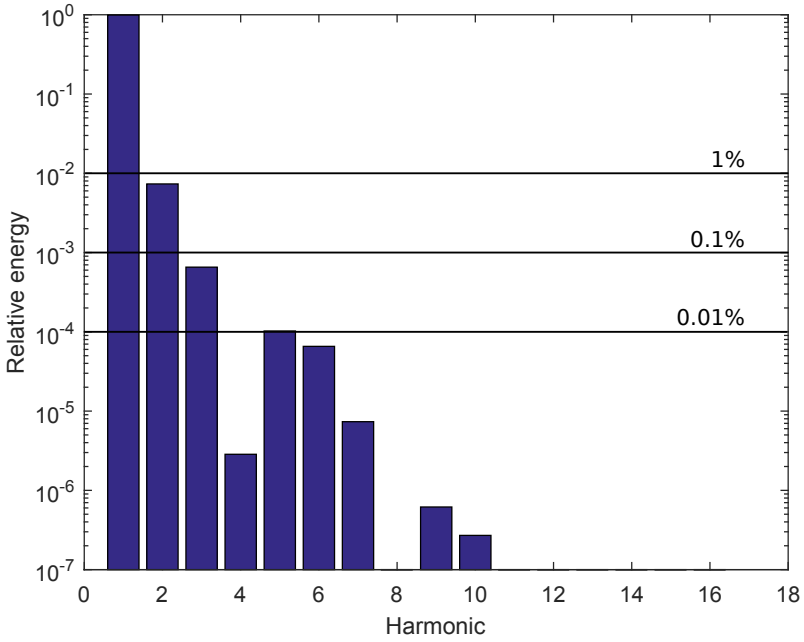

Figure 3.21 – Point on $2:1$ orbit - Harmonic description and threshold

tation of the second NNM is observed. A zoom on the top of the resonance is presented in Fig. 3.22b to see additional phenomena. One can see the appearance of several loops around the resonance associated to the first NNM. These loops are the result of the excitation of the branch of modal interaction $2:1$. To visualize such behaviors, the fictive force needs to have components on both the first and the second harmonic. This phenomenon cannot be observed if the fictive force is not accurate enough. For example, with the threshold $T_{thres} = 0.1\%$, one can see the appearance of the interaction. With the threshold $T_{thres} = 0.01\%$, almost half of the DOFs are conserved in the truncated fictive force. One can see in Fig. 3.22c that the responses curves with truncated and no truncated applied

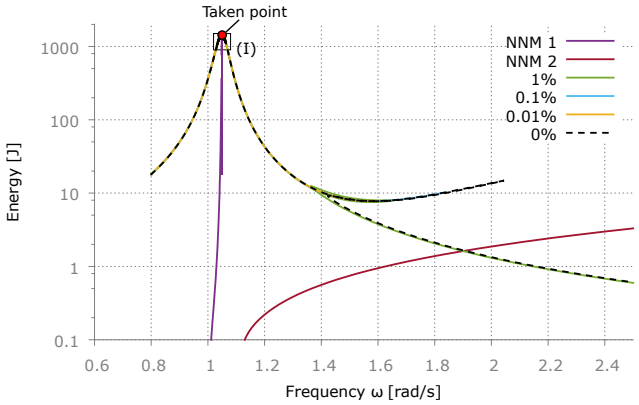

(a)

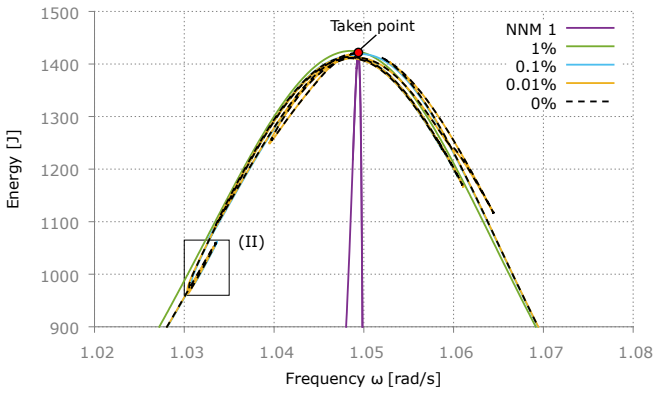

(b) Zoom I

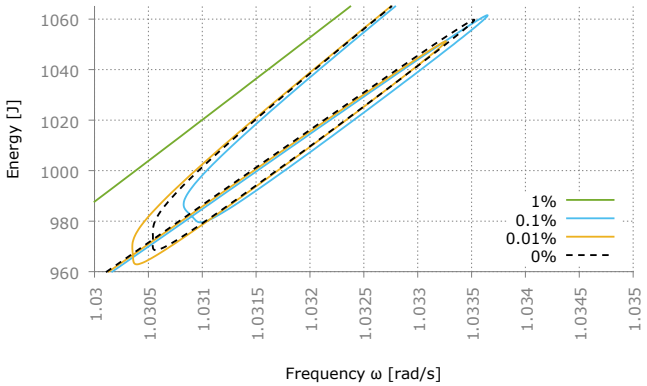

(c) Zoom II

Figure 3.22 – Point on the branch of modal interaction 2 : 1 - Comparison between forced response curves obtained with full or truncated fictive force

force are not yet superimposed. A threshold even lower than $T_{thres} = 0.01\%$ is required to observe the interaction phenomena correctly.

As a conclusion for this subsection, one can see that the fictive force can be used to target specific points on the NNM. The forcing vector needs to be taken almost equal to the exact fictive force to observe localized phenomena such as modal interactions and even more precise to observe phenomena relative to orbits of modal interaction. One of the perspectives of this work is to realize experimental tracking of phase and energy resonances with the help of their respective fictive force.

3.5.4 Validation of the energy resonance NMN

In this subsection, the design with cubic damping #4 of Tab. 3.1 is used. Presenting strong non-linear damping this design is chosen for validating the concept of energy resonance by comparing NNMs and frequency response curves. The NNMs in Fig. 3.23 are computed without stability and bifurcation analysis. Since the system is symmetric, the

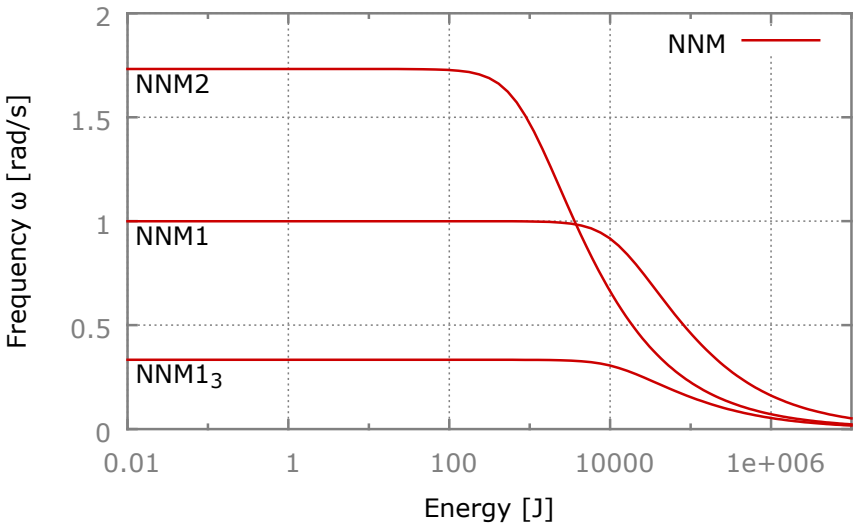

Figure 3.23 – Computation with the energy resonance criterion of the in-phase NNM1, its sub-harmonic 3 NNM1$_3$ and the out-of-phase NNM2

two pure NNMs of the system are respectively in-phase and out-of-phase. Therefore, the NNMs are orthogonal to each other and can be targeted specifically with a forcing vector respecting these symmetries. The in-phase NNM is targeted with various amplitude of forcing $f_0 = [0.1, 0.5, 1, 5, 10, 50, 100, 500]N$. The corresponding frequency response curves are presented in Fig. 3.24 .

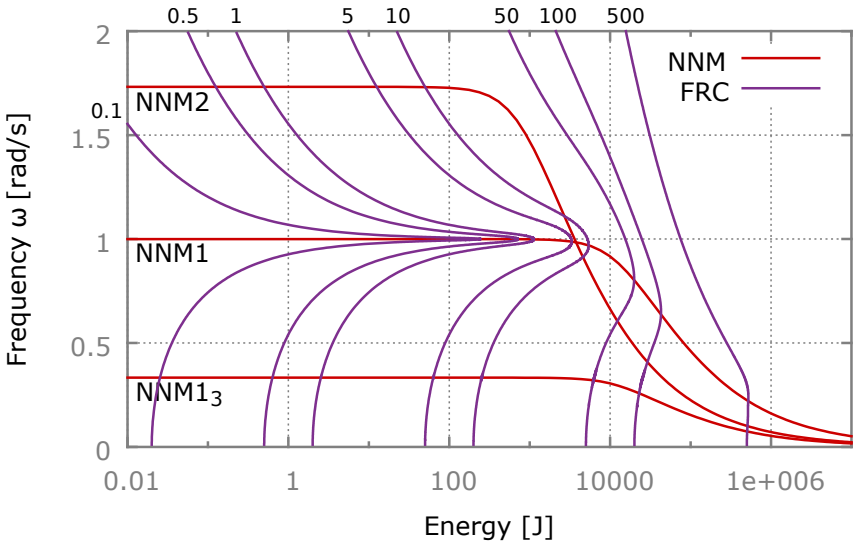

Figure 3.24 – Computation of the in-phase NNM1, its sub-harmonic 3 NNM1$_3$ and the out-of-phase NNM2 and the frequency response curves (FRC) for $f_0 = [0.1, 0.5, 1, 5, 10, 50, 100, 500]N$

3.6 Conclusions

A robust method for nonlinear modal analysis based on NNMs as a family of periodic solutions is presented. The continuation of NNMs is improved by the addition of an optimized phase condition in the frequency domain and a damping matrix multiplied by quasi-null coefficient. The concept of NNM is extended to take into account non-conservative equations of motions. It is shown that the non-conservative NNMs can be computed as periodical solutions at iso-energy level by introducing an appropriate fictive force in the system. Similarly to linear modal analysis, two definitions of this fictive force are provided to characterize the phase and the energy resonances of non-conservative NNMs. As a result, non-conservative NNMs can be computed with the same numerical methods as for the conservative case. The stability analysis is performed by considering a shifted version of the quadratic eigenvalue problem derived from Hill's method. It results in a robust method for the computation of all conservative or non-conservative NNM branches, their stability and bifurcation points.

Then, a 2-ddl system is analyzed with respect to several designs. With the first design, the complex dynamical behaviors of the system are analyzed under the light of an underlying symmetry. The topology of both tongues of modal interaction and BPs are explained. The robustness of the method is validated by the calculation of all the NNM branches in a single computation. With the second design, techniques of LP continuation are applied to the system in order to visualize the evolution of INNM with respect to a parameter that breaks the symmetry of the system. It is that LP continuation techniques are efficient tools for the analysis of INNM. Finally, the theory describing the energy resonance of the displacement vector is applied to the two last designs. First, viscous damping

is considered in the model simulating structural damping. For viscous damping of a few percentages, phase and energy resonances are almost equal. Thus, phase resonance can be taken over energy resonance for simulating system with structural damping. It is also shown that a sufficiently accurate fictive force can target specific points onto NNMs such as modal interaction points or orbits of modal interaction. This opens the possibility of experimental NNM tracking with a controlled fictive force targeting a specific resonance. Finally, a system with a cubic nonlinear damping is considered to validate the energy resonance NNM for more complex nonlinear damping.

Chapter 4

Dynamical analysis of MEMS array

This chapter investigates the mass-sensing potential of an array of identical resonant electrostatically actuated micro beams, as a first step toward the implementation of arrays of thousands of sensors for mass sensing. The effect of electrostatic coupling is studied on a 2-beam array. Predicted frequency responses exhibit complex branches of solutions with additional loops and synchronization in frequency of bifurcations due to the coupling between the beams. Then, the dynamic of a 2-beam array is analyzed with bifurcation tracking and Nonlinear Normal Modes (NNM) after a symmetry-breaking event induced by the addition of an added mass onto one beam of the MEMS array under symmetric configuration. Phenomena leading to the apparition or the merging of isolated solutions (IS) and isolated NNM (INNM) are analyzed. Finally, mechanism of detection using 2-beam and 3-beam array are proposed. Depending on the applied voltages, the solutions with and without added mass exhibit a large change in amplitude that can be used for detection. For symmetric configurations, exploiting the bifurcations of symmetry-breaking type permits improving mass sensing.

Contents

In this chapter builds on the previous chapters and addresses electrostatically actuated resonant MEMS array. An array of n identical clamped-clamped micro beams is considered in order to study the response change due to a very small added mass. The response change is analyzed numerically for various numbers of beams and several configurations of the beam array such as asymmetric and symmetric. The beams of the array are coupled only by electrostatic forces and exhibit complex dynamical behaviors which are used to provide additional methods for mass sensing.

In Section 4.1, a reduced-order model for an array of n clamped-clamped beams is considered. It is obtained through Galerkin expansion onto a finite number of linear eigenmodes and solved numerically by means of the Harmonic Balance Method (HBM) combined with the Asymptotic Numerical Method (ANM). In Section 4.2, the case of a two-beam array is investigated. The response change due to the electrostatic coupling between the beam is analyzed. Approximated solutions are used to distinguish and withdraw the coupling during the computation of the frequency responses. In Section 4.3, a symmetric two-beam array is analyzed before and after symmetry-breaking event induced by the addition of a small mass onto the first beam. Nonlinear modal analysis and parametric analysis are performed using the methods presented in the previous Chapters. First, the NNMs of the array are analyzed with LP tracking. INNM (INNM) are detected after the symmetry-breaking event. Secondly, the frequency responses are computed and analyzed with the previous NNM and LP tracking. Merging and birth of IS with symmetry-breaking event are explained. A localization of motion is also observed when the in-phase mode is excited after the symmetry-breaking event. In Section 4.4, mass detection mechanisms are introduced according to the specific dynamical behaviors of the beams. First, mechanism of detection based on hysteresis cycle with asymmetric voltages are proposed. Two- and three-beam arrays are examined. Secondly, mass detection based on symmetry-breaking event are analyzed on a three-beam array. An analysis related to location, possible detection as well as quantification of the added mass is conducted.

Conclusions are drawn in Section 4.5. The originality of this chapter lies in the analysis of complex phenomenon specific to MEMS array and their exploitation to provide alternative mechanisms for mass sensing.

4.1 n-Beam array model

Let an array of n clamped-clamped beams be considered as sketched in Fig. 4.1. All the beams are assumed to have identical dimensions (length l, width b, height h and moment of inertia I) and identical material properties (Young's modulus E and material density ρ). Each beam is subjected to the electrostatic forces from its adjacent beams. The two beams at both ends of the array (beam 0 and $n+1$) are totally clamped and non-deformable and just serve for actuation. Let g be the gap between two adjacent beams.

4.1.1 Case without added mass

Let the deflection be in the xz plane and let $\tilde{w}_s$ be the lateral displacement along the z-axis of the s^{th} beam and $V_{s,s+1} = V_{dc_{s,s+1}} + V_{ac_{s,s+1}} \cos(\tilde{\Omega}\tilde{t})$ the voltage between s^{th} and $(s+1)^{\text{th}}$ beams. $\tilde{\Omega}, \tilde{t}$ denote physical forcing frequency and time respectively. V_{dc}, V_{ac} denote bias and alternative voltages respectively. The s^{th} beam is subjected to two electrostatic forces

- the first one due to the $(s+1)^{\text{th}}$ beam

$$f^e_{s,s+1} = \frac{1}{2} b\varepsilon_0 C_n \frac{V^2_{s,s+1}}{(g + \tilde{w}_{s+1} - \tilde{w}_s)^2}. \tag{4.1}$$

- the second one due to the $(s-1)^{\text{th}}$ beam

$$f^e_{s-1,s} = -\frac{1}{2} b\varepsilon_0 C_n \frac{V^2_{s-1,s}}{(g + \tilde{w}_s - \tilde{w}_{s-1})^2}. \tag{4.2}$$

ε_0, C_n are the dielectric constant and fringing field coefficient respectively. Consequently the equation of motion of the s^{th} beam in a n-beam array is:

$$\begin{aligned} EI\frac{\partial^4 \tilde{w}_s(\tilde{x},\tilde{t})}{\partial \tilde{x}^4} + \rho bh\frac{\partial^2 \tilde{w}_s(\tilde{x},\tilde{t})}{\partial \tilde{t}^2} + \tilde{c}\frac{\partial \tilde{w}_s(\tilde{x},\tilde{t})}{\partial \tilde{t}} - \\ \left[\tilde{N}_s + \frac{Ebh}{2l}\int_0^l \left(\frac{\partial \tilde{w}_s(\tilde{x},\tilde{t})}{\partial \tilde{x}}\right)^2 \mathrm{d}\tilde{x}\right] \frac{\partial^2 \tilde{w}_s(\tilde{x},\tilde{t})}{\partial \tilde{x}^2} \\ = \frac{1}{2}\varepsilon_0 \frac{bC_n V^2_{s,s+1}}{\left(g + \tilde{w}_{s+1} - \tilde{w}_s\right)^2} - \frac{1}{2}\varepsilon_0 \frac{bC_n V^2_{s-1,s}}{\left(g + \tilde{w}_s - \tilde{w}_{s-1}\right)^2}, \end{aligned} \tag{4.3}$$

with $s = 1, .., n$ and $\tilde{N}_s$ the residual axial force acting on the s^{th} beam and resulting from an externally applied load or from manufacturing stress. Beams #0 and #$(n+1)$ are totally

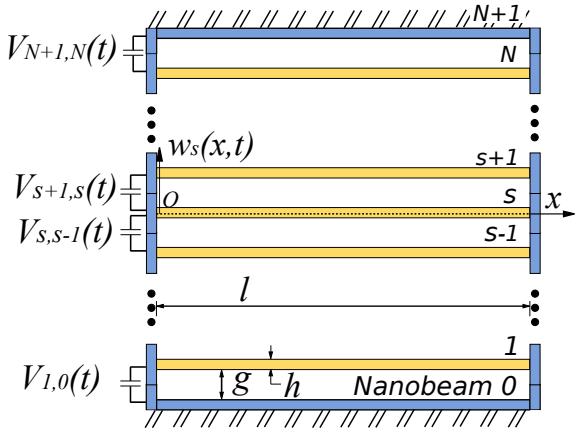

Figure 4.1 – Model of the clamped-clamped micro beam array.

clamped, so:

$$\tilde{w}_0(\tilde{x},\tilde{t}) = \tilde{w}_{n+1}(\tilde{x},\tilde{t}) = 0. \tag{4.4}$$

Introducing the following non-dimensional parameters

$$\begin{gathered} w_s = \frac{\tilde{w}_s}{g}; \quad x = \frac{\tilde{x}}{L}; \quad t = \frac{\tilde{t}}{\tau}; \\ c = \frac{\tilde{c}l^4}{EI\tau}; \quad N_s = \frac{\tilde{N}_s l^2}{EI}; \quad \alpha_1 = 6\big(\frac{g}{h}\big)^2; \\ \alpha_2 = 6C_n\frac{\varepsilon_0 l^4}{Eh^3g^3}; \quad \Omega = \tilde{\Omega}\tau, \end{gathered} \tag{4.5}$$

in Eq. (4.3), yields:

$$\begin{aligned} &\frac{\partial^4 w_s}{\partial x^4} + \frac{\partial^2 w_s}{\partial t^2} + c\frac{\partial w_s}{\partial t} - \Big[N_s + \alpha_1 \int_0^1 \big(\frac{\partial w}{\partial x}\big)^2 \mathrm{d}x\Big]\frac{\partial^2 w_s}{\partial x^2} \\ &\qquad = \alpha_2 \frac{V_{s,s+1}^2}{\big(1 + w_{s+1} - w_s\big)^2} - \alpha_2 \frac{V_{s-1,s}^2}{\big(1 + w_s - w_{s-1}\big)^2}. \end{aligned} \tag{4.6}$$

with $s = 1,..,n$ and the boundary conditions

$$w_s(0,t) = w_s(1,t) = \frac{\partial w_s}{\partial x}(0,t) = \frac{\partial w_s}{\partial x}(1,t) = 0, \tag{4.7}$$

$$w_0(x,t) = w_{n+1}(x,t) = 0, \tag{4.8}$$

By assumption, the n identical beams have identical linear undamped eigenmodes ϕ_k. Linear undamped eigenmodes ϕ_k are obtained from the simplification of the equation(4.6).

$$\frac{\partial^4 w}{\partial x^4} + \frac{\partial^2 w}{\partial t^2} = 0. \tag{4.9}$$

Then, a Galerkin expansion of the lateral displacement w_s is expressed with the N_m first modes:

$$w_s(x,t) \approx \sum_{k=1}^{N_m} \phi_k(x) a_k^s(t). \tag{4.10}$$

with $a_k(t)$ the time function and $\phi_k(x)$ the linear undamped eigenmodes solution of the following equation:

$$\frac{\partial^4 \phi_k(x)}{\partial x^4} - \lambda_k^4 \phi_k(x) = 0. \tag{4.11}$$

In [KAC 10a], ϕ_k is computed as such:

$$\phi_k(x) = A_k\Big(\cos\lambda_k x - \cosh\lambda_k x + \big[\frac{\cosh\lambda_k - \cos\lambda_k}{\sin\lambda_k - \sinh\lambda_k}\big]\big[\sin\lambda_k x - \sinh\lambda_k x\big]\Big), \tag{4.12}$$

with

$$A_k = \Big(\int_0^1 \Big[\frac{\phi_k(x)}{A_k} \Big]^2 \mathrm{d}x \Big)^{-\frac{1}{2}}. \tag{4.13}$$

and λ_k as the solution of the equation:

$$1 - \cos\lambda_k \cosh\lambda_k = 0. \tag{4.14}$$

Multiplying by the denominator or using Taylor series expansions are two methods to treat the electrostatic force in the RHS of Eq. (4.6). When using the multiplication by $(1+w_{s+1}-w_s)^2 \times (1+w_s-w_{s-1})^2$ in Eq. (4.6), additional terms with strong couplings are introduced and the difficulty of the problem increases. On the other hand, when using truncated Taylor series, the accuracy is usually bad at high amplitude [YOU 03]. To simplify the calculus during Taylor expansions, let the following notations be introduced:

$$X_s(x,t) = w_{s+1}(x,t) - w_s(x,t), \tag{4.15}$$

$$b_k^s(t) = a_k^{s+1}(t) - a_k^s(t), \tag{4.16}$$

with X_s the relative displacement and b_k the generalized coordinates between two consecutive beams, the relation between $X_s(x,t)$ and $b_k^s(x,t)$ being:

$$1 + w_{s+1} - w_s = 1 + \sum_{k=1}^{N_m} \phi_k(x) b_k^s(t) = 1 + X_s, \tag{4.17}$$

$$1 + w_s - w_{s-1} = 1 + \sum_{k=1}^{N_m} \phi_k(x) b_k^{s-1}(t) = 1 + X_{s-1}. \tag{4.18}$$

Since the resonators will operate at small amplitudes only (max $w_s \leq 0.45$), a seventh-order Taylor series is used [KAC 10a].

$$\begin{aligned} \frac{1}{(1+w_{s+1}-w_s)^2} \simeq & 1 - 2X_s + 3X_s^2 - \\ & 4X_s^3 + 5X_s^4 - 6X_s^5 + 7X_s^6 - 8X_s^7, \end{aligned} \tag{4.19}$$

$$\begin{aligned} \frac{1}{(1+w_s-w_{s-1})^2} \simeq & 1 - 2X_{s-1} + 3X_{s-1}^2 - 4X_{s-1}^3 + \\ & 5X_{s-1}^4 - 6X_{s-1}^5 + 7X_{s-1}^6 - 8X_{s-1}^7. \end{aligned} \tag{4.20}$$

The Galerkin procedure requires to multiply Eq. (4.6) by ϕ_i $(i = 1,..,N_m)$ and to integrate the result from 0 to 1 to obtain the second-order differential equations in time which are written in matrix form as follows:

$$\ddot{\boldsymbol{a}}^s + \boldsymbol{C}_0 \dot{\boldsymbol{a}}^s + \boldsymbol{K}_0 \boldsymbol{a}^s - \big(N + \alpha_1 T_2^s(\boldsymbol{a}^s)\big) \boldsymbol{K}_T \boldsymbol{a}^s =$$

$$\alpha_2 V_{s,s+1}^2 \boldsymbol{Q}_0 + \alpha_2 V_{s,s+1}^2 \Big[\boldsymbol{Q}_1 + \boldsymbol{Q}_2^s(\boldsymbol{b}^s) + \boldsymbol{Q}_3^s(\boldsymbol{b}^s) + \boldsymbol{Q}_4^s(\boldsymbol{b}^s) + \boldsymbol{Q}_5^s(\boldsymbol{b}^s) + \boldsymbol{Q}_6^s(\boldsymbol{b}^s) + \boldsymbol{Q}_7^s(\boldsymbol{b}^s) \Big] \boldsymbol{b}^s - \alpha_2 V_{s-1,s} V_{s-1,s}^2 \boldsymbol{P}_0 - \alpha_2 V_{s-1,s}^2 \Big[\boldsymbol{P}_1 + \boldsymbol{P}_2^s(\boldsymbol{b}^{s-1}) + \boldsymbol{P}_3^s(\boldsymbol{b}^{s-1}) + \boldsymbol{P}_4^s(\boldsymbol{b}^{s-1}) + \boldsymbol{P}_5^s(\boldsymbol{b}^{s-1}) + \boldsymbol{P}_6^s(\boldsymbol{b}^{s-1}) + \boldsymbol{P}_7^s(\boldsymbol{b}^{s-1}) \boldsymbol{b}^{s-1} \Big], \quad (4.21)$$

where $s = 1,..,n$, $\boldsymbol{a}^s = [a_1^s, a_2^s, ..., a_{N_m}^s]$ and $\boldsymbol{a}^{n+1} = \boldsymbol{a}^0 = 0$ resulting from Eq. (4.8). The matrices in Eq. (4.21) are detailed in 4.5.

The Harmonic Balance Method associated with the Asymptotic Numerical Method (HBM+ANM) [KAC 11] is used to solve Eq. (4.21). The ANM is preferred to a more conventional Newton-Raphson method because of the robustness of the ANM-based continuation and its ability to follow very complicated solution branches. First, Eq. (4.21) must be recast in quadratic form by introducing the following set of auxiliary variables:

	size
$\boldsymbol{y}^s = \dot{\boldsymbol{a}}^s$	N_m
$\boldsymbol{z}^s = \dot{\boldsymbol{y}}^s$	N_m
$\boldsymbol{\nu}^s = \boldsymbol{b}^s = \boldsymbol{a}^{s+1} - \boldsymbol{a}^s$	N_m
$\boldsymbol{bu}^s = \boldsymbol{b}^{s-1} = \boldsymbol{a}^s - \boldsymbol{a}^{s-1}$	N_m
$\boldsymbol{\nu 2}^s = \boldsymbol{\nu}^s \times \boldsymbol{\nu}^s$	N_m^2
$\boldsymbol{\nu 3}^s = \boldsymbol{\nu 2}^s \times \boldsymbol{\nu}^s$	N_m^3
$\boldsymbol{bu2}^s = \boldsymbol{bu}^s \times \boldsymbol{bu}^s$	N_m^2
$\boldsymbol{bu3}^s = \boldsymbol{bu2}^s \times \boldsymbol{bu}^s$	N_m^3
$\boldsymbol{AQ}^s = \boldsymbol{Q}_1 + \boldsymbol{Q}_2^s + \boldsymbol{Q}_3^s + \boldsymbol{Q}_4^s + \boldsymbol{Q}_5^s + \boldsymbol{Q}_6^s + \boldsymbol{Q}_7^s$	N_m^2
$\boldsymbol{BP}^s = \boldsymbol{P}_1 + \boldsymbol{P}_2^s + \boldsymbol{P}_3^s + \boldsymbol{P}_4^s + \boldsymbol{P}_5^s + \boldsymbol{P}_6^s + \boldsymbol{P}_7^s$	N_m^2
$v1^s = \alpha_2 V_{s,s+1}^2$	1
$v2^s = \alpha_2 V_{s-1,s}^2$	1
$t2^s = T_2^s(a^s)$	1
$\boldsymbol{AAQ}^s = v1^s \boldsymbol{AQ}^s$	N_m^2

$$\boldsymbol{BBP}^s = v2^s \boldsymbol{BP}^s \qquad N_m^2 \qquad (4.22)$$

so the new form of Eq. (4.21) adapted to HBM+ANM is:

$$\begin{array}{llll}
\dot{\boldsymbol{a}}^s = & & \boldsymbol{y}^s & \\
\dot{\boldsymbol{y}}^s = & & \boldsymbol{z}^s & \\
0 = & & \boldsymbol{\nu}^s - & \\
 & & (\boldsymbol{a}^{s+1} - \boldsymbol{a}^s) & \\
0 = & & \boldsymbol{bu}^s - & \\
 & & (\boldsymbol{a}^s - \boldsymbol{a}^{s-1}) & \\
0 = & & \boldsymbol{\nu}2^s - & \boldsymbol{\nu}^s \times \boldsymbol{\nu}^s \\
0 = & & \boldsymbol{\nu}3^s - & \boldsymbol{\nu}2^s \times \boldsymbol{\nu}^s \\
0 = & & \boldsymbol{bu}2^s - & \boldsymbol{bu}^s \times \boldsymbol{bu}^s \\
0 = & & \boldsymbol{bu}3^s - & \boldsymbol{bu}2^s \times \boldsymbol{bu}^s \\
0 = & -\boldsymbol{Q}_1 & +\boldsymbol{AQ}^s - \boldsymbol{Q}_2^s & -\boldsymbol{Q}_5^s - \boldsymbol{Q}_6^s \\
 & & -\boldsymbol{Q}_3^s - \boldsymbol{Q}_4^s & -\boldsymbol{Q}_7^s \\
0 = & -\boldsymbol{P}_1 & +\boldsymbol{BP}^s - \boldsymbol{P}_2^s & -\boldsymbol{P}_5^s - \boldsymbol{P}_6^s \\
 & & -\boldsymbol{P}_3^s - \boldsymbol{P}_4^s & -\boldsymbol{P}_7^s \\
0 = & \alpha_2 V_{s,s+1}^2 & -v1^s & \\
0 = & \alpha_2 V_{s-1,s}^2 & -v2^s & \\
0 = & & t2^s & -T_2^s(\boldsymbol{a}^s) \\
0 = & & \boldsymbol{AAQ} - & v1^s \times \boldsymbol{AQ}^s \\
0 = & & \boldsymbol{BBP} - & v2^s \times \boldsymbol{BP}^s \\
0 = & & \boldsymbol{z}^s + \boldsymbol{C}_0 \boldsymbol{y}^s + \boldsymbol{K}_0 \boldsymbol{a}^s & -\boldsymbol{AAQ} \times \boldsymbol{\nu} \\
 & & -v1^s \boldsymbol{Q}_0 + & +\boldsymbol{BBP} \times \boldsymbol{bu} \\
\underbrace{\qquad} & \underbrace{\qquad} & \underbrace{v2^s \boldsymbol{P}_0 - N\boldsymbol{K}_T \boldsymbol{a}^s} & \underbrace{-\alpha_1 t2^s \boldsymbol{K}_T \boldsymbol{a}^s} \\
m(\ddot{\boldsymbol{X}}^s) & = l_0(\Omega) & +l(\boldsymbol{X}^s) & +q(\boldsymbol{X}^s, \boldsymbol{X}^s)
\end{array} \qquad (4.23)$$

where: $\boldsymbol{X}^s$= ($\boldsymbol{a}^s$, $\boldsymbol{y}^s$, $\boldsymbol{z}^s$, $\boldsymbol{\nu}^s$, $\boldsymbol{bu}^s$, $\boldsymbol{\nu}2^s$, $\boldsymbol{\nu}3^s$, $\boldsymbol{bu}2^s$, $\boldsymbol{bu}3^s$, $\boldsymbol{AQ}^s$, $\boldsymbol{BP}^s$, $\boldsymbol{AAQ}^s$, $\boldsymbol{BBP}^s$, $v1^s$, $v2^s$, $t2^s$)^T is the unknown vector of size $5N_m + 3 + 6N_m^s + 2N_m^3$. For the array of n

beams, with $s = 1,..,n$, $\boldsymbol{X}$= $(\boldsymbol{X}^1, \boldsymbol{X}^2, \boldsymbol{X}^3, .., \boldsymbol{X}^n, \Omega)^T$ is the unknown vector of size $n \times (5N_m + 3 + 6N_m^s + 2N_m^3) + 1$.

4.1.2 Case with added mass

The presence of a small mass δm_p at position x_0 on the s_0^{th} beam introduces the extra term $\mu_0 \ddot{a}^s$ in Eq. (4.21), the matrix μ_0 being defined as follows:

$$\mu_{0ij} = \delta_{s_0}(s)\delta m \phi_i(x_0)\phi_j(x_0), \quad i,j = 1,..,N_m \tag{4.24}$$

with δ_{s_0} the Kronecker symbol, $\delta_{s_0}(s) = 1$ when $s = s_0$ and $\delta_{s_0}(s) = 0$ otherwise.

The mass ratio between the added mass δm_p and the mass of the beam is:

$$\delta m = \frac{\delta m_p}{\rho bhl} \tag{4.25}$$

It is used to replace the physical value of the added mass by a dimensionless value in the following sections.

4.1.3 Designs of beam array

This subsection describes the designs used in this chapter. The two-beam array of Section 4.2 is sketched in Fig. 4.2. All beams are identical with the material and design parameters: $h = 300nm$, $b = 160nm$, $l = 10\mu m$, $E = 1.69 \times 10^{11} N/m^2$, $\rho = 2330 kg/m^3$, the quality factor $Q = 5000$ and identical gaps $g = 200nm$ between two adjacent beams. The

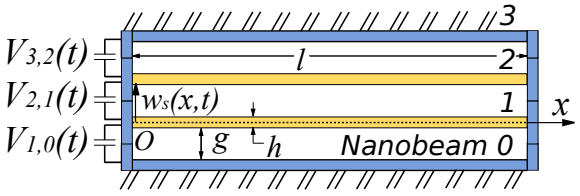

Figure 4.2 – Array of two clamped-clamped beams.

voltages combinations applied to the 2-beam array and given in Table (4.1) define three different designs. The three-beam array is considered with the same system parameters as in the two-beams array, see Fig. 4.3. The voltages combinations applied to the 3-beam array and given in Table (4.2) define four different designs.

4.1.4 Convergence in terms of Taylor expansion order

To validate the chosen Taylor expansion order T and number of spatial modes N_m of the model, the first design of two-beam array presented in Subsection 4.1.3 is considered, see Fig. (4.2). The beam responses plotted in Fig. 4.4 are tested with different Taylor-series

Table 4.1 – Actuation voltages in the two-beam array

Design	$V_{dc_{10}}(V)$ $V_{ac_{10}}(V)$	$V_{dc_{21}}(V)$ $V_{ac_{21}}(V)$	$V_{dc_{32}}(V)$ $V_{ac_{32}}(V)$
#1	0.3 0.3	0.45 0.45	0.6 0.6
#2	3 0.1	3 0	3 0.1
#3	3 -0.1	3 0	3 0.1

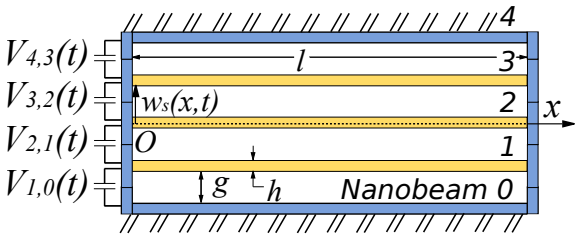

Figure 4.3 – Array of three clamped-clamped beams.

Table 4.2 – Symmetric actuation voltages of the 3-beam array.

Design	$Vdc_{10}(V)$ $Vac_{10}(V)$	$Vdc_{21}(V)$ $Vac_{21}(V)$	$Vdc_{32}(V)$ $Vac_{32}(V)$	$Vdc_{43}(V)$ $Vac_{43}(V)$
#1	0.5 0.5	0.3 0.3	0.5 0.5	0.4 0.4
#2	0 0	0.28 0.88	0.28 0.88	0 0
#3	0 0	5 1	5 1	0 0
#4	0 0	5.3 1	5.3 1	0 0

orders T and several modes N_m, by using HBM+ANM. For all the figures involving curves in colors below, the reader is referred to the on-line version of this paper. First, computa-

tions using third ($T = 3$), fifth ($T = 5$) and seventh ($T = 7$) order Taylor series are carried out with $N_m = 1$ mode. The difference between responses with fifth and seventh orders is negligible because Taylor series are accurate at small amplitude and responses seemingly converge with the seventh order Taylor series. Then, the influence of the number of modes in the Galerkin expansion is considered by using a Taylor series at order 7 with $N_m = 1$, $N_m = 2$ and $N_m = 3$. As seen in Fig. 4.4, the response is converged with $N_m = 2$ modes. Hence, using Taylor series at order 7 and $N_m = 2$ modes provides good accuracy. However, the computation with several modes is very time consuming and complicated. For the series at order 7, the relative error in frequency between $N_m = 1$ and $N_m = 2$ modes is less than $5.10^{-4}\%$ in frequency and quantitatively the response level does not change. For each case, the additional loops $D_1 - E_1$ (first beam) and $B_2 - C_2$ (second beam) on the response curves are the same. Consequently, Taylor series at order 7 and $N_m = 1$ mode are used to simplify the numerical calculation without loss of accuracy.

In Fig. 4.4, responses are more complicated than in the case of a single beam and present additional loops. A quasi-analytic solution obtained by the averaging method provides some explanations about the origin of these additional branches. In the following, the results are computed with the corresponding parameters, $H = 5$, $T = 7$, $N_m = 1$

4.2 Effect of the electrostatic coupling on a 2-beam array responses

In this section, effect of the electrostatic coupling is analyzed with the mean of averaging method. With the averaging method, the coupling terms can be identified. Once identified, the coupling terms can be withdrawn in order to visualize the effect of electrostatic coupling onto the responses curves. Then, the obtained results with averaging method are compared with time-integration methods to validate the results.

4.2.1 Averaging method

The beam lateral deflection is expanded on its fundamental mode only:

$$\begin{aligned} w_1(x,t) &= \phi_1(x) a_{11}(t) \\ w_2(x,t) &= \phi_1(x) a_{21}(t) \end{aligned} \tag{4.26}$$

First-order Taylor series are used to simplify the analytic calculation:

$$\begin{aligned} \frac{1}{(1+w_{s+1}-w_s)^2} &\simeq 1 - 2(w_{s+1} - w_s), \\ \frac{1}{(1+w_s-w_{s-1})^2} &\simeq 1 - 2(w_s - w_{s-1}). \end{aligned} \tag{4.27}$$

Using the averaging method and considering the solutions $a_{11}(t), a_{21}(t)$ in following forms

$$a_{11} = A_{11}(t)\cos(\Omega t) + B_{11}(t)\sin(\Omega t), \tag{4.28}$$

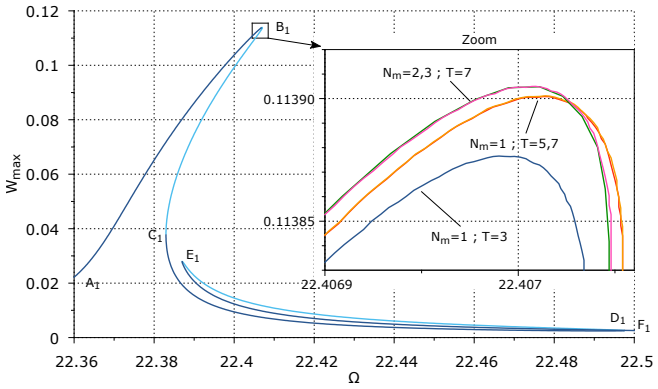

(a) Beam #1

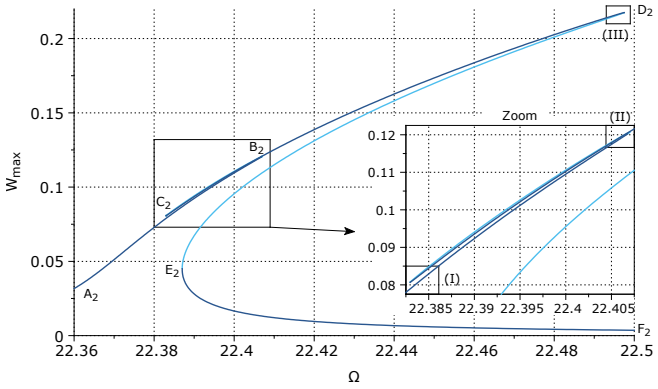

(b) Beam #2

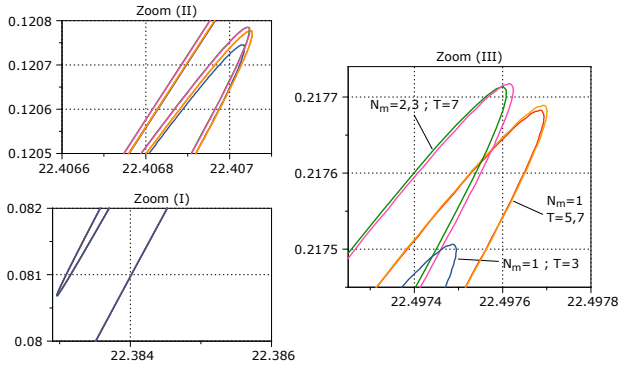

(c) Zoom of (I), (II), (III)

Figure 4.4 – 2-beam array with Design #1. Response curves of a two-beam array without added mass by HBM+ANM. Responses with third (blue), fifth (red) and seventh (orange) order Taylor series and $N_m = 1$ mode; responses with seventh-order Taylor series with $N_m = 2$ (pink) or $N_m = 3$ (green) modes. Dark and light blue colors indicate stable and unstable solutions respectively.

$$a_{21} = A_{21}(t)\cos(\Omega t) + B_{21}(t)\sin(\Omega t), \tag{4.29}$$

yields

$$\begin{aligned}\Omega\dot{A}_{11} \quad &= -B_{11}\omega_1\varepsilon\sigma_1 - \frac{1}{2}cA_{11}\Omega + \frac{3}{8}\beta_{11}A_{11}^2B_{11} \\ &+\frac{3}{8}\beta_{11}B_{11}^3 + \frac{1}{8}\beta_{13}B_{11} + \left(\frac{1}{2}\delta_{11} + \frac{1}{8}\delta_{13}\right)B_{21}\end{aligned} \tag{4.30}$$

$$\begin{aligned}\Omega\dot{B}_{11} \quad &= \frac{1}{2}cB_{11}\Omega + \frac{3}{8}\beta_{11}A_{11}^3 + \frac{3}{8}\beta_{13}A_{11} + \frac{1}{2}\gamma_{12} \\ &+\frac{3}{8}\beta_{11}A_{11}B_{11}^2 - A_{11}\omega_1\varepsilon\sigma_1 + \left(\frac{1}{2}\delta_{11} + \frac{3}{8}\delta_{13}\right)A_{21}\end{aligned} \tag{4.31}$$

$$\begin{aligned}\Omega\dot{A}_{21} \quad &= -B_{21}\omega_2\varepsilon\sigma_2 - \frac{1}{2}cA_{21}\Omega + \frac{3}{8}\beta_{21}A_{21}^2B_{21} \\ &+\frac{3}{8}\beta_{21}B_{21}^3 + \frac{1}{8}\beta_{23}B_{21} + \left(\frac{1}{2}\delta_{21} + \frac{1}{8}\delta_{23}\right)B_{11}\end{aligned} \tag{4.32}$$

$$\begin{aligned}\Omega\dot{B}_{21} \quad &= \frac{1}{2}cB_{21}\Omega + \frac{3}{8}\beta_{21}A_{21}^3 + \frac{3}{8}\beta_{23}A_{21} + \frac{1}{2}\gamma_{22} \\ &+\frac{3}{8}\beta_{21}A_{21}B_{21}^2 - A_{21}\omega_2\varepsilon\sigma_2 + \left(\frac{1}{2}\delta_{21} + \frac{3}{8}\delta_{23}\right)A_{11}\end{aligned} \tag{4.33}$$

The coefficients of Eq. (4.30-4.33) are defined in 4.5. In Eqs. (4.30-4.33), the coupling terms $(\frac{1}{2}\delta_{11} + \frac{1}{8}\delta_{13})B_{21}$ and $(\frac{1}{2}\delta_{11} + \frac{1}{8}\delta_{13})A_{21}$ represent the influence of the second beam on the first beam while the terms $(\frac{1}{2}\delta_{21} + \frac{1}{8}\delta_{23})B_{11}$, $(\frac{1}{2}\delta_{21} + \frac{3}{8}\delta_{23})A_{11}$ the influence of the first beam on the second beam. The steady-state motions occur when $\dot{A}_{11} = \dot{B}_{11} = \dot{A}_{21} = \dot{B}_{21} = 0$. This corresponds to an algebraic system of four nonlinear equations that can be solved numerically. The corresponding response curves are plotted in Figs. 4.5 and 4.6 and are in very good agreement with those of Fig. 4.4 obtained numerically by HBM+ANM.

4.2.2 Response curve analysis

Let Eqs. (4.30)-(4.33) be considered without these coupling terms. Therefore Eqs. (4.30)-(4.31) and (4.32)-(4.33) form two independent systems of equations. The response curves plotted in Figs. 4.5 and 4.6 are similar to those of a single beam because no loops are present.

With coupling terms Eqs. (4.30)-(4.33) are dependent, therefore they share the same bifurcations points and stability. Thus, the whole set of limits points on the two response

curves without coupling terms are present on each response with coupling terms. Figs. 4.5 and 4.6 show that, in the presence of coupling terms, points B_1 and C_1 on the first-beam response generate the loop $B_2 - C_2$ on the second-beam response. Identically, points D_2 and E_2 on the second-beam response produce the loop $D_1 - E_1$ on the first-beam response. The synchronization of stability leads to the appearance of additional loops on the response curve.

Moreover, the first-beam amplitude changes from $W_{max} = 0.15$ to $W_{max} = 0.11$, whereas the second-beam amplitude is weakly affected. This is because the amplitude of the $B_2 - C_2$ generated loop is larger than the $D_1 - E_1$ one. So, the amount of energy transferred from the first beam to the second beam due to the coupling is larger than the amount of energy transferred from the second-beam to the first-beam.

4.2.3 Comparison of the responses obtained with HBM+ANM and with time-integration methods.

The results obtained by these two methods for the two-beam array without added mass are represented in Fig. 4.7 and fit well. However, because of the response complexity, it is impossible to obtain all the stable branches by time integration with a simple frequency sweep-up and sweep-down. For example, in Fig. 4.7, the stable branches $jE_1 - jB_1$ (first beam) and $jE_2 - B_2$ (second beam) are not obtained. For the first beam, with a frequency sweep-down the response path is $F_1 - E_1 - jE_1 - C_1 - jC_1 - A_1$ where the letter j indicates an amplitude jump. Unlike the single-beam response, there are two jumps from E_1 to jE_1 and from C_1 to jC_1. For the second beam, the response path is $F_2 - E_2 - jE_2 - A_2$ with a jump from E_2 to jE_2 and point jE_2 is not on the stable branch $A_2 - B_2 - D_2 - jD_2 - F_2$ obtained by a frequency sweep-up but on the stable part of the $B_2 - C_2$ loop. Therefore, the pseudo arc-length continuation used in the HBM+ANM proves its efficiency and robustness here since it permits obtaining the complete response curve.

4.3 Dynamics of MEMS array after symmetry-breaking event induced by an added mass

In this section, the influence of an added mass on the dynamics of symmetric MEMS is analyzed. By adding a mass onto a symmetric beam array a symmetry-breaking event is induced. After such an event, the dynamics of the beam array is greatly influenced. An analysis of dynamic with/without symmetry-breaking event is performed on a 2-beam and a 3-beam array. The NNM of the array are computed before and after the symmetry-breaking event. Then, a parametric analysis with respect to the value of the added mass is performed by using tracking of LP. The bifurcation tracking reveals phenomena of INNM. Then, analysis of frequency responses before and after symmetric-breaking event is performed. Two analysis are performed with forces targeting successively the two NNMs. The use of those forces and energy balance allow to uncover IS of frequency

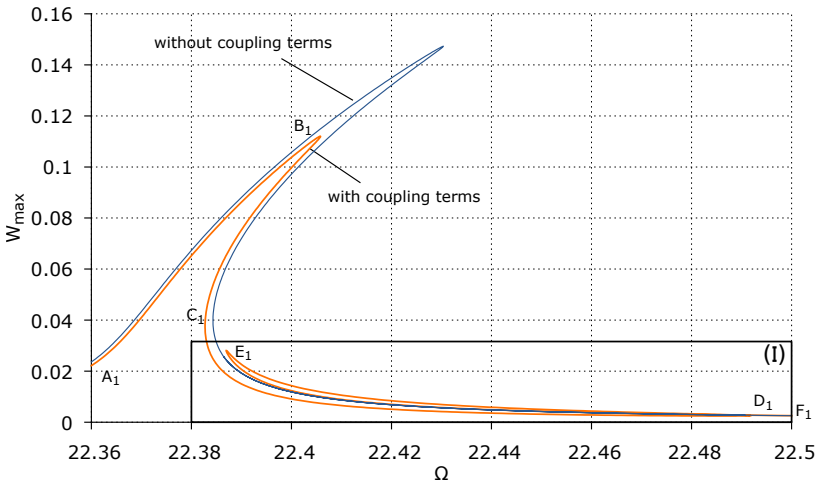

(a)

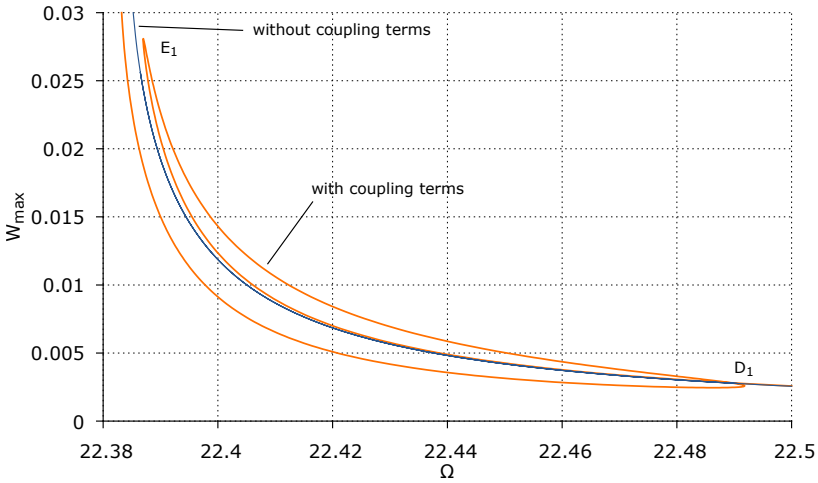

(b) Zoom I

Figure 4.5 – 2-beam array with Design #1 without added mass of Beam #1. Response by neglecting the coupling terms (blue), complete response (orange).

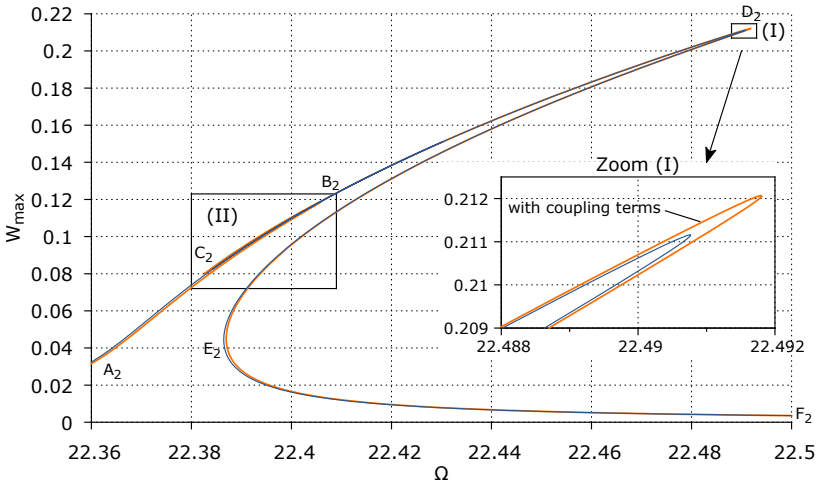

(a)

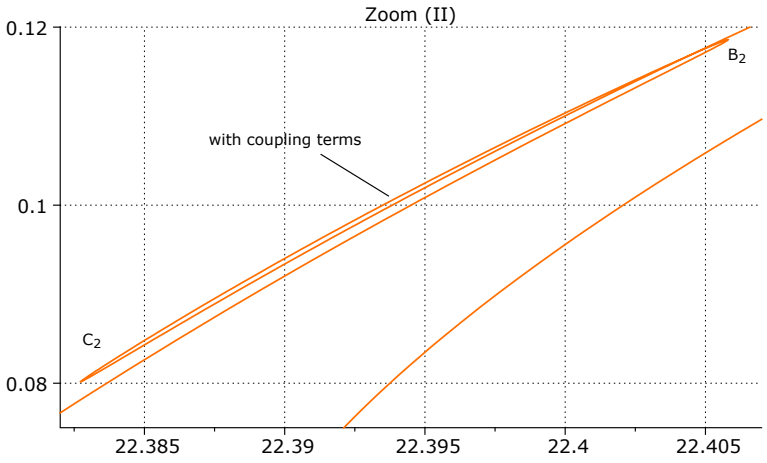

(b) Zoom II

Figure 4.6 – 2-beam array with Design #1 without added mass of Beam #2. Response by neglecting the coupling terms (blue), complete response (orange).

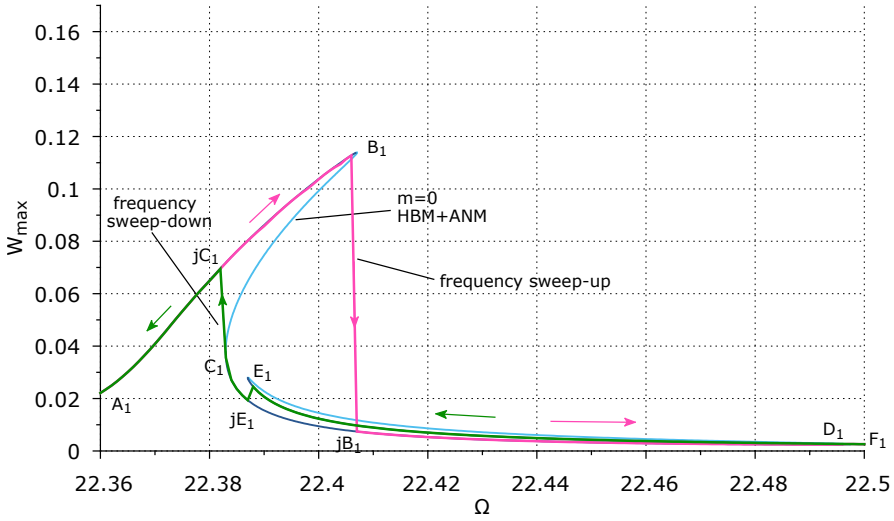

(a) Beam #1

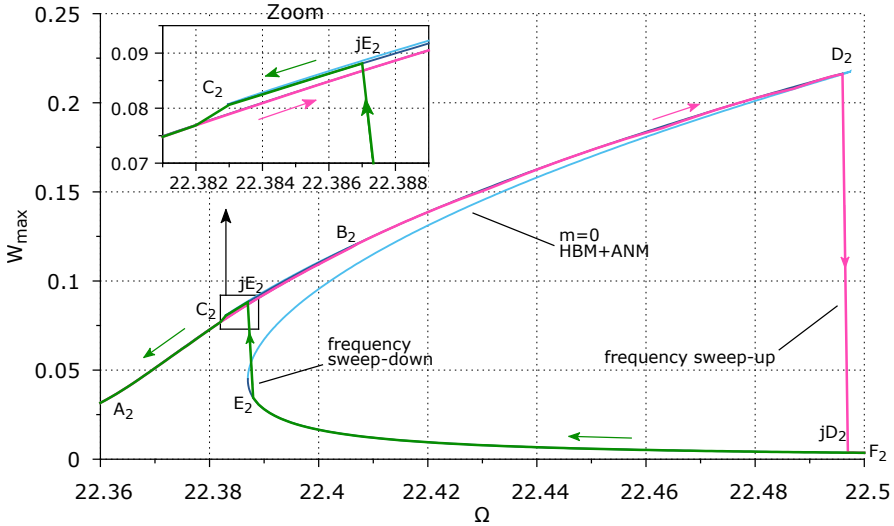

(b) Beam #2

Figure 4.7 – 2-beam array with Design #1. Comparison between HBM+ANM (dark blue: stable branches, light blue: unstable branches) and time integration method with a frequency sweep-up (pink curves) and a frequency sweep-down (green curves).

responses. Explanations of appearance and merging of IS are proposed. In this section bifurcation analysis needs to be performed. Therefore, all the computation in this section are made by using HBM+Galerkin+Taylor with respectively $H = 5$, $N_m = 1$ and $T = 7$.

4.3.1 Parametric analysis of NNM

In this subsection, the NNM of a symmetric two-beam array are computed before and after a symmetry breaking event induced by an added mass $\delta m = 10^{-4}$. The design #5 from Table (4.1) is considered to perform the NNM computation. The system exhibits two pure

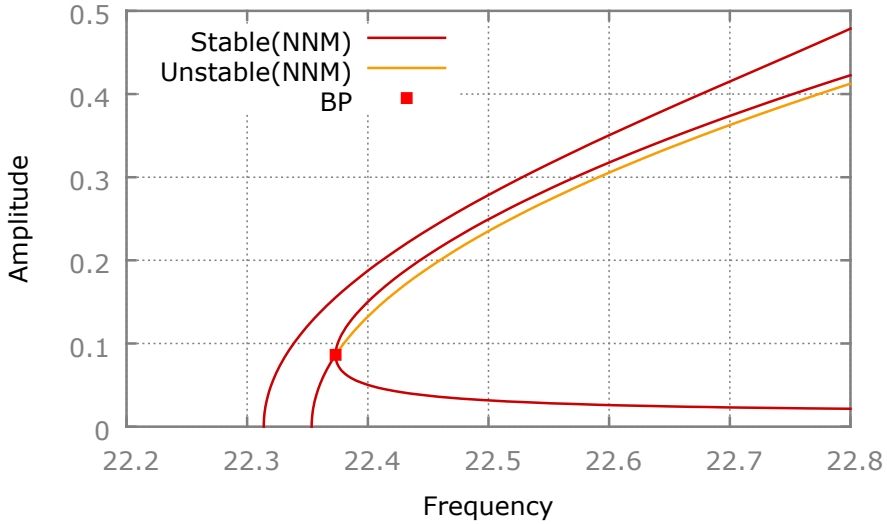

Figure 4.8 – 2-beam array with Design #2. Representation of NNM of the two beams ($\delta_m = 0$)

NNMs initialized using the Linear Normal Modes frequency and modal shape, see Fig 4.8. The denomination pure and mixed NNM below are defined as in [GOL 12a] [GOL 12b]. One can see on the NNM, that a BP appears on the second pure NNM initialized at the Frequency $\omega = 22.35$. The BP, also known as symmetry breaking point, is symptomatic of a symmetric system. Beyond the BP, the pure NNM becomes unstable and a new stable mixed NNM. A mixed NNM has a modal shape mixing modal shapes of the pure NNM of the system and therefore does not respect the symmetry of the problem. The given voltages from Design #2 , see Table(4.1), excite the first pure NNM and the mixed NNM. The first and second pure NNM correspond respectively to the out-of-phase and the in-phase NNM. Then, the added mass ($\delta_m = 10^{-4}$) is dropped onto the beam 1 inducing a symmetry-breaking event. The NNM of the beam array are computed with the added mass, see Fig. 4.9. With the added mass onto beam #1, the dynamic of the second NNM is completely changed. The BP has disappeared and the second NNM is now different on each beam. One beam #1, the second pure NNM is composed by the previous lower energy part of the second pure NNM and lower energy mixed NNM. Moreover

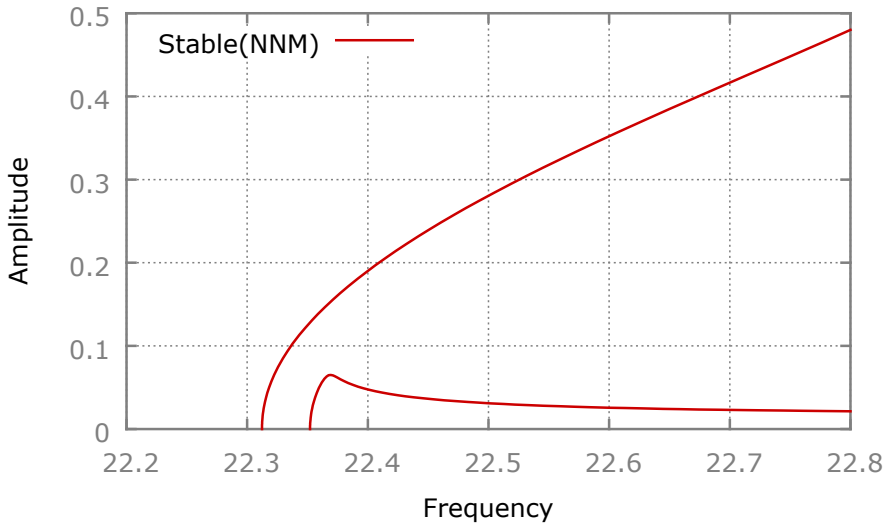

(a) Beam #1

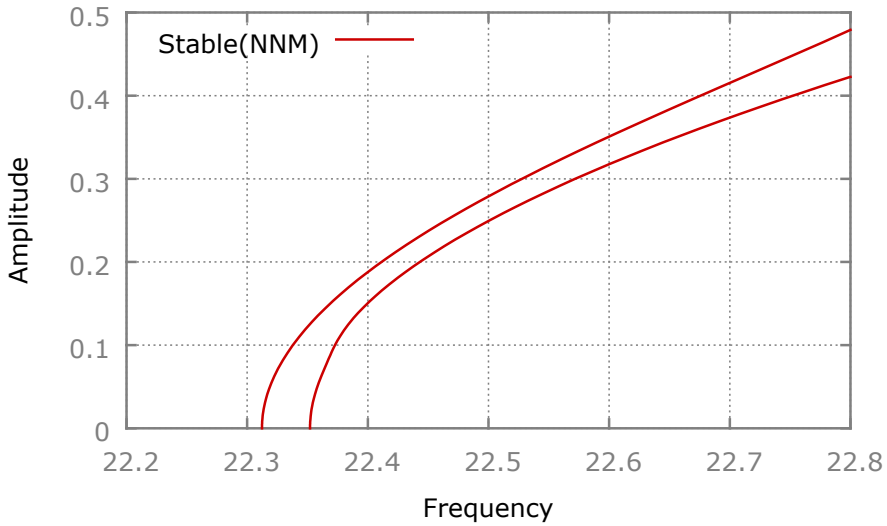

(b) Beam #2

Figure 4.9 – 2-beam array with Design #2. Representation of NNM after symmetry breaking with a added mass $\delta_m = 10^{-4}$

the system now being non-symmetric has different modal shape on each beam. On the second beam after symmetry breaking, the left part of the previous second pure NNM and the mixed NNM form the second pure NNM. A phenomenon of localization of motion can be observed. The beam where the mass is added has an amplitude of motion on the second pure NNM lower than on the other beam. In the Subsection 3.5.2, such localization phenomenon has already been encountered and linked to the birth of IS onto INNM. To verify the presence of IS and INNM, a bifurcation tracking of LP point along the value of the added mass initialized with the BP at $\delta m = 0$ is performed. With the use of LP tracking, the NNMs presented in Fig. 4.10 have been obtained. INNMs are detected and obtained with a branching method a the value of the added mass $\delta m = 10^{-4}$. One the first beam the INNM is composed by the upper part of the second pure NNM and mixed NNM, while the right part of the previous second pure NNM and mixed NNM compose the INNM on the second beam. To better analyze the evolution of the dynamic when the symmetry-breaking event occurs, the parametric analysis using bifurcation tracking of the LP is presented, see Fig. 4.11. One can see that the more the mass of the added value increase the more the NNMs move away from the location of the previous BP. In this subsection, the effect of symmetry-breaking event induced by the addition of a added mass onto the first beam of a two-beam array has been investigated with the help of NNM. The breaking of the symmetry induces the breaking of the BP generating INNM and a phenomena of localization of motion. In the next subsection, the analysis of symmetry-breaking event is analyzed with the use of frequency responses.

4.3.2 Analysis of frequency responses

In this subsection, the analysis of symmetry-breaking is performed in the light of frequency responses. The first NNM (out-of-phase) is targeted with a forcing vector respecting the symmetry of the mode, see Design #2 in Tab. 4.1. Then, the second NNM (in-phase) is targeted with the voltages in Design #3 in Tab. 4.1. Particular behaviors on the IS depend on which type of NNM the IS are linked to. The originality lies in the detection and analysis of IS and NNM before and after symmetry breaking in a MEMS array using bifurcation tracking, continuation methods and energy balance.

Out-of-phase NNM excited First, the frequency responses curves are computed with respect to the Design #2 in Tab. 4.1, see Fig. 4.12. The two NNMs are either in-phase or out-of-phase due to the symmetry of the system and are therefore orthogonal to each other. One can see that the first NNM is well targeted with the symmetrical voltages V_{ac} and that the second NNM do not respond due to the orthogonality of the two modes. In Fig. 4.8, a mixed NNM is emanating from the in-phase mode. The modal shape of the mixed NNM is composed by both modal shape of the two pure NNMs. Therefore, one could suppose that IS are present on those mixed NNM branches.

To verify this hypothesis, an energy balance can be performed to observe the multiplier coefficient d that has to be applied to V_{ac} in order to target specific point onto the NNM. Since MEMS present low damping the fictive force obtained with undamped

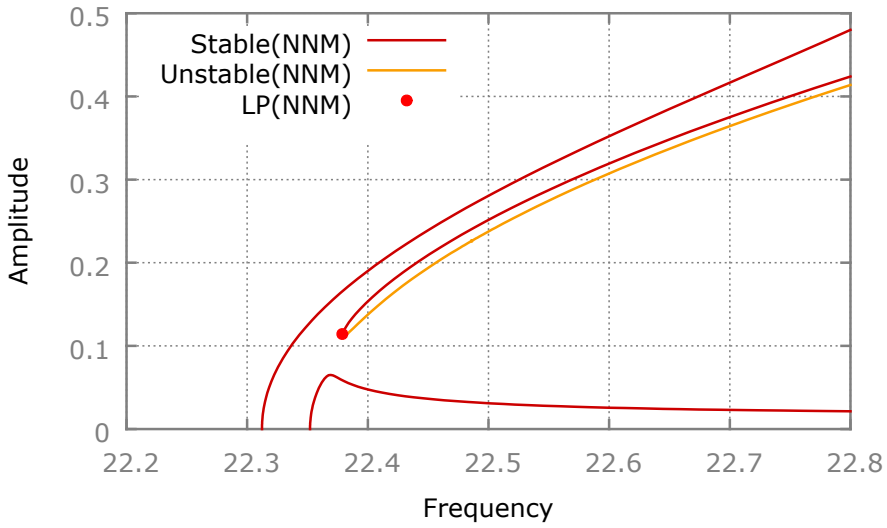

(a) Beam #1

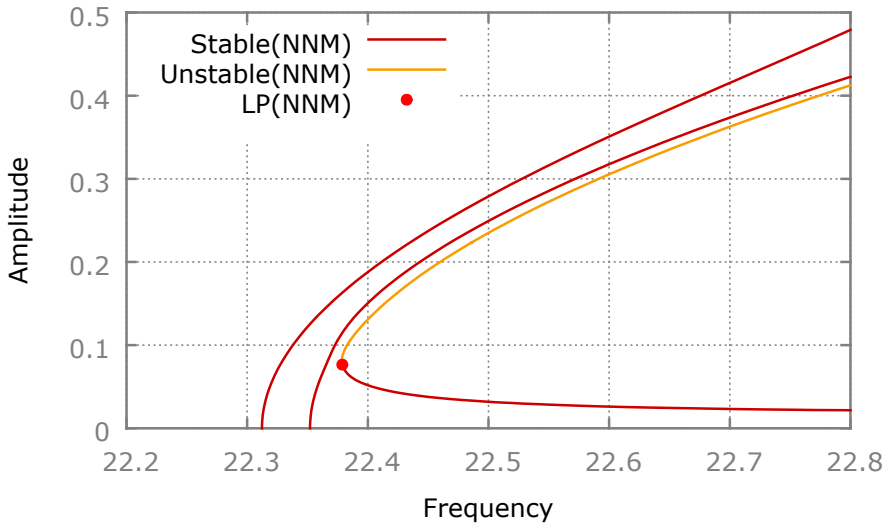

(b) Beam #2

Figure 4.10 – 2-beam array with Design #2. Representation of NNMs with their IS branches ($\delta_m = 10^{-4}$)

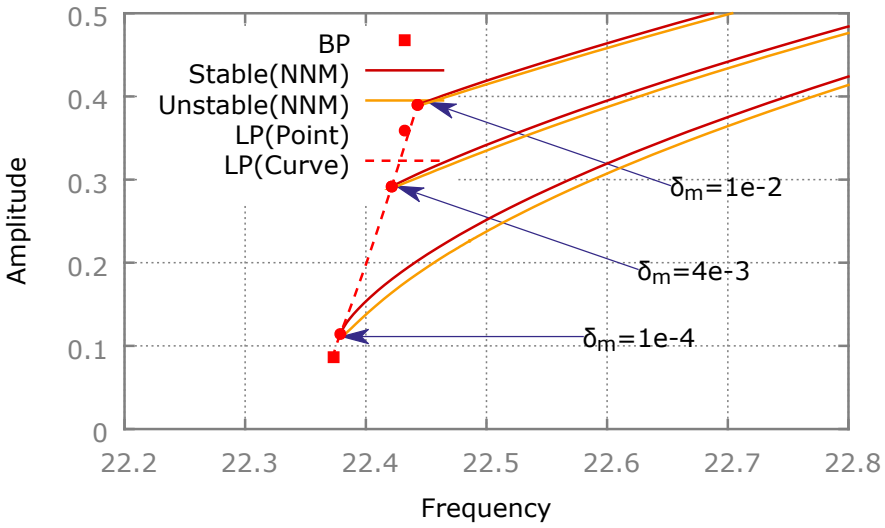

(a) Beam #1

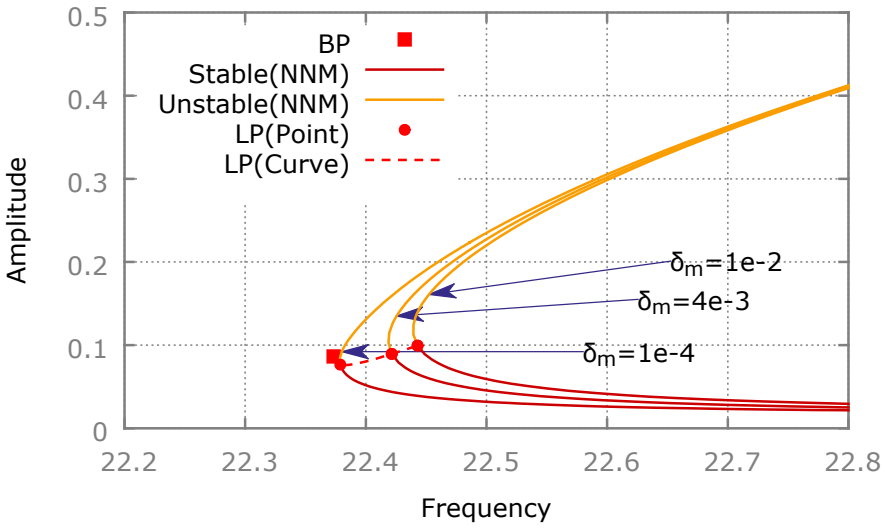

(b) Beam #2

Figure 4.11 – 2-beam array with Design #2. Bifurcation tracking of LP for the characterization of the isolated branches of NNM

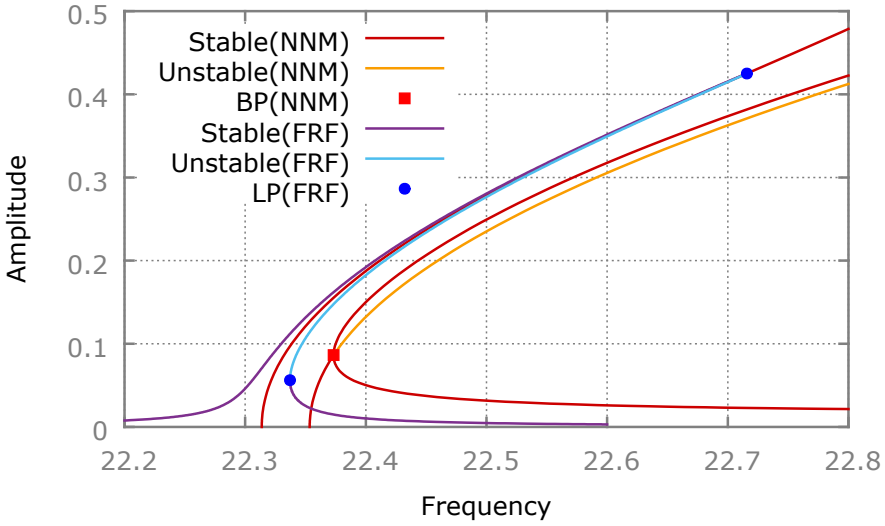

Figure 4.12 – 2-beam array with Design #2 before symmetry-breaking. Frequency response with the out-of-phase mode excited ($\delta_m = 0$)

phase resonance is used to perform the energy balance. The fictive force when the phase resonance is computed can be calculated such as:

$$\boldsymbol{F}_{fic}^{\phi} = (\nabla \otimes \boldsymbol{C})\,\boldsymbol{X} \tag{4.34}$$

The forcing vector $\boldsymbol{F}$ in the MEMS array is proportional to V^2. Therefore, $\boldsymbol{F}$ can be decomposed in three vectors $(\boldsymbol{F}_0, \boldsymbol{F}_1, \boldsymbol{F}_2)$ proportional respectively to $(1, V_{ac}, V_{ac}^2)$. $\boldsymbol{F}_0$ being a conservative force can be withdrawn from the energy balance equation. Then, the multiplier coefficient d can be computed from the energy balance, see Eq. (4.35).

$$\boldsymbol{X}^T \left(\nabla^2 \otimes \boldsymbol{C}\right) \boldsymbol{X} = d\boldsymbol{X}^T (\nabla \otimes \boldsymbol{I})\,\boldsymbol{F}_1 + d^2 \boldsymbol{X}^T (\nabla \otimes \boldsymbol{I})\,\boldsymbol{F}_2 \tag{4.35}$$

With respect the voltages presented in the Design #2, the multiplier coefficient d is obtained along the NNM, see Fig. 4.13. The y-axis represent the multiplier coefficient d applied to the forcing vector in order to target NNMs. The mixed NNM present a asymptotic behavior when it approaches the BP. A infinite multiplier coefficient d would be needed for the BP to be targeted by the frequency response with respect to the Design #2. This behavior is the direct consequence of the two pure NNMs being orthogonal to each other. For a multiplier coefficient of $d = 1$, the mixed NNM is crossed in four points $(A2, A3, A4, A5)$. Therefore, with the Design #2, ISs should be found on each side of the mixed NNM. At those four points, the corresponding frequency and Fourier coefficient of the displacement vectors are used to initialized the computation of those ISs, see Fig. 4.14. One can see that the points $(A1, A2, A5)$ are superposed with LPs contrarily to the two points $(A3, A4)$ closer to the second NNM. A symmetry-breaking event is generate by the addition of an added mass $(\delta m = 10^{-4})$ onto the first beam of the array. Then an mass of $\delta m = 10^{-4}$ is added onto the first beam of the array to generate a symmetry-breaking

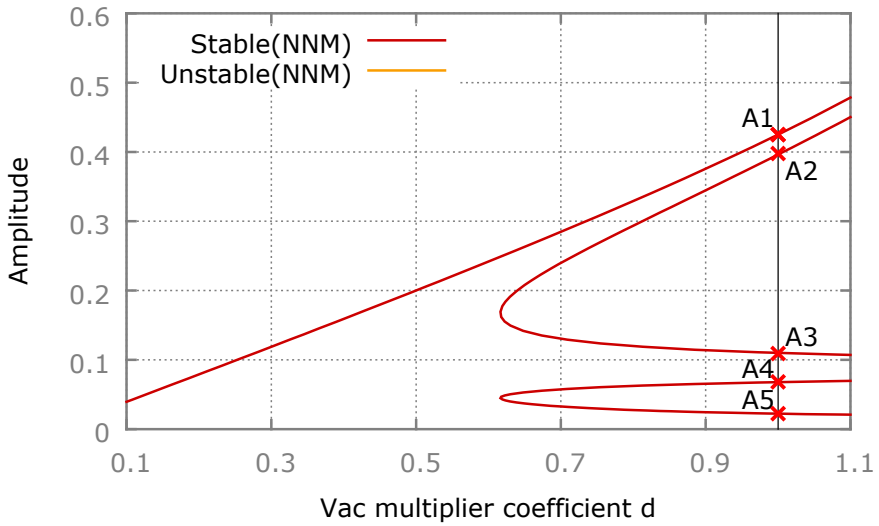

Figure 4.13 – 2-beam array with Design #2 before symmetry-breaking. Energy balance with $\delta_m = 0$

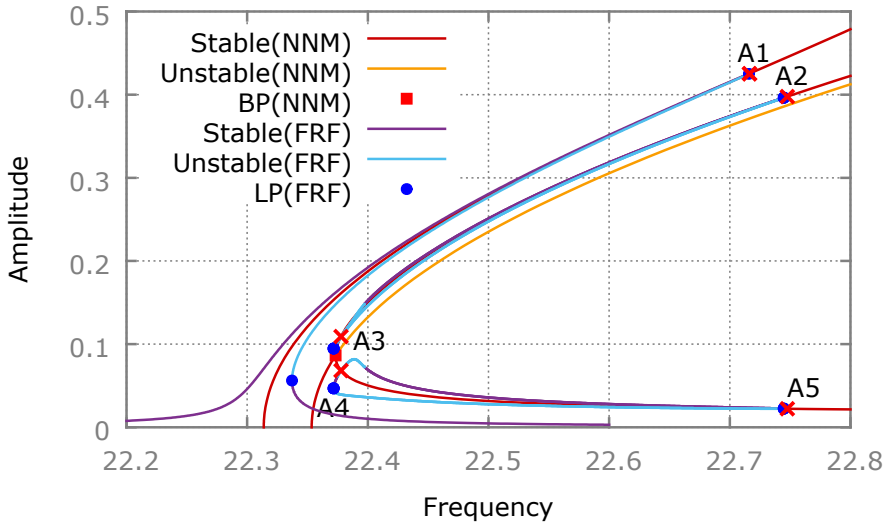

Figure 4.14 – 2-beam array with Design #2 before symmetry-breaking. Frequency responses and IS with the out-of-phase mode excited ($\delta_m = 0$)

event. After the event, the following frequency responses are computed. The energy balance is used to provide solutions points for the initialization of IS computation, see Fig. 4.15. The frequency responses and the NNMs fit well. Since the symmetry of the system

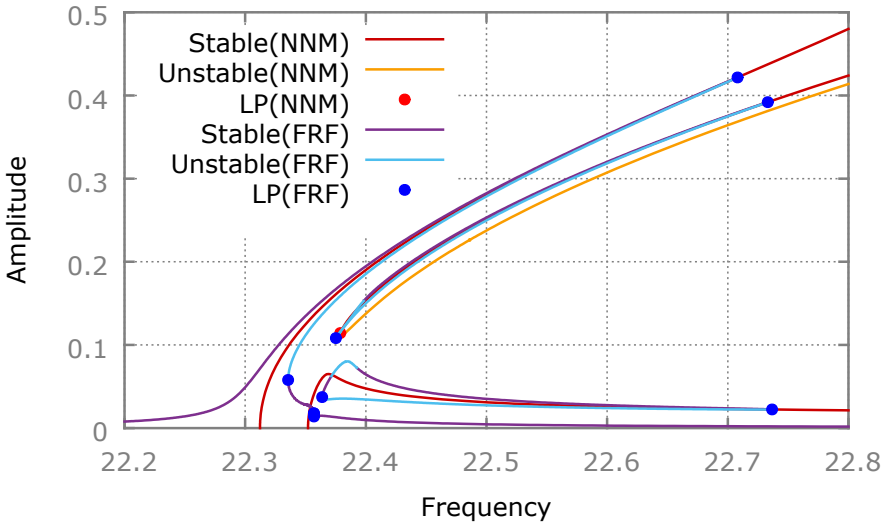

(a) Beam #1

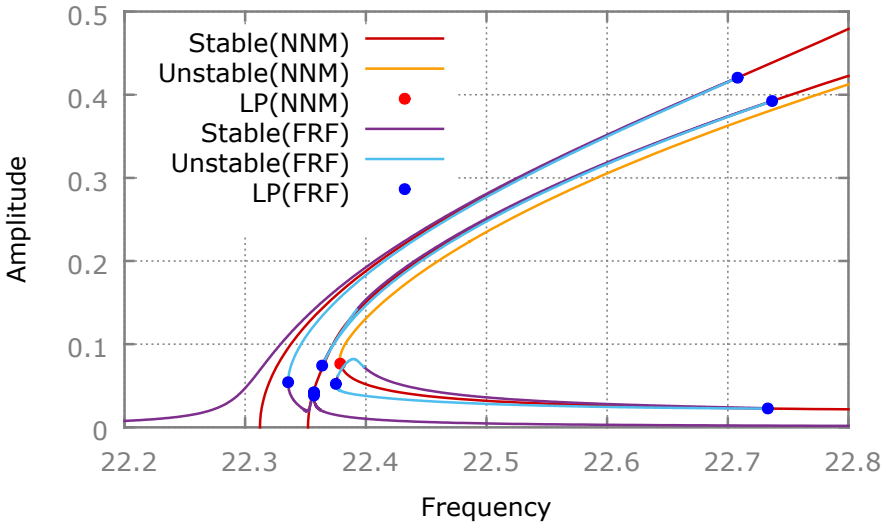

(b) Beam #2

Figure 4.15 – 2-beam array with Design #2 after symmetry-breaking. Frequency responses and IS with the out-of-phase mode excited ($\delta_m = 10^{-4}$)

has been broken, the two NNMs are no longer orthogonal. Therefore, the second pure NNM is now composed partially by the previous mixed NNM and responds to the current excitation. The IS found onto the second pure NNM is supported by an excited NNM. Consequently, for a high enough amplitude of voltages with respect to the current shape of excitation, the IS supported by the second pure NNM could merged with the response

curve. On the other hand, the IS found onto the INNM is totally isolated from any excited NNM. Hence, the IS will remain isolated even for higher amplitude and/or other shapes of excitation. A LP bifurcation tracking is performed with respect to the amplitude of the forcing vector to analyze the merging behaviors of the IS, see Figs. 4.16 and 4.17. The LP

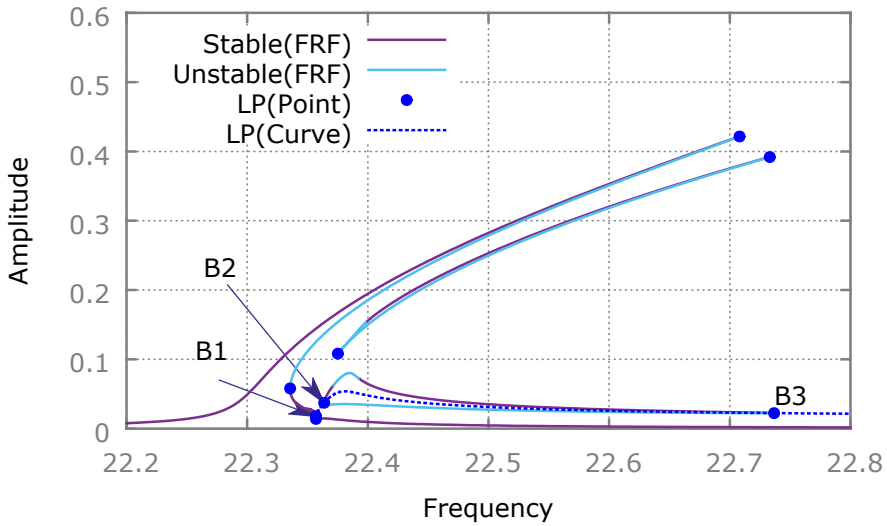

(a) Beam #1

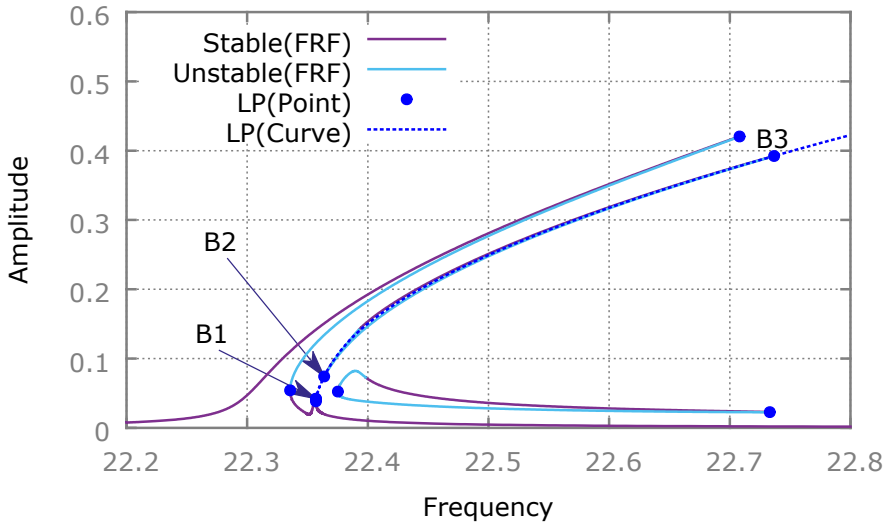

(b) Beam #2

Figure 4.16 – 2-beam array with Design #2. LP tracking with respect to the amplitude of forcing ($\delta_m = 10^{-4}$)

curve passes by the IS present on the excited pure NNM at points $(B2, B3)$. The evolution of the multiplier coefficient d during the LP tracking presented is used to detect the presence of IS. An IS is detected when the system parameter that has been liberated to perform the continuation crosses back its initial value. In Fig. 4.17, the IS can be detected when

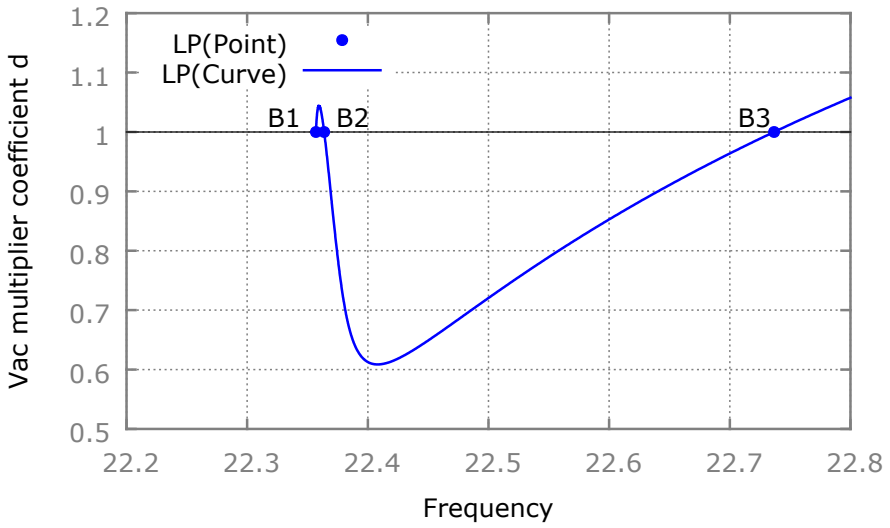

Figure 4.17 – 2-beam array with Design #2. Visualization of LP tracking in the d-Frequency plane ($\delta_m = 10^{-4}$)

the LP curve has a multiplier coefficient $d = 1$. Since the LP curve crosses $d = 1$ at two points $(B2, B3)$ that are not on the main frequency response, IS are detected and branching method can be used to compute them. Therefore, LP tracking is another way to detected and computed the IS. Moreover, this method is more adapted for frequency responses analysis compared to the method involving energy balance that is more adapted for NNM analysis. The LP curve can also be used to obtain the multiplier coefficient d threshold at which merging and birth of IS occurs. One can see that the IS and the frequency response merge for a forcing vector multiplied by $d \approx 1.05$. The minimum multiplier coefficient necessary for IS to appear can be also determined at $d \approx 0.61$. The other IS supported by the INNM is not linked to the frequency response by the LP tracking. Consequently, IS supported by INNM can never merge with the frequency response for any amplitude and shape of excitation with respect to the taken system parameters. Another way to obtain the IS would be to perform a LP tracking with respect to the value of the added mass. In Fig. 4.19a, the evolution of IS with respect to the added mass is presented with respect to the frequency and the value of the added mass δm. The curve $\delta m = 10^{-4}$ is crossed twice at the same two points $(B2, B3)$. Those points are used to initialized the IS supported by the pure NNM, see Figs. 4.18a and 4.18b. Therefore, IS found onto a pure NNM can be initialized using LP tracking with respect to the value of the added mass. On the zoom Fig. 4.19b, the IS merge with the main frequency response for $\delta m > 1.21 \times 10^{-4}$. Consequently, the IS can be reattached to the main frequency response by increasing the break in the symmetry of the system. To our knowledge, the use of this phenomenon for mass detection purposes is limited because the ISs are positioned in the unstable part of the out-of-phase NNM and therefore cannot be easily reached by frequency sweep. However, in the next paragraph, the mass detection based on symmetry-breaking of the in-phase mode is more promising.

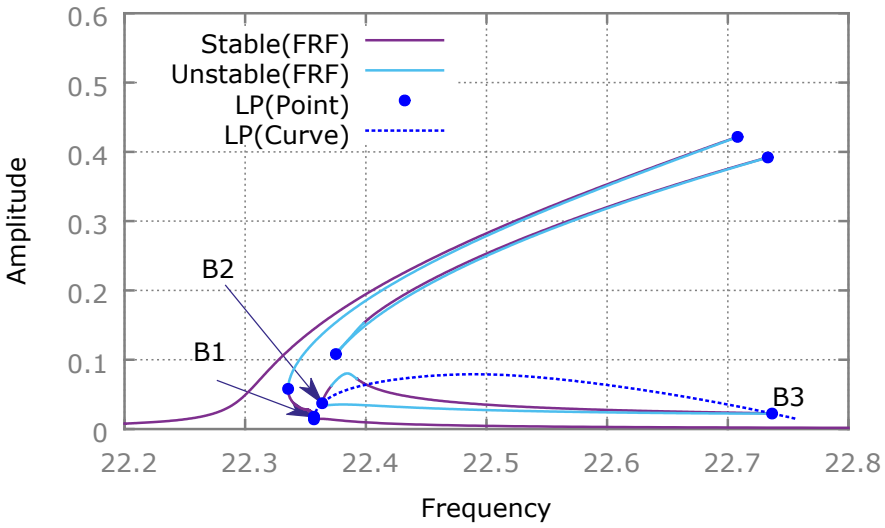

(a) Beam #1

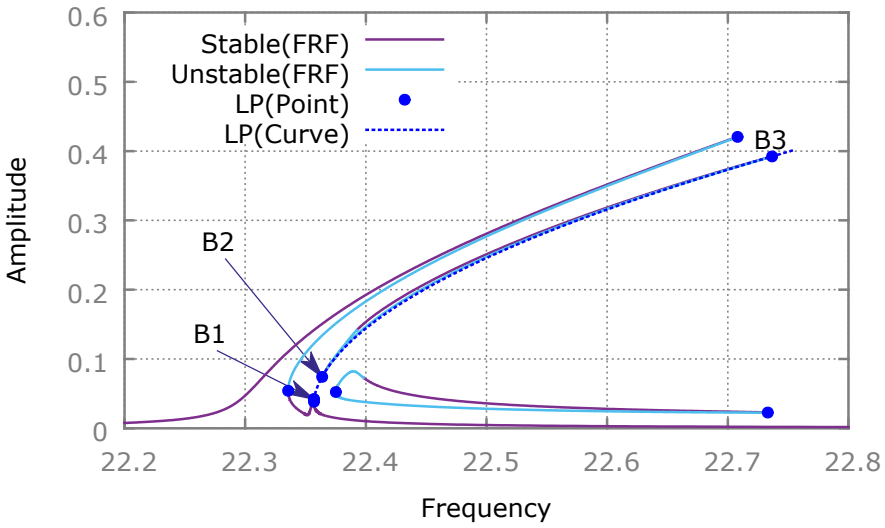

(b) Beam #2

Figure 4.18 – 2-beam array with Design #2. LP tracking with respect to the value of the added mass δm. Frequency responses obtained for $\delta_m = 10^{-4}$

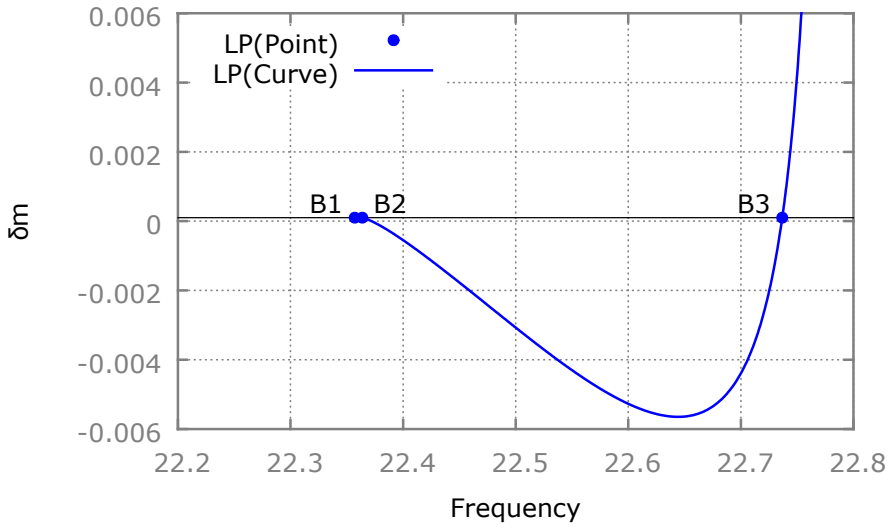

(a)

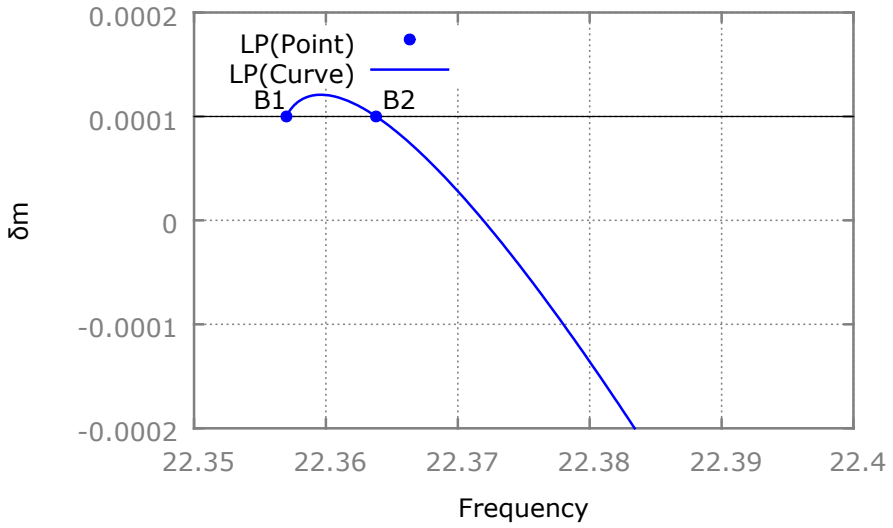

(b) Zoom

Figure 4.19 – 2-beam array with Design #2. Visualization of the LP tracking in the δ_m-Frequency plane

In-phase NNM excited The frequency responses are computed with respect to Design #3, Tab. 4.1. To better visualized the frequency responses with their corresponding NNM, the part emanating from BP bifurcations and the other part are plotted separately, see Fig. 4.20. The second NNM is well targeted with the symmetrical voltages V_{ac} and

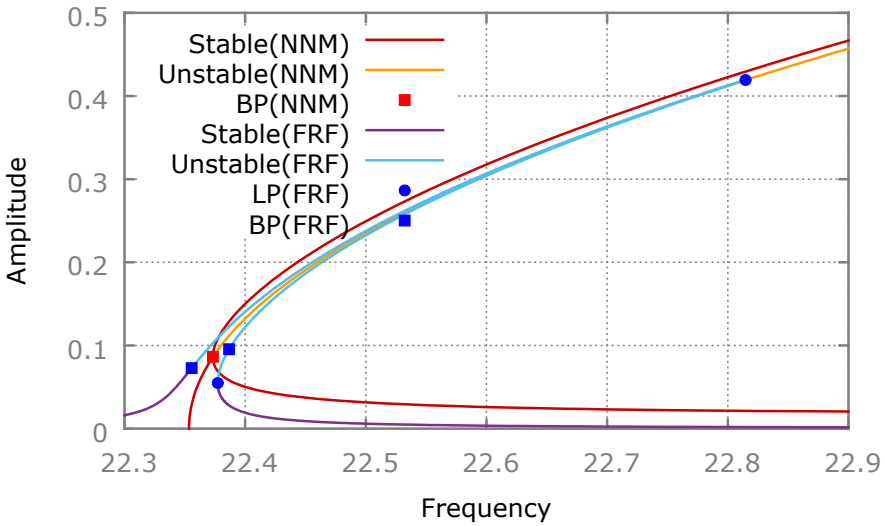

(a) Beam #1 and #2 (Without branching of Frequency responses)

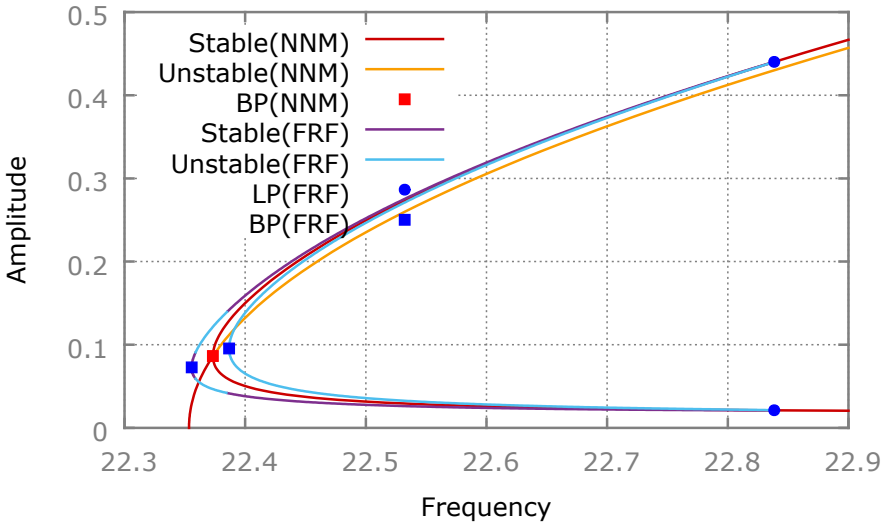

(b) Beam #1 and #2 (With only the branched Frequency responses)

Figure 4.20 – 2-beam array with Design #3 before symmetry-breaking. Frequency response with the in-phase mode excited ($\delta_m = 0$)

that the first NNM does not respond due to the orthogonality of the two modes. On the stable part of the excited pure NNM, the frequency responses are stable until BP are encountered. Then, the frequency responses become unstable and are supported by the unstable part of the excited pure NNM, see Fig. 4.20a. The BP encountered onto the

frequency response represent a symmetry-breaking bifurcation. From those BP, additional branches of frequency responses appear, see Fig. 4.20b. Being supported by a mixte NNM, these frequency responses do not respect the symmetry of the system.

Then, the added mass ($\delta m = 10^{-4}$) is added onto the first beam of the array to generate a symmetry-breaking event breaking the underlying symmetry of the system. Once the symmetry is broken, the following responses curves are obtained, see Fig. 4.21. With the current Design #3 targeting the in-phase NNM, the symmetry-breaking event influence way more the dynamic of the MEMS array. After the symmetry-breaking event induced by the addition of an added mass onto the first beam, a localization of motion appears onto the second beam. The obtained frequency responses are in good agreement with the NNM presented in Fig. 4.10.

As explained in Subsection 3.5.2, after symmetry-breaking event, the NNMs are composed of pure NNMs and INNM, both composed from previous part of both mixed and pure NNMs. Since IS are found onto the INNM when the out-of-phase NNM is excited, see Fig. 4.20, it could be supposed ISs to be present onto the INNM. To verify this hypothesis an energy balance is performed, see Eq. 4.35 and Fig. 4.22.

After symmetry-breaking event, the obtained energy balance onto the NNMs is different from the one obtained with the out-of-phase NNM excited, see Fig. 4.22. With the in-phase NNM excited and the symmetry broken, the IS onto the INNM starts to appear on point of NNM the closest to the previous second NNM. This is why no infinite asymptote in d is present close to the second NNM and that IS starts to appears close to the LP supported by the INNM at $d \approx 0.28$. For a multiplier coefficient of $d = 1$ the INNM is crossed in two points $(C2, C3)$. Therefore, a single IS supported by all the INNM should be present onto the frequency responses. At the points $(C2, C3)$, the corresponding frequency and Fourier coefficient are used to initialized the ISs, see Fig. 4.23. One can see that the IS is well detected and computed. Moreover, the IS is supported by the entirely INNM and not only the INNM composed essentially by the previous mixed NNM as in the results obtained with the Design #2.

Another way to detect those ISs is to exploit the merge of the IS and the frequency response when the MEMS array is symmetrical. LP tracking can detect and compute the IS if the IS and the frequency response are merged in the symmetrical configuration. To exploit such property, a LP tracking with respect to the value of the added mass is performed, see Fig. 4.24 During the LP tracking, the first part of the curve have $\delta m < 0$. Then the LP curve cross the first time $\delta m = 10^{-4}$ at point $D2$. At this point, one known that a IS is present and a branching method can be applied to compute the IS. The rest of the curve represent the evolution of the IS with respect to the value of the added mass δm. It reaches a peak a $\delta m \approx 0.02$. So for any added mass $\delta m > 0.02$, no IS are present onto the INNM with respect to the current voltages.

In symmetrical configuration, NNMs of the MEMS array are composed of mixed and pure NNMs. The mode shape of the mixed NNMs are composed by a mix of mode shape of pure NNMs of the system. When mixed NNM possesses IS, two cases can be distinguished. When the pure NNM that support the mixed NNM is not excited, then the IS cannot merge with the frequency response for any amplitude of forcing. When the pure

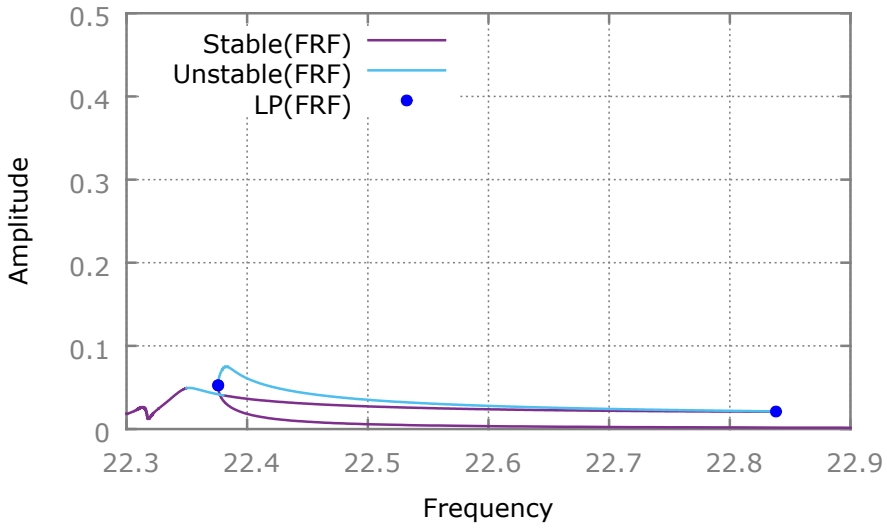

(a) Beam #1

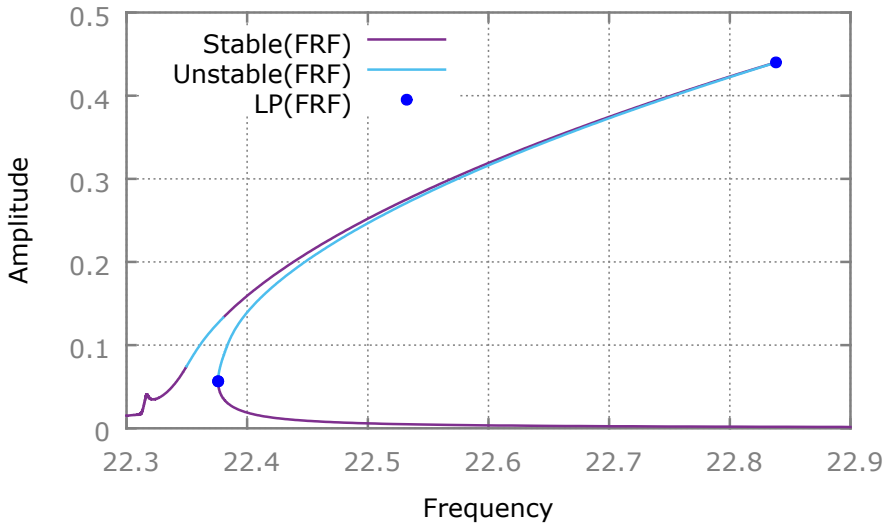

(b) Beam #2

Figure 4.21 – 2-beam array with Design #3 after symmetry-breaking. Frequency responses with the in-phase mode excited ($\delta_m = 10^{-4}$)

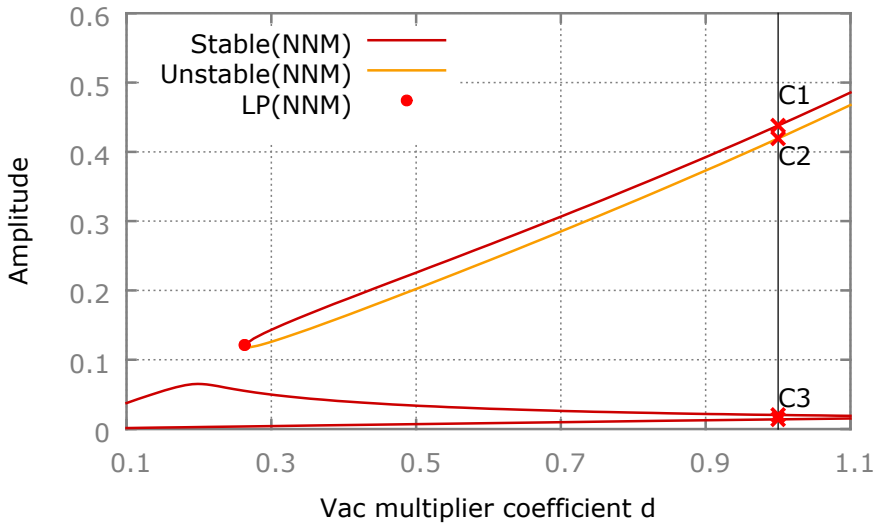

(a) Beam #1

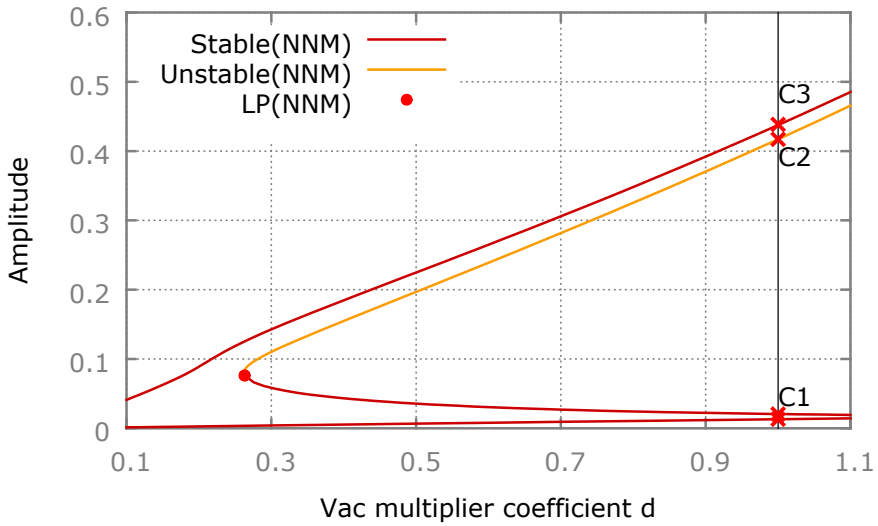

(b) Beam #2

Figure 4.22 – 2-beam array with Design #3 after symmetry-breaking. Energy balance with the in-phase mode excited ($\delta_m = 10^{-4}$)

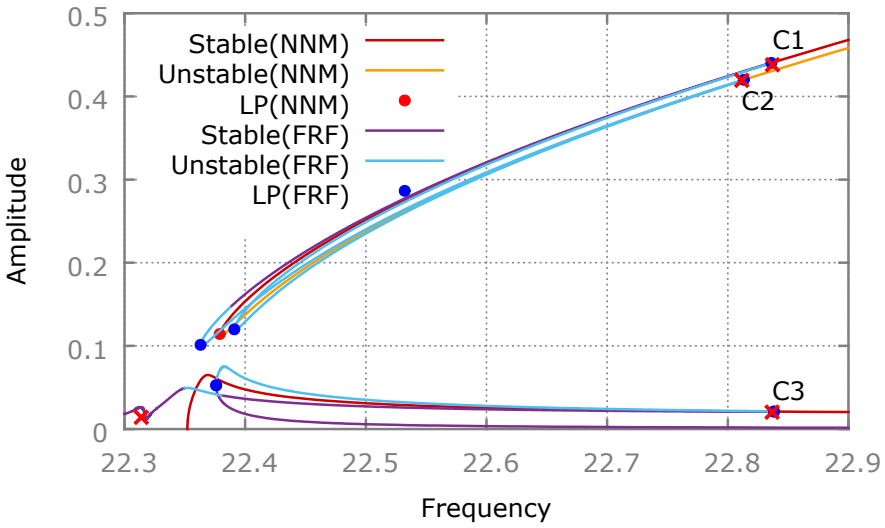

(a) Beam #1

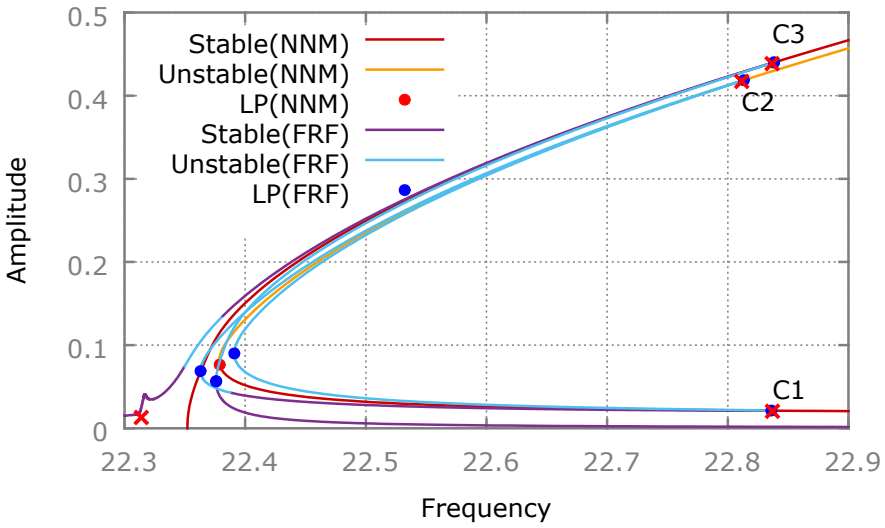

(b) Beam #2

Figure 4.23 – 2-beam array with Design #3 after symmetry-breaking. Frequency response and IS with the in-phase mode excited ($\delta_m = 10^{-4}$)

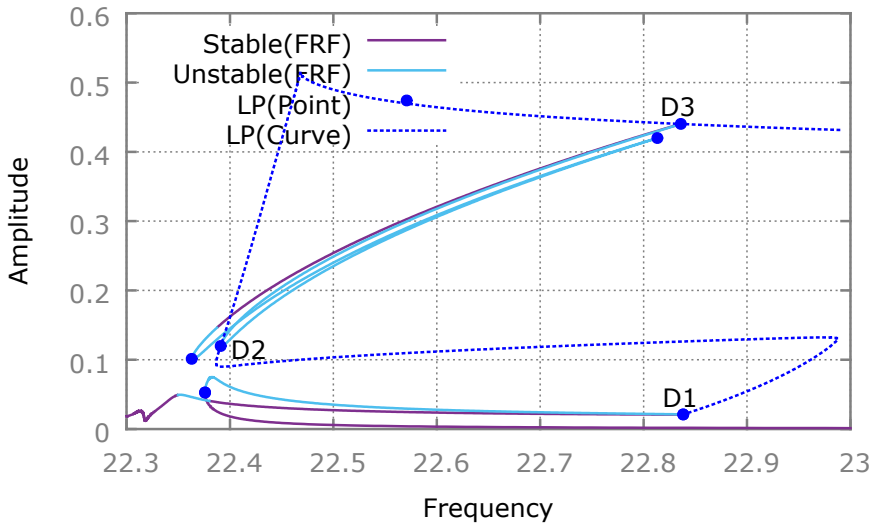

(a) Beam #1

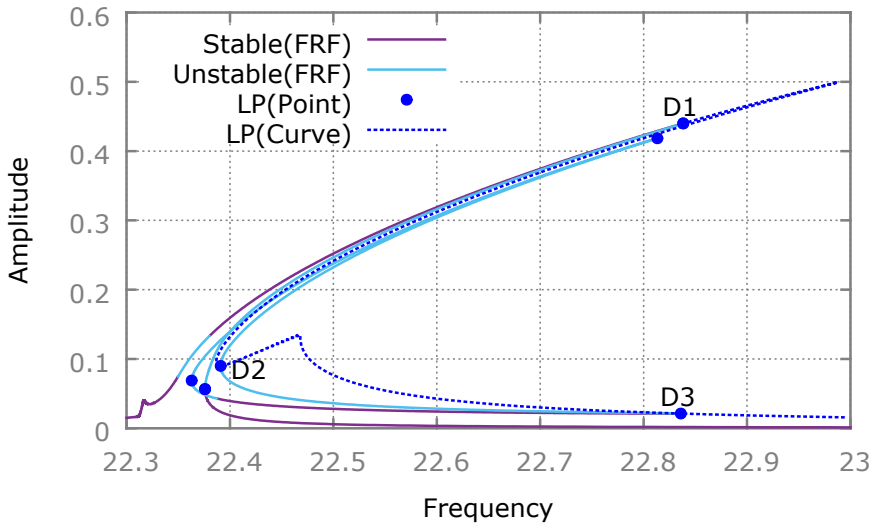

(b) Beam #2

Figure 4.24 – 2-beam array with Design #3. LP tracking with respect to the amplitude of forcing with the in-phase mode excited. Frequency responses obtained for $\delta_m = 10^{-4}$

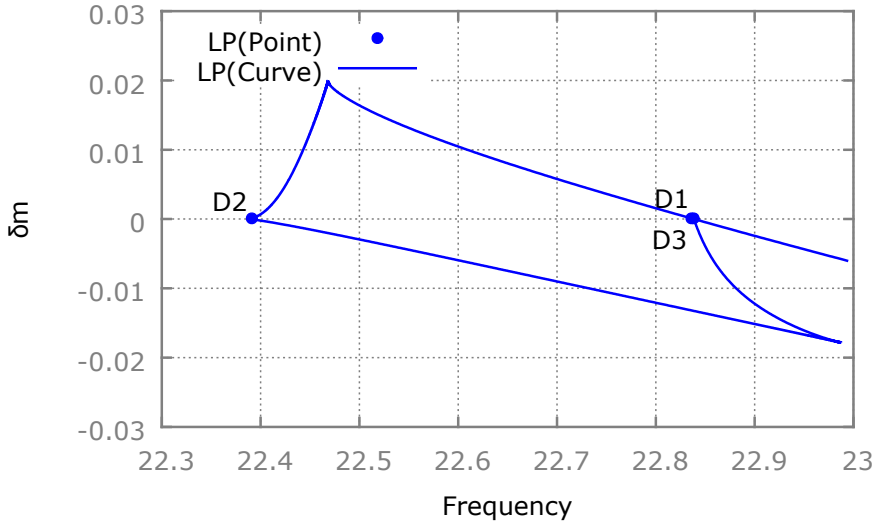

Figure 4.25 – 2-beam array with Design #3. Visualization of LP tracking in the δ_m-Frequency plane

NNM that support the mixed NNM is excited, then the IS are merging with the frequency response for a high enough amplitude of forcing. In asymmetrical configuration, NNMs of the MEMS array are composed of pure NNMs and INNMs. When pure NNMs possesses IS, the IS are merging with the frequency response for a high enough amplitude of forcing. The INNMs can possess IS as long as the forcing vector targets the pure NNMs that compose the INNM. Moreover, these IS cannot merge with the frequency response for any shape and amplitude of the forcing vector. In MEMS array, symmetry-breaking event affect greatly the dynamic of the system. When the out-of-phase NNM is excited, ISs are in the unstable region of the out-of-phase NNM and are not easily exploitable by frequency sweep. However, when the in-phase NNM is excited the symmetry-breaking generates great change in maximum of amplitude in the MEMS array and can be easily exploitable by frequency sweep. In the next section, one will see how the dynamic of MEMS arrays can be exploited for mass detection purposes.

4.4 Mechanisms of detection

In this section, mechanisms of detection with beam array based on hysteresis cycle and symmetry-breaking event are presented. First in Subsection 4.4.1, the mass detection method for 2-beam with asymmetric voltages is addressed. The additional loops that appears due to electrostatic coupling of the beam are used to provide a mass detection mechanism based on hysteresis cycle. Secondly in Subsection 4.3, 2-beam and 3-beam arrays are considered with symmetric voltages. The symmetric configuration of the array is then broken by a mass added onto the first beam of the array. The resulting symmetry-breaking event is then exploited to detect and quantify the added mass.

4.4.1 Based on frequency shift and hysteresis cycle (Design #1)

In this subsection, a 2-beam array is considered with respect to the Design #1 presented in Tab 4.2. It is presented a mechanism of detection based on the merging behavior of the additional loops caused by bifurcation synchronisation in frequency to generate important changes in the hysteresis cycle after the addition of an added mass.

Let the added mass fall on the second beam at $x_0 = 0.5$. Figure. 4.26 presents the responses of the first and second beams with and without an added mass $\delta m = 10^{-4}$ determined by the HBM+ANM. The stable/unstable parts of the responses are plotted for $\delta m = 0$ and $\delta m = 10^{-4}$. Fig. 4.27 presents the response curves for the case of an added mass $\delta m = 10^{-4}$. It permits the comparison between the results obtained by HBM+ANM and by time integration method with a frequency sweep-up and a frequency sweep-down.

From Fig. 4.26, it appears that the added mass makes the beams responses more complicated due to the presence of several additional loops. For the second beam, the amplitude is almost unchanged with an added mass ($W_{max} = 0.22$) and there is a small frequency shift, while the first-beam amplitude changes from $W_{max}(B_1) \approx 0.11$ to $W_{max}(F_1) \approx 0.17$. In the objective to carry out an experimental investigation, it is necessary to verify, using the time integration method, that such an amplitude difference is detectable. In Fig. 4.27a, it can be observed that a simple sweep-up or sweep-down does not permit the detection of the added mass. Indeed, the frequency responses obtained by time-integration combined with sweep-up and sweep-down coincide with the stable part of the response curve for $\delta m = 0$ of Fig. 4.26a and the branches up to H_1 and F_1 are not obtained. The only difference concerns the position of the amplitude jump. During sweep-down, for the first beam the jump occurs at C_1 without added mass and at I_1 with added mass; for the second beam, it occurs at H_2 and at G_2 respectively. However, these differences are very difficult to distinguish for a small added mass.

To detect the added mass by means of amplitude difference, let both frequency sweeps be combined, see Fig. 4.28. First, the frequency is swept down from point J to a frequency value Ω_{min} which is set between $\Omega(C_1)$ and $\Omega(I_1)$, then increased.

When using the time integration method, the response of the first beam is $J_1 - i_1 - ji_1 - C_1 - J_1$ ($W_{max} = 0.02$) without added mass and $J_1 - I_1 - jI_1 - G_1 - H_1 - jH_1 - J_1$ ($W_{max} = 0.15$) for $\delta m = 10^{-4}$. The response of the second beam is $J_2 - i_2 - ji_2 - g_2 - d_2 - jd_2 - J_2$ ($W_{max} = 0.22$) without added mass and $J_2 - I_2 - jI_2 - G_2 - J_2$ ($W_{max} = 0.04$) for $\delta m = 10^{-4}$. Hence, the added mass is clearly detected by the difference of amplitude.

If the mass $\delta m = 10^{-4}$ is added on the first beam instead of the second one, the beam-array response is almost unchanged because, as considered in the previous section, the influence of the second beam on the first beam is stronger than the influence of the first beam on the second beam. Hence, a perturbation of the second-beam will cause a larger amplitude variation than a perturbation of the first beam.

The threshold of detection can be set by adjusting voltages. In order to adjust the mass threshold, Ω_{A_1} has to be superior to $\Omega_{A_2 m}$ and inferior to Ω_{A_2}, see Fig. 4.29. For example, when decreasing $V_{dc_{32}}$ and $V_{ac_{32}}$ to $0.575V$ instead of $0.6V$ while keeping the

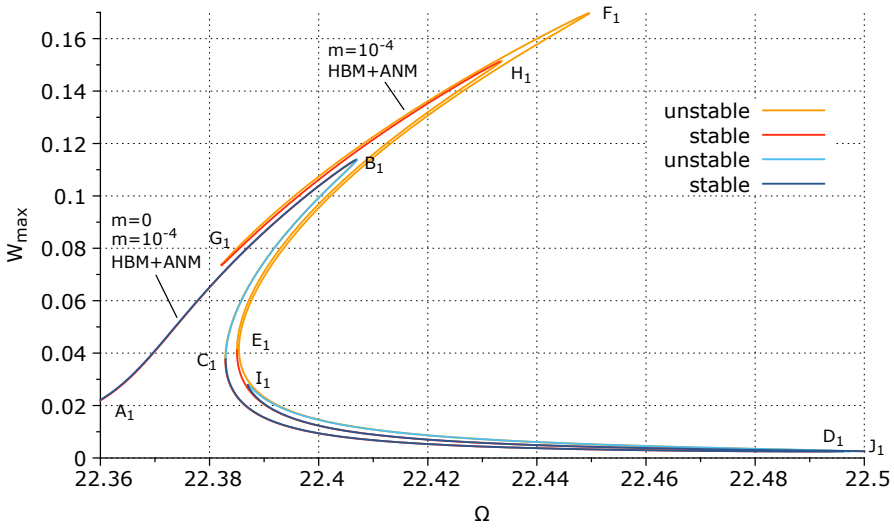

(a) Beam #1

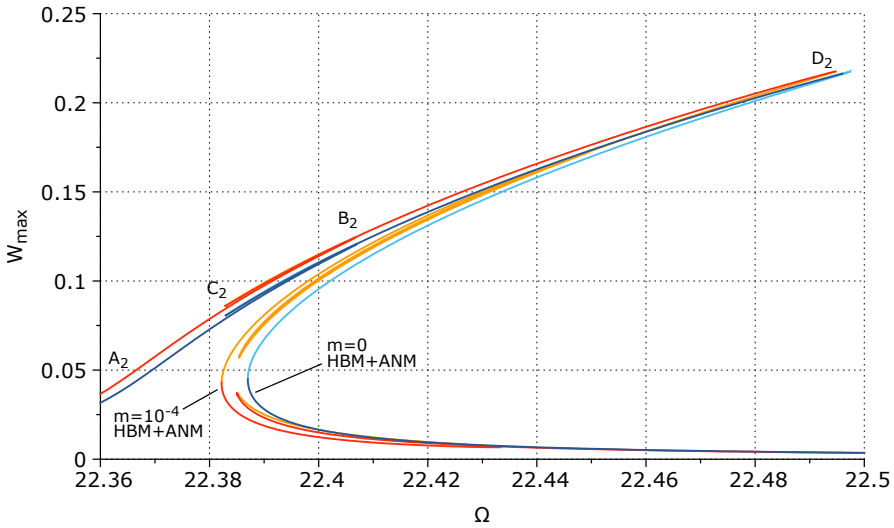

(b) Beam #2

Figure 4.26 – 2-beam array with Design #1. Responses determined by the HBM+ANM with an added mass $\delta m = 10^{-4}$ (red: stable branches, orange: unstable branches) and without added mass (dark blue: stable branches, light blue: unstable branches).

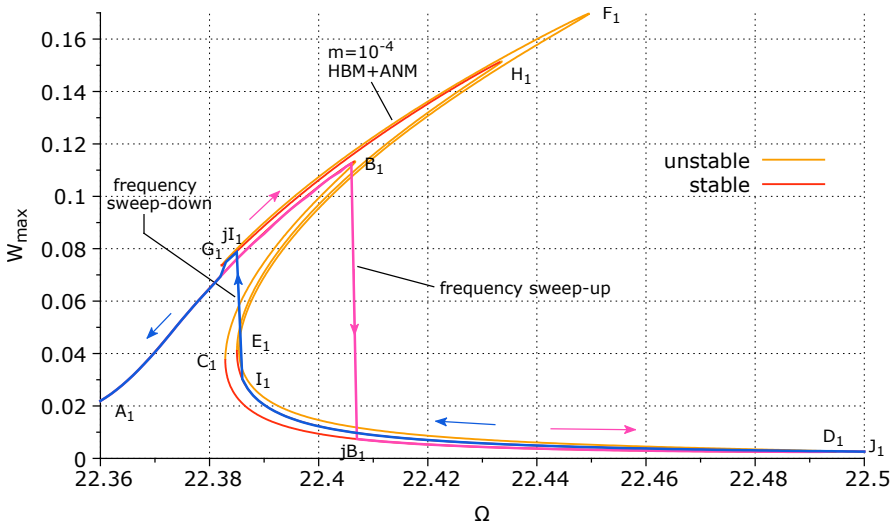

(a) Beam #1

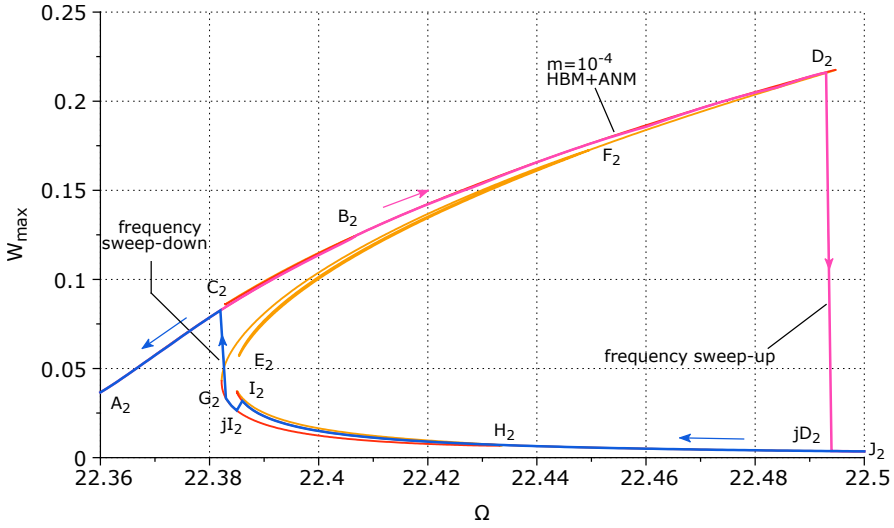

(b) Beam #2

Figure 4.27 – 2-beam array with Design #1. Responses with added mass $\delta m = 10^{-4}$. Comparison between HBM+ANM (red: stable branches, orange: unstable branches) and time integration method with a frequency sweep-up (pink curves) and a frequency sweep-down (blue curves).

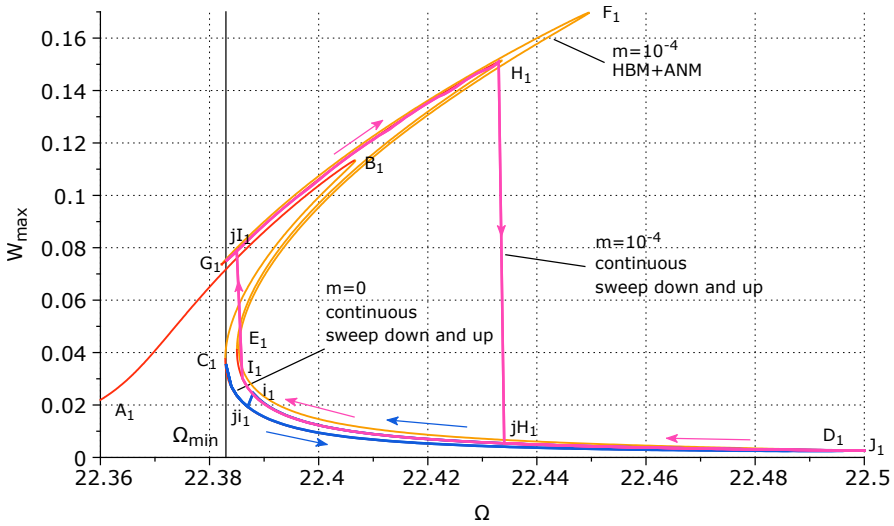

(a) Beam #1

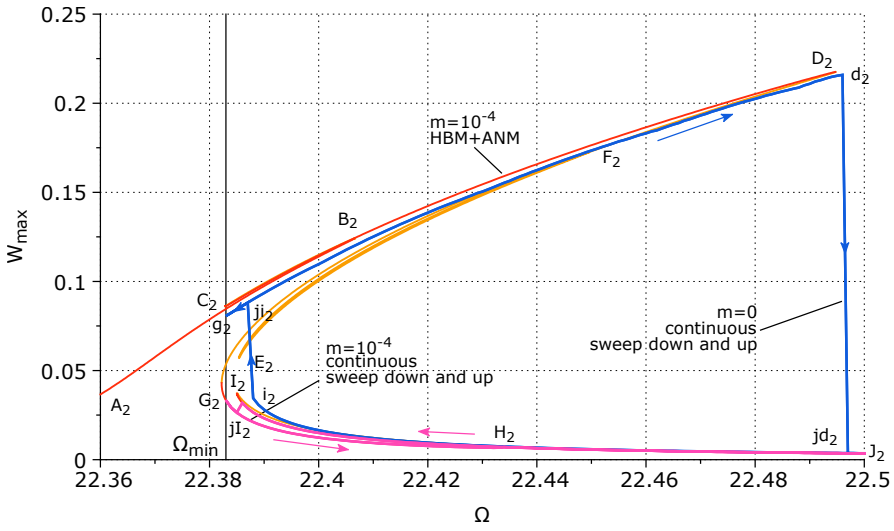

(b) Beam #2

Figure 4.28 – 2-beam array with Design #1. Responses determined by time integration method without added mass (blue curves $J_1 - i_1 - ji_1 - C_1 - J_1$ and $J_2 - i_2 - ji_2 - g_2 - d_2 - jd_2 - J_2$) and with added mass $\delta m = 10^{-4}$ (pink curves $J_1 - I_1 - jI_1 - G_1 - H_1 - jH_1 - J_1$ and $J_2 - I_2 - jI_2 - G_2 - J_2$) ; responses determined by HBM+ANM with added mass $\delta m = 10^{-4}$ (red: stable branches, orange: unstable branches).

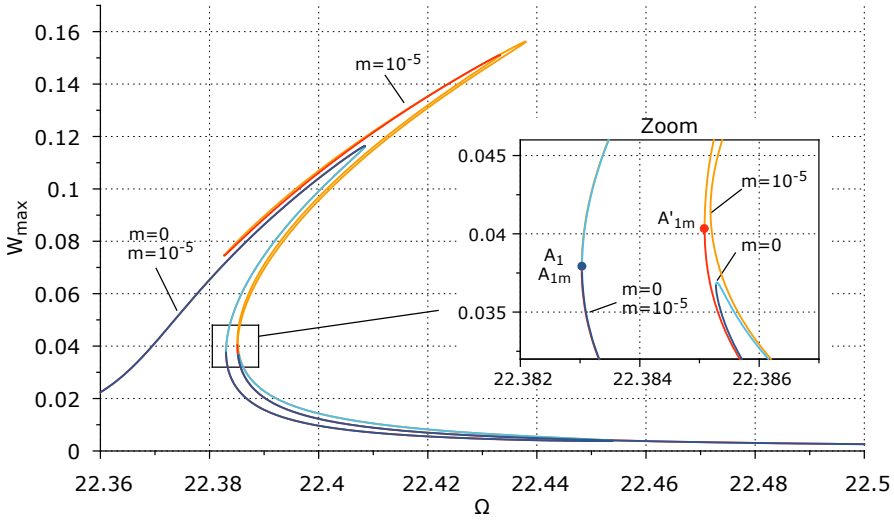

(a) Beam #1

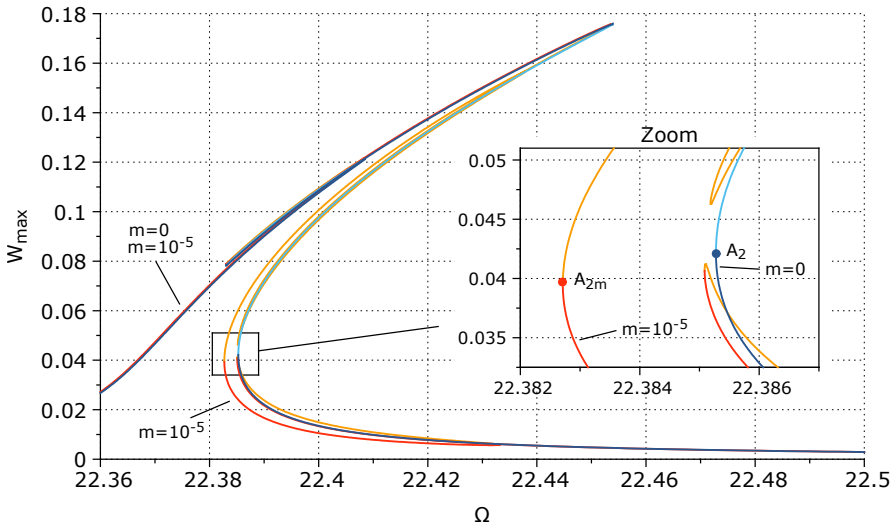

(b) Beam #2

Figure 4.29 – 2-beam array with Design #1. Response with $V_{dc_{32}} = V_{ac_{32}} = 0.575V$ and other voltages as in Table 1, without mass (dark/light blue) and with $\delta m = 10^{-5}$ (red/orange).

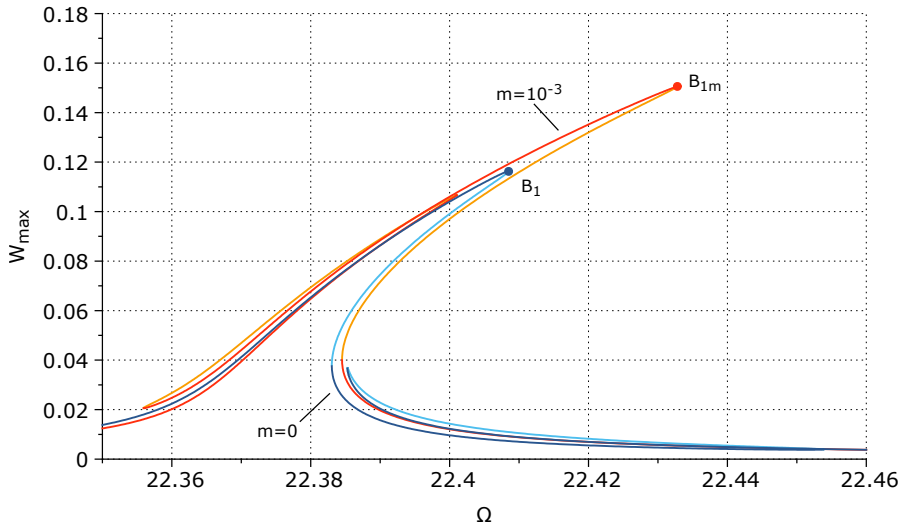

(a) Beam #1

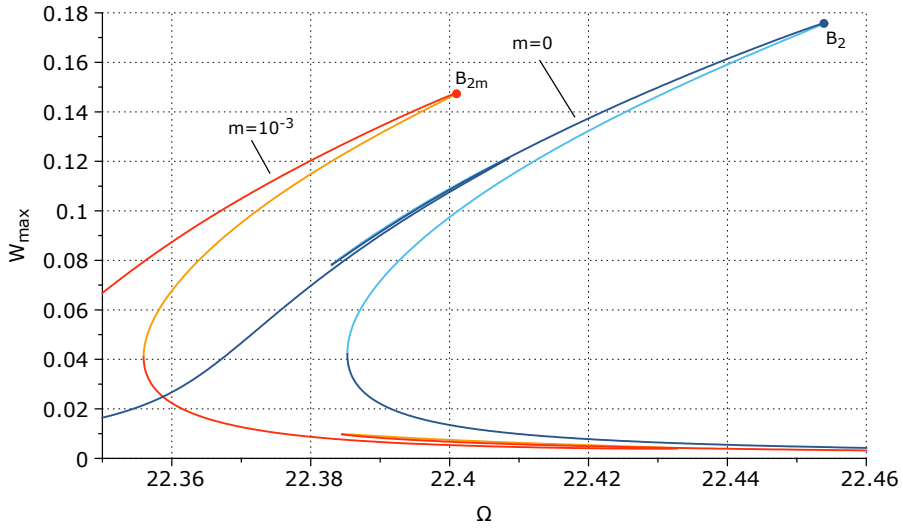

(b) Beam #2

Figure 4.30 – 2-beam array with Design #1. Response with $V_{dc_{32}} = V_{ac_{32}} = 0.575V$ and other voltages as in Table 1, without mass (dark/light blue) and with $\delta m = 10^{-3}$ (red/orange).

other voltages unchanged, see Table 4.1, Ω_{A_2} becomes closer to Ω_{A_1}. Therefore, smaller masses, such as $\delta m = 10^{-5}$, can also be detected by a large amplitude change. For a bigger mass, such as $\delta m = 10^{-3}$, the second beam response has a lower amplitude, see Fig. 4.30. By adding a mass bigger then an upper threshold, $\Omega_{B_2 m}$ becomes larger than $\Omega_{B_1 m}$ and the amplitude of the second beam response decreases. Therefore, larger masses such as $\delta m = 10^{-3}$ can this time be detected by a reduced amplitude on the second beam response curve. To sum up, there exist two mass thresholds. When the first one is exceeded

there is a large amplitude jump on the first beam amplitude. Then, when the added mass is higher than the second threshold, the amplitude of the second beam starts to decrease. But for added masses between these two thresholds, the responses are not so different. Therefore quantifying these masses is difficult.

4.4.2 Based on symmetry-breaking event

This subsection considers a 3-beam array with symmetric voltages. Designs with small (Design #2) and large (Designs #3 and #4) voltages are investigated with values presented in Table 4.2. A mechanism of detection based on symmetry-breaking event induced by an added mass on the MEMS array is investigated.

Small symmetrical voltages (Design #2) Due to the symmetric voltages, the electrostatic forces on both sides of the second beam are balanced. Hence the second beam does not vibrate. If the added mass falls on it, the system is still symmetric and the second beam remains at rest. However, if the added mass falls on the first or third beam, the system loses its symmetry and the response changes. Depending on the value of added mass, the response change for the first and third beams can be very small and difficult to identify. This is why the detection is based on the second-beam response instead.

Fig. 4.31 shows the case of an added mass $\delta m = 10^{-3}$ at the middle of Beam #1 ($x_0 = 0.5$). Without the added mass, the responses of Beams #1 and #3 are identical. With the added mass, the response of Beam #1 is shifted to the left and loops appear on the responses of Beams #1 and #3. However, the response amplitudes do not change in comparison with the case without added mass. The amplitude of beam #2 is nil ($W_{max} = 0$) without added mass but large with $\delta m = 10^{-3}$ as a result of symmetry breaking.

When voltages $V_{ac_{21}}$ and $V_{dc_{21}}$ between the beams #1 and #2 are identical to voltages $V_{ac_{32}}$ and $V_{dc_{32}}$ between the beams #2 and #3, the electrostatic forces and the second-beam displacement depend only on the difference between deflections of beams #1 and #3. The larger the added mass is, the more different these displacements are, and the larger the second-beam displacement is. This is illustrated in Fig. 4.32 showing the second-beam response for several values of the added mass.

With a mass $\delta m = 10^{-3}$ added on the Beam #1, the deflections of Beams #1 and #3 are different. Let points A, B, C, D be considered as defined in Figs. 4.31 and 4.32a. At these points, the displacements of Beams #1 and #3 are plotted in Fig. 4.32b. For each value of time t, these displacements are the most different at point C and the less different at point B. Therefore, it results that $W_C > W_D > W_A > W_B$ as observed in Fig. 4.32a.

The amplitude of Beam #2 is large, with $W_{max} = 0.25$ at point C. However, this branch is unstable, thus not observable experimentally. Fig. 4.33 represents the responses obtained by time integration with frequency sweep-up and sweep-down. As for the two-beam system, these responses are not coincident. As shown in Fig. 4.33a, with a frequency sweep-up the maximum amplitude $W_{max} = 0.04$ is reached just before the jump down to point E and $W_{max} = 0.04$ whereas, with a sweep down, the maximum amplitude is $W_{max} = 0.05$ at point F.

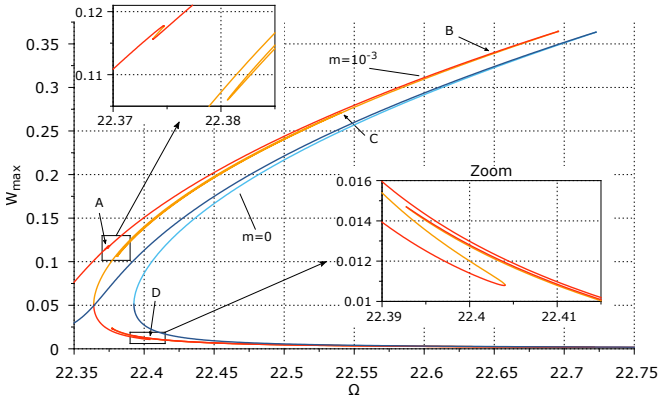

(a) Beam #1

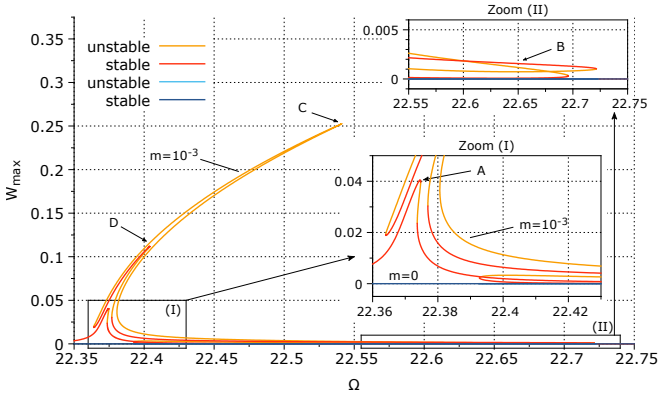

(b) Beam #2

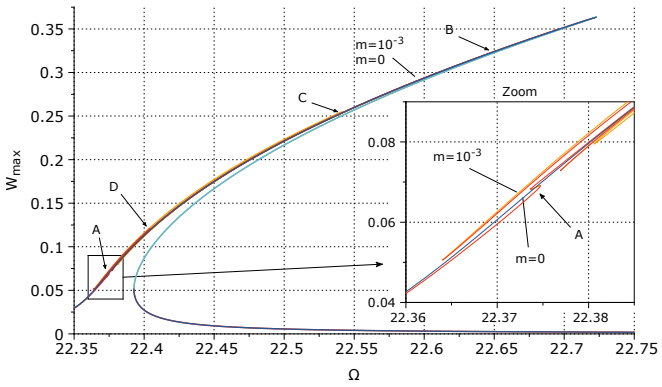

(c) Beam #3

Figure 4.31 – 3-beam array with Design #2: response with a mass $\delta m = 10^{-3}$ added on the first beam (red/orange) and without added mass (dark/light blue). Without added mass, the second-beam amplitude is nil.

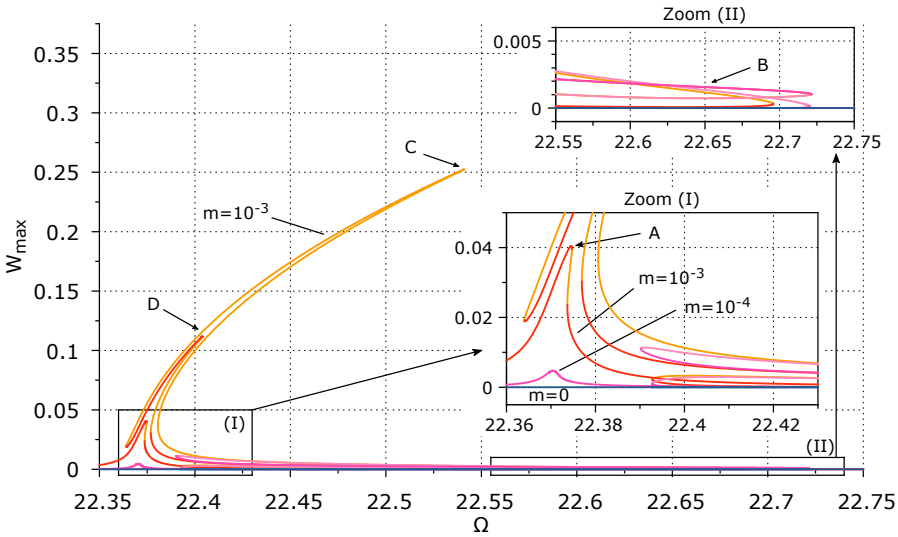

(a) Response of Beam #2 without (blue curve) and with $\delta m = 10^{-4}$ (pink curve) or $\delta m = 10^{-3}$ (red/orange curve) added on Beam #1.

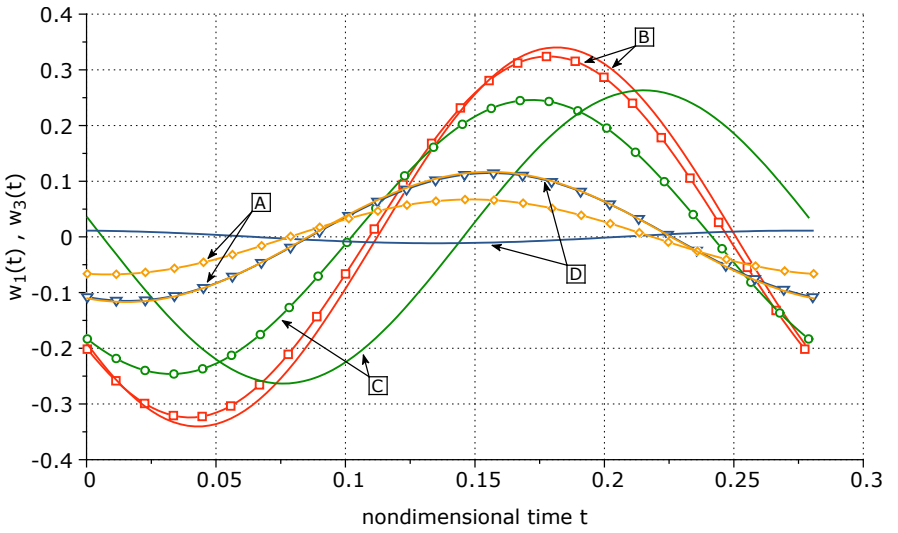

(b) Displacement of Beam #1 (solid line) and Beam #3 (dotted line) at points A (yellow curves), B (red curves), C (green curves) and D (blue curves) with $\delta m = 10^{-3}$.

Figure 4.32 – 3-beam array with Design #2

A larger amplitude can be reached if the two frequency sweeps are combined as follows (see Fig. 4.33b): first a sweep-down until the jump at point F, then a sweep-up, resulting in a maximum amplitude $W_{max} = 0.11$ at point D that can be easily detected.

However, with a smaller added mass, e.g. $\delta m = 10^{-4}$, the difference between the displacements of Beams #1 and #3 is small. Thus the deflection of Beam #2 is also small, as shown in Fig. 4.32a, making the detection difficult. As explained in Section 4.4 there is a threshold of added mass, above which additional loops increase the response amplitude. Therefore the added mass has to be larger than the threshold for the symmetry breaking to generate a high amplitude on Beam #2. To detect smaller added masses, let Design #3 be considered.

Large symmetrical voltages (Design #3 and #4) In this paragraph, the considered large symmetrical voltages generates large amplitude responses. Therefore, an analysis of convergence in term of Taylor expansion T and number of spatial mode N_m is necessary.

The responses for Design #3 are presented in Fig. 4.34. The considered voltages are large enough for a frequency sweep-up from $\Omega = 22.35$ to $\Omega = 22.75$ to make the resonator collapse by pull-in ($W_{max} \geq 1$). Hence, the sweep-up is performed only in the interval $\Omega = [22.17 - 22.23]$ where the resonator has not yet collapsed. Without added mass, the calculation with one mode and a third-order Taylor series shows convergent responses. The array remains symmetric, so beam #2 does not vibrate.

With a mass $\delta m = 10^{-4}$ added on the first beam, because of the symmetry-breaking, the second-beam amplitude is large. The calculations have been limited to 3 modes and seventh-order Taylor series in order to keep an affordable computational time. In Fig. 4.34, with the same order of Taylor series ($T = 3, 5$ or 7), responses with $N_m = 1$ or $N_m = 2$ modes are almost unchanged. On the contrary, with a fixed number of modes, responses change a lot when using the third or fifth order, while the seventh order does not improve the solution anymore. For smaller added masses, the influence of high orders is more significant.

Fig. 4.35 shows the responses for Design #4 (slightly higher symmetric voltage, see Table 4.2), calculated with $N_m = 1$ mode. Using third order Taylor series, an added mass $\delta m = 10^{-6}$ can be detected by a small difference between the responses with and without added mass. However, with seventh-order series, a smaller added mass $\delta m = 10^{-12}$ can be detected because a larger difference is observed. Theoretically, any infinitesimal perturbation causes the symmetry-breaking of the three-beam array. However, from a numerical point of view, the detection threshold depends on the accuracy of the model. Thus, the detection threshold can be improved by increasing the order of the Taylor series. It is however limited by the computational cost and the numerical accuracy of the algorithms.

Fig. 4.36 presents responses calculated with $N_m = 1$ and seventh-order Taylor series for increasing values of δm. Without added mass, the amplitude of beam #2 is $W_{max} = 0$ and it changes from $W_{max} = 0.05$ for $\delta m = 10^{-12}$ to $W_{max} = 0.2$ for $\delta m = 5 \times 10^{-4}$ (cyan). For large values of δm ($\delta m > 10^{-6}$), the quantification is possible.

To better visualized the evolution of the response curve with respect to the value of

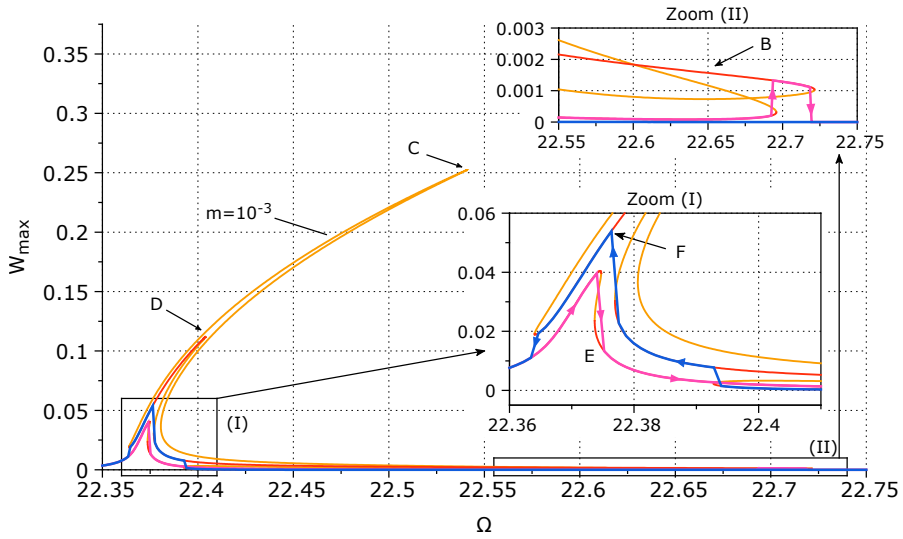

(a) HBM+ANM (red/orange curve), time integration with a sweep-up (pink curve) and a sweep-down (blue curve)

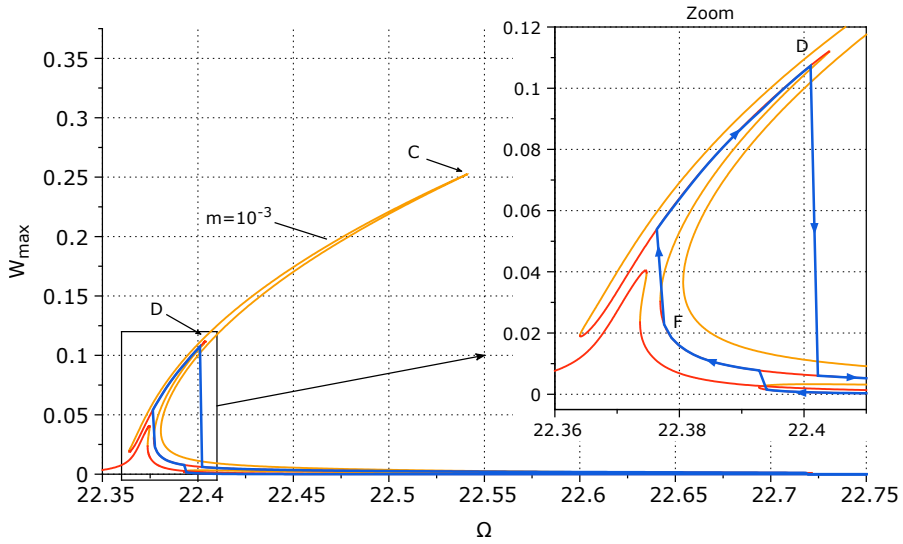

(b) HBM+ANM (red/orange curve), time integration method combining a frequency sweep-down then sweep-up (blue curve).

Figure 4.33 – 3-beam array with Design #2. Response of Beam #2 with $\delta m = 10^{-3}$ added on Beam #1.

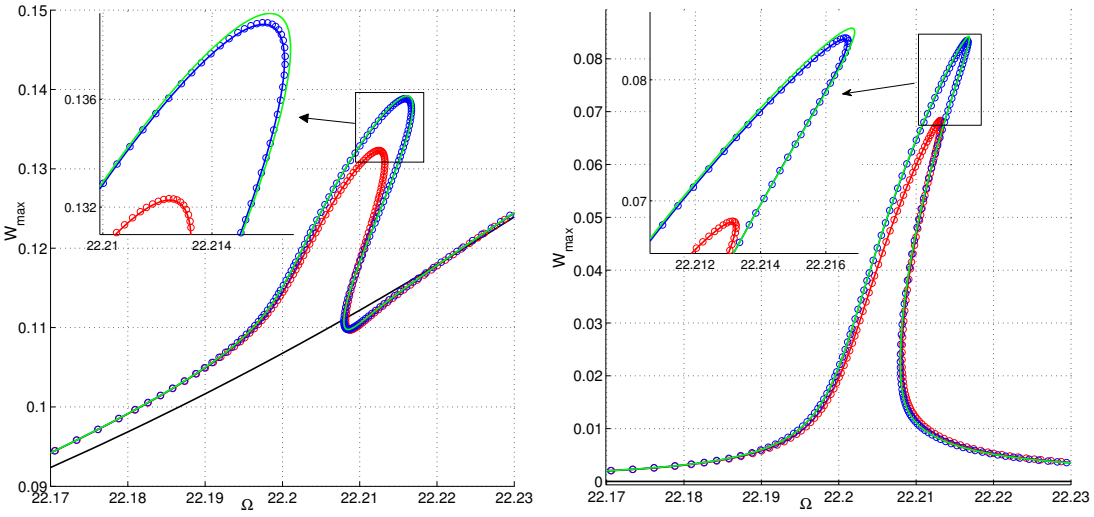

(a) Beam #1

(b) Beam #2

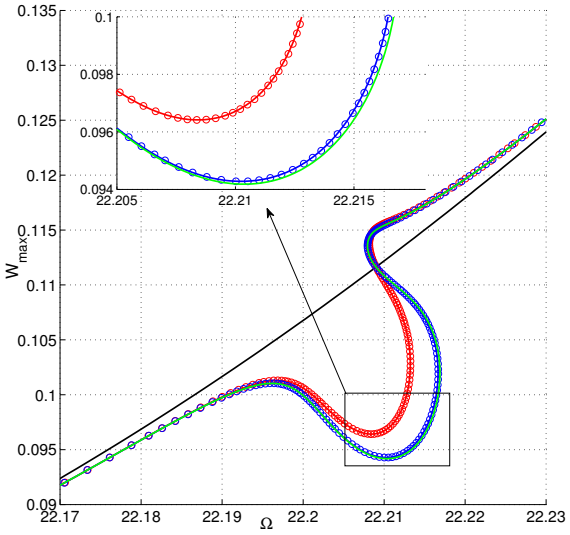

(c) Beam #3

Figure 4.34 – 3-beam array with Design #3. Responses with an added mass $\delta m = 10^{-4}$ on the first beam determined by using third (red), fifth (blue) and seventh (green) order Taylor series with $N_m = 1$ (solid line) or $N_m = 2$ (circle) modes; responses without added mass (black).

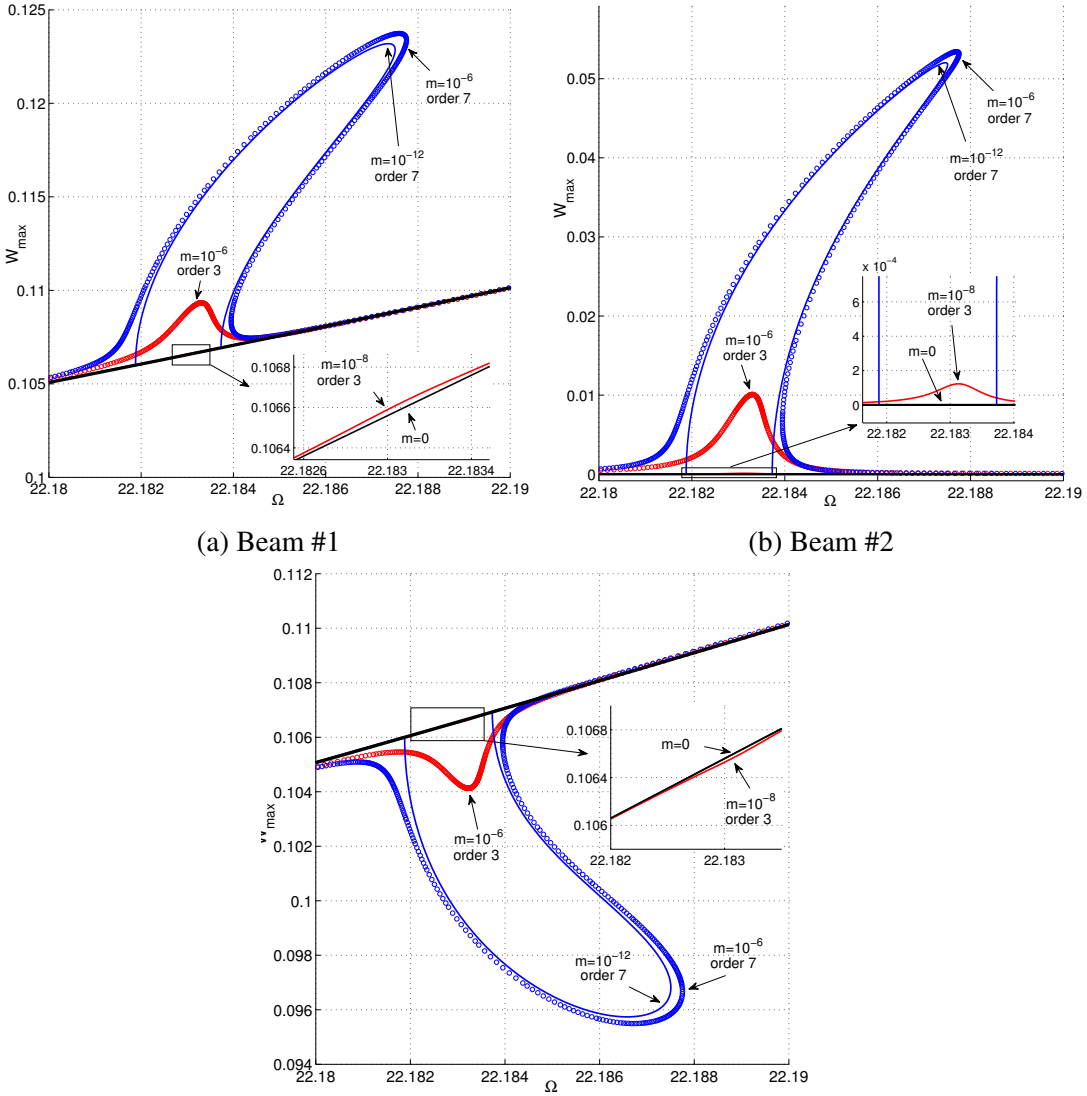

(a) Beam #1

(b) Beam #2

(c) Beam #3

Figure 4.35 – 3-beam array with Design #4. Responses with $N_m = 1$ mode. Red curves: responses with $\delta m = 10^{-8}$ (solid line) or $\delta m = 10^{-6}$ (circle) on the first beam determined by third-order Taylor series. Blue curves: responses with $\delta m = 10^{-12}$ (solid line) or $\delta m = 10^{-6}$ (circle) on the first beam determined by seventh-order Taylor series. Black curves: responses without added mass.

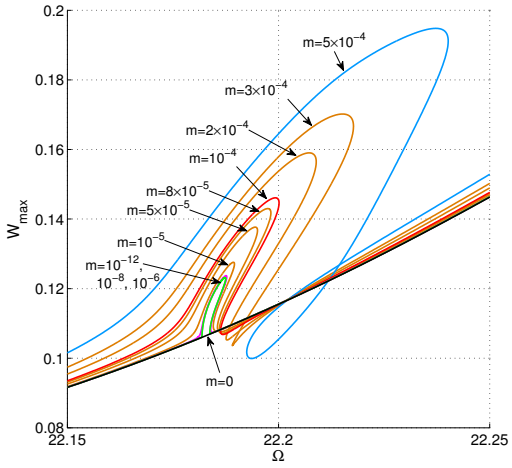

(a) Beam #1

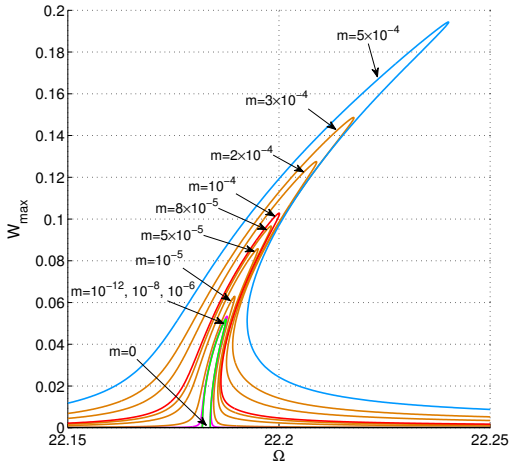

(b) Beam #2

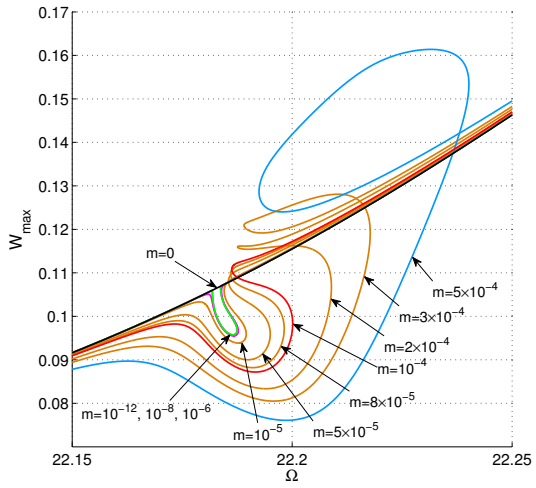

(c) Beam #3

Figure 4.36 – 3-beam array with Design #4. Responses with $N_m = 1$ mode and seventh order Taylor series, without added mass (black), with $\delta m = 10^{-12}$ (green), $\delta m = 10^{-6}$ (magenta), $\delta m = 10^{-4}$ (red), $\delta m = 5 \times 10^{-4}$ (blue) added on the first beam.

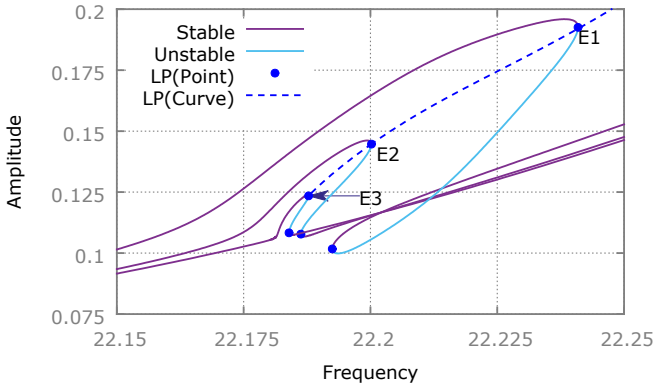

(a) Beam #1

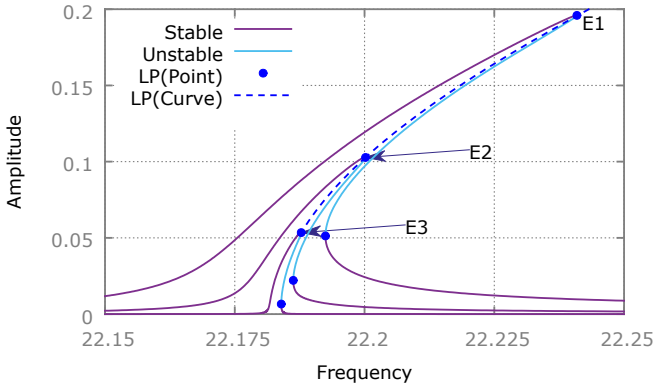

(b) Beam #2

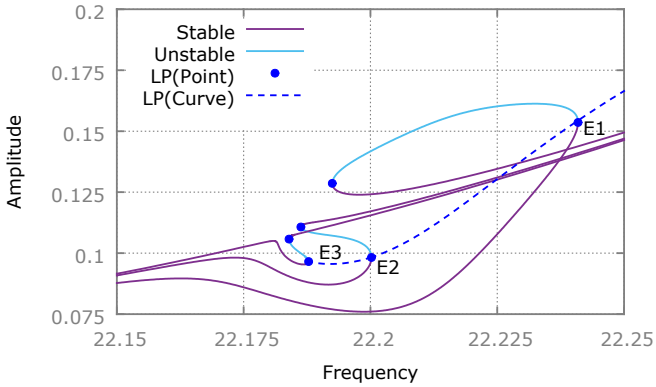

(c) Beam #3

Figure 4.37 – 3-beam array with Design #4.

added mass $(\delta m > 0)$, a parametric analysis by LP tracking is made, see Fig. 4.37. The results are obtained using HBM without ANM with $N_m = 1$, $H = 5$ and seventh-order Taylor series. The LP tracking with respect to the value of the added mass allows to obtain a continuous parametric analysis. In Fig. 4.38 , the LP curve presented with

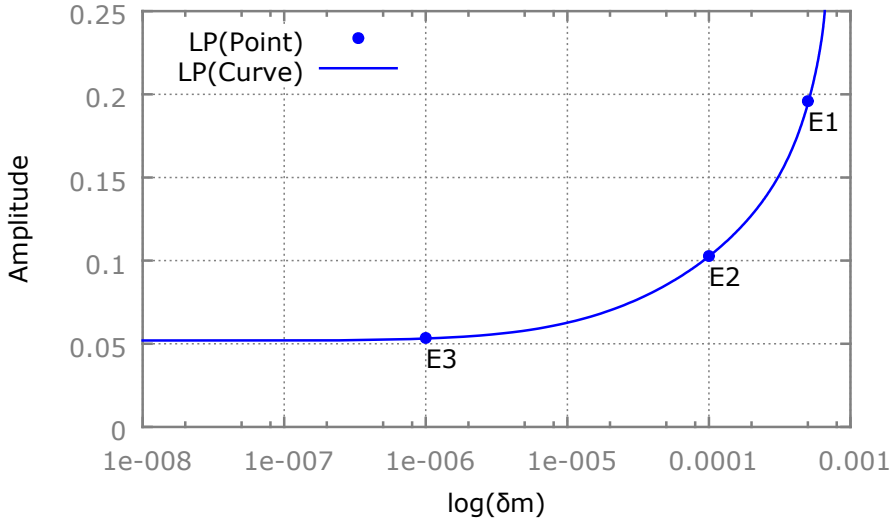

Figure 4.38 – 3-beam array with Design #4. Maximum of amplitude Max(W_{max}) with respect to added mass δm for Beam #2.

respect to the value of the added mass ($\delta m > 0$) and the amplitude of the second beam can be used to determine direct the value of the added mass in function of the maximum of amplitude of the second beam. For small values of δm ($\delta m < 10^{-6}$) the difference in amplitude is very small so an accurate quantification is difficult. When the quantification of the non-dimensional ratio δm is made, the corresponding physical added mass δm_p is obtained with Eq. (4.25) as listed in Table 4.3 for a few values of δm. The parametric

Table 4.3 – Correspondence between the non dimensional mass ratio δm and the physical value of the added mass δm_p

δm	10^{-3}	10^{-4}	5×10^{-4}
$\delta m_p(kg)$	1.1184^{-18}	1.1184^{-19}	2.2368^{-20}
δm	5×10^{-6}	10^{-6}	10^{-8}
$\delta m_p(kg)$	5.5920^{-21}	1.1184^{-21}	1.1184^{-23}

analysis has been made with respect to the value of the added mass superior to $\delta_m > 0$. In Fig. 4.39, the entire LP tracking for amplitude of the second beam between 0 and 0.5 is displayed. For amplitude below 0.5, the value of the added mass becomes negative until it reaches zero. Then, the value of the added mass becomes positive again indicating the presence of IS. The IS appears for value of the added mass below $\delta m \approx 6.4\times10^{-5}$. The LP curve crosses the value of the added mass $\delta_m = 5\times10^{-6}$ in three points $(F1, F2, F3)$ indicating the presence of an IS.

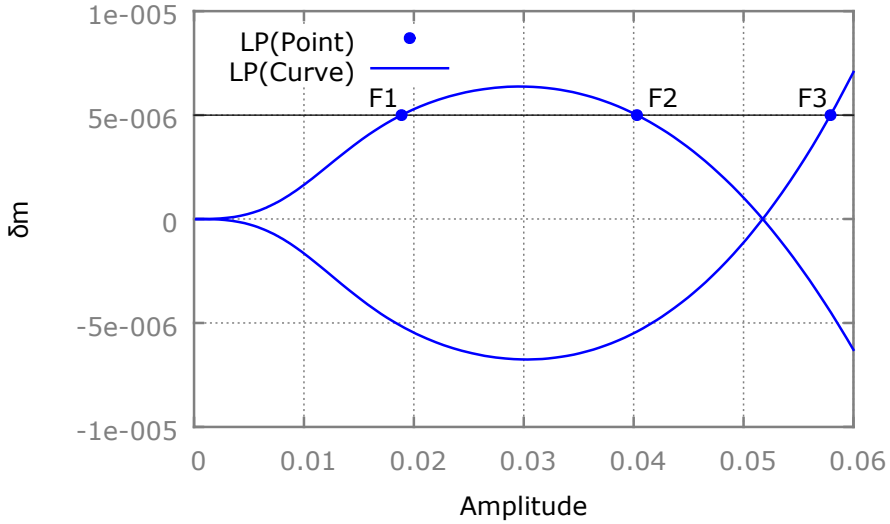

Figure 4.39 – 3-beam array with Design #4. Maximum of amplitude Max(W_{max}) with respect to added mass δm for Beam #2.

The frequency response with $\delta m = 5 \times 10^{-6}$ is computed and initialized with LP tracking, see Fig. 4.40. One can see the IS delimited by the two points $(F1, F2)$. For beam #1 and #3, the IS is one the other side of the frequency curves, whereas for beam #2, the IS is localized inside the frequency curves.

To better visualize the evolution of the IS, several others ISs are plotted with respect to $\delta m = (3 \times 10^{-6}, 6 \times 10^{-6})$ in Fig. 4.41. The particular point at $\delta_m = 0$ is also used to compute what seems to be an undetected bifurcated branch of solution. One can see that for $\delta m \to 0$, the frequency response tends towards a branch emanating from BPs on the main branch at $\delta m = 0$. One can observe the evolution of IS with respect to $\delta m < (\approx 6.4 \times 10^{-6})$ on the other side of the frequency response obtained with $\delta m = 0$. The IS computed with $\delta m = 6 \times 10^{-6}$ is smaller than the one obtained with $\delta m = 3 \times 10^{-6}$. This is because the value of δm is closer to the isolat center than the other IS.

On the curve obtained with $\delta m = 0$, two BPs were not detected with the previous frequency response computation due to the small frequency range of the phenomena. Indeed with a too long step size, two BPs can be undetected by the indicator if those BP are close enough to each other to be located between the two periodic solutions computed successively. A branch of solution emanating from previously undetected BPs is obtained. The two BP are symmetry-breaking bifurcation. Indeed in symmetric configuration, the system cannot have his second beam moving without breaking the symmetry of the system. This phenomenon is similar to buckling behaviors, with a high symmetric voltages the beam array loose its stability around the asymmetric NNM of the system leading to symmetry-breaking motion. This phenomenon is interesting since the asymptote in amplitude can be tuned by amplifying the alternative voltages V_{ac} by the multiplier coefficient d. Consequently, the maximum amplitude of the bifurcated branch can be tuned to be outside the zone dominated by ambient noise.

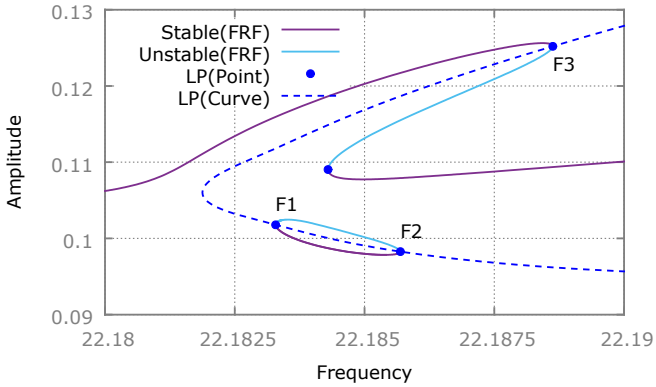

(a) Beam #1

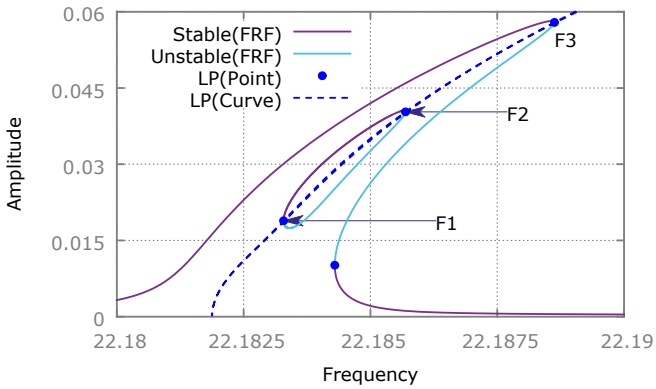

(b) Beam #2

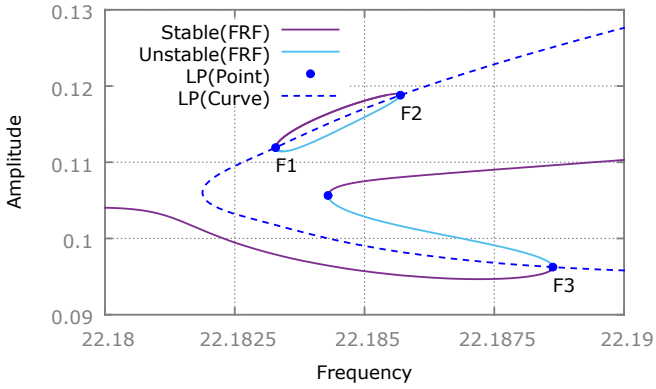

(c) Beam #3

Figure 4.40 – 3-beam array with Design #4.

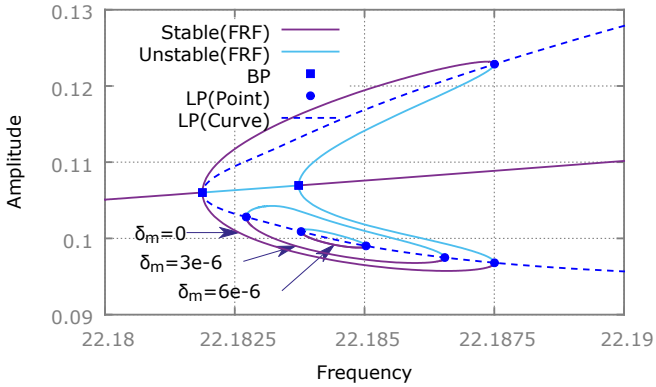

(a) Beam #1

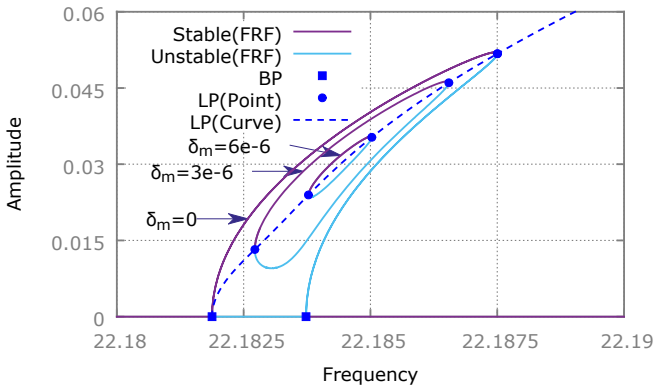

(b) Beam #2

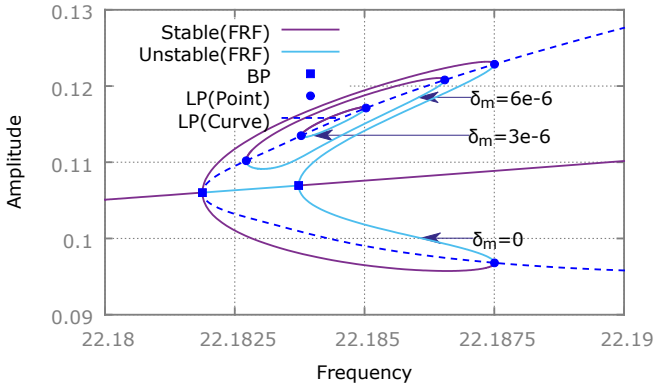

(c) Beam #3

Figure 4.41 – 3-beam array with Design #4.

4.4.3 Perspectives for mass detection

One perspective is the exploitation of localization of motion that occurs with/without symmetry-breaking event to provide mechanism of detection and quantification of multiple mass in parallel by using a asymmetric n-beam array. When n-beam with the maximum number of symmetries is considered, one of its NNMs present multiple successive symmetry-breaking bifurcations of the lattice. Each of those symmetries are then detuned leading to as many localization of motion as there are symmetries. Each symmetry if detuned can lead to two possible asymmetric configurations. Especially, the system can go from one asymmetric configuration to one other by adding masses onto the MEMS array. Moreover, the mass detection threshold associated to each broken symmetry can be tuned with the bias voltages V_{dc}. The mechanism of detection is based on this inversion of localization of motion that appears when the symmetry-breaking events are crossed from one asymmetric configuration to the other. The quantification of the masses can then be performed by LP continuation as in Subsection 4.3.

4.5 Conclusion

In this chapter, the influence of electrostatic coupling between the beams has been analyzed with time integration and averaging methods. The time integration method is used to simulate experimental results. The averaging method permits to visualize the influence of electrostatic coupling between the beams by comparing the responses curves with and without the identified coupling terms. Because of this influence, each beam response presents a very complicated nonlinear behavior with several loops, the influence of distant beams being weaker. A phenomenon of frequency synchronization of the bifurcations points has been uncovered.

Afterwards, the influence of symmetry-breaking event onto the dynamics of a symmetric beam array has been analyzed. The symmetry-breaking event has been induced by the addition of a small mass onto the first beam of the 2-beam array. The results show that symmetry-breaking events generate INNM and IS. Moreover, it has been shown that merging and birth properties of IS is linked to NNM properties. If a IS is supported by a INNM, the merging cannot happen. However, if the IS is supported by a pure or a mixte NNM, it can only merge with the main frequency response if both of the NNM are excited by the input force.

For mass detection topic, results based on time integration show that the combination of two frequency sweeps (down then up) is necessary for the experimental detection of an added mass. For an asymmetric beam array, a small added mass can be detected by tuning voltages to a threshold. In particular, in symmetric configurations, the mass detection can be highly improved by using bifurcations of symmetry-breaking type. Moreover, the amplitude of the voltages can be used to put the amplitude range for mass detection outside the zone dominated by the ambient noise.

General conclusion and perspectives

General conclusion

In the first part of this thesis, the topic of parametric analysis for nonlinear systems has been addressed. The methods of detection, localization and tracking of bifurcations have been recalled for codimention-1 and developed for R1 and LPNS bifurcations. Bifurcation tracking has been applied to a NLTVA and a Jeffcott rotor to visualize the evolution of the dynamics of the system with respect to a single parameter. For the NLTVA, the evolution of LP and NS have been computed with respect to the forcing amplitude as varying parameter. For the Jeffcott rotor, the LP and NS bifurcations have been tracked with respect to the friction coefficient. Then, an original method, based on HBM, has been developed to perform a multi-parametric recursive continuation for parametric analysis of nonlinear systems. The originality lies in the implementation of a recursive continuation process based on a extremum characterization adapted for continuation techniques. At the end of the analysis, the evolution of a specific initial point and all associated extremum points with respect to several parameters are obtained. Therefore, the presented method can perform both parametric analysis and optimization of the chosen system. The algorithm has then been applied to a NLTVA to push the birth of ISs at higher forcing amplitude. The evolution, limits of existence and extremum of birth and merging of ISs have been uncovered with respect to the chosen parameters. The obtained results permit optimizing and better understanding how the NLTVA's ISs are evolving with respect to the forcing amplitude, the nonlinear stiffness and the damping coefficients. It results in new configurations that can decorrelate system parameters from the birth of ISs, push the birth of IS at higher forcing amplitude and even totally withdraw the ISs from the dynamics of the system. A comparison of the efficiency shows that each configuration presents a range of forcing amplitude in which the efficiency of the NLTVA is the best.

In the second part of the thesis, a robust method for the computation of NNMs as a family of periodic solutions has been developed. The continuation process of NNM has been improved by the addition of an optimized phase condition and a damping matrix multiplied by a quasi-null coefficient. Then, an extension of conservative NNM to non-conservative equations of motion has been provided. As in linear modal analysis, the extension to non-conservatives NNMs characterizes the phase resonance and the resonance of the energy of displacement. Moreover, the same methods used to provide non-conservative LNMs have been used to obtain non-conservative NNMs. The original-

ity of the approach lies in the characterization of non-conservative NNM with conservative equations and in the direct extension of non-conservative LNMs to non-conservative NNMs.

Then, the problems of stability and bifurcations computation have been addressed. A shifted Quadratic Eigenvalue Problem obtained by Hill's method has been introduced for the NNM stability and bifurcation analysis. It results in a method that can compute conservative and non-conservative NNMs with their corresponding stability and bifurcations. Then, multiple configurations of a 2-ddl system have been analyzed with the proposed method. First, the dynamics of the system has been analyzed with respect to the underlying symmetries of the system and conservative NNMs. Several phenomena such as INNM, merging and birth of ISs, tongues of modal interactions, birth and degeneracy of BPs have been explained based on symmetry considerations. Moreover, NNMs with complex topology have been computed in a single calculation, proving the robustness of the method. Secondly, the theory describing the energy resonance of the displacement has been validated with viscous, cubic and sinusoidal damping. Then, it has been shown that an appropriate fictive force can accurately target specific NNM points such as branches of modal interaction, modal interaction points and points on the main NNM branch. A sensitivity analysis with respect to the accuracy of the fictive force has also been performed. Finally, the concept of energy resonance has been validated on a system with cubic nonlinear damping.

In the last part of the thesis, the influence of electrostatic coupling between the beams of a MEMS array has been analyzed. It has been shown that, because of the coupling, each beam presents complicated behaviors such as the birth of loops and synchronization of bifurcation points. Then, the effect of symmetry-breaking on the global dynamic of a resonant MEMS array has been studied. A symmetric 2-beam MEMS array has been considered. The results show that symmetry-breaking events generate INNM that support ISs. Moreover, the merging and birth of ISs are related to NNM properties. If an IS is supported by an INNM, the merging of IS with the main frequency cannot happen. However, if the IS is supported by a pure or a mixed NNM, it can only merge with the main frequency response if both NNMs are excited by the input force. Then, these preliminary works have been used to provide new mechanisms for mass detection. In an asymmetric configuration, it is based on a threshold of detection induced by the effect of electrostatic coupling. If the value of the added mass is greater than the value of the threshold, the mass is detected and identified by a classical hysteresis cycle. Concerning the symmetric configuration, the mass detection can be improved by using symmetry-breaking bifurcations. Moreover, by choosing a high bias voltage, a phenomenon similar to buckling but for periodic solutions could be used to put the amplitude range of detection outside of the zone dominated by the ambient noise.

Perspectives

The results of this work open the following perspectives:

- The newly developed tool for parametric analysis with respect to multiple parameter could be used on large nonlinear systems modeled with FEM to observe the evolution of specific points with respect to multiple parameters.
- One could try to use the same concept of recursion to characterize bifurcations in increasing co-dimensions based on the multiplicity of specific eigenvalues.
- The multi-parametric recursive continuation permits to follow a specific augmented system with respect to multiple system parameters. So, one could use the method to perform the continuation of multiple initial points characterized by a single augmented system. For example, it could be used to obtain the evolution of several maximums of energy with respect to several parameters. One could even introduce equations constraining the several peaks at the same amplitude.
- The theory developed to compute NNMs could be used for the nonlinear modal analysis of any nonlinear system. Moreover, the fictive forces associated to the non-conservative NNM could be used to target specific NNMs and therefore perform experimental tracking of NNM including branches of solutions appearing from BP bifurcation.
- The implementation of stability and bifurcation analysis for energy resonance NNMs.
- One could adapt the concept of non-conservative NNM to compute "free-oscillations" modes. Those modes would be excited by transient phenomena until all energy is dissipated. This extension could then be used to provide a way to identify NNMs using impact characterization.
- The computation of NNMs could be extended to equations of motion composed of nonsmooth nonlinear forces without regularization of those forces.
- Based on the work made on the influence of symmetry-breaking event, one could detect a small added mass by using the localization of motion induced by multiple symmetry-breaking events. This method could be used to tune several mass thresholds associated to each symmetry of the system. Especially, it could be used to detect multiple masses in parallel.

Synthèse des contributions

Cette thèse a pour buts de fournir des méthodes numériques pour une meilleure analyse de la dynamique globale des systèmes mécaniques nonlinéaires oscillants. Ces méthodes sont appliquées à un absorbeur de vibration nonlinéaire ajusté pour améliorer ses performances et aux tableaux de MEMS pour la détection de masses infimes afin de fournir des méthodes alternatives de détection. Les contributions sont principalement:

1. La caractérisation des points de bifurcations de résonance 1:1 (R1) et Point Limite Neimark Sacker (LPNS) en utilisant la méthode de la Balance Harmonique. Cette caractérisation améliore l'analyse des points de bifurcations à l'aide de méthodes de résolutions basées sur la balance harmonique. Ces points de bifurcations de co-dimensions 2 rendent possible une analyse de point de bifurcations selon deux paramètres du système.

2. La création d'une méthode d'analyse paramétrique de systèmes nonlinéaires selon de multiple paramètres. Cette méthode peut être appliquée à n'importe quel point initial caractérisé par un système augmenté. En utilisant notre caractérisation récursive de point extrémal sous forme de système augmenté, la méthode assure la continuation du point initial et de ses extremums. Ainsi les résultats fournis sont les points extrémaux ainsi que les courbes d'évolutions de ceux-ci selon l'intégralité des paramètres système choisis.

3. L'amélioration d'un absorbeur nonlinéaire ajusté de vibration (NLTVA). L'étude a été réalisée à l'aide de la méthode d'analyse multi-paramétrique présentée précédemment appliquée aux solutions isolées. L'analyse des résultats a fourni l'évolution des solutions isolées selon les plusieurs paramètres de l'absorbeur. Il en résulte plusieurs configurations repoussant à plus haute amplitude de forçage l'apparition des solutions isolées (ISs) et augmentant ainsi sa plage opérationnelle. En plus de cela, certaines configurations arrivent à décorréler l'apparition de solutions isolées avec certains paramètres de l'absorbeur.

4. La création de méthodes numériques pour le calcul des modes normaux nonlinéaires, ainsi que leur stabilité et leurs points de bifurcations. La méthode de continuation des modes normaux nonlinéaires est basée sur une condition de phase spécifique et une relaxation de l'équation de mouvement. Il en résulte une méthode numérique robuste de continuation modes normaux nonlinéaires. Une double

régularisation du problème quadratique aux valeurs propres obtenue par méthode de Hill a été effectuée afin de calculer la stabilité des modes et d'obtenir les équations caractérisant les points limites (LPs) et de points de branchements (BPs). De plus une extension aux modes normaux nonlinéaires non-conservatif est proposée afin de calculer les résonances de phase et d'énergie en déplacement.

5. L'analyse de la dynamique des tableaux de MEMS à l'aide des méthodes développées, ainsi que la proposition de mécanismes de détection alternatifs basées sur la dynamique nonlinéaires des tableaux de MEMS. L'analyse des tableaux de MEMS à l'aide de méthode d'analyse paramétrique et de calcul de modes normaux nonlinéaires a permis de comprendre les changements sur la dynamique induits par des phénomènes complexes. Ainsi, il est expliqué que le couplage électrostatique engendre un phénomène de synchronisation en fréquence des points de bifurcations présents sur les différentes poutres du tableau de MEMS. De même l'influence sur la dynamique des brisures de symétries générées par l'ajout d'une masse à quantifier est expliquée. Ces deux phénomènes sont par la suite exploités pour former des mécanismes alternatifs de détection de masses infimes.

Analyse et caractérisation de résonance 1:1 (R1) et de point limite de neimarck sacker (LPNS)

Les points de bifurcations jouent un rôle important dans la dynamique globale des systèmes nonlinéaires. Ces points sont des solutions de l'équation de mouvement où le théorème de fonction implicite est mal posé et où les changements de dynamique se produisent. Ainsi, l'analyse paramétrique des points de bifurcations représente un bon moyen d'appréhender la dynamique des systèmes nonlinéaires. Les points de bifurcations peuvent être catégorisés en fonction de leur codimension. Les points de bifurcations rencontrés sur les courbes de réponses sont de codimension 1. De même, les points de bifurcations rencontrés sur les courbes de codimension 1 sont de codimension 2. Dans la section 2.1, les détections, les localisations et les suivies des points de bifurcations de codimension 1 sont rappelés. Dans cette section un résumé de la caractérisant les bifurcations R1 et LPNS de codimension-2 est présenté. Des exemples d'analyse paramétriques de bifurcations sont ensuite détaillés.

Résonance 1:1 (R1) Ce point de bifurcation apparait sur des courbes de LPs, il est notamment lié à la topologie présentée dans la Fig. 4.42a. Les points de Neimark-Sacker (NS) sont des bifurcations délimitant les zones de solutions quasi-périodiques. Par conséquent, il est intéressant de détecter les bifurcations R1 car elles représentent la fin ou le début de courbes de bifurcations de NS pour identifier les limites d'évolution des plages de solutions de quasi-périodique selon le paramètre utilisé lors de l'analyse paramétrique.

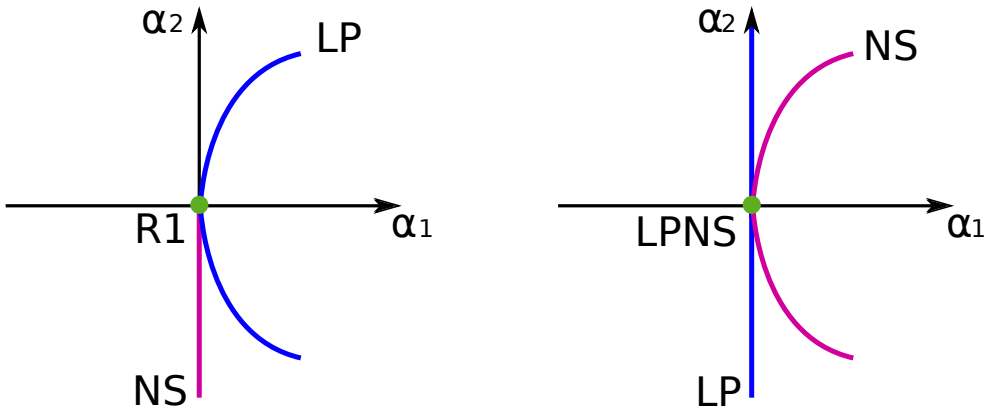

(a) Bifurcation R1 (b) Bifurcation LPNS

Figure 4.42 – Bifurcations de codimension-2

Le point de bifurcation peut être calculé à l'aide du système augmenté suivant:

$$R1(\boldsymbol{Y}) = \begin{pmatrix} \boldsymbol{R} \\ \boldsymbol{R_X}\phi_1 \\ \boldsymbol{R_X}\phi_2 + \boldsymbol{\Delta}_1\phi_1 \\ \phi_1^T\phi_1 - 1 \\ \phi_2^T\phi_1 \end{pmatrix} = \mathbf{0}_{3L+2} \tag{4.36}$$

où $\boldsymbol{Y} = (\boldsymbol{X}, \phi_1, \phi_2, \omega, \alpha)$ avec α le paramètre utilisé lors de la continuation des LPs ou des NSs, $\boldsymbol{X}$ les coefficients de Fourier du vecteur déplacements solution de l'équation de mouvement $\boldsymbol{R} = \mathbf{0}_L$, $\boldsymbol{R_X}$ la jacobienne de l'équation de mouvement, ω la fréquence d'excitation et (ϕ_1, ϕ_2) des vecteurs utiles au calcul.

Point limite de Neimarck Sacker (LPNS) Ce point de bifurcation apparait sur des courbes de point limites, il est notamment lié à la topologie présenté dans la Fig. 4.42b. Ce point représente l'endroit où deux courbes de LPS et de NSs coïncident. Le point de bifurcation est calculé à l'aide du système augmenté suivant:

$$LPNS(\boldsymbol{Y}) = \begin{pmatrix} \boldsymbol{R} \\ \boldsymbol{R_X}\phi_1 \\ \boldsymbol{R_X}\phi_2 - \kappa\boldsymbol{\Delta}_1\phi_3 - \kappa^2\boldsymbol{\Delta}_2\phi_2 \\ \boldsymbol{R_X}\phi_3 + \kappa\boldsymbol{\Delta}_1\phi_2 - \kappa^2\boldsymbol{\Delta}_2\phi_3 \\ \phi_1^T\phi_1 - 1 \\ \boldsymbol{q}^T\phi_2 \\ \phi_2^T\phi_2 - 1 \end{pmatrix} = \mathbf{0}_{4L+3} \tag{4.37}$$

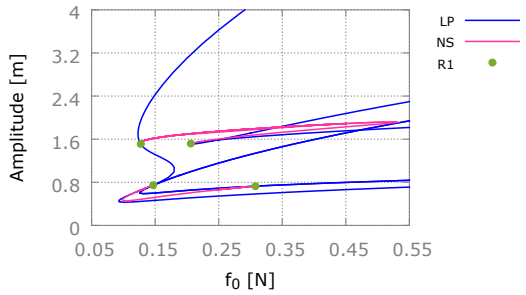

(a) NLTVA - Courbes de LPs et de NSs.
f_0: Amplitude de forçage

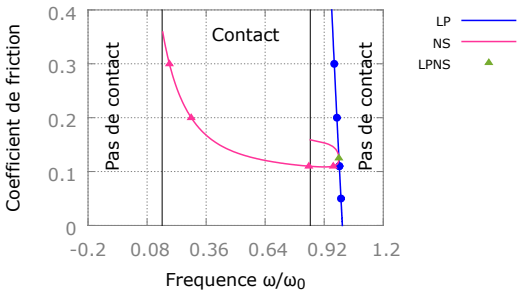

(b) Jeffcott - Courbes de LPs et de NSs

Figure 4.43 – Résultats de l'analyse paramétrique

où $\boldsymbol{Y} = (\boldsymbol{X}, \phi_1, \phi_2, \phi_3, \omega, \alpha)$ avec α le paramètre utilisé lors de la continuation des LPs ou des NSs, $\boldsymbol{X}$ les coefficients de fourrier du vecteur déplacements solution de l'équation de mouvement $\boldsymbol{R} = \boldsymbol{0}_L$, $\boldsymbol{R}_{\boldsymbol{X}}$ la jacobienne de l'équation de mouvement, ω la fréquence d'excitation et (ϕ_1, ϕ_2, ϕ_3) des vecteurs utiles au calcul.

Analyse de bifurcation Deux analyses paramétriques ont été réalisées sur un absorbeur nonlinéaire ajusté de vibrations (NLTVA) tiré de [DET 15a] et un modèle de rotor Jeffcott tiré du papier [XIE 16b]. Voici les résultats finaux dans la Fig. 4.43 représentants les points de bifurcations de codimension 1 et 2 selon des paramètres systèmes. Les points de codimension-1 sont correctement suivis et ceux de codimension-2 bien localisés. Différents phénomènes sont expliqués plus en détails dans la section 2.1.4. Notamment sur les résultats du NLTVA, la courbe de LP la plus à gauche a la forme d'un S caractéristique de la présence d'une IS.

L'analyse de bifurcation est réalisée sur deux exemples que sont le NLTVA et le rotor de Jeffcott. Bien que limitées à un unique paramètre variable, ces méthodes sont utiles pour effectuer des analyses paramétriques de systèmes non-linéaires car elles donnent directement un aperçu de la dynamique des systèmes selon le paramètre étudié. Ces méthodes ont démontré la présence de solutions isolées dans les réponses du NLTVA.

Méthode d'analyse multi-paramétrique par continuation récursive

Les méthodes de continuation sont des outils très efficaces pour réaliser des analyses paramétriques de systèmes non-linéaires et plus précisément du suivi de bifurcations. Cependant, les méthodes de continuations actuelles sont toutes mono-paramétriques. Les systèmes non-linéaires étant complexes, ceux-ci ne peuvent pas être analysés correctement dans tous les cas avec de telles méthodes. Par conséquent, il est nécessaire de créer des méthodes d'analyse paramétriques selon de multiples paramètres. Pour faire

cela la méthode proposée effectue des niveaux de continuation récursive des bifurcations et de ces extremums. Ainsi, on obtient une méthode rapide pour analyser l'entièreté de l'évolution du point de bifurcation et de ces extremums selon les paramètres choisis.

La méthode d'analyse multi-paramétrique est initiliasée par le calcul précis du point à continuer $\boldsymbol{Y}_0$ solution d'un système augmenté $\boldsymbol{G}_0(\boldsymbol{Y}_0) = \boldsymbol{0}$. Ensuite, un paramètre α_1 est libéré afin d'effectuer le niveau 1 de continuation représentant la branche de solution $\boldsymbol{G}_0(\boldsymbol{Y}_0, \alpha_1) = \boldsymbol{0}$. S'en suit une détection et une localisation des 1-extremums de la branche de solution à l'aide de localisation précise des extremums basée sur la caractérisation récursive suivante:

$$\boldsymbol{G}_k(\boldsymbol{Y}_k) = \begin{pmatrix} \boldsymbol{G}_{k-1}(\boldsymbol{Y}_{k-1}, \alpha_k) \\ \boldsymbol{G}_{k-1_{\boldsymbol{Y}_{k-1}^j}} \phi_k \\ \phi_k^T \phi_k - 1 \end{pmatrix} = \boldsymbol{0} \quad \text{with} \quad \begin{array}{rcl} \boldsymbol{Y}_k & = & (\boldsymbol{Y}_{k-1}, \phi_k, \alpha_k) \\ \boldsymbol{Y}_{k-1}^j & = & \big((\boldsymbol{Y}_{k-1}, \alpha_k) \setminus \alpha_j, \alpha_k\big) \end{array} \tag{4.38}$$

avec $\boldsymbol{G}_k$ le k-extremum localisé sur un niveau $(k-1)$ de continuation, $\boldsymbol{\alpha}$ le vecteur des paramètres choisis pour effectuer l'analyse, $\boldsymbol{G}_{k-1_{\boldsymbol{Y}_{k-1}^j}}$ la jacobienne de $\boldsymbol{G}_{k-1}$ par rapport au vecteur $\boldsymbol{Y}_{k-1}^j$. Les extremums obtenus servent alors comme nouveaux points initiaux pour le niveau de continuation suivant. La méthode d'analyse multi-paramétrique par continuation récursive peut être résumée à l'aide de l'algorithme présenté dans la Tab. 4.4

De cette méthode, il résulte les branches de solutions du point initial et de ces extremums formant un arbre avec de courbes et de ramifications indiquant le changement de niveau de continuation. Les extremums de cette arbre peuvent alors être utilisés pour fournir les sets de paramètres $\boldsymbol{\alpha}$ correspondant aux optimums locaux. Alors que, les branches de solutions obtenues par continuation fournissent les zones d'existences des points suivis délimitées par les extremums locaux. Par la suite, ces informations peuvent être exploitées pour visualiser l'évolution de certain phénomènes selon de multiple paramètres ou encore pour fournir des sets de paramètres améliorant les systèmes existants.

Amélioration d'un absorbeur nonlinéaire ajusté de vibration (NLTVA)

Dans la Section 2.3, la méthode d'analyse multi-paramétrique par continuation récursive est utilisée pour analyser les ISs présentes dans les réponses du NLTVA de [DET 15a], voir Fig. 4.44. Les paramètres choisis pour effectuer l'analyse sont l'amplitude de forçage f_0, les coefficients de raideur non-linéaire knl_2 et d'amortissement c_2 de l'amortisseur. Avec cette analyse, l'évolution des ISs sont analysées et mieux visualisées selon les paramètres choisis et fourni des dimensionnements améliorant l'efficacité du NLTVA.

Voici un résumé des résultats obtenus (Fig. 4.45) lors de l'analyse multi-paramétrique du NLTVA schématisé dans la Fig. 4.44. Sur la Fig. 4.45a est repérée la forme de S

Étape 0:	Initialisation - Choisir l'ensemble p paramètres système $\boldsymbol{\alpha} = (\alpha_1, .., \alpha_p)$ à utiliser pour la continuation multi-paramétrique récursive. - Définir les domaines fermés $\boldsymbol{D}_{\boldsymbol{\alpha}} = \boldsymbol{D}_{\alpha_1} \times ... \times \boldsymbol{D}_{\alpha_p}$ au sein desquels l'ensemble $\boldsymbol{\alpha}$ des paramètres varie. - Résoudre le système augmenté $\boldsymbol{G}_0(\boldsymbol{Y}_0) = \boldsymbol{0}_{2L+1}$ pour localiser le point initial $\boldsymbol{Y}_0$ à continuer.
Étape 1:	Niveau 1 de continuation et détection des 1-extremums (a) Niveau 1 de continuation * Prendre α_1 comme une nouvelle inconnue. * Continuer la branche $\boldsymbol{G}_0(\boldsymbol{Y}_0, \alpha_1) = \boldsymbol{0}$ avec α_1 balayant $\boldsymbol{D}_{\alpha_1}$ * Détecter tout les 1-extremums avec l'indicateur $\Delta_{\alpha_1} = 0$ (b) Résoudre le système augmenté $\boldsymbol{G}_1(\boldsymbol{Y}_1) = \boldsymbol{0}$ pour localiser précisément tout les 1-extremums $\boldsymbol{Y}_1$. (c) Finir l'algorithme si aucun 1-extremum n'est détecté. Autrement, aller à l'étape 2.
Étape k: $k = [2, ..., p]$	Niveau k de continuation et détection des k-extremums Pour chaque $(k-1)$-extremum $\boldsymbol{Y}_{k-1}$ détectés durant l'étape $k-1$: (a) Niveau k de continuation * Prendre α_k comme une nouvelle inconnue. * Continuer la branche $\boldsymbol{G}_{k-1}(\boldsymbol{Y}_{k-1}, \alpha_k) = \boldsymbol{0}$ avec α_k balayant $\boldsymbol{D}_{\alpha_k}$ * Détecter tous les k-extremums selon chaque paramètre $\alpha_j \in [\alpha_1, .., \alpha_k]$ avec les indicateurs $\Delta\alpha_j = 0$ (b) Résoudre le système augmenté $\boldsymbol{G}_k(\boldsymbol{Y}_k) = \boldsymbol{0}$ pour localiser précisément tout les k-extremums $\boldsymbol{Y}_k$ détectés dans (a) (c) Finir l'algorithme si aucun k-extremum n'est détecté ou si $k = p$. Autrement, aller à l'étape $(k+1)$.

Table 4.4 – Algorithme d'analyse multi-paramétrique par continuation récursive.

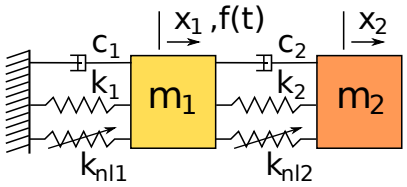

Figure 4.44 – Modèle mécanique du NLTVA

évoquée précédemment représentant le niveau 1 de continuation de LP selon l'amplitude du forçage f_0. Celle-ci est caractéristique de la présence de ISs. Les deux extremums sur le S représentent la naissance et la fusion de l'IS avec la courbe de réponse. On peut voir que pour une amplitude de forçage f_0 plus grande que celle obtenue au niveau de la fusion de l'IS, il existe un grand saut en amplitude résultant de la fusion de l'IS avec la courbe de réponse diminuant ainsi fortement l'efficacité de l'absorbeur. Par conséquent, afin d'améliorer la plage opérationnelle, le point de fusion doit être repoussé à des amplitudes de forçage plus hautes. Pour visualiser l'évolution des points de naissance et de fusion de l'IS, le suivi de ces points de 1-extemums est réalisé avec le coefficient de raideur nonlinéaire comme paramètre variable additionnel, voir Fig. 4.45b. La plage opérationnelle peut être multipliée par 16 en prenant la configuration ($D2$) du point 2-extremum avec l'amplitude de forçage la plus haute possible (soit celui-ci de plus à droite). De plus, pour des coefficients de raideur nonlinéaire supérieurs à $knl_2 > 0.0076N/m^3$, les ISs ne peuvent pas apparaitre et cela quelque soit la valeur de l'amplitude de forçage f_0. Afin d'obtenir encore plus d'informations sur l'évolution des ISs, la continuation des 2-extremums représentant la coïncidence des points de naissance et de fusion de l'IS est réalisée, voir Figs. 4.45c et 4.45d. Deux 3-extremums selon les paramètres knl_2 et c_2 y sont distingués. De la même manière qu'au niveau 2 de continuation, des zones sans IS sont constatées et délimitées par les extremums $D3$ et $D4$, voir Fig. 4.45c. Ces zones sont intéressantes car elles fournissent des configurations décorrélant l'apparition de le IS avec certains paramètres du NLTVA. Le point $D4$ présente un intérêt limité car l'amplitude de forçage associé est très faible. Par conséquent la configuration de paramètre associé à ce point est incapable d'élargir la plage opérationnelle. La point $D3$ quant à lui est intéressant car il permet de multiplier la plage opérationnelle par 9 tout en limitant l'influence des paramètres knl_2 et c_2 sur la présence de solutions isolées.

Les différentes configurations retenues $D2, D3, D4$ sont comparés avec le "Equal Peak" de [DET 15a] dans la Fig. 4.46. Chaque configuration est optimale dans la plage d'amplitude de forçage composée de sa plage opérationnelle moins l'ensemble des plages opérationnelles propres aux autres configurations. Ainsi $D2$ permet d'élargir le plus la plage opérationnelle mais possède une mauvaise efficacité pour les faibles amplitudes. la configuration$D3$ présente les moins bonnes performances à basse amplitude de forçage mais a l'avantage d'avoir les coefficients de raideur nonlinéaire et de d'amortissement qui influencent peu ou pas l'apparition de la IS. De plus, il présente aussi la meilleure efficacité dans la plage $f0 = 0.18N - 1.1N$. la configuration$D1$, quant à lui, n'est pas présenté faute de place dans ce résumé succinct.

Pour conclure, les résultats obtenus conduisent à une meilleure visualisation de la structure des ISs du NLTVA selon l'amplitude de forçage, les coefficients de raideur nonlinéaire et d'amortissement de l'amortisseur. L'analyse paramétrique prodigue de multiples résultats tels que les zones d'existence des ISs selon les paramètres systèmes et les configurations permettant d'améliorer l'efficacité du NLTVA. En utilisant ces designs, la plage opérationnelle peut être grandement augmentée et l'apparition de IS décorrélée de certains paramètres du système. Ainsi, la méthode d'analyse multi-paramétrique améliore l'efficacité du NLTVA tout en le rendant moins sujet à l'apparition de ISs.

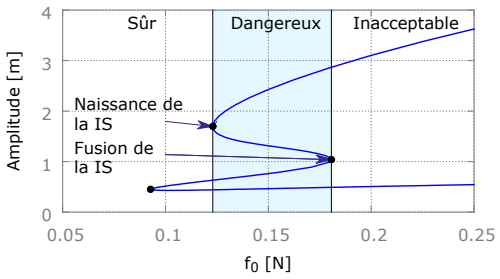

(a) Niveau 1 de continuation des LPs dans le plan amplitude-f_0.
LP (Bleu foncé), 1-extremum (Noire)

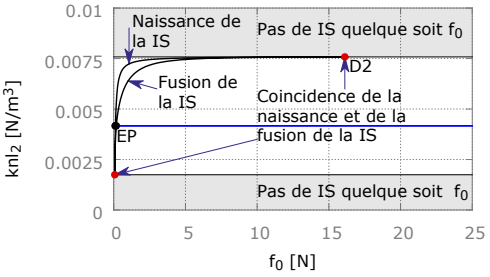

(b) Niveau 2 de continuation. Continuation des 1-extremums de LP dans le plan knl_2-f_0. LP (Bleu foncé), 1-extremum (Noir), 2-extremum (Rouge)

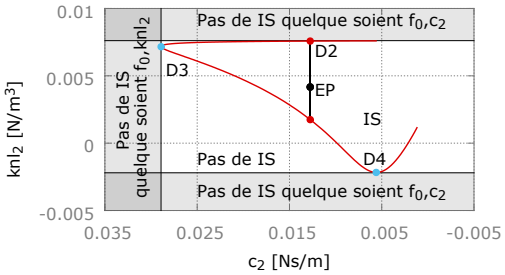

(c) Niveau 3 de continuation. Continuation des 2-extremums de LP dans le plan knl_2-c_2. 1-extremum (Noir), 2-extremum (Rouge), 3-extremum (Bleu ciel)

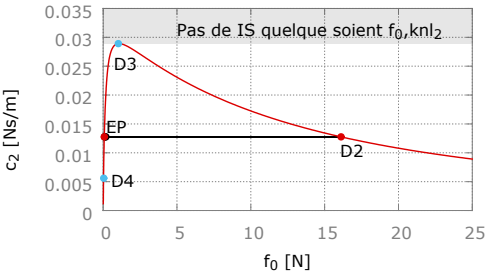

(d) Niveau 3 de continuation. Continuation des 2-extremums de LP dans le plan c_2-f_0. 1-extremum (Noir), 2-extremum (Rouge), 3-extremum (Bleu ciel)

Figure 4.45 – Résultats de l'analyse multi-paramétrique du NLTVA.

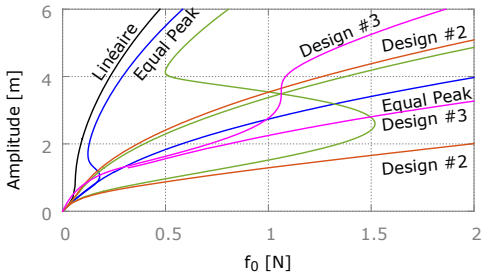

(a) Comparaison de l'efficacité des designs retenus

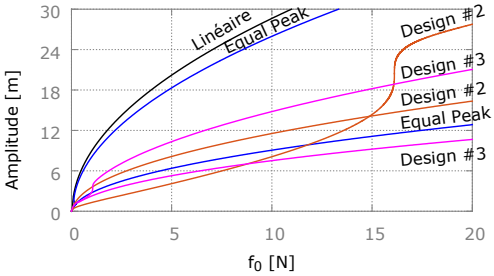

(b) Comparaison de l'efficacité des designs retenus (vue étendue)

Figure 4.46 – Linéaire avec $knl_2 = 0N/m^3$ (Noire), "Equal Peak" avec $knl_2 = 0.0042N/m^3$ (Bleu), Design #2 avec $knl_2 \approx 0.0076N/m^3$ (Orange), Design #3 avec $(knl_2, c_2) \approx (0.0072N/m^3, 0.029Ns/m)$ (Magenta)

Calcul de Modes normaux nonlinéaires (NNM)

Une méthode de le calcul par continuation des NNMs conservatifs, de leur stabilité et de leurs points de bifurcations (LP et BP) est proposée. Puis, deux extensions du concept de NNMs pour calculer les résonances de phase et d'énergie en déplacement d'équations de mouvement non-conservatives autonomes sont présentées.

Calcul des NNMs conservatifs, de leur stabilité et de leurs bifurcations

Pour calculer les NMNs d'une équation de mouvement, le forçage doit être imposé à zéro ($\boldsymbol{F} = 0_L$) afin d'obtenir l'équation autonome suivante:

$$\boldsymbol{R}(\boldsymbol{X}, \omega) = \boldsymbol{Z}(\omega)\boldsymbol{X} + \boldsymbol{F}_{nl}(\boldsymbol{X}, \omega) = \boldsymbol{0}_L \tag{4.39}$$

avec $\boldsymbol{Z}$ la partie linéaire, $\boldsymbol{X}$ le vecteur de déplacement et $\boldsymbol{F}_{nl}$ le vecteur des forces non-linéaires.

Condition de phase Pour réaliser la continuation des NNMs conservatif, une condition de phase adaptée est introduite et résolue en parallèle avec l'équation de mouvement autonome présentée dans l'Eq. (4.39) résultant en un système augmenté à solution unique localement mais sur-contraint.

$$g(\boldsymbol{X}) = \boldsymbol{X}_{j-1}^T (\boldsymbol{\nabla} \otimes \boldsymbol{I}_n) \boldsymbol{X} = 0 \tag{4.40}$$

avec $\boldsymbol{X}_{j-1}^T$ le vecteur de déplacement au pas de continuation précédant $(j-1)$.

Relaxation de l'équation du mouvement Afin d'obtenir un système augmenté capable de calculer les NNMs, le système augmenté sur-contraint composé de l'équation de mouvement et de la condition de phase présenté Eq. (4.40) est relaxé en ajoutant une partie non-conservative multipliée par un coefficient quasi-nul à l'équation de mouvement:

$$\boldsymbol{M}\ddot{\boldsymbol{x}}(t) + \mu \boldsymbol{e}_{fic}(\dot{\boldsymbol{x}}) + \boldsymbol{K}\boldsymbol{x}(t) + \boldsymbol{f}_{nl}(\boldsymbol{x}, \dot{\boldsymbol{x}}) = \boldsymbol{0}_n \tag{4.41}$$

Il en résulte l'équation suivante en HBM:

$$\boldsymbol{R}(\boldsymbol{X}, \omega, \mu) = \boldsymbol{Z}(\omega)\boldsymbol{X} + \boldsymbol{F}_{nl}(\boldsymbol{X}, \omega) + \mu \left(\boldsymbol{\nabla} \otimes \boldsymbol{I}_n\right) \boldsymbol{X} = \boldsymbol{0}_L \tag{4.42}$$

Le système augmenté composé de l'équation de mouvement relaxée, Eq. (4.42), et de la condition de phase, Eq. (4.40), permet alors le calcul des NNMs.

Calcul de stabilité Le système augmenté résultant ayant une jacobienne carrée, la stabilité du NNM peut être calculé à l'aide du problème quadratique aux valeurs propres (QEP) obtenu par la méthode de Hill.

$$\boldsymbol{Q}(\boldsymbol{X}, \lambda, \phi) = (\boldsymbol{R}_X + \Lambda\boldsymbol{\Delta}_1 + \Lambda^2\boldsymbol{\Delta}_2)\phi = \boldsymbol{0}_L \tag{4.43}$$

avec

$$\Lambda_k = \lambda_j + il\omega$$
$$\text{avec} \quad j \in [0,2n]\,,\, k \in [0,2L]\,,\, l \in [-H,H]\,,\, 2L = 2n \times (2H+1) \text{ et } i^2 = -1 \quad (4.44)$$

avec $\phi = \phi_r + i\phi_i$ les vecteurs propres associés, $\boldsymbol{R_X}$ la jacobienne de l'équation de mouvement, voir Eq. (1.24) et $(\boldsymbol{\Delta}_1, \boldsymbol{\Delta}_2)$ des matrices définies dans les Eqs. (1.43) et (1.44). Les λ_j représentent les exposants de Floquet pour le calcul de la stabilité. Cependant, ce QEP possède une double singularité et n'est pas utilisable comme tel. Il doit tout d'abord être régularisé doublement.

$$\begin{aligned} \tilde{\tilde{\boldsymbol{Q}}}_(\boldsymbol{X}, \tilde{\tilde{\Lambda}}, \tilde{\tilde{\phi}}, \varphi_1, \boldsymbol{\xi}) &= (\tilde{\tilde{\boldsymbol{R}}}_{\boldsymbol{X}} + \tilde{\tilde{\Lambda}}\tilde{\tilde{\boldsymbol{\Delta}}}_1 + \tilde{\tilde{\Lambda}}^2\tilde{\tilde{\boldsymbol{\Delta}}}_2)\tilde{\tilde{\phi}} &&= \mathbf{0}_L \\ &= [\boldsymbol{R}_{\boldsymbol{X}} + \boldsymbol{\Delta}_1(\varphi_1\varphi_1^* + \boldsymbol{\xi}\boldsymbol{\xi}^*) + \boldsymbol{\Delta}_2(\varphi_1\varphi_1^*\boldsymbol{\xi}\boldsymbol{\xi}^*) &&= \mathbf{0}_L \\ &\quad + \tilde{\tilde{\Lambda}}(\boldsymbol{\Delta}_1 + \boldsymbol{\Delta}_2(\varphi_1\varphi_1^* + \boldsymbol{\xi}\boldsymbol{\xi}^*)) + \tilde{\tilde{\Lambda}}^2\boldsymbol{\Delta}_2]\tilde{\tilde{\phi}} \end{aligned} \quad (4.45)$$

avec

$$\begin{aligned} &\bar{\varphi_1} = (\nabla \otimes \boldsymbol{I}_n)\boldsymbol{X}, \quad \boldsymbol{R}_X\bar{\varphi_2} = -\boldsymbol{\Delta}_1\bar{\varphi_1} \\ &\bar{\boldsymbol{\xi}} = \bar{\varphi_1} + \bar{\varphi_2}, \qquad \varphi_1 = \tfrac{\bar{\varphi_1}}{||\bar{\varphi_1}||}, \qquad \boldsymbol{\xi} = \tfrac{\bar{\boldsymbol{\xi}}}{||\bar{\boldsymbol{\xi}}||} \end{aligned} \quad (4.46)$$

Caractérisation des LPs et BPs Le QEP modifié obtenu est ensuite utilisé pour le calcul de stabilité et la caractérisation des LPs et BPs.

- LPs: Contrairement aux solutions d'un système forcé, les LPs rencontrés sur les NNMs ne représentent pas un extremum selon la fréquence de la solution. Par conséquent, seul le critère lié au changement de stabilité peut être utilisé afin de le caractériser. En introduisant $\Lambda = 0$ dans le QEP régularisé, les LPs peuvent être caractérisés. Il en résulte le système augmenté suivant:

$$LP(\boldsymbol{Y}) = \begin{pmatrix} \boldsymbol{R}(\boldsymbol{X}, \omega, \mu) \\ g(\boldsymbol{X}) \\ \tilde{\tilde{\boldsymbol{R}}}_{\boldsymbol{X}}(\boldsymbol{X}, \omega, \varphi_1, \varphi_2)\phi \\ \phi^T\phi - 1 \end{pmatrix} = \mathbf{0}_{2L+2} \quad (4.47)$$

  avec $\boldsymbol{Y} = (\boldsymbol{X}, \omega, \mu, \varphi_1, \varphi_2, \phi)$.

- BPs: Les BPs présents sur les NNMs conservent les mêmes propriétés liées aux changement de stabilités et à l'apparition d'une nouvelle branche de solution. En introduisant $\Lambda = 0$ dans le QEP régularisé, le changement de stabilité lié aux BPs peut être caractérisé. Il faut encore rajouter à cela l'équation caractérisant l'apparition d'une nouvelle branche de solution ($\boldsymbol{R}_\omega^T\phi = 0$ avec $\boldsymbol{R}_\omega$ la jacobienne selon la

fréquence de la solution) pour obtenir l'ensemble des équations permettant le calcule des BPs. Cette equation additionnelle permet de simplifier l'équation caractérisant le changement de stabilité. En faisant cela le système augmenté permettant le calcul des BPs est obtenue:

$$BP(\boldsymbol{Y}) = \begin{pmatrix} \boldsymbol{R}(\boldsymbol{X},\omega,\mu) \\ g(\boldsymbol{X}) \\ \bar{\boldsymbol{R}_{\boldsymbol{X}}}(\boldsymbol{X},\omega,\varphi_1,\varphi_2)\phi \\ \boldsymbol{R}_\omega^T\phi \\ \phi^T\phi - 1 \end{pmatrix} = \mathbf{0}_{2L+3} \tag{4.48}$$

avec $\boldsymbol{Y} = (\boldsymbol{X},\omega,\mu,\varphi_1,\varphi_2,\phi)$.

Extension des NNMs aux équations non-conservatives Deux extensions permettant de calculer les résonances de phase et d'énergie de déplacements d'équations non-linéaires non-conservatives sont présentées.

- Résonance de phase

  La phase ϕ entre solution périodique $\boldsymbol{X}$ et le forçage $\boldsymbol{F}$ de l'Eq. (1.5) est calculée ainsi:

$$\phi = \arctan\left(\frac{((\nabla_{bis}\otimes\boldsymbol{I}_n)\boldsymbol{X})^T(\boldsymbol{R}_{nc})}{\boldsymbol{X}^T(\boldsymbol{R}_c)}\right) \quad \text{où} \quad \nabla_{bis} = \begin{bmatrix} 0 & \mathbf{0}_{1\times 2L} \\ \mathbf{0}_{2L\times 1} & \boldsymbol{I}_H \otimes \begin{bmatrix} 0 & -1 \\ -1 & 0 \end{bmatrix} \end{bmatrix} \tag{4.49}$$

  avec $(\boldsymbol{R}_c,\boldsymbol{R}_{nc})$ les parties conservatives et non-conservatives de l'Eq. (1.5) calculées à l'aide de l'Eq. (3.20). Pour avoir une résonance de phase, il faut que $\boldsymbol{X}^T(\boldsymbol{R}_c) = 0$ et que $\boldsymbol{X}^T(\boldsymbol{R}_{nc}) \neq 0$. Comme $\boldsymbol{X} \neq \mathbf{0}_L$, l'équation correspondant à la résonance de phase est la suivante:

$$\boldsymbol{R}_\phi = \left(\Omega\nabla^2\otimes\boldsymbol{M} + \boldsymbol{I}\otimes\boldsymbol{K}\right)\boldsymbol{X} + \boldsymbol{F}_{nlc} = \mathbf{0}_L \tag{4.50}$$

  On peut remarquer qu'il s'agit de la même que celle utilisée pour calculer les NNMs conservatifs.

- Résonance d'énergie

  La résonance d'énergie se produit lorsque:

$$\frac{\partial \boldsymbol{X}^T\boldsymbol{X}}{\partial\omega} = 0 \tag{4.51}$$

  Après maints calculs, l'équation caractérisant cette propriété est la suivante:

$$\boldsymbol{R}_E = \left(\left(\Omega\nabla^2 \otimes \boldsymbol{M} + \boldsymbol{I} \otimes \boldsymbol{K}\right)\boldsymbol{X} + \left(\boldsymbol{F}_{nlc}\right)\right) - \frac{1}{2}\left(\nabla_1^2 \otimes \boldsymbol{M} + \frac{1}{2\omega}\frac{\partial(\mathbf{MatF_{nl}}_c^T)_1}{\partial\omega}\right)^{-1}$$
$$\left(\nabla \otimes \boldsymbol{C} + \frac{\partial \mathbf{MatF_{nl}}_{nc}^T}{\partial\omega}\right)\left(\left(\nabla \otimes \boldsymbol{C}\right)\boldsymbol{X} + \frac{\boldsymbol{F}_{nlnc}}{\omega}\right) = \mathbf{0}_L \quad (4.52)$$

avec $(\frac{\partial \mathbf{MatF_{nl}}_c^T}{\partial\omega}, \frac{\partial \mathbf{MatF_{nl}}_{nc}^T}{\partial\omega})$ les matrices présentées dans la Sous-section 4.5.

Force fictive Pour cibler précisément un point du NNM caractérisé par l'équation $\boldsymbol{R}_\phi = \mathbf{0}_L$ ou $\boldsymbol{R}_E = \mathbf{0}_L$ à l'aide d'une réponse forcée solution de l'équation $\boldsymbol{R} = \mathbf{0}_L$, il suffit d'utiliser le vecteur de force fictive obtenue de la sorte:

$$\begin{pmatrix} \boldsymbol{R} = \boldsymbol{Z}\boldsymbol{X} + \boldsymbol{F}_{nl} - \boldsymbol{F}_{fic} = \mathbf{0}_L \\ \boldsymbol{R}_\phi = \mathbf{0}_L \text{ ou } \boldsymbol{R}_E = \mathbf{0}_L \end{pmatrix} \Rightarrow \boldsymbol{F}_{fic} = \boldsymbol{Z}\boldsymbol{X} + \boldsymbol{F}_{nl} - (\boldsymbol{R}_\phi \text{ ou } \boldsymbol{R}_E) \quad (4.53)$$

Les vecteurs de forces sont appelés "fictives" car il s'agit de la force à injecter dans le système forcé pour compenser la perte d'énergie respective aux NNMs non-conservatifs garantissant la non-modification de la variété invariante. Les forces fictives obtenues correspondant aux résonances de phase et d'énergie sont les suivantes:

- Résonance de phase

$$\boldsymbol{F}_{fic}^{\phi} = \boldsymbol{\omega}\left(\nabla \otimes \boldsymbol{C}\right)\boldsymbol{X} + \boldsymbol{F}_{nlnc} \quad (4.54)$$

- Résonance d'énergie

$$\boldsymbol{F}_{fic}^{E} = \boldsymbol{\omega}\left(\nabla \otimes \boldsymbol{C}\right)\boldsymbol{X} + \boldsymbol{F}_{nlnc} + \frac{1}{2}\left(\nabla^2 \otimes \boldsymbol{M} + \frac{1}{2\omega}\frac{\partial(\mathbf{MatF_{nl}}_c)}{\partial\omega}\right)^{-1}$$
$$\left(\nabla \otimes \boldsymbol{C} + \frac{\partial \mathbf{MatF_{nl}}_{nc}}{\partial\omega}\right)\left(\left(\nabla \otimes \boldsymbol{C}\right)\boldsymbol{X} + \frac{1}{\omega}\boldsymbol{F}_{nlnc}\right) \quad (4.55)$$

Cette méthode a ensuite été appliquée à un système à 2-DDLs, soumis à plusieurs configurations, étudié dans de nombreuses recherches telles que [KER 09] et connu pour présenter une dynamique non-linéaire complexe, voir Section 3.5.

Analyse des résonance de phase à l'aide des symétries sous-jacentes du système Les résultats obtenus avec la configuration#1 présenté dans la Tab. 3.1 confirment la robustesse de la méthode en obtenant notamment le mode en phase en un seul calcul, voir Fig. 4.47. De plus, des explications pour mieux comprendre la topologie du NNM et de ces BPs sont présentées. Celles-ci sont basées sur l'étude des symétries sous-jacentes présentes dans le système.

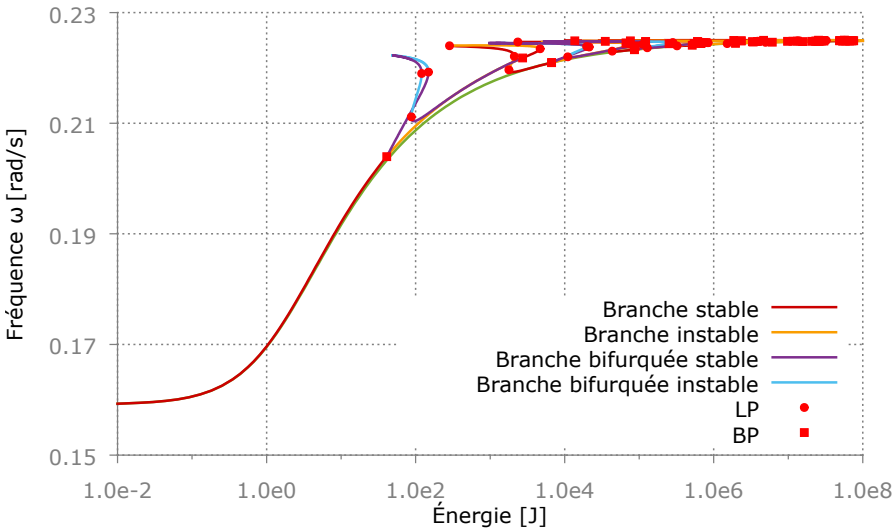

Figure 4.47 – Coube du NNM en phase

Étude d'une brisure de symétrie à l'aide d'un suivi de LP Dans la Sous-section 3.5.2, l'influence d'une brisure de symétrie sur les NNMs est étudié à l'aide du design #2 de la Tab. 3.1 et d'un suivi de LP selon un paramètre Δknl afin de briser la symétrie en question, voir Fig. 4.48. La brisure de symétrie génère des NNMs isolés (INNMs) s'éloignant de

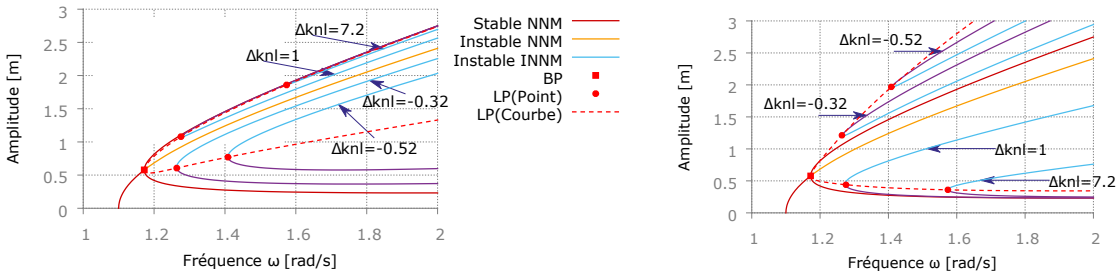

(a) Masse 1

(b) Masse 2

Figure 4.48 – Évolution des INNMs selon Δknl. INNM pour $\Delta knl = [7.2, 1, -0.32, -0.52] N/m^3$

la configuration symétrique au fur et à mesure que $||\Delta knl||$ augmente.

Analyse de sensibilité des courbes de réponses forcées à l'aide de forces fictives Dans la Sous-section 3.5.3, la configuration#3 de la Tab. 3.1 possédant un amortissement visqueux proportionnel à $\gamma = 5 \times 10^{-2}[s]$ fois la matrice de raideur $\boldsymbol{K}$ est pris afin de voir l'influence d'un amortissement structurel sur la résonance d'énergie. De plus, plusieurs forces fictives sont calculées et utilisées pour calculer les réponses forcées du système, voir Fig. 4.49. Les courbes obtenues suivent bien le NNM de résonance d'énergie, de plus celui-ci est quasi-identique au NNM de résonance phase. Cela montre l'intérêt du

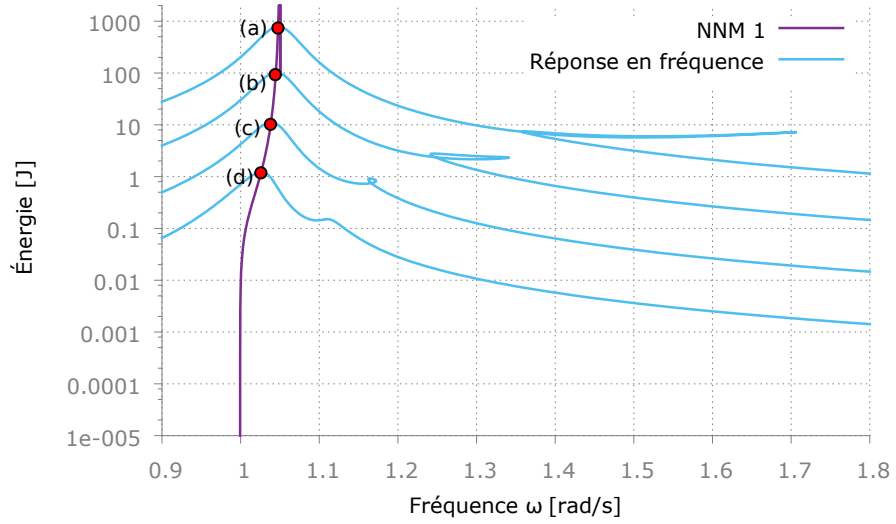

Figure 4.49 – NNMs en phase et en opposition de phase avec les courbes de réponses

concept de force fictive qui cible précisément un point du NNM. Par la suite, la précision est testé en tronquant les coefficients de Fourier des forces fictives ayant une contribution en énergie relative supérieur à un seuil. Trois cas de force fictives sont testés: une ciblant la branche principale loin de toutes interactions modales, une ciblant un point proche de l'interaction modale 3 : 1 et une ciblant un point sur l'orbite d'interaction modale 2 : 1. Il en résulte que plus la composition de la force fictive permettant de ciblé un point précis du NNM est riche, plus il est nécessaire d'avoir une force fictive précise afin d'observer la dynamique associée au point de NNM ciblé. De plus, pour un amortissement visqueux proportionnel de quelque pour-cents, il a été montré que le NNM de résonance de phase est suffisant pour caractériser les modes du systèmes.

Validation du concept de résonance d'énergie sur un système possédant un amortissement cubique Dans la Sous-section 3.5.4, la configuration#4 de la Tab. 3.1 présentant un amortissement cubique est utilisé pour valider le concept de résonance d'énergie. La résonance d'énergie en phase et sa sous-harmonique 3, ainsi que la résonance d'énergie en opposition de phase sont calculées. Puis, les réponses forcées sont obtenues à l'aide d'une force ciblant le NNM en phase pour diverses amplitudes $f_0 = [0.1, 0.5, 1, 5, 10, 50, 100, 500]N$ de forçage, voir Fig. 4.50. Le NNM en phase de résonance d'énergie correspond bien aux résonances en énergie des réponses forcées.

Tableaux de MEMS pour la détection de masses infimes

Un tableaux de n nano-poutres encastrées-encastrées excitées électrostatiquement (Fig. 4.51) est étudié afin de mettre en lumière de nouveaux phénomènes propres aux tableaux de MEMS exploitables pour de la détection de masse infime.

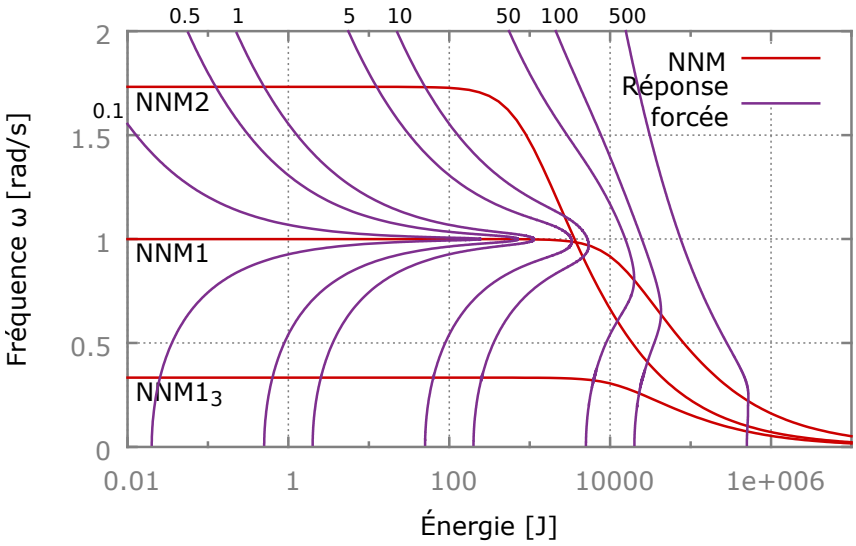

Figure 4.50 – NNM en phase (NNM1), sa sous-harmonique 3 (NNM1$_3$), NNM en opposition de phase (NNM3) et les réponses forcées pour $f_0 = [0.1, 0.5, 1, 5, 10, 50, 100, 500]N$

Synchronisation en fréquence des bifurcations

Premièrement, l'effet du couplage éléctrostatique sur la réponse du tableaux de MEMS a été analysé sur un tableaux de deux MEMS identiques, voir Section 4.2. Pour cela des solutions approchées obtenues par méthode de la moyenne sont utilisées pour distinguer et enlever les termes de couplages entre les poutres afin d'analyser leur influence sur la dynamique du système.

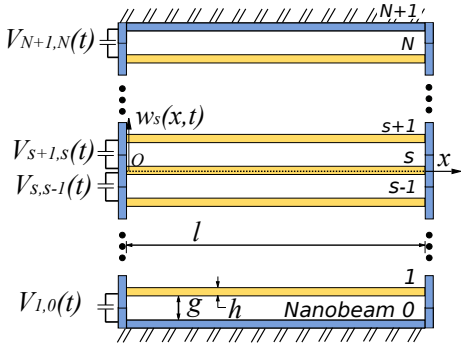

Figure 4.51 – Tableaux de MEMS à n-poutres.

La Fig. 4.52 montre que lorsque les termes de couplages ne sont pas pris en comptes, les réponses des poutres ressemblent à celles de deux MEMS simples. Autrement, il y a une complexification des réponses avec l'apparition de boucles ainsi que des points de bifurcations apparaissant aux mêmes fréquences sur les réponses des deux poutres.

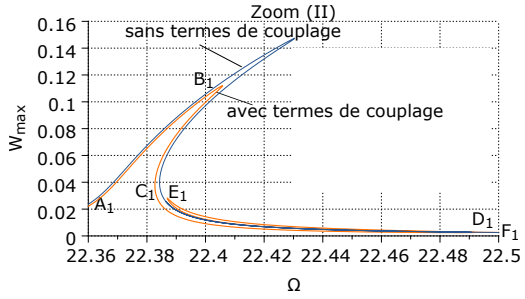

(a) Poutre 1

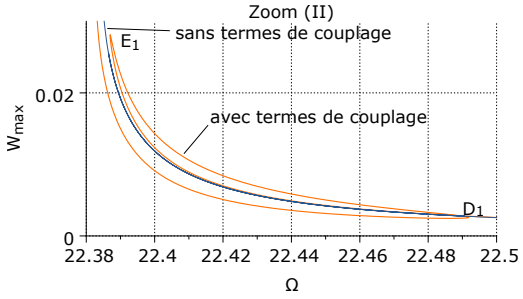

(b) Poutre 1 (Zoom I)

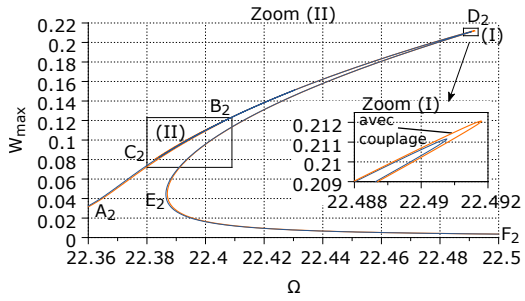

(c) Poutre 2

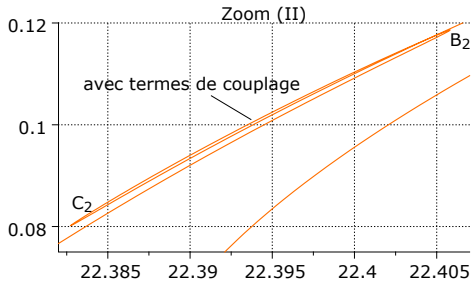

(d) Poutre 2 (Zoom II)

Figure 4.52 – Tableaux à deux poutres. Réponses sans les termes de couplages (blue), avec les termes de couplages (orange).

Influence d'une brisure de symétrie

Un suivi de bifurcation et des calcul de modes normaux non-linéaires ont été utilisées afin d'analyser l'influence d'une brisure de symétrie induite par un ajout de masse sur la première poutre d'un tableau symétrique de 2 poutres, voir Section 4.3. L'analyse met en évidence des phénomènes de localisation de mouvement, de création d'ISs et de modes normaux non-linéaires isolés (INNMs). Une analyse a montrée que les ISs pouvaient être supportées par des modes normaux non-linéaires pouvant dans certain cas être isolés. De plus, il a été montré que les propriétés d'apparition et de fusion des ISs dépendaient du type de modes normal non-linéaire sur lequel elles étaient (pure, mixte, isolé). Un cas d'étude où le mode en phase est excité est particulièrement intéressant car il présent un phénomène de localisation de mouvement important pouvant potentiellement être exploité pour réaliser de la détection de masse. Sur la Fig. 4.53, la localisation du mouvement a lieu sur la seconde poutre. De plus, il y a la présence de ISs portées par un INNM. En brisant la symétrie dans l'autre sens avec un ajout de masse, un important changement d'amplitude est induit par l'inversion de la localisation de mouvement pouvant être exploité pour détecter et quantifier la masse ajoutée.

Mécanismes de détection

Des mécanismes de détection de masses utilisant un tableau à 2-poutres et à 3-poutres sont présentés, voir Section 4.4.

Détection fondée sur le décalage en fréquence et des cycles hystérétiques Le mécanisme de détection proposé est basé sur le phénomène de synchronisation en fréquence des bifurcations. Après l'ajout d'une masse, le décalage en fréquence engendre la fusion des boucles additionnelles générant d'importants changements dans les cycles hystérétiques, voir Fig. 4.54. La masse ajoutée sur la poutre 2 engendre un décalage du pic de résonance vers les basses fréquences et ainsi la création de boucles additionnelles faisant passer le maximum d'amplitude de la première poutre de $W_{max}(B_1) \approx 0.11$ à $W_{max}(F_1) \approx 0.17$. Pour détecter la masse ajoutée grâce à la différence en amplitude, deux balayages en fréquence respectivement montant et descendant sont utilisés. La fréquence minimale doit être prise entre $\Omega(C_1)$ et $\Omega(I_1)$; la fréquence maximale doit être prise supérieure à $\Omega(J_1)$. La réponse de la première poutre est obtenue avec une amplitude maximale de $W_{max} = 0.02$ avant l'ajout de masse et $W_{max} = 0.15$ pour une masse de $\delta m = 10^{-4}$; une réponse de la seconde poutre avec une amplitude maximale de $W_{max} = 0.22$ avant l'ajout de masse et de $W_{max} = 0.04$ pour une masse de $\delta m = 10^{-4}$. Par conséquent, la masse ajoutée est clairement détectée par la différence d'amplitude. Deux seuils de détection causés par le phénomène de synchronisation en fréquence de bifurcation peuvent être ajustés à l'aide du courant continus V_{dc} et V_{ac} afin de détecter de faibles masses et des masses plus importantes.

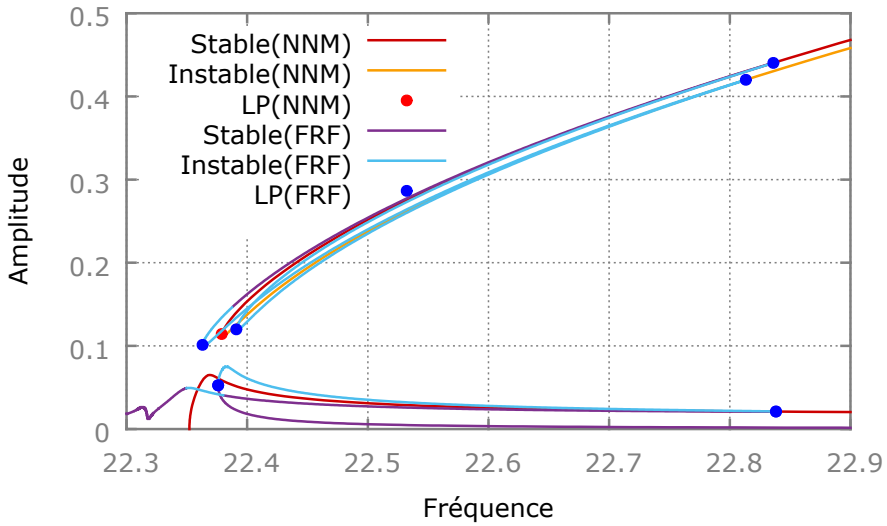

(a) Poutre 1

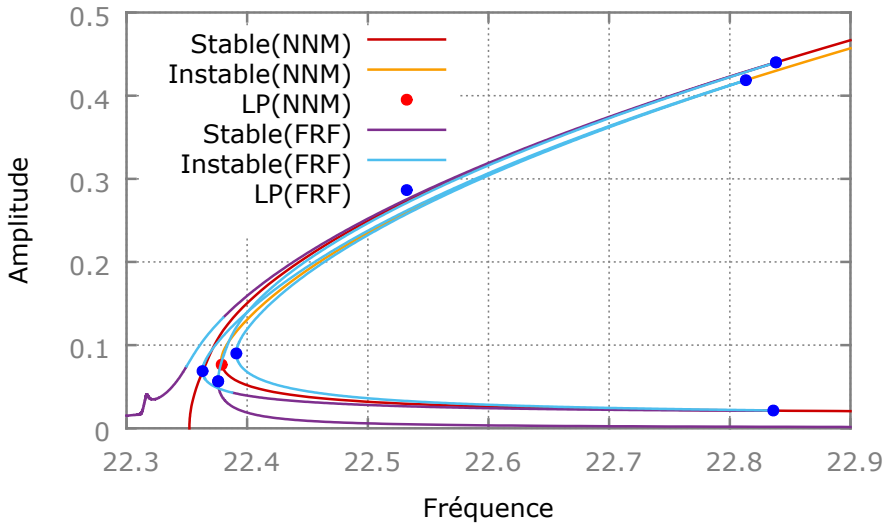

(b) Poutre 2

Figure 4.53 – Tableaux de MEMS à 2-poutres après brisure de symétrie. Courbe de réponses et IS avec le mode en opposition existé ($\delta_m = 10^{-4}$)

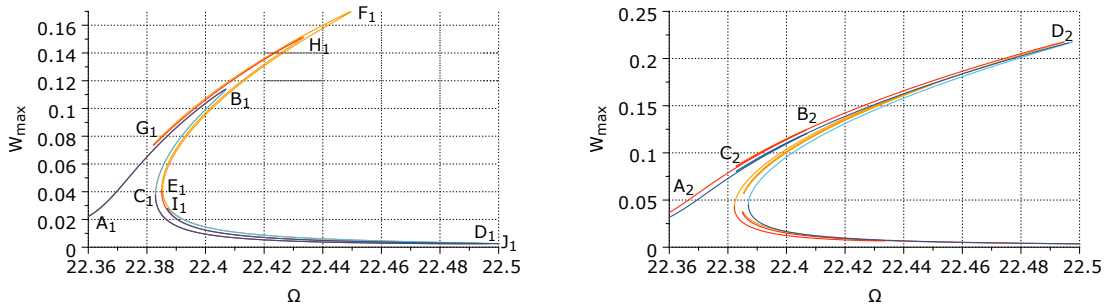

(a) Poutre 1 (b) Poutre 2

Figure 4.54 – HBM+ANM avec une masse de $\delta m = 10^{-4}$ (rouge: stable, orange: instable) et sans masse (bleu foncé: stable, bleu clair: instable).

Détection fondée sur la brisure de symétrie Un tableau symétrique à 3-poutres est considéré pour cette étude. Comme celui est symétriquement excité, la poutre du milieu ne peut pas bouger. Une masse ajoutée est par la suite ajoutée sur la première poutre brisant la symétrie et générant un grand saut d'amplitude sur la courbe de réponse de la poutre du milieu, permettant la détection de la masse. Ce grand saut d'amplitude peut ensuite être utilisé afin de quantifier la masse. Deux configurations ont été utilisés afin de détecter une masse ajoutée, seul le second design est présenté dans ce résumé. La résonance associé au mode normal asymétrique du tableaux est utilisée, voir Fig. 4.55. Un important gain en amplitude a lieu sur la second poutre. Afin d'obtenir un abaque pour quantifier la masse, un suivi direct de LP est réalisée en fonction de la valeur du paramètre de la masse ajoutée δ_m, voir Fig. 4.55d. L'abaque obtenu dans la Fig. 4.55d permet directement de quantifier la masse en fonction du maximum d'amplitude de la poutre 2. De plus, l'asymptote en amplitude présente dans la Fig. 4.55d peut être ajustée en fonction du courant continu V_{dc} de l'excitation électrostatique. Par conséquent, il est possible d'ajuster cette asymptote en amplitude afin que celle-ci soit en dehors de la plage dominée par le bruit ambiant.

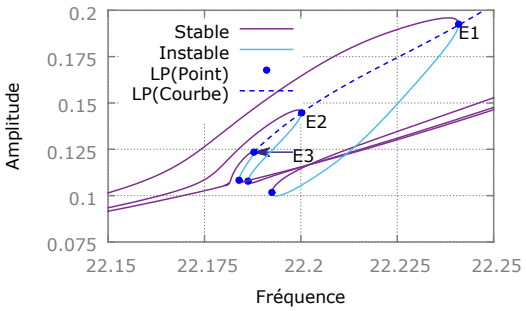

(a) Poutre #1

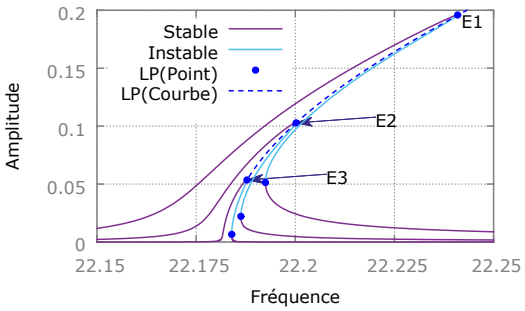

(b) Poutre 2

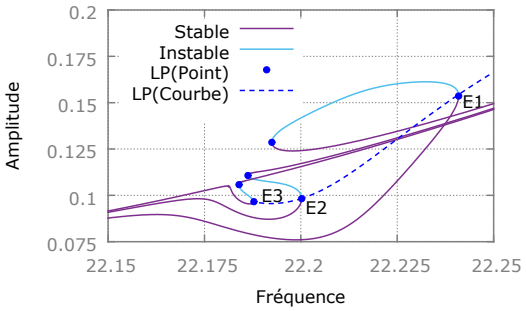

(c) Poutre #3

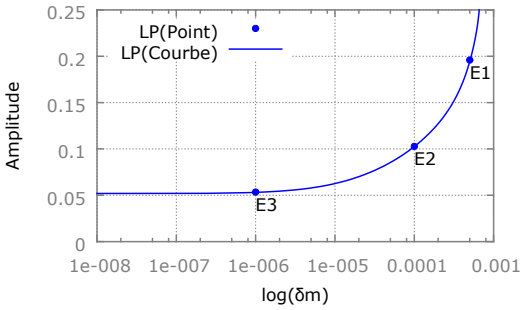

(d) Maximum d'amplitude Max(W_{max}) selon la valeur de δm pour la poutre 2.

Figure 4.55 – Tableaux de 3-poutres.

Annexes

Annexe A

The Eq. (3.24) is multiplied by a matrix $(\boldsymbol{AX})^*$ representing its complex conjugate in the time domain.

$$\boldsymbol{X}^*\boldsymbol{A}^*\boldsymbol{AX} = \boldsymbol{F}^T\boldsymbol{F} \tag{4.56}$$

Since $\boldsymbol{A}$ possesses complex eigenvalues, $\boldsymbol{X}$ must be composed by at least two eigenvectors ϕ_1, ϕ_2 their imaginary part compensating each other. Since we want to be at an energy resonance, $\boldsymbol{X}$ can be written as $\boldsymbol{X} = \alpha_1\phi_1 + \alpha_2\phi_2$. Therefore, Eq. (4.56) becomes:

$$\lambda_1^2\alpha_1^2\phi_1^T\phi_1 + \lambda_2^2\alpha_2^2\phi_2^T\phi_2 = \boldsymbol{F}^T\boldsymbol{F} \tag{4.57}$$

with (λ_1, λ_2) the eigenvalues associated wit ϕ_1 and ϕ_2. In order to have the imaginary parts of $(\lambda_1\alpha_1\phi_1, \lambda_2\alpha_2\phi 2)$ compensating each other, α_1,ϕ_1,$\phi 2$,α_2 must verify:

$$\alpha_1 = \alpha_2 \qquad \phi_1^* = \phi_2 = \phi_r + i\phi_i \qquad \lambda_1^* = \lambda_2 = \lambda_r + i\lambda_1 \tag{4.58}$$

with $i^2 = -1$ and where the subscript $_r$ and $_i$ stand for the real and imaginary parts respectively. Introducing Eq. (4.58) in Eq. (4.56), the following equation is obtained:

$$(\lambda_r^2 - \lambda_i^2)\boldsymbol{X}^T\boldsymbol{X} = \boldsymbol{F}^T\boldsymbol{F} \tag{4.59}$$

The derivation with respect to $\Omega = \omega^2$ is then performed:

$$\frac{\partial \lambda_r^2 - \lambda_i^2}{\partial \Omega}\boldsymbol{X}^T\boldsymbol{X} + (\lambda_r^2 - \lambda_i^2)\frac{\partial \boldsymbol{X}^T\boldsymbol{X}}{\partial \Omega} = \boldsymbol{0}_L \tag{4.60}$$

Since we want to be at the resonance characterized by Eq. (3.23), i.e., $\frac{\partial \boldsymbol{X}^T\boldsymbol{X}}{\partial \Omega} = 0$, the following equation is obtained:

$$\frac{\partial \lambda_r^2 - \lambda_i^2}{\partial \Omega}\boldsymbol{X}^T\boldsymbol{X} = 0 \tag{4.61}$$

which is equivalent to:

$$\frac{\partial \boldsymbol{A}^*\boldsymbol{A}}{\partial \Omega}\boldsymbol{X} = \boldsymbol{0}_L \tag{4.62}$$

In order to complete this derivative, $\boldsymbol{A}$ is first split up into a conservative part $\boldsymbol{A}_c$ and a non-conservative part $\boldsymbol{A}_{nc}$ with the help of Eq. (3.20); so that $\boldsymbol{A} = \boldsymbol{A}_c + \boldsymbol{A}_{nc}$ and:

$$\boldsymbol{A}^* \boldsymbol{A} = \boldsymbol{A}_c^T \boldsymbol{A}_c + \boldsymbol{A}_{nc}^T \boldsymbol{A}_{nc} \tag{4.63}$$

Thus, Eq. (4.62) is equivalent to:

$$\frac{\partial \boldsymbol{A}_c^T \boldsymbol{A}_c}{\partial \Omega} \boldsymbol{X} + \frac{\partial \boldsymbol{A}_{nc}^T \boldsymbol{A}_{nc}}{\partial \Omega} \boldsymbol{X} = \boldsymbol{0}_L \tag{4.64}$$

Let's compute separately $\frac{\partial \boldsymbol{A}_c^T \boldsymbol{A}_c \boldsymbol{X}}{\partial \Omega} \boldsymbol{X}$ and $\frac{\partial \boldsymbol{A}_{nc}^T \boldsymbol{A}_{nc}}{\partial \Omega} \boldsymbol{X}$.

$$\begin{aligned} \frac{\partial \boldsymbol{A}_c^T \boldsymbol{A}_c}{\partial \Omega} \boldsymbol{X} &= \frac{\partial \left(\Omega^2 \nabla^2 \otimes \boldsymbol{M} + \boldsymbol{I} \otimes \boldsymbol{K} + \mathbf{MatF_{nl}}_c\right)^T \left((\Omega^2 \nabla^2 \otimes \boldsymbol{M} + \boldsymbol{I} \otimes \boldsymbol{K}) \boldsymbol{X} + \boldsymbol{F}_{nlc}\right)}{\partial \Omega} \\ &= 2 \left(\nabla^2 \otimes \boldsymbol{M} + \frac{1}{2\omega} \frac{\partial \mathbf{MatF_{nl}}_c}{\partial \omega}^T\right) \left((\Omega \nabla^2 \otimes \boldsymbol{M} + \boldsymbol{I} \otimes \boldsymbol{K}) \boldsymbol{X} + \boldsymbol{F}_{nlc}\right) \quad \text{because } \nabla^{2^T} = \nabla^2 \end{aligned} \tag{4.65}$$

$$\begin{aligned} \frac{\partial \boldsymbol{A}_{nc}^T \boldsymbol{A}_{nc}}{\partial \Omega} \boldsymbol{X} &= \frac{\partial (\omega \nabla \otimes \boldsymbol{C} + \mathbf{MatF_{nl}}_{nc})^T (\omega (\nabla \otimes \boldsymbol{C}) \boldsymbol{X} + \boldsymbol{F}_{nlnc})}{\partial \Omega} \\ &= -\left(\nabla \otimes \boldsymbol{C} - \frac{\partial \mathbf{MatF_{nl}}_{nc}^T}{\partial \omega}\right) \left((\nabla \otimes \boldsymbol{C}) \boldsymbol{X} + \frac{\boldsymbol{F}_{nlnc}}{\omega}\right) \quad \text{because } \nabla^T = -\nabla \end{aligned} \tag{4.66}$$

with $(\frac{\partial \mathbf{MatF_{nl}}_c^T}{\partial \omega}, \frac{\partial \mathbf{MatF_{nl}}_{nc}^T}{\partial \omega})$ the matrix presented in Eq. (4.71). The complete derivative with respect to Ω can be obtained:

$$\begin{aligned} &\left(\nabla^2 \otimes \boldsymbol{M} + \frac{1}{2\omega} \frac{\partial \mathbf{MatF_{nl}}_c^T}{\partial \omega}\right) \left((\Omega \nabla^2 \otimes \boldsymbol{M} + \boldsymbol{I} \otimes \boldsymbol{K}) \boldsymbol{X} + \boldsymbol{F}_{nlc}\right) \\ &\qquad - \frac{1}{2} \left(\nabla \otimes \boldsymbol{C} - \frac{\partial \mathbf{MatF_{nl}}_{nc}^T}{\partial \omega}\right) \left((\nabla \otimes \boldsymbol{C}) \boldsymbol{X} + \frac{\boldsymbol{F}_{nlnc}}{\omega}\right) = \boldsymbol{0}_L \end{aligned} \tag{4.67}$$

However, the matrix $\left(\nabla^2 \otimes \boldsymbol{M} + \frac{1}{2\omega} \frac{\partial \mathbf{MatF_{nl}}_c^T}{\partial \omega}\right)$ is singular and can not be inverted in order to simplify the formulation. Since the singularity of the matrix is induced by the constant Fourier coefficient, the Eq. (4.67) is compared with the following static equation verified by the constant terms:

$$\boldsymbol{K} + (\boldsymbol{F}_{nlc})_0 = \boldsymbol{0}_n \tag{4.68}$$

with $(\boldsymbol{F}_{nlc})_0$ the constant part of the conservative nonlinear forces. In order for the two constant parts of the equations to be equal, the matrix $\left(\nabla^2 \otimes \boldsymbol{M} + \frac{1}{2\omega} \frac{\partial \mathbf{MatF_{nl}}_c^T}{\partial \omega}\right)$ is regularized by replacing ∇ by a new matrix ∇_1 defined as follows:

$$\nabla_1 = \mathrm{diag}(1, \nabla_{Harm}) = \mathrm{diag}(\zeta, \nabla_1, ..., \nabla_j, ..., \nabla_H) \quad \text{with} \quad \nabla_j = j \begin{bmatrix} 0 & 1 \\ -1 & 0 \end{bmatrix} \tag{4.69}$$

where 1 and ∇_{Harm} are related to the constant and the harmonic parts of the Fourier coefficients. So:

$$\boldsymbol{R}_E = \left(\left(\omega^2\nabla^2\otimes\boldsymbol{M}+\boldsymbol{I}\otimes\boldsymbol{K}\right)\boldsymbol{X}+\left(\boldsymbol{F}_{nlc}\right)\right)-\frac{1}{2}\left(\nabla_1^2\otimes\boldsymbol{M}+\frac{1}{2\omega}\frac{\partial(\mathbf{MatF_{nl}}_c^T)_1}{\partial\omega}\right)^{-1}$$
$$\left(\nabla\otimes\boldsymbol{C}+\frac{\partial\mathbf{MatF_{nl}}_{nc}^T}{\partial\omega}\right)\left(\left(\nabla\otimes\boldsymbol{C}\right)\boldsymbol{X}+\frac{\boldsymbol{F}_{nlnc}}{\omega}\right)=\mathbf{0}_L \quad (4.70)$$

with $(\mathbf{MatF_{nl}}_c^T)_1$ calculated with ∇_1.

Computation of energy resonance partial derivatives

During the computation of the residue presented in Eq. (3.25), the terms $(\frac{\partial(\mathbf{MatF_{nl}}_c^T)_1}{\partial\omega},\frac{\partial(\mathbf{MatF_{nl}}_{nc}^T)_1}{\partial\omega})$ are computed as such:

$$\begin{aligned}\frac{\partial(\mathbf{MatF_{nl}}_c^T)_1}{\partial\omega} &= -\omega\nabla\otimes\boldsymbol{I}_n\Gamma^T\frac{\partial\boldsymbol{f}_{nlc}}{\partial\dot{\boldsymbol{x}}}\Gamma^{-1}\\ \frac{\partial(\mathbf{MatF_{nl}}_{nc}^T)_1}{\partial\omega} &= -\omega\nabla\otimes\boldsymbol{I}_n\Gamma^T\frac{\partial\boldsymbol{f}_{nlnc}}{\partial\dot{\boldsymbol{x}}}\Gamma^{-1}\end{aligned} \quad (4.71)$$

with $\boldsymbol{f}_{nlnc}$ and $\boldsymbol{f}_{nlc}$ computed with Eq. (3.20). Then, during the continuation method presented in Section 3.1, the jacobians of Eq. (3.25) are computed as follows:

$$\begin{aligned}\boldsymbol{R}_{E\boldsymbol{X}} &= \left(Z+\frac{\partial\boldsymbol{F}_{nlc}}{\partial\boldsymbol{X}}\right)-\frac{1}{2}\left(\nabla_1^2\otimes\boldsymbol{M}+\frac{1}{2\omega}\frac{\partial(\mathbf{MatF_{nl}}_c^T)_1}{\partial\omega}\right)^{-1}\\ &\left(\frac{\partial\mathbf{MatF_{nl}}_{nc}^T}{\partial\omega\partial\boldsymbol{X}}\left(\left(\nabla\otimes\boldsymbol{C}\right)\boldsymbol{X}+\frac{\boldsymbol{F}_{nlnc}}{\omega}\right)+\left(\nabla\otimes\boldsymbol{C}+\frac{\partial\mathbf{MatF_{nl}}_{nc}^T}{\partial\omega}\right)\left(\nabla\otimes\boldsymbol{C}+\frac{1}{\omega}\frac{\partial\boldsymbol{F}_{nlnc}}{\partial\boldsymbol{X}}\right)\right)\\ &-\frac{1}{2\omega}\left(\left(\frac{\partial(\mathbf{MatF_{nl}}_c^T)_1}{\partial\omega}\right)^{-1}\frac{\partial(\mathbf{MatF_{nl}}_c^T)_1}{\partial\omega\partial\boldsymbol{X}}\right)\left(\nabla\otimes\boldsymbol{C}+\frac{\partial\mathbf{MatF_{nl}}_{nc}^T}{\partial\omega}\right)\left(\left(\nabla\otimes\boldsymbol{C}\right)\boldsymbol{X}+\frac{\boldsymbol{F}_{nlnc}}{\omega}\right)\\ \boldsymbol{R}_{E\omega} &= \left(Z_w\boldsymbol{X}+\frac{\partial\boldsymbol{F}_{nlc}}{\partial\omega}\right)-\frac{1}{2}\left(\nabla_1^2\otimes\boldsymbol{M}+\frac{1}{2\omega}\frac{\partial(\mathbf{MatF_{nl}}_c^T)_1}{\partial\omega}\right)^{-1}\\ &\left(\frac{\partial^2\mathbf{MatF_{nl}}_{nc}^T}{\partial\omega^2}\left(\left(\nabla\otimes\boldsymbol{C}\right)\boldsymbol{X}+\frac{\boldsymbol{F}_{nlnc}}{\omega}\right)+\left(\nabla\otimes\boldsymbol{C}+\frac{\partial\mathbf{MatF_{nl}}_{nc}^T}{\partial\omega}\right)\left(\frac{1}{\omega}\frac{\partial\boldsymbol{F}_{nlnc}}{\partial\omega}-\frac{\boldsymbol{F}_{nlnc}}{\omega^2}\right)\right)\\ &-\frac{1}{2}\left(\frac{\partial(\mathbf{MatF_{nl}}_c^T)_1}{\partial\omega}\right)^{-1}\left(\frac{1}{\omega}\frac{\partial^2(\mathbf{MatF_{nl}}_c^T)_1}{\partial\omega^2}-\frac{\boldsymbol{I}_L}{\omega^2}\right)\left(\nabla\otimes\boldsymbol{C}+\frac{\partial\mathbf{MatF_{nl}}_{nc}^T}{\partial\omega}\right)\left(\left(\nabla\otimes\boldsymbol{C}\right)\boldsymbol{X}+\frac{\boldsymbol{F}_{nlnc}}{\omega}\right)\end{aligned} \quad (4.72)$$

with the derivatives of $(\frac{\partial(\mathbf{MatF_{nl}}_c^T)_1}{\partial\omega},\frac{\partial(\mathbf{MatF_{nl}}_{nc}^T)_1}{\partial\omega})$ computed with:

$$\begin{aligned}\frac{\partial^2(\mathbf{MatF_{nl}}_c{}^T)_1}{\partial\omega^2}\boldsymbol{\phi} &= -\omega\nabla\otimes\boldsymbol{I}_n\Gamma^T\left(\frac{\partial\overline{\boldsymbol{f}_{nlc}\boldsymbol{\varphi}}}{\partial\dot{\boldsymbol{x}}^2}\Gamma\nabla\otimes\boldsymbol{I}_n\right)\\ \frac{\partial^2(\mathbf{MatF_{nl}}_c{}^T)_1}{\partial\omega\partial\boldsymbol{X}}\boldsymbol{\phi} &= -\omega\nabla\otimes\boldsymbol{I}_n\Gamma^T\\ &\left(\frac{\partial\overline{\boldsymbol{f}_{nlc}\boldsymbol{\varphi}}}{\partial\dot{\boldsymbol{x}}\partial\boldsymbol{x}}\Gamma+\frac{\partial\overline{\boldsymbol{f}_{nlc}\boldsymbol{\varphi}}}{\partial\dot{\boldsymbol{x}}^2}\Gamma\omega\nabla\otimes\boldsymbol{I}_n\right)\\ \frac{\partial^2(\mathbf{MatF_{nl}}_{nc}{}^T)_1}{\partial\omega^2}\boldsymbol{\phi} &= -\omega\nabla\otimes\boldsymbol{I}_n\Gamma^T\left(\frac{\partial\overline{\boldsymbol{f}_{nlnc}\boldsymbol{\varphi}}}{\partial\dot{\boldsymbol{x}}\partial\boldsymbol{x}}\Gamma\nabla\otimes\boldsymbol{I}_n\right)\\ \frac{\partial^2(\mathbf{MatF_{nl}}_{nc}{}^T)_1}{\partial\omega\partial\boldsymbol{X}}\boldsymbol{\phi} &= -\omega\nabla\otimes\boldsymbol{I}_n\Gamma^T\\ &\left(\frac{\partial\overline{\boldsymbol{f}_{nlnc}\boldsymbol{\varphi}}}{\partial\dot{\boldsymbol{x}}\partial\boldsymbol{x}}\Gamma+\frac{\partial\overline{\boldsymbol{f}_{nlnc}\boldsymbol{\varphi}}}{\partial\dot{\boldsymbol{x}}^2}\Gamma\omega\nabla\otimes\boldsymbol{I}_n\right)\end{aligned} \quad (4.73)$$

The derivatives in the time domain are computed as in Subsection. 2.1.3 with $\boldsymbol{\varphi}=\Gamma^{-1^T}\boldsymbol{\phi}$.

Annexes B

Computation of the shifted QEP

Let's calculate the problem shifted once using the method presented in [MEI 13]. In order to be shift the two zeros eigenvalues to -1 the problems $\boldsymbol{Q}$, defined in Eq. 1.42, and $\tilde{\boldsymbol{Q}}$ must have eigenvectors with the following proprieties.

$$\exists \boldsymbol{\nu}_1 \in \mathbb{R}^L / \quad \left[\begin{array}{l} \boldsymbol{Q}(0, \boldsymbol{\nu}_1) = \mathbf{0}_L \\ \boldsymbol{\nu}_1^T \boldsymbol{\nu}_1 = 1 \end{array} \right. \tag{4.74}$$

$$\exists \boldsymbol{\nu}_2 \in \mathbb{R}^L / \quad \left[\begin{array}{l} \tilde{\boldsymbol{Q}}(0, \boldsymbol{\nu}_2) = \mathbf{0}_L \\ \boldsymbol{\nu}_2^T \boldsymbol{\nu}_2 = 1 \end{array} \right. \tag{4.75}$$

with

$$\begin{array}{lll} \tilde{\tilde{\boldsymbol{\Delta}}}_2 = \tilde{\boldsymbol{\Delta}}_2 & = \boldsymbol{\Delta}_2 & \\ \tilde{\tilde{\boldsymbol{\Delta}}}_1 = \tilde{\boldsymbol{\Delta}}_1 + \tilde{\boldsymbol{\Delta}}_2 \left(\boldsymbol{\nu}_2 \boldsymbol{\nu}_2^T \right) & = \boldsymbol{\Delta}_1 & + \boldsymbol{\Delta}_2 \left(\boldsymbol{\nu}_1 \boldsymbol{\nu}_1^T + \boldsymbol{\nu}_2^T \boldsymbol{\nu}_2 \right) \\ \tilde{\tilde{\boldsymbol{R}}}_{\boldsymbol{X}} = \tilde{\boldsymbol{R}}_{\boldsymbol{X}} + \tilde{\boldsymbol{\Delta}}_1 \left(\boldsymbol{\nu}_2 \boldsymbol{\nu}_2^T \right) & = \boldsymbol{R}_{\boldsymbol{X}} & + \boldsymbol{\Delta}_1 \left(\boldsymbol{\nu}_1 \boldsymbol{\nu}_1^T + \boldsymbol{\nu}_2 \boldsymbol{\nu}_2^T \right) \\ & & + \boldsymbol{\Delta}_2 \left(\boldsymbol{\nu}_1 \boldsymbol{\nu}_1^T \boldsymbol{\nu}_2 \boldsymbol{\nu}_2^T \right) \end{array} \tag{4.76}$$

In order to find those eigenvectors, the following vectors are defined:

$$\begin{array}{ll} \bar{\boldsymbol{\varphi}}_2 \in \mathbb{R}^L / & \boldsymbol{R}_X \bar{\boldsymbol{\varphi}}_2 = -\boldsymbol{\Delta}_1 \bar{\boldsymbol{\varphi}}_1 \\ \bar{\boldsymbol{\xi}} \in \mathbb{R}^L / & \bar{\boldsymbol{\xi}} = \bar{\boldsymbol{\varphi}}_1 + \bar{\boldsymbol{\varphi}}_2 \\ \boldsymbol{\varphi}_1 \in \mathbb{R}^L / & \boldsymbol{\varphi}_1 = \frac{\bar{\boldsymbol{\varphi}}_1}{||\bar{\boldsymbol{\varphi}}_1||} \\ \boldsymbol{\varphi}_2 \in \mathbb{R}^L / & \boldsymbol{\varphi}_2 = \frac{\bar{\boldsymbol{\varphi}}_2}{||\bar{\boldsymbol{\varphi}}_2||} \\ \boldsymbol{\xi} \in \mathbb{R}^L / & \boldsymbol{\xi} = \frac{\bar{\boldsymbol{\xi}}}{||\bar{\boldsymbol{\xi}}||} \end{array} \tag{4.77}$$

Let's prove that $\boldsymbol{\nu}_1 = \boldsymbol{\varphi}_1$ and $\boldsymbol{\nu}_2 = \boldsymbol{\xi}$ are suitable to shift $\boldsymbol{Q}$.

- $\boldsymbol{\nu}_1 = \boldsymbol{\varphi}_1$

$$\left[\begin{array}{l} \boldsymbol{Q}(0, \boldsymbol{\varphi}_1) = \mathbf{0}_L \\ \boldsymbol{\varphi}_1^T \boldsymbol{\varphi}_1 = 1 \end{array} \right. \tag{4.78}$$

$$\left[\begin{array}{l} \boldsymbol{R}_X \boldsymbol{\varphi}_1 = \mathbf{0}_L \\ \boldsymbol{\varphi}_1^T \boldsymbol{\varphi}_1 = 1 \end{array} \right. \tag{4.79}$$

  So $\boldsymbol{\varphi}_1$ verify the property (4.74) and is thus suitable to shift the problem the first time.

- $\boldsymbol{\nu_2 = \xi}$

$$\begin{aligned}
& \tilde{\boldsymbol{Q}}(0,\xi) && = \mathbf{0}_L \\
\Leftrightarrow\ & \tilde{\boldsymbol{R}}_{\boldsymbol{X}}\xi && = \mathbf{0}_L \\
\Leftrightarrow\ & \left[\boldsymbol{R}_{\boldsymbol{X}} + \boldsymbol{\Delta}_1\left(\varphi_1\varphi_1^T\right)\right]\boldsymbol{\xi} && = \mathbf{0}_L \\
\Leftrightarrow\ & \boldsymbol{R}_{\boldsymbol{X}}\boldsymbol{\xi} + \boldsymbol{\Delta}_1\left(\varphi_1\varphi_1^T\right)\boldsymbol{\xi} && = \mathbf{0}_L \\
\Leftrightarrow\ & \boldsymbol{R}_{\boldsymbol{X}}\left(\tfrac{\bar{\varphi}_1+\bar{\varphi}_2}{||\bar{\varphi}_1+\bar{\varphi}_2||_2}\right) + \boldsymbol{\Delta}_1\left(\varphi_1\varphi_1^T\right)\left(\tfrac{\bar{\varphi}_1+\bar{\varphi}_2}{||\bar{\varphi}_1+\bar{\varphi}_2||_2}\right) && = \mathbf{0}_L \\
\Leftrightarrow\ & -\boldsymbol{\Delta}_1\tfrac{\bar{\varphi}_1}{||\bar{\varphi}_1+\bar{\varphi}_2||_2} + \boldsymbol{\Delta}_1\tfrac{\bar{\varphi}_1}{||\bar{\varphi}_1+\bar{\varphi}_2||_2} + \boldsymbol{\Delta}_1\left(\varphi_1\varphi_1^T\right)\tfrac{\bar{\varphi}_2}{||\bar{\varphi}_1+\bar{\varphi}_2||_2} && = \mathbf{0}_L \\
\Leftrightarrow\ & \boldsymbol{\Delta}_1\left(\varphi_1\varphi_1^T\right)\tfrac{\bar{\varphi}_2}{||\bar{\varphi}_1+\bar{\varphi}_2||_2} && = \mathbf{0}_L \\
\Leftrightarrow\ & \varphi_1^T\bar{\varphi}_2 && = 0
\end{aligned} \tag{4.80}$$

To be equal to zero φ_1 and φ_2 have to be orthogonal to each other. In order to prove this propriety, the QEP $\boldsymbol{Q}$ is rewritten as a linear problem $\boldsymbol{B}$.

$$(\boldsymbol{B} - \Lambda\cdot\boldsymbol{I}_{2L})\bar{\varphi} = \mathbf{0}_{2L} \tag{4.81}$$

$$\boldsymbol{B} = \begin{bmatrix} \mathbf{0}_L & I_L \\ -{\Delta_2}^{-1}\boldsymbol{R}_{\boldsymbol{X}} & -{\Delta_2}^{-1}\Delta_1 \end{bmatrix} \qquad \text{and} \qquad \bar{\phi} = \begin{pmatrix} \phi \\ \Lambda\phi \end{pmatrix} \tag{4.82}$$

When represented as a linear problem the solution Λ and ϕ of the QEP represent its eigenvalues and associated eigenvectors. The idea is to compute the two eigenvectors $(\bar{\phi}_1,\ \bar{\phi}_2)$ associated with the two zeros eigenvalues and to use the orthogonal property ${\bar{\phi}_2}^T\bar{\phi}_1 = 0$ to verify $\varphi_1^T\bar{\varphi}_2 = 0$. The eigenvector $\bar{\phi}_1$ verify:

$$\begin{aligned}
& \boldsymbol{B}\bar{\phi}_1 = \begin{bmatrix} \mathbf{0}_L & \boldsymbol{I}_L \\ -{\Delta_2}^{-1}\boldsymbol{R}_{\boldsymbol{X}} & -{\Delta_2}^{-1}\Delta_1 \end{bmatrix}\begin{pmatrix} \phi_{11} \\ \mathbf{0}_L \end{pmatrix} && = \mathbf{0}_{2L} \\
\Leftrightarrow\ & -{\Delta_2}^{-1}\boldsymbol{R}_{\boldsymbol{X}}\phi_{11} && = \mathbf{0}_L
\end{aligned} \tag{4.83}$$

Therefore, $\bar{\phi}_1$ equals to $\begin{pmatrix} \bar{\varphi}_1 \\ \mathbf{0}_L \end{pmatrix}$ is a solution to the equations. The eigenvector $\bar{\phi}_2$ verify:

$$\begin{aligned}
& \boldsymbol{B}\bar{\phi}_2 && = \bar{\phi}_1 \\
\Leftrightarrow\ & \begin{bmatrix} \mathbf{0}_L & \underline{\mathrm{I}}_L \\ -{\Delta_2}^{-1}\boldsymbol{R}_{\boldsymbol{X}} & -{\Delta_2}^{-1}\Delta_1 \end{bmatrix}\begin{pmatrix} \phi_{21} \\ \phi_{22} \end{pmatrix} && = \begin{pmatrix} \bar{\varphi}_1 \\ \mathbf{0}_L \end{pmatrix} \\
\Leftrightarrow\ & \begin{pmatrix} \phi_{22} \\ -{\Delta_2}^{-1}\boldsymbol{R}_{\boldsymbol{X}}\phi_{21} - {\Delta_2}^{-1}\Delta_1\phi_{22} \end{pmatrix} && = \begin{pmatrix} \bar{\varphi}_1 \\ \mathbf{0}_L \end{pmatrix}
\end{aligned} \tag{4.84}$$

Therefore, $\bar{\phi}_2$ equals to $\begin{pmatrix} \bar{\varphi}_2 \\ \bar{\varphi}_1 \end{pmatrix}$ is solution of the equations. Since two eigenvectors $(\bar{\phi}_1,\ \bar{\phi}_2)$ are orthogonal, $\bar{\varphi}_1$ and $\bar{\varphi}_2$ are orthogonal to each other, the propriety presented in Eq. (4.75) is valid for $\boldsymbol{\nu_2 = \xi}$. Therefore $\boldsymbol{\nu_2 = \xi}$ is a suitable vector to shift the problem a second time.

As a result, $\boldsymbol{\nu}_1 = \boldsymbol{\varphi}_1$ and $\boldsymbol{\nu}_2 = \xi$ are the suitable vectors to shift the two zeros eigenvalues to -1. Hence the following shifted QEP with the two zero eigenvalues shifted to -1 is obtained:

$$\begin{aligned}\tilde{\tilde{\boldsymbol{Q}}}_(\boldsymbol{X},\tilde{\tilde{\Lambda}},\tilde{\tilde{\boldsymbol{\phi}}},\boldsymbol{\varphi}_1,\boldsymbol{\xi}) &= [\boldsymbol{R}_{\boldsymbol{X}} + \boldsymbol{\Delta}_1(\boldsymbol{\varphi}_1\boldsymbol{\varphi}_1^* + \boldsymbol{\xi}\boldsymbol{\xi}^*) + \boldsymbol{\Delta}_2(\boldsymbol{\varphi}_1\boldsymbol{\varphi}_1^*\boldsymbol{\xi}\boldsymbol{\xi}^*) \\ &\quad + \tilde{\tilde{\Lambda}}(\boldsymbol{\Delta}_1 + \boldsymbol{\Delta}_2(\boldsymbol{\varphi}_1\boldsymbol{\varphi}_1^* + \boldsymbol{\xi}\boldsymbol{\xi}^*)) \\ &\quad + \tilde{\tilde{\Lambda}}^2\boldsymbol{\Delta}_2\Big]\,\tilde{\tilde{\boldsymbol{\phi}}} = \boldsymbol{0}_L\end{aligned} \tag{4.85}$$

Computation of nonlinearities and derivatives during NNM's bifurcation point continuation

The derivatives from the Jacobian of the augmented system with respect to the parameters $(\boldsymbol{X},\omega,\mu)$ are the following:

$$\begin{aligned}\boldsymbol{R}_X &= \boldsymbol{Z}(\omega) + \frac{\partial \boldsymbol{F}_{nl}}{\partial \boldsymbol{X}}, & \boldsymbol{R}_\omega &= \boldsymbol{Z}_\omega \boldsymbol{X} + \frac{\partial \boldsymbol{F}_{nl}}{\partial \omega} \\ \boldsymbol{R}_\mu &= (\boldsymbol{\nabla}\otimes\boldsymbol{I}_n)\,\boldsymbol{X}, & g_{\boldsymbol{X}} &= (\boldsymbol{\nabla}\otimes\boldsymbol{I}_n)\,\boldsymbol{X}_{j-1} = \boldsymbol{\varphi}_{1\,j-1}\end{aligned} \tag{4.86}$$

where $\boldsymbol{X}_{k-1}$ correspond to the solution of the previous step of continuation. $\boldsymbol{Z}_\omega$ and $\boldsymbol{Z}_\mu$ are equal to:

$$\boldsymbol{Z}_\omega = \frac{\partial \boldsymbol{Z}}{\partial \omega} = 2\omega\nabla^2\otimes\boldsymbol{M} \qquad \boldsymbol{Z}_\mu = \frac{\partial \boldsymbol{Z}}{\partial \mu} = \nabla\otimes\boldsymbol{I}_n \tag{4.87}$$

The computation of nonlinearities and derivatives during NNM's bifurcation point continuation terms appearing during the BP and LP computation method are calculated analytically:

$$\begin{aligned}\left(\tilde{\tilde{\boldsymbol{R}}}_{\boldsymbol{X}}\boldsymbol{\phi}\right)_{\boldsymbol{X}} &= (\boldsymbol{F}_{nl\,\boldsymbol{X}}\boldsymbol{\phi})_{\boldsymbol{X}} & &+ \boldsymbol{\Delta}_{1\boldsymbol{X}}(\boldsymbol{\varphi}_1\boldsymbol{\varphi}_1^* + \boldsymbol{\xi}\boldsymbol{\xi}^*)\,\boldsymbol{\phi} \\ & & &+ \boldsymbol{\Delta}_1\left(\frac{\partial \boldsymbol{\varphi}_1\boldsymbol{\varphi}_1^*}{\partial \boldsymbol{X}}\boldsymbol{\phi} + \frac{\partial \boldsymbol{\xi}\boldsymbol{\xi}^*}{\partial \boldsymbol{X}}\boldsymbol{\phi}\right) \\ & & &+ \boldsymbol{\Delta}_2\left(\frac{\partial \boldsymbol{\varphi}_1\boldsymbol{\varphi}_1^*}{\partial \boldsymbol{X}}\boldsymbol{\xi}\boldsymbol{\xi}^*\boldsymbol{\phi} + \boldsymbol{\varphi}_1\boldsymbol{\varphi}_1^*\frac{\partial \boldsymbol{\xi}\boldsymbol{\xi}^*}{\partial \boldsymbol{X}}\boldsymbol{\phi}\right) \\ \left(\tilde{\tilde{\boldsymbol{R}}}_{\boldsymbol{X}}\boldsymbol{\phi}\right)_{\omega} &= \boldsymbol{Z}_\omega\boldsymbol{\phi} + (\boldsymbol{F}_{nl\,\boldsymbol{X}}\boldsymbol{\phi})_\omega & &+ \boldsymbol{\Delta}_{1\omega}(\boldsymbol{\varphi}_1\boldsymbol{\varphi}_1^* + \boldsymbol{\xi}\boldsymbol{\xi}^*)\,\boldsymbol{\phi} \\ & & &+ \boldsymbol{\Delta}_1\left(\boldsymbol{\varphi}_1\boldsymbol{\varphi}_1^*\boldsymbol{\phi} + \frac{\partial \boldsymbol{\xi}\boldsymbol{\xi}^*}{\partial \omega}\boldsymbol{\phi}\right) + \boldsymbol{\Delta}_2\left(\boldsymbol{\varphi}_1\boldsymbol{\varphi}_1^*\frac{\partial \boldsymbol{\xi}\boldsymbol{\xi}^*}{\partial \omega}\boldsymbol{\phi}\right) \\ \left(\tilde{\tilde{\boldsymbol{R}}}_{\boldsymbol{X}}\boldsymbol{\phi}\right)_{\mu} &= (\boldsymbol{\nabla}\otimes\boldsymbol{I}_n)\,\boldsymbol{\phi} & &+ \boldsymbol{\Delta}_{1\mu}(\boldsymbol{\varphi}_1\boldsymbol{\varphi}_1^* + \boldsymbol{\xi}\boldsymbol{\xi}^*)\,\boldsymbol{\phi} \\ & & &+ \boldsymbol{\Delta}_1\left(\boldsymbol{\varphi}_1\boldsymbol{\varphi}_1^*\boldsymbol{\phi} + \frac{\partial \boldsymbol{\xi}\boldsymbol{\xi}^*}{\partial \mu}\boldsymbol{\phi}\right) + \boldsymbol{\Delta}_2\left(\boldsymbol{\varphi}_1\boldsymbol{\varphi}_1^*\frac{\partial \boldsymbol{\xi}\boldsymbol{\xi}^*}{\partial \mu}\boldsymbol{\phi}\right) \\ \left(\bar{\boldsymbol{R}}_{\boldsymbol{X}}\boldsymbol{\phi}\right)_{\boldsymbol{X}} &= (\boldsymbol{F}_{nl\,\boldsymbol{X}}\boldsymbol{\phi})_{\boldsymbol{X}} & &+ \frac{\partial \boldsymbol{\varphi}_1\boldsymbol{\varphi}_1^*}{\partial \boldsymbol{X}}\boldsymbol{\phi}\end{aligned}$$

$$
\begin{aligned}
\left(\bar{\boldsymbol{R}}_{\boldsymbol{X}}\boldsymbol{\phi}\right)_{\omega} &= \left(\boldsymbol{R}_{\boldsymbol{X}}\boldsymbol{\phi}\right)_{\omega} \\
\left(\bar{\boldsymbol{R}}_{\omega}\boldsymbol{\phi}\right)_{\omega} &= \left(\boldsymbol{R}_{\omega}\boldsymbol{\phi}\right)_{\omega} \\
\left(\bar{\boldsymbol{R}}_{\boldsymbol{X}}\boldsymbol{\phi}\right)_{\mu} &= \left(\nabla\otimes\boldsymbol{I}_n\right)\boldsymbol{\phi}
\end{aligned}
$$

where $(\boldsymbol{F}_{nl\,\boldsymbol{X}}\boldsymbol{\phi})_{\boldsymbol{X}}$, $(\boldsymbol{F}_{nl\,\boldsymbol{X}}\boldsymbol{\phi})_{\omega}$, $(\boldsymbol{R}_{\boldsymbol{X}}\boldsymbol{\phi})_{\omega}$, $(\boldsymbol{R}_{\omega}\boldsymbol{\phi})_{\omega}$) are defined in Eqs. (2.38) and (2.40). $\boldsymbol{X}_{k-1}$ correspond to the solution of the previous step of continuation. $\boldsymbol{Z}_{\omega}$, $\boldsymbol{\varphi}_1$ and $\boldsymbol{\varphi}_2$ have been defined in equation (4.87), (3.6) and (3.32). ($\boldsymbol{\Delta}_{1\,\boldsymbol{X}}$, $\boldsymbol{\Delta}_{1\,\omega}$) are defined in Eq. (2.38) and $\boldsymbol{\Delta}_{1\,\mu}$ is computed as such:

$$
\boldsymbol{\Delta}_{1\,\mu} = \boldsymbol{I}_{2H+1}\otimes\boldsymbol{I}_n \tag{4.88}
$$

In order to complete the formulation of the equation (4.86) the derivatives of the normalized vector have to be calculated.

$$
\begin{aligned}
\frac{\partial\boldsymbol{\varphi}_1\boldsymbol{\varphi}_1^*}{\partial\boldsymbol{X}}\boldsymbol{\phi} &= \frac{1}{\left(\bar{\boldsymbol{\varphi}}_1{}^*\bar{\boldsymbol{\varphi}}_1\right)^2}\left(\frac{\partial\bar{\boldsymbol{\varphi}}_1\bar{\boldsymbol{\varphi}}_1{}^*}{\partial\boldsymbol{X}}\left(\bar{\boldsymbol{\varphi}}_1{}^*\bar{\boldsymbol{\varphi}}_1\right)\boldsymbol{\phi}-\bar{\boldsymbol{\varphi}}_1\bar{\boldsymbol{\varphi}}_1{}^*\boldsymbol{\phi}\left(\frac{\partial\bar{\boldsymbol{\varphi}}_1{}^*\bar{\boldsymbol{\varphi}}_1}{\partial\boldsymbol{X}}\right)^*\right) \\
\frac{\partial\boldsymbol{\xi}\boldsymbol{\xi}^*}{\partial\boldsymbol{X}}\boldsymbol{\phi} &= \frac{1}{\left(\left(\bar{\boldsymbol{\varphi}}_1+\bar{\boldsymbol{\varphi}}_2\right)^*\left(\bar{\boldsymbol{\varphi}}_1+\bar{\boldsymbol{\varphi}}_2\right)\right)^2} \\
&\quad\left(\left(\frac{\partial\bar{\boldsymbol{\varphi}}_2\bar{\boldsymbol{\varphi}}_2{}^*}{\partial\boldsymbol{X}}+\frac{\partial\bar{\boldsymbol{\varphi}}_1\bar{\boldsymbol{\varphi}}_2{}^*}{\partial\boldsymbol{X}}+\frac{\partial\bar{\boldsymbol{\varphi}}_2\bar{\boldsymbol{\varphi}}_1{}^*}{\partial\boldsymbol{X}}+\frac{\partial\bar{\boldsymbol{\varphi}}_1\bar{\boldsymbol{\varphi}}_1{}^*}{\partial\boldsymbol{X}}\right)\left(\bar{\boldsymbol{\varphi}}_1+\bar{\boldsymbol{\varphi}}_2\right)^*\left(\bar{\boldsymbol{\varphi}}_1+\bar{\boldsymbol{\varphi}}_2\right)\boldsymbol{\phi}\right. \\
&\quad\left.-\left(\bar{\boldsymbol{\varphi}}_1+\bar{\boldsymbol{\varphi}}_2\right)\left(\bar{\boldsymbol{\varphi}}_1+\bar{\boldsymbol{\varphi}}_2\right)^*\left(\boldsymbol{\phi}\left(\frac{\partial\bar{\boldsymbol{\varphi}}_2{}^*\bar{\boldsymbol{\varphi}}_2}{\partial\boldsymbol{X}}+2\frac{\partial\bar{\boldsymbol{\varphi}}_1{}^*\bar{\boldsymbol{\varphi}}_2}{\partial\boldsymbol{X}}+\frac{\partial\bar{\boldsymbol{\varphi}}_1{}^*\bar{\boldsymbol{\varphi}}_1}{\partial\boldsymbol{X}}\right)^*\right)\right) \\
\frac{\partial\boldsymbol{\xi}\boldsymbol{\xi}^*}{\partial\boldsymbol{\omega}} &= \frac{1}{\left(\left(\bar{\boldsymbol{\varphi}}_1+\bar{\boldsymbol{\varphi}}_2\right)^*\left(\bar{\boldsymbol{\varphi}}_1+\bar{\boldsymbol{\varphi}}_2\right)\right)^2}\left(\left(\frac{\partial\bar{\boldsymbol{\varphi}}_2\bar{\boldsymbol{\varphi}}_2{}^*}{\partial\boldsymbol{\omega}}+\frac{\partial\bar{\boldsymbol{\varphi}}_1\bar{\boldsymbol{\varphi}}_2{}^*}{\partial\boldsymbol{\omega}}+\frac{\partial\bar{\boldsymbol{\varphi}}_2\bar{\boldsymbol{\varphi}}_1{}^*}{\partial\boldsymbol{\omega}}\right)\left(\bar{\boldsymbol{\varphi}}_1+\bar{\boldsymbol{\varphi}}_2\right)^*\left(\boldsymbol{\varphi}_1+\boldsymbol{\varphi}_2\right)\right. \\
&\quad\left.-\left(\bar{\boldsymbol{\varphi}}_1+\bar{\boldsymbol{\varphi}}_2\right)\left(\bar{\boldsymbol{\varphi}}_1+\bar{\boldsymbol{\varphi}}_2\right)^*\left(\frac{\partial\bar{\boldsymbol{\varphi}}_2{}^*\bar{\boldsymbol{\varphi}}_2}{\partial\boldsymbol{\omega}}+2\frac{\partial\bar{\boldsymbol{\varphi}}_1{}^*\bar{\boldsymbol{\varphi}}_2}{\partial\boldsymbol{\omega}}\right)\right) \\
\frac{\partial\boldsymbol{\xi}\boldsymbol{\xi}^*}{\partial\boldsymbol{\mu}} &= \frac{1}{\left(\left(\bar{\boldsymbol{\varphi}}_1+\bar{\boldsymbol{\varphi}}_2\right)^*\left(\bar{\boldsymbol{\varphi}}_1+\bar{\boldsymbol{\varphi}}_2\right)\right)^2}\left(\left(\frac{\partial\bar{\boldsymbol{\varphi}}_2\bar{\boldsymbol{\varphi}}_2{}^*}{\partial\boldsymbol{\mu}}+\frac{\partial\bar{\boldsymbol{\varphi}}_1\bar{\boldsymbol{\varphi}}_2{}^*}{\partial\boldsymbol{\mu}}+\frac{\partial\bar{\boldsymbol{\varphi}}_2\bar{\boldsymbol{\varphi}}_1{}^*}{\partial\boldsymbol{\mu}}\right)\left(\bar{\boldsymbol{\varphi}}_1+\bar{\boldsymbol{\varphi}}_2\right)^*\left(\boldsymbol{\varphi}_1+\boldsymbol{\varphi}_2\right)\right. \\
&\quad\left.-\left(\bar{\boldsymbol{\varphi}}_1+\bar{\boldsymbol{\varphi}}_2\right)\left(\bar{\boldsymbol{\varphi}}_1+\bar{\boldsymbol{\varphi}}_2\right)^*\left(\frac{\partial\bar{\boldsymbol{\varphi}}_2{}^*\bar{\boldsymbol{\varphi}}_2}{\partial\boldsymbol{\mu}}+2\frac{\partial\bar{\boldsymbol{\varphi}}_1{}^*\bar{\boldsymbol{\varphi}}_2}{\partial\boldsymbol{\mu}}\right)\right)
\end{aligned}
$$

where the derivatives of the non-normalized vectors are the following

$$
\begin{aligned}
\frac{\partial\bar{\boldsymbol{\varphi}}_1\bar{\boldsymbol{\varphi}}_1{}^*}{\partial\boldsymbol{X}}\boldsymbol{\phi} &= \bar{\boldsymbol{\varphi}}_1\boldsymbol{\phi}^*\left(\nabla\otimes\boldsymbol{I}_n\right)+\left(\nabla\otimes\boldsymbol{I}_n\right)\bar{\boldsymbol{\varphi}}_1{}^*\boldsymbol{\phi}; \\
\frac{\partial\bar{\boldsymbol{\varphi}}_1{}^*\bar{\boldsymbol{\varphi}}_1}{\partial\boldsymbol{X}} &= 2\left(\nabla\otimes\boldsymbol{I}_n\right)^T\bar{\boldsymbol{\varphi}}_1 \\
\frac{\partial\bar{\boldsymbol{\varphi}}_1\bar{\boldsymbol{\varphi}}_2{}^*}{\partial\boldsymbol{X}}\boldsymbol{\phi} &= \left(\nabla\otimes\boldsymbol{I}_n\right)\left(\bar{\boldsymbol{\varphi}}_2{}^*\boldsymbol{\phi}\right)-\left(\bar{\boldsymbol{\varphi}}_1\boldsymbol{\phi}^*\right)\left(\boldsymbol{R}_{\boldsymbol{X}}{}^{-1}\frac{\partial\boldsymbol{R}_{\boldsymbol{X}}}{\partial\boldsymbol{X}}\bar{\boldsymbol{\varphi}}_2+\boldsymbol{R}_{\boldsymbol{X}}{}^{-1}\left(\Delta_1\left(\nabla\otimes\boldsymbol{I}_n\right)+\Delta_{1\,\boldsymbol{X}}\bar{\boldsymbol{\varphi}}_1\right)\right); \\
\frac{\partial\bar{\boldsymbol{\varphi}}_2\bar{\boldsymbol{\varphi}}_1{}^*}{\partial\boldsymbol{X}}\boldsymbol{\phi} &= -\left(\boldsymbol{R}_{\boldsymbol{X}}{}^{-1}\frac{\partial\boldsymbol{R}_{\boldsymbol{X}}}{\partial\boldsymbol{X}}\bar{\boldsymbol{\varphi}}_2+\boldsymbol{R}_{\boldsymbol{X}}{}^{-1}\left(\Delta_1\left(\nabla\otimes\boldsymbol{I}_n\right)+\Delta_{1\,\boldsymbol{X}}\bar{\boldsymbol{\varphi}}_1\right)\right)\left(\bar{\boldsymbol{\varphi}}_1{}^*\boldsymbol{\phi}\right)+\left(\bar{\boldsymbol{\varphi}}_2\boldsymbol{\phi}^*\right)\left(\nabla\otimes\boldsymbol{I}_n\right)
\end{aligned}
$$

$$
\begin{aligned}
\frac{\partial \bar{\varphi_1}^* \bar{\varphi_2}}{\partial \boldsymbol{X}} &= \frac{\partial \bar{\varphi_2}^* \bar{\varphi_1}}{\partial \boldsymbol{X}} = (\nabla \otimes \boldsymbol{I}_n)^T \bar{\varphi_2} - \left(\boldsymbol{R_X}^{-1} \frac{\partial \boldsymbol{R_X}}{\partial \boldsymbol{X}} \bar{\varphi_2} + \boldsymbol{R_X}^{-1} \left(\Delta_1 (\nabla \otimes \boldsymbol{I}_n) + \Delta_{1\boldsymbol{X}} \bar{\varphi_1} \right) \right)^T \bar{\varphi_1} \\
\frac{\partial \bar{\varphi_2} \bar{\varphi_2}^*}{\partial \boldsymbol{X}} \phi &= -\left(\boldsymbol{R_X}^{-1} \frac{\partial \boldsymbol{R_X}}{\partial \boldsymbol{X}} \bar{\varphi_2} + \boldsymbol{R_X}^{-1} \left(\Delta_1 (\nabla \otimes \boldsymbol{I}_n) + \Delta_{1\boldsymbol{X}} \bar{\varphi_1} \right) \right) (\bar{\varphi_2}^* \phi) \\
\frac{\partial \bar{\varphi_2}^* \bar{\varphi_2}}{\partial \boldsymbol{X}} &= -2 \left(\boldsymbol{R_X}^{-1} \frac{\partial \boldsymbol{R_X}}{\partial \boldsymbol{X}} \bar{\varphi_2} + \boldsymbol{R_X}^{-1} \left(\Delta_1 (\nabla \otimes \boldsymbol{I}_n) + \Delta_{1\boldsymbol{X}} \bar{\varphi_1} \right) \right)^T \bar{\varphi_2} \\
&\quad - (\bar{\varphi_2} \phi^*) \left(\boldsymbol{R_X}^{-1} \frac{\partial \boldsymbol{R_X}}{\partial \boldsymbol{X}} \bar{\varphi_2} + \boldsymbol{R_X}^{-1} \Delta_1 (\nabla \otimes \boldsymbol{I}_n) \right) \\
\frac{\partial \bar{\varphi_1} \bar{\varphi_2}^*}{\partial \boldsymbol{\omega}} &= \frac{\partial \bar{\varphi_2} \bar{\varphi_1}^*}{\partial \boldsymbol{\omega}} = -\bar{\varphi_1} \left(\boldsymbol{R_X}^{-1} \left(-\frac{\partial \boldsymbol{R_X}}{\partial \boldsymbol{\omega}} \boldsymbol{R_X}^{-1} \Delta_1 + \Delta_{1\omega} \right) \bar{\varphi_1} \right)^T \\
\frac{\partial \bar{\varphi_1}^* \bar{\varphi_2}}{\partial \boldsymbol{\omega}} &= \frac{\partial \bar{\varphi_2}^* \bar{\varphi_1}}{\partial \boldsymbol{\omega}} = -\bar{\varphi_1}^T \left(\boldsymbol{R_X}^{-1} \left(-\frac{\partial \boldsymbol{R_X}}{\partial \boldsymbol{\omega}} \boldsymbol{R_X}^{-1} \Delta_1 + \Delta_{1\omega} \right) \bar{\varphi_1} \right) \\
\frac{\partial \bar{\varphi_2} \bar{\varphi_2}^*}{\partial \boldsymbol{\omega}} &= \left(\boldsymbol{R_X}^{-1} \left(-\frac{\partial \boldsymbol{R_X}}{\partial \boldsymbol{\omega}} \boldsymbol{R_X}^{-1} \Delta_1 + \Delta_{1\omega} \right) \bar{\varphi_1} \right) \left(\boldsymbol{R_X}^{-1} \Delta_1 \bar{\varphi_1} \right)^T \\
&\quad + \left(\boldsymbol{R_X}^{-1} \Delta_1 \bar{\varphi_1} \right) \left(\boldsymbol{R_X}^{-1} \left(-\frac{\partial \boldsymbol{R_X}}{\partial \boldsymbol{\omega}} \boldsymbol{R_X}^{-1} \Delta_1 + \Delta_{1\omega} \right) \bar{\varphi_1} \right)^T \\
\frac{\partial \bar{\varphi_2}^* \bar{\varphi_2}}{\partial \boldsymbol{\omega}} &= -2 \left(\boldsymbol{R_X}^{-1} \left(-\frac{\partial \boldsymbol{R_X}}{\partial \boldsymbol{\omega}} \boldsymbol{R_X}^{-1} \Delta_1 + \Delta_{1\omega} \right) \bar{\varphi_2} \right)^T \bar{\varphi_2} \\
\frac{\partial \bar{\varphi_1} \bar{\varphi_2}^*}{\partial \mu} &= \frac{\partial \bar{\varphi_2} \bar{\varphi_1}^*}{\partial \mu} = -\bar{\varphi_1} \left(\boldsymbol{R_X}^{-1} \left(-\frac{\partial \boldsymbol{R_X}}{\partial \mu} \boldsymbol{R_X}^{-1} \Delta_1 + \Delta_{1\mu} \right) \bar{\varphi_1} \right)^T \\
\frac{\partial \bar{\varphi_1}^* \bar{\varphi_2}}{\partial \mu} &= \frac{\partial \bar{\varphi_2}^* \bar{\varphi_1}}{\partial \mu} = -\bar{\varphi_1}^T \left(\boldsymbol{R_X}^{-1} \left(-\frac{\partial \boldsymbol{R_X}}{\partial \mu} \boldsymbol{R_X}^{-1} \Delta_1 + \Delta_{1\mu} \right) \bar{\varphi_1} \right) \\
\frac{\partial \bar{\varphi_2} \bar{\varphi_2}^*}{\partial \mu} &= \left(\boldsymbol{R_X}^{-1} \left(-\frac{\partial \boldsymbol{R_X}}{\partial \mu} \boldsymbol{R_X}^{-1} \Delta_1 + \Delta_{1\mu} \right) \bar{\varphi_1} \right) \left(\boldsymbol{R_X}^{-1} \Delta_1 \bar{\varphi_1} \right)^T \\
&\quad + \left(\boldsymbol{R_X}^{-1} \Delta_1 \bar{\varphi_1} \right) \left(\boldsymbol{R_X}^{-1} \left(-\frac{\partial \boldsymbol{R_X}}{\partial \mu} \boldsymbol{R_X}^{-1} \Delta_1 + \Delta_{1\mu} \right) \bar{\varphi_1} \right)^T \\
\frac{\partial \bar{\varphi_2}^* \bar{\varphi_2}}{\partial \mu} &= -2 \left(\boldsymbol{R_X}^{-1} \left(-\frac{\partial \boldsymbol{R_X}}{\partial \mu} \boldsymbol{R_X}^{-1} \Delta_1 + \Delta_{1\mu} \right) \bar{\varphi_1} \right)^T \bar{\varphi_2}
\end{aligned}
$$

Annexe C

Reduced-order model

The non-dimensional equation of motion for beam s is

$$\frac{\partial^4 w_s}{\partial x^4}+\frac{\partial^2 w_s}{\partial t^2}+c\frac{\partial w_s}{\partial t}-\left[N+\ \alpha_1\int_0^1\left(\frac{\partial w}{\partial x}\right)^2\mathrm{d}x\right]\frac{\partial^2 w_s}{\partial x^2} = \alpha_2\frac{V_{s,s+1}^2}{\left(1+w_{s+1}-w_s\right)^2}-\alpha_2\frac{V_{s-1,s}^2}{\left(1+w_s-w_{s-1}\right)^2}. \tag{4.89}$$

By using the Galerkin method and seventh-order Taylor series Eq.4.89 is replaced by a set of equations in the following matrix form:

$$\begin{aligned}\ddot{\boldsymbol{a}}^s+\boldsymbol{C}_0\dot{\boldsymbol{a}}^s+\boldsymbol{K}_0\boldsymbol{a}^s-\left(N+\alpha_1 T_2^s(\boldsymbol{a}^s)\right)\boldsymbol{K}_T\boldsymbol{a}^s = \\ \alpha_2 V_{s,s+1}^2\boldsymbol{Q}_0+\alpha_2 V_{s,s+1}^2\Big[\boldsymbol{Q}_1+\boldsymbol{Q}_2^s(\boldsymbol{b}^s)+\boldsymbol{Q}_3^s(\boldsymbol{b}^s)+\boldsymbol{Q}_4^s(\boldsymbol{b}^s) \\ +\boldsymbol{Q}_5^s(\boldsymbol{b}^s)+\boldsymbol{Q}_6^s(\boldsymbol{b}^s)+\boldsymbol{Q}_7^s(\boldsymbol{b}^s)\Big]\boldsymbol{b}^s-\alpha_2 V_{s-1,s}V_{s-1,s}^2\boldsymbol{P}_0 \\ -\alpha_2 V_{s-1,s}^2\Big[\boldsymbol{P}_1+\boldsymbol{P}_2^s(\boldsymbol{b}^{s-1})+\boldsymbol{P}_3^s(\boldsymbol{b}^{s-1})+\boldsymbol{P}_4^s(\boldsymbol{b}^{s-1}) \\ +\boldsymbol{P}_5^s(\boldsymbol{b}^{s-1})+\boldsymbol{P}_6^s(\boldsymbol{b}^{s-1})+\boldsymbol{P}_7^s(\boldsymbol{b}^{s-1})\Big]\boldsymbol{b}^{s-1}\end{aligned} \tag{4.90}$$

The components of the matrices are given by:

$$\boldsymbol{C}_{0ij} = c_i\delta_{ij}, \quad \boldsymbol{K}_{0ij} = \lambda_i^4\delta_{ij}, \quad T_2^s(\boldsymbol{a}^s) = \sum_{k=1}^{N_m}\sum_{l=1}^{N_m}\left(\int_0^1 \phi_k'\phi_l'\mathrm{d}x\right)\boldsymbol{a}_k^s\boldsymbol{a}_l^s,$$

$$\boldsymbol{K}_{Tij} = \int_0^1 \phi_j''\phi_i\mathrm{d}x, \quad \boldsymbol{Q}_{0i}^s = \int_0^1 \phi_i\mathrm{d}x,$$

$$\boldsymbol{Q}_{1ij}^s = -2\int_0^1 \phi_i\phi_j\mathrm{d}x, \quad \boldsymbol{Q}_{2ij}^s = 3\sum_{k=1}^{N_m}\left(\int_0^1 \phi_i\phi_j\phi_k\mathrm{d}x\right)\boldsymbol{b}_k^s,$$

$$\boldsymbol{Q}_{3ij}^s = -4\sum_{k=1}^{N_m}\sum_{l=1}^{N_m}\left(\int_0^1 \phi_i\phi_j\phi_k\phi_l\mathrm{d}x\right)\boldsymbol{b}_k^s\boldsymbol{b}_l^s,$$

$$\boldsymbol{Q}_{4ij}^s = 5\sum_{k=1}^{N_m}\sum_{l=1}^{N_m}\sum_{m=1}^{N_m}\left(\int_0^1 \phi_i\phi_j\phi_k\phi_l\phi_m\mathrm{d}x\right)\boldsymbol{b}_k^s\boldsymbol{b}_l^s\boldsymbol{b}_m^s,$$

$$\boldsymbol{Q}_{5ij}^s = -6\sum_{k=1}^{N_m}\sum_{l=1}^{N_m}\sum_{m=1}^{N_m}\sum_{n=1}^{N_m}\left(\int_0^1 \phi_i\phi_j\phi_k\phi_l\phi_m\phi_n\mathrm{d}x\right)\boldsymbol{b}_k^s\boldsymbol{b}_l^s\boldsymbol{b}_m^s\boldsymbol{b}_n^s,$$

$$\boldsymbol{Q}_{6ij}^s = 7\sum_{k=1}^{N_m}\sum_{l=1}^{N_m}\sum_{m=1}^{N_m}\sum_{n=1}^{N_m}\sum_{o=1}^{N_m}\left(\int_0^1 \phi_i\phi_j\phi_k\phi_l\phi_m\phi_n\phi_o\mathrm{d}x\right)\boldsymbol{b}_k^s\boldsymbol{b}_l^s\boldsymbol{b}_m^s\boldsymbol{b}_n^s\boldsymbol{b}_o^s,$$

$$\boldsymbol{Q}_{7ij}^s = -8\sum_{k=1}^{N_m}\sum_{l=1}^{N_m}\sum_{m=1}^{N_m}\sum_{n=1}^{N_m}\sum_{o=1}^{N_m}\sum_{p=1}^{N_m}\left(\int_0^1 \phi_i\phi_j\phi_k\phi_l\phi_m\phi_n\phi_o\phi_p\mathrm{d}x\right)\boldsymbol{b}_k^s\boldsymbol{b}_l^s\boldsymbol{b}_m^s\boldsymbol{b}_n^s\boldsymbol{b}_o^s\boldsymbol{b}_p^s, \tag{4.91}$$

$$\boldsymbol{P}_{0i} = \int_0^1 \phi_i\mathrm{d}x,\ \boldsymbol{P}_{1ij} = -2\int_0^1 \phi_i\phi_j\mathrm{d}x,\ \boldsymbol{P}_{2ij}^s = 3\sum_{k=1}^{N_m}\left(\int_0^1 \phi_i\phi_j\phi_k\mathrm{d}x\right)\boldsymbol{b}_k^{s-1},$$

$$\boldsymbol{P}_{3ij}^s = -4\sum_{k=1}^{N_m}\sum_{l=1}^{N_m}\left(\int_0^1 \phi_i\phi_j\phi_k\phi_l\mathrm{d}x\right)\boldsymbol{b}_k^{s-1}\boldsymbol{b}_l^{s-1},$$

$$\boldsymbol{P}_{4ij}^s = 5\sum_{k=1}^{N_m}\sum_{l=1}^{N_m}\sum_{m=1}^{N_m}\left(\int_0^1 \phi_i\phi_j\phi_k\phi_l\phi_m\mathrm{d}x\right)\boldsymbol{b}_k^{s-1}\boldsymbol{b}_l^{s-1}\boldsymbol{b}_m^{s-1},$$

$$\boldsymbol{P}_{5ij}^s = -6\sum_{k=1}^{N_m}\sum_{l=1}^{N_m}\sum_{m=1}^{N_m}\sum_{n=1}^{N_m}\left(\int_0^1 \phi_i\phi_j\phi_k\phi_l\phi_m\phi_n\mathrm{d}x\right)\boldsymbol{b}_k^{s-1}\boldsymbol{b}_l^{s-1}\boldsymbol{b}_m^{s-1}\boldsymbol{b}_n^{s-1},$$

$$\boldsymbol{P}_{6ij}^s = 7\sum_{k=1}^{N_m}\sum_{l=1}^{N_m}\sum_{m=1}^{N_m}\sum_{n=1}^{N_m}\sum_{o=1}^{N_m}\left(\int_0^1 \phi_i\phi_j\phi_k\phi_l\phi_m\phi_n\phi_o\mathrm{d}x\right)$$
$$\times\boldsymbol{b}_k^{s-1}\boldsymbol{b}_l^{s-1}\boldsymbol{b}_m^{s-1}\boldsymbol{b}_n^{s-1}\boldsymbol{b}_o^{s-1},$$

$$\boldsymbol{P}_{7ij}^s = -8\sum_{k=1}^{N_m}\sum_{l=1}^{N_m}\sum_{m=1}^{N_m}\sum_{n=1}^{N_m}\sum_{o=1}^{N_m}\sum_{p=1}^{N_m}\left(\int_0^1 \phi_i\phi_j\phi_k\phi_l\phi_m\phi_n\phi_o\phi_p\mathrm{d}x\right)$$
$$\times\boldsymbol{b}_k^{s-1}\boldsymbol{b}_l^{s-1}\boldsymbol{b}_m^{s-1}\boldsymbol{b}_n^{s-1}\boldsymbol{b}_o^{s-1}\boldsymbol{b}_p^{s-1}, \text{with } i,j = 1,..,N_m$$

Annexe D

Averaging method for a two-beam array

By using Galerkin method with the fundamental mode as follows

$$\begin{aligned} w_1(x,t) &= \phi_1(x)a_{11}(t) \\ w_2(x,t) &= \phi_1(x)a_{21}(t) \end{aligned} \tag{4.92}$$

and first-order Taylor series for the electrostatic forces as follows

$$\begin{aligned} \frac{1}{(1+w_{s+1}-w_s)^2} &= 1-2(w_{s+1}-w_s), \\ \frac{1}{(1+w_s-w_{s-1})^2} &= 1-2(w_s-w_{s-1}). \end{aligned} \tag{4.93}$$

Eq. (4.21) becomes

$$\begin{aligned} \ddot{a}_{11}+c\dot{a}_{11}+\omega_1 a_{11}+\beta_{11}a_{11}^3+\left(\beta_{12}\cos\Omega t+\beta_{13}\cos^2\Omega t\right)a_{11}+ \\ \left(\delta_{11}+\delta_{12}\cos\Omega t+\delta_{13}\cos^2\Omega t\right)a_{21}+ \\ \left(\gamma_{11}+\gamma_{12}\cos\Omega t+\gamma_{13}\cos^2\Omega t\right)=0 \end{aligned} \tag{4.94}$$

$$\begin{aligned} \ddot{a}_{21}+c\dot{a}_{21}+\omega_2 a_{21}+\beta_{21}a_{21}^3+\left(\beta_{22}\cos\Omega t+\beta_{23}\cos^2\Omega t\right)a_{21}+ \\ \left(\delta_{21}+\delta_{22}\cos\Omega t+\delta_{23}\cos^2\Omega t\right)a_{11}+ \\ \left(\gamma_{21}+\gamma_{22}\cos\Omega t+\gamma_{23}\cos^2\Omega t\right)=0 \end{aligned} \tag{4.95}$$

where

$$\begin{gathered} \beta_{s1}=151.35\alpha_1;\ \beta_{s2}=-4\alpha_2\left(V_{dc_{s,s+1}}V_{ac_{s,s+1}}+V_{dc_{s-1,s}}V_{ac_{s-1,s}}\right); \\ \beta_{s3}=-2\alpha_2\left(V_{ac_{s-1,s}}^2+V_{ac_{s,s+1}}^2\right);\quad \delta_{11}=\delta_{21}=2\alpha_2V_{dc_{12}}^2; \\ \delta_{12}=\delta_{22}=4\alpha_2V_{dc_{12}}V_{ac_{12}}; \\ \delta_{13}=\delta_{23}=2\alpha_2V_{ac_{12}}^2;\ \gamma_{s1}=0.83\alpha_2\left(V_{dc_{s,s+1}}^2-V_{dc_{s-1,s}}^2\right); \\ \gamma_{s2}=1.66\alpha_2\left(V_{dc_{s,s+1}}V_{ac_{s,s+1}}-V_{dc_{s-1,s}}V_{ac_{s-1,s}}\right); \\ \gamma_{s3}=0.83\alpha_2\left(V_{ac_{s,s+1}}^2-V_{ac_{s-1,s}}^2\right) \end{gathered}$$

and $s=1,2$.
Let the relation between Ω and ω_s be

$$\Omega=\omega_s+\varepsilon\sigma_s, \tag{4.96}$$

where ω_s is determined by

$$\omega_s=\frac{\lambda_s^4-2\alpha_2\left(V_{dc_{s,s+12}}^2+V_{dc_{s-1,s}}^2\right)}{1+\delta_{s_0}(s)m\phi_1(x_0)^2}. \tag{4.97}$$

Bibliography

[ABR 55] ABRAMSON H.
Response curves for a system with softening restoring force. *JOURNALOPAPPLIED-MECHA NICS*, vol. 22, n° 3, 1955, pp. 434–435. 25

[AKG 11] AKGUL M., REN Z., NGUYEN C. T.-C.
Voltage-controlled tuning to optimize MEMS resonator array-composite output power. *Frequency Control and the European Frequency and Time Forum (FCS), 2011 Joint Conference of the IEEE International* IEEE, 2011, pp. 1–6. 39

[ALB 91] ALBRECHT T., GRUTTER P., HORNE D., RUGAR D.
Frequency modulation detection using high-Q cantilevers for enhanced force microscope sensitivity. *Journal of Applied Physics*, vol. 69, n° 2, 1991, pp. 668-673. 34

[ALD 05] ALDRIDGE J. S., CLELAND A. N.
Noise-Enabled Precision Measurements of a Duffing Nanomechanical Resonator. *Phys. Rev. Lett.*, vol. 94, 2005, Page 156403, American Physical Society. 37

[ARQ 06] ARQUIER R., BELLIZZI S., BOUC R., COCHELIN B.
Two methods for the computation of nonlinear modes of vibrating systems at large amplitudes. *Computers & Structures*, vol. 84, n° 24, 2006, pp. 1565 - 1576. Nonlinear Dynamics of Structures and Mechanical Systems. 31, 32, 90

[ARQ 07] ARQUIER R.
A computation method for non linear vibration modes of non linear structures. Theses, Université de la Méditerranée - Aix-Marseille II, April 2007. Site internet de MANLAB : http://manlab.lma.cnrs-mrs.fr/. 10

[ARR 16] ARROYO S. I., ZANETTE D. H.
Duffing revisited: phase-shift control and internal resonance in self-sustained oscillators. *The European Physical Journal B*, vol. 89, n° 1, 2016, pp. 1–8, Springer. 25

[ASC 79] ASCHER U., CHRISTIANSEN J., RUSSELL R. D.
A collocation solver for mixed order systems of boundary value problems. *Mathematics of Computation*, vol. 33, n° 146, 1979, pp. 659–679. 7

[ASH 18] ASHOK A., KUMAR P. M., SINGH S. S., RAJU P., PAL P., PANDEY A. K.
Achieving wideband micromechanical system using coupled non-uniform beams array. *Sensors and Actuators A: Physical*, vol. 273, 2018, pp. 12–18, Elsevier. 39

[BAG 02] BAGUET S., COCHELIN B.
Stability of thin-shell structures and imperfection sensitivity analysis with the Asymptotic Numerical Method. *Revue Européenne des Eléments*, vol. 11, n° 2-4, 2002, pp. 493–509, Taylor & Francis. 23

[BAL 12] BALARAM B., NARAYANAN M., RAJENDRAKUMAR P.
Optimal design of multi-parametric nonlinear systems using a parametric continuation based genetic algorithm approach. *Nonlinear Dynamics*, vol. 67, n° 4, 2012, pp. 2759–2777, Springer. 25

[BAT 03] BATTINI J.-M., PACOSTE C., ERIKSSON A.
Improved minimal augmentation procedure for the direct computation of critical points. *Computer methods in applied mechanics and engineering*, vol. 192, n° 16-18, 2003, pp. 2169–2185, Elsevier. 15

[BEY 07] BEYN W.-J., THUMMLER V.
Phase conditions, symmetries and PDE continuation. *Numerical continuation methods for dynamical systems*, pp. 301–330 Springer, 2007. 32

[BIT 15] BITAR D., KACEM N., BOUHADDI N., COLLET M.
Collective dynamics of periodic nonlinear oscillators under simultaneous parametric and external excitations. *Nonlinear Dynamics*, vol. 82, n° 1-2, 2015, pp. 749–766, Springer. 38

[BIT 17] BITAR D., KACEM N., BOUHADDI N.
Multistability and Bifurcation Topology in Electrostatically Coupled Nanobeams Under Parametric Resonance. *ASME 2017 International Design Engineering Technical Conferences and Computers and Information in Engineering Conference* American Society of Mechanical Engineers, 2017, pp. V004T09A007–V004T09A007. 38

[BUK 02] BUKS E., ROUKES M. L.
Electrically tunable collective response in a coupled micromechanical array. *J. Microelectromech. Syst.*, vol. 11, n° 6, 2002, pp. 802-807. 38

[BUK 06] BUKS E., YURKE B.
Mass detection with a nonlinear nanomechanical resonator. *Physical Review E*, vol. 74, n° 4, 2006, Page 046619, APS. 37

[CAM 89] CAMERON T., GRIFFIN J.
An alternating frequency/time domain method for calculating the steady-state response of nonlinear dynamic systems. *Journal of applied mechanics*, vol. 56, n° 1, 1989, pp. 149–154, American Society of Mechanical Engineers. 8, 9

[CAR 12] CARR J.
Applications of centre manifold theory, vol. 35. Springer Science & Business Media, 2012. 28

[CAR 14] CARPINETO N., LACARBONARA W., VESTRONI F.
Hysteretic tuned mass dampers for structural vibration mitigation. *Journal of Sound and Vibration*, vol. 333, n° 5, 2014, pp. 1302–1318, Elsevier. 25

[CHU 75] CHUA L. O., LIN P. Y.
Computer-Aided Analysis of Electronic Circuits: Algorithms and Computational Techniques. Prentice Hall Professional Technical Reference, 1975. 32

[CIR 17] CIRILLO G., HABIB G., KERSCHEN G., SEPULCHRE R.
Analysis and design of nonlinear resonances via singularity theory. *Journal of Sound and Vibration*, vol. 392, 2017, pp. 295–306, Elsevier. 26

[COC 94] COCHELIN B.
A path-following technique via an asymptotic numerical method. *Computers and Structures*, vol. 53, n° 5, 1994, pp. 1181–1192. 10

[COC 09] COCHELIN B., VERGEZ C.
A high order purely frequency-based harmonic balance formulation for continuation of periodic solutions. *Journal of Sound and Vibration*, vol. 324, n° 1-2, 2009, pp. 243 - 262. 8

[CRI 81] CRISFIELD M.
A fast incremental/iterative solution procedure that handles "snap-through". *Computational Methods in Nonlinear Structural and Solid Mechanics*, pp. 55–62 Elsevier, 1981. 8, 57

[CRO 04] CROSS M. C., ZUMDIECK A., LIFSHITZ R., ROGERS J. L.
Synchronization by Nonlinear Frequency Pulling. *Phys. Rev. Lett.*, vol. 93, 2004, Page 224101, American Physical Society. 38

[DAN 11] DANKOWICZ H., SCHILDER F.
An extended continuation problem for bifurcation analysis in the presence of constraints. *Journal of Computational and Nonlinear Dynamics*, vol. 6, n° 3, 2011, Page 031003, American Society of Mechanical Engineers. 7, 23

[DAV 07] DAVIS Z. J., SVENDSEN W., BOISEN A.
Design, fabrication and testing of a novel MEMS resonator for mass sensing applications. *Microelectronic Engineering*, vol. 84, n° 5-8, 2007, pp. 1601–1605, Elsevier. 35

[DES 09] DESTINO G., ABREU G.
Solving the source localization problem via global distance continuation. *2009 IEEE International Conference on Communications Workshops* IEEE, 2009, pp. 1–6. 24

[DET 15a] DETROUX T., HABIB G., MASSET L., KERSCHEN G.
Performance, robustness and sensitivity analysis of the nonlinear tuned vibration absorber. *Mechanical Systems and Signal Processing*, vol. 60-61, 2015, pp. 799 - 809. 26, 27, 72, 188, 189, 191

[DET 15b] DETROUX T., RENSON L., MASSET L., KERSCHEN G.
The harmonic balance method for bifurcation analysis of large-scale nonlinear mechanical systems. *Computer Methods in Applied Mechanics and Engineering*, vol. 296, 2015, pp. 18–38, Elsevier. 24

[DHO 03] DHOOGE A., GOVAERTS W., KUZNETSOV Y. A.
MATCONT: a MATLAB package for numerical bifurcation analysis of ODEs. *ACM Transactions on Mathematical Software (TOMS)*, vol. 29, n° 2, 2003, pp. 141–164, ACM. 7, 10, 23

[DIB 14] DIBERARDINO L. A., DANKOWICZ H.
Accounting for Nonlinearities in Open-Loop Protocols for Symmetry Fault Compensation. *Journal of Computational and Nonlinear Dynamics*, vol. 9, n° 2, 2014, Page 021002, American Society of Mechanical Engineers. 25

[DIE 68] DIEUDONNÉ J. A.
Calcul infinitésimal. , 1968, Fayard. 16

[DOE 81] DOEDEL E. J.
AUTO: A program for the automatic bifurcation analysis of autonomous systems. *Congr. Numer*, vol. 30, 1981, pp. 265–284. 32, 89

[DOE 98] DOEDEL E. J., CHAMPNEYS A. R., FAIRGRIEVE T. F., KUZNETSOV Y. A., ORN SANDSTEDE B., WANG X.
AUTO 97: CONTINUATION AND BIFURCATION SOFTWARE. , 1998. 7

[DOE 03] DOEDEL E. J., GOVAERTS W., KUZNETSOV Y. A.
Computation of periodic solution bifurcations in ODEs using bordered systems. *SIAM Journal on Numerical Analysis*, vol. 41, n° 2, 2003, pp. 401–435, SIAM. 33

[DOE 07] DOEDEL E. J., CHAMPNEYS A. R., DERCOLE F., FAIRGRIEVE T., YU A., OLDEMAN B., PAFFENROTH R., SANDSTEDE B., WANG X., ZHANG C. et al.
AUTO-07P: Continuation and bifurcation software for ordinary differential equations. , 2007. 7, 10, 23

[DUL 12] DULAC H.
Solutions d'un système d'équations différentielles dans le voisinage de valeurs singulières. *Bull. Soc. Math. France*, vol. 40, 1912, pp. 324–383. 28

[EKI 04] EKINCI K. L., HUANG X. M. H., ROUKES M. L.
Ultrasensitive nanoelectromechanical mass detection. *Applied Physics Letters*, vol. 84, n° 22, 2004, pp. 4469 -4471. 33

[ENG 00] ENGELBORGHS K., LUZYANINA T., SAMAEY G.
DDE-BIFTOOL: a Matlab package for bifurcation analysis of delay differential equations. *TW Report*, vol. 305, 2000. 7

[ERI 99] ERIKSSON A., PACOSTE C., ZDUNEK A.
Numerical analysis of complex instability behaviour using incremental-iterative strategies. *Computer Methods in Applied Mechanics and Engineering*, vol. 179, n° 3-4, 1999, pp. 265–305, Elsevier. 23

[GAT 10] GATTI G., KOVACIC I., BRENNAN M. J.
On the response of a harmonically excited two degree-of-freedom system consisting of a linear and a nonlinear quasi-zero stiffness oscillator. *Journal of Sound and Vibration*, vol. 329, n° 10, 2010, pp. 1823–1835, Elsevier. 26

[GAT 16a] GATTI G.
On the undamped vibration absorber with cubic stiffness characteristics. *Journal of Physics: Conference Series*, vol. 744 IOP Publishing, 2016, Page 012225. 26

[GAT 16b] GATTI G.
Uncovering inner detached resonance curves in coupled oscillators with nonlinearity. *Journal of Sound and Vibration*, vol. 372, 2016, pp. 239–254, Elsevier. 26

[GAT 18] GATTI G.
Fundamental insight on the performance of a nonlinear tuned mass damper. *Meccanica*, vol. 53, n° 1-2, 2018, pp. 111–123, Springer. 26

[GE 01] GE Z.-M., YANG C.-H., CHEN H.-H., LEE S.-C.
Non-linear dynamics and chaos control of a physical pendulum with vibrating and rotating support. *Journal of Sound and Vibration*, vol. 242, n° 2, 2001, pp. 247-264. 14

[GEN 04] GENDELMAN O. V.
Bifurcations of nonlinear normal modes of linear oscillator with strongly nonlinear damped attachment. *Nonlinear Dynamics*, vol. 37, n° 2, 2004, pp. 115–128, Springer. 31

[GOL 12a] GOLUBITSKY M., SCHAEFFER D. G.
Singularities and groups in bifurcation theory, vol. 1. Springer Science & Business Media, 2012. 102, 142

[GOL 12b] GOLUBITSKY M., STEWART I., SCHAEFFER D. G.
Singularities and groups in bifurcation theory, vol. 2. Springer Science & Business Media, 2012. 102, 142

[GOU 14] GOURC E., MICHON G., SEGUY S., BERLIOZ A.
Experimental investigation and design optimization of targeted energy transfer under

periodic forcing. *Journal of Vibration and Acoustics*, vol. 136, n° 2, 2014, Page 021021, American Society of Mechanical Engineers. 26

[GOV 00] GOVAERTS W.
Numerical bifurcation analysis for ODEs. *Journal of computational and applied mathematics*, vol. 125, n° 1-2, 2000, pp. 57–68, Elsevier. 15, 23, 44

[GRI 83] GRIEWANK A., REDDIEN G.
The calculation of Hopf points by a direct method. *IMA Journal of Numerical Analysis*, vol. 3, n° 3, 1983, pp. 295–303, Oxford University Press. 48

[GRI 84] GRIEWANK A., REDDIEN G. W.
Characterization and computation of generalized turning points. *SIAM journal on numerical analysis*, vol. 21, n° 1, 1984, pp. 176–185, SIAM. 15

[GRO 12] GROLET A., THOUVEREZ F.
On a new harmonic selection technique for harmonic balance method. *Mechanical Systems and Signal Processing*, vol. 30, 2012, pp. 43 - 60. 8

[GUC 13] GUCKENHEIMER J., HOLMES P.
Nonlinear oscillations, dynamical systems, and bifurcations of vector fields, vol. 42. Springer Science & Business Media, 2013. 15

[GUD 88] GUDDAT J., JONGEN H. T., NOWACK D.
Parametric optimization: pathfollowing with jumps. *Approximation and Optimization*, pp. 43–53 Springer, 1988. 25

[GUS 08] GUSKOV M., SINOU J.-J., THOUVEREZ F.
Multi-dimensional harmonic balance applied to rotor dynamics. *Mechanics Research Communications*, vol. 35, n° 8, 2008, pp. 537–545, Elsevier. 8

[GUT 08] GUTSCHMIDT S., GOTTLIEB O.
Nonlinear internal resonances of a microbeam array near the pull-in point. *Proc. ENOC-2008*, Saint Petersburg, June, 30 -July, 4 2008 Page http://lib.physcon.ru/doc?id=7f9212f410ba. 38

[GUT 10a] GUTSCHMIDT S., GOTTLIEB O.
Bifurcations and loss of orbital stability in nonlinear viscoelastic beam arrays subject to parametric actuation. *J. Sound Vib.*, vol. 329, 2010, pp. 3835-3855. 38

[GUT 10b] GUTSCHMIDT S., GOTTLIEB O.
Internal resonances and bifurcations of an array below the first pull-in instability. *Int. J. Bifurcation Chaos*, vol. 20, n° 3, 2010, pp. 605-618. 38

[GUT 12] GUTSCHMIDT S., GOTTLIEB O.
Nonlinear dynamic behavior of a microbeam array subject to parametric actuation at

low, medium and large DC-voltages. *Nonlinear Dynamics*, vol. 67, n° 1, 2012, pp. 1–36. 38

[HAB 15] HABIB G., DETROUX T., VIGUIÉ R., KERSCHEN G.
Nonlinear generalization of Den Harto's equal-peak method. *Mechanical Systems and Signal Processing*, vol. 52-53, 2015, pp. 17 - 28. v, 25, 26, 56, 57

[HAB 17] HABIB G., CIRILLO G. I., KERSCHEN G.
Isolated resonances and nonlinear damping. *arXiv preprint arXiv:1707.03561*, , 2017. 26, 27

[HAG 02] HAGLEITNER C., LANGE D., HIERLEMANN A., BRAND O., BALTES H.
CMOS single-chip gas detection system comprising capacitive, calorimetric and mass-sensitive microsensors. *Solid-State Circuits, IEEE Journal*, vol. 37, n° 12, 2002, pp. 1867-1878. 34

[HAJ 12] HAJHASHEMI M., AMINI A., BAHREYNI B.
A micromechanical bandpass filter with adjustable bandwidth and bidirectional control of centre frequency. *Sensors and Actuators A: Physical*, vol. 187, 2012, pp. 10–15, Elsevier. 37

[HAN 95] HANSEN J. M.
Synthesis of spatial mechanisms using optimization and continuation methods. *Computational Dynamics in Multibody Systems*, pp. 183–196 Springer, 1995. 24

[HAN 12] HANAY M., KELBER S., NAIK A., CHI D., HENTZ S., BULLARD E., COLINET E., DURAFFOURG L., ROUKES M.
Single-protein nanomechanical mass spectrometry in real time. *Nat. Nanotechnol.*, vol. 7, 2012, pp. 602-608. 34

[HIL 16] HILL T., NEILD S., CAMMARANO A.
An analytical approach for detecting isolated periodic solution branches in weakly nonlinear structures. *Journal of Sound and Vibration*, vol. 379, 2016, pp. 150–165, Elsevier. 26, 27, 111

[HOL 81] HOLMES P. J.
Center manifolds, normal forms and bifurcations of vector fields with application to coupling between periodic and steady motions. *Physica D: Nonlinear Phenomena*, vol. 2, n° 3, 1981, pp. 449–481, Elsevier. 7

[HSU 13] HSU C. S.
Cell-to-cell mapping: a method of global analysis for nonlinear systems, vol. 64. Springer Science & Business Media, 2013. 7

[JAB 16] JABER N., RAMINI A., CARRENO A. A., YOUNIS M. I.
Higher order modes excitation of electrostatically actuated clamped–clamped microbeams: experimental and analytical investigation. *Journal of Micromechanics and Microengineering*, vol. 26, n° 2, 2016, Page 025008, IOP Publishing. 35

[JAU 10] JAUMOUILLÉ V., SINOU J.-J., PETITJEAN B.
An adaptive harmonic balance method for predicting the nonlinear dynamic responses of mechanical systems - application to bolted structures. *Journal of sound and vibration*, vol. 329, n° 19, 2010, pp. 4048–4067, Elsevier. 8

[JEP 85] JEPSON A., SPENCE A.
Folds in solutions of two parameter systems and their calculation. Part I. *SIAM journal on numerical analysis*, vol. 22, n° 2, 1985, pp. 347–368, SIAM. 23

[JEZ 91] JEZEQUEL L., LAMARQUE C.-H.
Analysis of non-linear dynamical systems by the normal form theory. *Journal of sound and vibration*, vol. 149, n° 3, 1991, pp. 429–459, Elsevier. 28

[JIA 09] JIANG J.
Determination of the global responses characteristics of a piecewise smooth dynamical system with contact. *Nonlinear Dynamics*, vol. 57, n° 3, 2009, pp. 351-361, Springer Netherlands. 62

[JOH 79] JOHNSON T., RAND R.
On the existence and bifurcation of minimal normal modes. *International Journal of Non-Linear Mechanics*, vol. 14, n° 1, 1979, pp. 1–12, Elsevier. 31

[JON 86] JONGEN H. T., JONKER P., TWILT F.
Critical sets in parametric optimization. *Mathematical programming*, vol. 34, n° 3, 1986, pp. 333–353, Springer. 25

[KAC 10a] KACEM N., ARCAMONE J., PEREZ-MURANO F., HENTZ S.
Dynamic range enhancement of nonlinear nanomechanical resonant cantilevers for highly sensitive NEMS gas/mass sensor applications. *J. Micromech. Microeng.*, vol. 20, n° 4, 2010, Page 045023. v, 36, 38, 129, 130

[KAC 10b] KACEM N., BAGUET S., HENTZ S., DUFOUR R.
Nonlinear phenomena in nanomechanical resonators: mechanical behaviors and physical limitations. *Mec. Ind.*, vol. 11, n° 6, 2010, pp. 521-529. 36

[KAC 11] KACEM N., BAGUET S., HENTZ S., DUFOUR R.
Computational and quasi-analytical models for non-linear vibrations of resonant MEMS and NEMS sensors. *Int. J. Non Linear Mech.*, vol. 46, n° 3, 2011, pp. 532 - 542. 131

[KAC 12] KACEM N., BAGUET S., HENTZ S., DUFOUR R.
Pull-In Retarding in Nonlinear Nanoelectromechanical Resonators Under Superharmonic Excitation. *Journal of Computational and Nonlinear Dynamics*, vol. 7, n° 2, 2012, Page 021011. CEA LETI and I@L Carnot institutes (NEMS Project). 36

[KAC 15] KACEM N., BAGUET S., DURAFFOURG L., JOURDAN G., DUFOUR R., HENTZ S.
Overcoming limitations of nanomechanical resonators with simultaneous resonances. *Appl. Phys. Lett.*, vol. 107, n° 7, 2015, Page 073105. 36

[KAM 15] KAMBALI P., SWAIN G., PANDEY A., BUKS E., GOTTLIEB O.
Coupling and tuning of modal frequencies in direct current biased microelectromechanical systems arrays. *Appl. Phys. Lett.*, vol. 107, n° 6, 2015, Page 063104. 38

[KAR 09] KARABALIN R. B., CROSS M. C., ROUKES M. L.
Nonlinear dynamics and chaos in two coupled nanomechanical resonators. *Phys. Rev. B*, vol. 79, 2009, Page 165309, American Physical Society. 38

[KER 90] KERNEVEZ J., LIU Y., SEOANE M., DOEDEL E.
Optimization by continuation. *Continuation and Bifurcations: Numerical Techniques and Applications*, pp. 349–362 Springer, 1990. 23, 25, 26

[KER 09] KERSCHEN G., PEETERS M., GOLINVAL J.-C., VAKAKIS A. F.
Nonlinear normal modes, Part I: A useful framework for the structural dynamicist. *Mechanical Systems and Signal Processing*, vol. 23, n° 1, 2009, pp. 170–194, Elsevier. v, 31, 101, 196

[KER 14] KERSCHEN G.
Computation of nonlinear normal modes through shooting and pseudo-arclength computation. *Modal Analysis of Nonlinear Mechanical Systems*, pp. 215–250 Springer, 2014. 7

[KHA 09] KHATER M. E., ABDEL-RAHMAN E. M., NAYFEH A. H.
A Mass Sensing Technique for Electrostatically-Actuated MEMS. *ASME Conference Proceedings*, , n° 49033, 2009, pp. 655-661, ASME. 37

[KHA 11] KHATER M. E., ABDEL-RAHMAN E. M., NAYFEH A. H.
Nonlinear Phenomena in MEMS and NEMS A Micro Sensor for Measuring Minute Gas and Biological Masses. *ENOC* Rome Italy, 24-29 July 2011. 37

[KRA 13] KRACK M., VON SCHEIDT L. P., WALLASCHEK J.
A high-order harmonic balance method for systems with distinct states. *Journal of Sound and Vibration*, vol. 332, n° 21, 2013, pp. 5476 - 5488. 8, 32

[KRA 14] KRACK M., PANNING-VON SCHEIDT L., WALLASCHEK J.
On the computation of the slow dynamics of nonlinear modes of mechanical systems. *Mechanical Systems and Signal Processing*, vol. 42, n° 1, 2014, pp. 71–87, Elsevier. v, 33, 34

[KRA 15] KRACK M.
Nonlinear modal analysis of nonconservative systems: extension of the periodic motion concept. *Computers & Structures*, vol. 154, 2015, pp. 59–71, Elsevier. 92

[KRY 16] KRYLOV N. M., BOGOLIUBOV N. N.
Introduction to Non-Linear Mechanics.(AM-11), vol. 11. Princeton University Press, 2016. 8

[KUE 15] KUETHER R. J., RENSON L., DETROUX T., GRAPPASONNI C., KERSCHEN G., ALLEN M. S.
Nonlinear normal modes, modal interactions and isolated resonance curves. *Journal of Sound and Vibration*, vol. 351, 2015, pp. 299–310, Elsevier. 92, 95

[KUM 12] KUMAR V., YANG Y., BOLEY J., CHIU G.-C., RHOADS J.
Modeling, Analysis, and Experimental Validation of a Bifurcation-Based Microsensor. *Journal of Microelectromechanical Systems*, vol. 21, n° 3, 2012, pp. 549 -558. 37

[KUZ 13] KUZNETSOV Y. A.
Elements of applied bifurcation theory, vol. 112. Springer Science & Business Media, 2013. 15, 19, 22, 23, 44, 51, 60

[LAX 09] LAXALDE D., THOUVEREZ F.
Complex non-linear modal analysis for mechanical systems: Application to turbomachinery bladings with friction interfaces. *Journal of sound and vibration*, vol. 322, n° 4-5, 2009, pp. 1009–1025, Elsevier. 33

[LAZ 10] LAZARUS A., THOMAS O.
A harmonic-based method for computing the stability of periodic solutions of dynamical systems. *Comptes Rendus Mécanique*, vol. 338, n° 9, 2010, pp. 510 - 517. 19

[LEE 05] LEE Y. S., KERSCHEN G., VAKAKIS A. F., PANAGOPOULOS P., BERGMAN L., MCFARLAND D. M.
Complicated dynamics of a linear oscillator with a light, essentially nonlinear attachment. *Physica D: Nonlinear Phenomena*, vol. 204, n° 1, 2005, pp. 41–69, Elsevier. 31

[LEG 04] LEGRAND M., JIANG D., PIERRE C., SHAW S. W.
Nonlinear normal modes of a rotating shaft based on the invariant manifold method. *International Journal of Rotating Machinery*, vol. 10, n° 4, 2004, pp. 319–335, Hindawi Publishing Corporation. 33

[LEW 94] LEWANDOWSKI R.
Non-linear free vibrations of beams by the finite element and continuation methods. *Journal of Sound and Vibration*, vol. 170, n° 5, 1994, pp. 577–593, Elsevier. 32

[LEW 97a] LEWANDOWSKI R.
Computational formulation for periodic vibration of geometrically nonlinear structures - part 1: theoretical background. *International journal of solids and structures*, vol. 34, n° 15, 1997, pp. 1925–1947, Elsevier. 32

[LEW 97b] LEWANDOWSKI R.
Computational formulation for periodic vibration of geometrically nonlinear structures - part 2: numerical strategy and examples. *International journal of solids and structures*, vol. 34, n° 15, 1997, pp. 1949–1964, Elsevier. 32

[LI 17] LI L. L., POLUNIN P. M., DOU S., SHOSHANI O., SCOTT STRACHAN B., JENSEN J. S., SHAW S. W., TURNER K. L.
Tailoring the nonlinear response of MEMS resonators using shape optimization. *Applied Physics Letters*, vol. 110, n° 8, 2017, Page 081902, AIP Publishing. 37

[LIF 03] LIFSHITZ R., CROSS M. C.
Response of parametrically driven nonlinear coupled oscillators with application to micromechanical and nanomechanical resonator arrays. *Phys. Rev. B*, vol. 67, 2003, Page 134302, American Physical Society. 38

[LIF 11] LIFSHITZ R., KENIG E., CROSS M.
Collective dynamics in arrays of coupled nonlinear resonators. *arXiv preprint arXiv:1111.2967*, , 2011. 38

[LIU 99] LIU A.-X., YANG T.-L.
Finding all solutions to unconstrained nonlinear optimization for approximate synthesis of planar linkages using continuation method. *Journal of Mechanical Design*, vol. 121, n° 3, 1999, pp. 368–374, American Society of Mechanical Engineers. 24

[LOB 08] LOBONTIU N., LUPEA I., ILIC R., CRAIGHEAD H. G.
Modeling, design, and characterization of multisegment cantilevers for resonant mass detection. *Journal of Applied Physics*, vol. 103, n° 6, 2008, Page 064306. 35

[MAL 16] MALHER A., TOUZÉ C., DOARÉ O., HABIB G., KERSCHEN G.
Passive control of airfoil flutter using a nonlinear tuned vibration absorber. *11th International Conference on Flow-induced vibrations, FIV2016*, 2016. 25

[MAN 72] MANEVICH L., MIKHLIN I.
On periodic solutions close to rectilinear normal vibration modess. *Journal of Applied Mathematics and Mechanics*, vol. 36, n° 6, 1972, pp. 988 - 994. 31

[MAN 16] MANGUSSI F., ZANETTE D. H.
Internal resonance in a vibrating beam: a zoo of nonlinear resonance peaks. *PloS one*, vol. 11, n° 9, 2016, Page e0162365, Public Library of Science. 25

[MEI 13] MEINI B.
A shift-and-deflate technique for quadratic matrix polynomials. *Linear Algebra and its Applications*, vol. 438, n° 4, 2013, pp. 1946 - 1961. 96, 208

[MIK 10] MIKHLIN Y. V., AVRAMOV K. V.
Nonlinears normal modes for vibrating mechanical systems. Review of theoretical developments. *Applied Mechanics Reviews*, vol. 63, n° 6, 2010, Page 060802, American Society of Mechanical Engineers. 31

[MOB 15] MOBAHI H., FISHER III J. W.
A Theoretical Analysis of Optimization by Gaussian Continuation. *AAAI*, 2015, pp. 1205–1211. 24

[MOO 80] MOORE G., SPENCE A.
The calculation of turning points of nonlinear equations. *SIAM Journal on Numerical Analysis*, vol. 17, n° 4, 1980, pp. 567–576, SIAM. 15

[MOO 05] MOORE G.
Floquet Theory as a Computational Tool. *SIAM Journal on Numerical Analysis*, vol. 42, n° 6, 2005, pp. 2522-2568. 19

[MOU 13] MOUSSI E. H., BELLIZZI S., COCHELIN B., NISTOR I.
Nonlinear normal modes of a two degree of freedom oscillator with a bilateral elastic stop. *arXiv preprint arXiv:1302.0805*, , 2013. 32

[MUN 03] MUNOZ-ALMARAZ F. J., FREIRE E., GALÁN J., DOEDEL E., VANDERBAUWHEDE A.
Continuation of periodic orbits in conservative and Hamiltonian systems. *Physica D: Nonlinear Phenomena*, vol. 181, n° 1, 2003, pp. 1–38, Elsevier. 32, 90

[NAC 03] NACIVET S., PIERRE C., THOUVEREZ F., JEZEQUEL L.
A dynamic Lagrangian frequency-time method for the vibration of dry-friction-damped systems. *Journal of Sound and Vibration*, vol. 265, n° 1, 2003, pp. 201 - 219. 8

[NAR 98] NARAYANAN S., SEKAR P.
A frequency domain based numerical-analytical method for non-linear dynamical systems. *Journal of Sound and Vibration*, vol. 211, n° 3, 1998, pp. 409-424. 13

[NAY 94] NAYFEH A., NAYFEH S.
On nonlinear modes of continuous systems. *Journal of Vibration and Acoustics*, vol. 116, n° 1, 1994, pp. 129–136, American Society of Mechanical Engineers. 31

[NAY 07] NAYFEH A., YOUNIS M., ABDEL-RAHMAN E.
Dynamic pull-in phenomenon in MEMS resonators. *Nonlinear Dynamics*, vol. 48, 2007, pp. 153-163, Springer Netherlands. 36

[NAY 08a] NAYFEH A. H., BALACHANDRAN B.
Applied Nonlinear Dynamics: Analytical, Computational and Experimental Methods. John Wiley & Sons, 2008. 7, 15

[NAY 08b] NAYFEH A. H., MOOK D. T.
Nonlinear oscillations. John Wiley & Sons, 2008. 7

[NET 15] NET M., SÁNCHEZ J.
Continuation of bifurcations of periodic orbits for large-scale systems. *SIAM Journal on Applied Dynamical Systems*, vol. 14, n° 2, 2015, pp. 674–698, SIAM. 33

[NG 02] NG K.-M.
A continuation approach for solving nonlinear optimization problems with discrete variables. Theses, Stanford university, 2002. 24

[NGU 13] NGUYEN V.-N.
Alternative principles for ultimate mass detection via the nonlinear dynamics of M/NEMS resonant sensors. Theses, INSA de Lyon, December 2013. v, 29

[NGU 15] NGUYEN V. N., BAGUET S., LAMARQUE C.-H., DUFOUR R.
Bifurcation-based micro-/nanoelectromechanical mass detection. *Nonlinear Dynamics*, vol. 79, n° 1, 2015, pp. 647-662, Springer Verlag. 34, 37

[PAL 17] PALLAY M., DAEICHIN M., TOWFIGHIAN S.
Dynamic behavior of an electrostatic MEMS resonator with repulsive actuation. *Nonlinear Dynamics*, vol. 89, n° 2, 2017, pp. 1525–1538, Springer. 36

[PEE 09] PEETERS M., VIGUIÉ R., SÉRANDOUR G., KERSCHEN G., GOLINVAL J.-C.
Nonlinear normal modes, Part II: Toward a practical computation using numerical continuation techniques. *Mechanical Systems and Signal Processing*, vol. 23, n° 1, 2009, pp. 195 - 216. Special Issue: Non-linear Structural Dynamics. 7, 28, 31, 102

[PEL 14] PELETAN L., BAGUET S., TORKHANI M., JACQUET-RICHARDET G.
Quasi-periodic harmonic balance method for rubbing self-induced vibrations in rotor–stator dynamics. *Nonlinear Dynamics*, vol. 78, n° 4, 2014, pp. 2501–2515, Springer. 8, 17, 62

[PEN 06] PENG H. B., CHANG C. W., ALONI S., YUZVINSKY T. D., ZETTL A.
Ultrahigh Frequency Nanotube Resonators. *Phys. Rev. Lett.*, vol. 97, 2006, Page 087203, American Physical Society. 34

[PES 01a] PESHECK E., PIERRE C., SHAW S.
Accurate reduced-order models for a simple rotor blade model using nonlinear normal modes. *Mathematical and Computer Modelling*, vol. 33, n° 10-11, 2001, pp. 1085–1097, Elsevier. 31

[PES 01b] PESHECK E., BOIVIN N., PIERRE C., SHAW S. W.
Nonlinear modal analysis of structural systems using multi-mode invariant manifolds. *Nonlinear Dynamics*, vol. 25, n° 1-3, 2001, pp. 183–205, Springer. 33

[PET 16] PETROV E.
Analysis of Bifurcations in Multiharmonic Analysis of Nonlinear Forced Vibrations of Gas Turbine Engine Structures With Friction and Gaps. *Journal of Engineering for Gas Turbines and Power*, vol. 138, n° 10, 2016, Page 102502, American Society of Mechanical Engineers. 15

[PIC 94] PICCARDI C.
Bifurcations of limit cycles in periodically forced nonlinear systems: The harmonic balance approach. *IEEE Transactions on Circuits and Systems I: Fundamental Theory and Applications*, vol. 41, n° 4, 1994, pp. 315–320, IEEE. 20

[PIL 85] PILIPCHUK V.
The calculation of strongly non-linear systems close to vibration impact systems. *Journal of Applied Mathematics and Mechanics*, vol. 49, n° 5, 1985, pp. 572–578, Elsevier. 31

[POI 15] POINCARÉ H.
Les méthodes nouvelles de la mécanique céleste. Tome 1. Gauthier-Villars et fils (Paris), 2015. 28

[POR 08] PORFIRI M.
Vibrations of parallel arrays of electrostatically actuated microplates. *J. Sound Vib.*, vol. 315, n° 4, 2008, pp. 1071-1085. 39

[RAN 92] RAND R., PAK C., VAKAKIS A.
Bifurcation of nonlinear normal modes in a class of two degree of freedom systems. *Advances in Dynamic Systems and Stability*, pp. 129–146 Springer, 1992. 31

[RAO 89] RAO J., PAPALAMBROS P.
A non-linear programming continuation strategy for one parameter design optimization problems. *Proceedings of ASME Design Automation Conference, Montreal, Quebec, Canada*, 1989, pp. 77–89. 24

[REN 14] RENSON L., DELIÉGE G., KERSCHEN G.
An effective finite-element-based method for the computation of nonlinear normal modes of nonconservative systems. *Meccanica*, vol. 49, n° 8, 2014, pp. 1901–1916, Springer. 33

[REN 16] RENSON L., KERSCHEN G., COCHELIN B.
Numerical computation of nonlinear normal modes in mechanical engineering. *Journal of Sound and Vibration*, vol. 364, 2016, pp. 177 - 206. 32

[REZ 14] REZAIEE-PAJAND M., MOGHADDASIE B.
Stability boundaries of two-parameter non-linear elastic structures. *International Journal of Solids and Structures*, vol. 51, n° 5, 2014, pp. 1089–1102, Elsevier. 23

[RHO 10] RHOADS J., SHAW S., TURNER K.
Nonlinear Dynamics and Its Applications in Micro- and Nanoresonators. *J. Dyn. Syst. Meas. Contr.*, vol. 132, n° 3, 2010, Page 034001, ASME. 37

[RIB 99a] RIBEIRO P., PETYT M.
Non-linear vibration of beams with internal resonance by the hierarchical finite-element method. *Journal of Sound and vibration*, vol. 224, n° 4, 1999, pp. 591–624, Elsevier. 32

[RIB 99b] RIBEIRO P., PETYT M.
Nonlinear vibration of plates by the hierarchical finite element and continuation methods. *International Journal of Mechanical Sciences*, vol. 41, n° 4-5, 1999, pp. 437–459, Elsevier. 32

[RIN 80] RINZEL J., MILLER R. N.
Numerical calculation of stable and unstable periodic solutions to the Hodgkin-Huxley equations. *Mathematical Biosciences*, vol. 49, n° 1-2, 1980, pp. 27–59, Elsevier. 32

[ROO 85] ROOSE D., HLAVACEK V.
A direct method for the computation of Hopf bifurcation points. *SIAM journal on applied mathematics*, vol. 45, n° 6, 1985, pp. 879–894, SIAM. 48

[ROS 62] ROSENBERG R. M.
The normal modes of nonlinear n-degree-of-freedom systems. *Journal of applied Mechanics*, vol. 29, n° 1, 1962, pp. 7–14, American Society of Mechanical Engineers. 28

[RUZ 13] RUZZICONI L., LENCI S., YOUNIS M.
An imperfect microbeam under an axial load and electric excitation: nonlinear phenomena and dynamical integrity. *Int. J. Bifurcation Chaos*, vol. 23, n° 02, 2013, Page 1350026, World Scientific Publishing Co. 36

[SAL 05] SALINGER A. G., BURROUGHS E., PAWLOWSKI R. P., PHIPPS E. T., ROMERO L. A.
Bifurcation tracking algorithms and software for large scale applications. *International Journal of Bifurcation and Chaos*, vol. 15, n° 03, 2005, pp. 1015–1032, World Scientific. 23

[SAR 11] SARROUY E., GROLET A., THOUVEREZ F.
Global and bifurcation analysis of a structure with cyclic symmetry. *International Journal of Non-Linear Mechanics*, vol. 46, n° 5, 2011, pp. 727–737, Elsevier. 32

[SCH 05] SCHÜTZE O., DELL'AERE A., DELLNITZ M.
On continuation methods for the numerical treatment of multi-objective optimization problems. *Dagstuhl Seminar Proceedings* Schloss Dagstuhl-Leibniz-Zentrum für Informatik, 2005. 25

[SCH 06] SCHILDER F., VOGT W., SCHREIBER S., OSINGA H. M.
Fourier methods for quasi-periodic oscillations. *International journal for numerical methods in engineering*, vol. 67, n° 5, 2006, pp. 629–671, Wiley Online Library. 8

[SCH 16] SCHREYER F., LEINE R. I.
A Mixed Shooting–Harmonic Balance Method for Unilaterally Constrained Mechanical Systems. *Archive of Mechanical Engineering*, vol. 63, n° 2, 2016, pp. 297–314, De Gruyter Open. 8

[SEY 79a] SEYDEL R.
Numerical computation of branch points in nonlinear equations. *Numerische Mathematik*, vol. 33, n° 3, 1979, pp. 339–352, Springer. 15

[SEY 79b] SEYDEL R.
Numerical computation of branch points in ordinary differential equations. *Numerische Mathematik*, vol. 32, n° 1, 1979, pp. 51–68, Springer. 15

[SEY 09] SEYDEL R.
Practical bifurcation and stability analysis, vol. 5. Springer Science & Business Media, 2009. 7, 8, 10, 15, 21, 32, 44, 46, 89

[SHA 91] SHAW S., PIERRE C.
Non-linear normal modes and invariant manifolds. *Journal of Sound and Vibration*, vol. 150, n° 1, 1991, pp. 170-173, Elsevier. 28, 33

[SHA 93] SHAW S. W., PIERRE C.
Normal modes for non-linear vibratory systems. *Journal of sound and vibration*, vol. 164, n° 1, 1993, pp. 85–124, Elsevier. 33

[SPL 08] SPLETZER M., RAMAN A., SUMALI H., SULLIVAN J. P.
Highly sensitive mass detection and identification using vibration localization in coupled microcantilever arrays. *Applied Physics Letters*, vol. 92, n° 11, 2008, Page 114102, AIP. 39

[STA 09] STAROSVETSKY Y., GENDELMAN O.
Vibration absorption in systems with a nonlinear energy sink: nonlinear damping. *Journal of Sound and Vibration*, vol. 324, n° 3, 2009, pp. 916–939, Elsevier. 26

[STO 11] STOYKOV S., RIBEIRO P.
Nonlinear free vibrations of beams in space due to internal resonance. *Journal of Sound and Vibration*, vol. 330, n° 18-19, 2011, pp. 4574–4595, Elsevier. 32

[STO 14] STOYKOV S., MARGENOV S.
Numerical computation of periodic responses of nonlinear large-scale systems by shooting method. *Computers & Mathematics with Applications*, vol. 67, n° 12, 2014, pp. 2257–2267, Elsevier. 7

[SUN 97] SUNDARARAJAN P., NOAH S.
Dynamics of forced nonlinear systems using shooting/arc-length continuation method—application to rotor systems. *Journal of vibration and acoustics*, vol. 119, n° 1, 1997, pp. 9–20, American Society of Mechanical Engineers. 7

[TAO 18] TAO G., CHOUBEY B.
Variability Induced Sensitivity Degradation in Coupled Nano/Micro Resonant Sensors. *IEEE Transactions on Nanotechnology*, , 2018, IEEE. 39

[THI 09] THIRUVENKATANATHAN P., YAN J., WOODHOUSE J., SESHIA A. A.
Enhancing parametric sensitivity in electrically coupled MEMS resonators. *Journal of Microelectromechanical Systems*, vol. 18, n° 5, 2009, pp. 1077–1086, IEEE. 39

[THO 13] THOMAS O., MATHIEU F., MANSFIELD W., HUANG C., TROLIER-MCKINSTRY S., NICU L.
Efficient parametric amplification in micro-resonators with integrated piezoelectric actuation and sensing capabilities. *Appl. Phys. Lett.*, vol. 102, n° 16, 2013, Page 163504, American Institute of Physics. 35

[TUR 01] TURNER K., ZHANG W.
Design and analysis of a dynamic MEM chemical sensor. *American Control Conference, 2001. Proceedings of the 2001*, vol. 2, 2001, pp. 1214-1218 vol.2. 35

[VAK 01] VAKAKIS A. F., MANEVITCH L. I., MIKHLIN Y. V., PILIPCHUK V. N., ZEVIN A. A.
Normal modes and localization in nonlinear systems. Springer, 2001. 31

[VAN 01] VANDERBECK F.
A nested decomposition approach to a three-stage, two-dimensional cutting-stock problem. *Management Science*, vol. 47, n° 6, 2001, pp. 864–879, INFORMS. 25

[VER 06] VERHULST F.
Nonlinear differential equations and dynamical systems. Springer Science & Business Media, 2006. 7, 15

[VER 18] VERHULST F.
Averaging methods in nonlinear dynamical systems / J. A. Sanders, F. Verhulst. , 2018. 7

[VON 01] VON GROLL G., EWINS D. J.
The harmonic balance method with arc-length continuation in rotor/stator contact problems. *Journal of sound and vibration*, vol. 241, n° 2, 2001, pp. 223–233, Elsevier. 8, 17

[WAL 16] WALTER V., BOURBON G., LE MOAL P., KACEM N., LARDIÈS J.
Electrostatic actuation to counterbalance the manufacturing defects in a MEMS mass detection sensor using mode localization. *Procedia Engineering*, vol. 168, 2016, pp. 1488–1491, Elsevier. 37

[WAN 11] WANG M.
Feasibility study of nonlinear tuned mass damper for machining chatter suppression. *Journal of Sound and Vibration*, vol. 330, n° 9, 2011, pp. 1917–1930, Elsevier. 25

[WAN 12] WANG D. F., CHATANI K., IKEHARA T., MAEDA R.
Mode localization analysis and characterization in a 5-beam array of coupled nearly identical micromechanical resonators for ultra-sensitive mass detection and analyte identification. *Microsystem technologies*, vol. 18, n° 11, 2012, pp. 1923–1929, Springer. 39

[WIG 03] WIGGINS S.
Introduction to Applied Nonlinear Dynamical Systems and Chaos, vol. 2. Springer Science & Business Media, 2003. 15

[WOL 96] WOLF D. M., SANDERS S. R.
Multiparameter homotopy methods for finding dc operating points of nonlinear circuits. *IEEE Transactions on Circuits and Systems I: Fundamental Theory and Applications*, vol. 43, n° 10, 1996, pp. 824–838, IEEE. 25

[WRI 90] WRIGGERS P., SIMO J.
A general procedure for the direct computation of turning and bifurcation points. *International journal for numerical methods in engineering*, vol. 30, n° 1, 1990, pp. 155–176, Wiley Online Library. 15

[XIE 08] XIE H., VITARD J., HALIYO S., RÉGNIER S.
Enhanced sensitivity of mass detection using the first torsional mode of microcantilevers. *Meas. Sci. Technol.*, vol. 19, n° 5, 2008, Page 055207. 35

[XIE 16a] XIE L., BAGUET S., PRABEL B., DUFOUR R.
Bifurcation tracking by Harmonic Balance Method for performance tuning of nonlinear dynamical systems. *Mechanical Systems and Signal Processing*, , 2016, Elsevier. v, 15, 24, 43, 45, 46, 57, 68

[XIE 16b] XIE L., BAGUET S., PRABEL B., DUFOUR R.
Numerical Tracking of Limit Points for Direct Parametric Analysis in Nonlinear Rotordynamics. *Journal of Vibration and Acoustics*, vol. 138, n° 2, 2016, Page 021007, American Society of Mechanical Engineers. 57, 62, 188

[YAN 06] YANG Y. T., CALLEGARI C., FENG X. L., EKINCI K. L., ROUKES M. L.
Zeptogram-Scale Nanomechanical Mass Sensing. *Nano Letters*, vol. 6, n° 4, 2006, pp. 583-586. 36

[YOU 03] YOUNIS M., ABDEL-RAHMAN E., NAYFEH A.
A reduced-order model for electrically actuated microbeam-based MEMS. *J. Microelectromech. Syst.*, vol. 12, n° 5, 2003, pp. 672-680. 130

[YOU 08] YOUNIS M. I., SALEEM F. M. A.
New Conceps of Mass Sensors Based on Nonlinear Dynamic Principles. *Proceeding of the XIth International Congress and Exposition*, Orlando, Florida USA, 2-5 June 2008. 35

[YOU 09] YOUNIS M., ALSALEEM F.
Exploration of New Concepts for Mass Detection in Electrostatically-Actuated Structures Based on Nonlinear Phenomena. *J. Comput. Nonlinear Dyn.*, vol. 4, n° 2, 2009, Page 021010, ASME. 35, 37

[YUR 95] YURKE B., GREYWALL D. S., PARGELLIS A. N., BUSCH P. A.
Theory of amplifier-noise evasion in an oscillator employing a nonlinear resonator. *Phys. Rev. A*, vol. 51, 1995, pp. 4211–4229, American Physical Society. 37

[YUR 06] YURKE B., BUKS E.
Performance of Cavity-Parametric Amplifiers, Employing Kerr Nonlinearites, in the Presence of Two-Photon Loss. *J. Lightwave Technol.*, vol. 24, n° 12, 2006, pp. 5054–5066, OSA. 37

[ZHA 04] ZHANG W., TURNER K. L.
A mass sensor based on parametric resonance. *Solid-State Sensor, Actuator and Microsystems Workshop*, 6-10June, 2004. 35

[ZHA 05] ZHANG W., TURNER K.
Application of parametric resonance amplification in a single-crystal silicon micro-oscillator based mass sensor. *Sens. Actuators, A*, vol. 122, n° 1, 2005, pp. 23-30. 35

[ZHA 16] ZHAO C., MONTASERI M. H., WOOD G. S., PU S. H., SESHIA A. A., KRAFT M.
A review on coupled MEMS resonators for sensing applications utilizing mode localization. *Sensors and Actuators A: Physical*, vol. 249, 2016, pp. 93–111, Elsevier. 39

[ZHO 15] ZHOU B., THOUVEREZ F., LENOIR D.
A variable-coefficient harmonic balance method for the prediction of quasi-periodic response in nonlinear systems. *Mechanical Systems and Signal Processing*, vol. 64-65, 2015, pp. 233 - 244. 8

FOLIO ADMINISTRATIF
THÈSE DE L'UNIVERSITE DE LYON OPEREE AU SEIN DE L'INSA LYON

NOM: GRENAT DATE de SOUTENANCE: 30/08/2018

Prénoms: Clément

TITRE: Nonlinear Normal Modes and multi-parametric continuation of bifurcations: application to vibration absorbers and architectured MEMS sensors for mass detection

NATURE: Doctorat Numéro d'ordre: 2018LYSEI078

École doctorale: MEGA

Spécialité: Mécanique - Génie Mécanique - Génie Civil

RÉSUMÉ:

Un des buts de cette thèse est d'approfondir la compréhension de la dynamique non-linéaire, notamment celle des MEMS, en proposant de nouvelles méthodes d'analyse paramétrique et de calcul de modes normaux non-linéaires. Dans une première partie, les méthodes de détection, de localisation et de suivi de points de bifurcation selon un unique paramètre sont rappelées. Ensuite, une nouvelle méthode d'analyse multi-paramétrique basée sur la continuation récursive d'extremums est présentée. Cette méthode est ensuite appliquée à un absorbeur de vibration non-linéaire afin de repousser l'apparition de solutions isolées. Deuxièmement, une méthode de calcul de modes normaux non-linéaires est présentée. Une condition de phase optimale et une régularisation de l'équation de mouvement sont proposées afin d'obtenir une méthode de continuation plus robuste. Ensuite, un problème quadratique aux valeurs propres modifié pour le calcul de stabilité et de points de bifurcation est présenté. Finalement, le calcul de modes normaux non-linéaires a été étendu aux systèmes non-conservatifs permettant la continuation des résonances d'énergie en déplacement et des résonances de phase. Troisièmement, la dynamique non-linéaire de réseaux de MEMS basé sur plusieurs micro-poutres résonantes est analysée à l'aide des méthodes proposées. Tout d'abord, un phénomène de synchronisation de points de bifurcations dû au couplage électrostatique dans les réseaux de MEMS est expliqué. Puis, la dynamique non-linéaire d'un réseau dissymétrisé par l'ajout d'une petite masse sur une micro-poutre est analysée. Enfin, des mécanismes de détection de masse exploitant ces phénomènes non-linéaires sont présentés.

MOTS-CLÉS: Dynamique nonlinéaire, Analyse paramétrique, Continuation récursive multi-paramétrique, Modes normaux nonlinéaires, Non-conservatif, Modes normaux nonlinéaire isolés, Solutions isolées, Tableaux de MEMS, Quantification de masse, Méthode de la Balance Harmonique.

Laboratoire(s) de recherche: Laboratoire de Mécanique des Contacts et des Structures
UMR CNRS 5259 - INSA de Lyon
18-20 rue des Sciences
69621 Villeurbanne Cedex FRANCE

Directeur de thèse: M. Régis DUFOUR

Co-Directeur de thèse: M. Sébastien BAGUET

Co-Encadrant de thèse: M. Claude-Henri LAMARQUE

Présidente du jury: Mme. Anne TANGUY

Composition du jury:

A. Tanguy	G. Kerschen
S. Hentz	R. Dufour
B. Cochelin	C-H. Lamarque
E. Sarrouy	S. Baguet